SYNTHESIS AND REACTIVITY OF FLUORESCENT RARE-EARTH DOPED CERIUM OXIDE NANOMATERIALS

by

ANNE ELIZABETH D'ACHILLE

Bachelor of Science, 2012
Grove City College
Grove City, Pennsylvania

Submitted to the Graduate Faculty of the
College of Science and Engineering
Texas Christian University
in partial fulfillment of the requirements
for the degree of

Doctor of Philosophy

May 2019

SYNTHESIS AND REACTIVITY OF FLUORESCENT RARE EARTH-DOPED CERIUM OXIDE NANOMATERIALS

By

Anne D'Achille

Dissertation Approved:

Major Professor

For The College of Science and Engineering

ACKNOWLEDGMENTS

This process has been an incredible adventure that would not have been possible without a host of people. I cannot possibly list everyone, but to my advisor Dr. Coffer, our collaborator Dr. Anton Naumov, my committee Dr. Green, Dr. Annunziata, and Dr. Neilson, and to my friends, family, fellow graduate students, and all the teachers and professors who have invested in me-thank you. In addition, thank you to the College of Science and Engineering at TCU for funding.

Dr. Coffer, you have been incredible example of what a mentor and advisor should be. Thank you for giving me the opportunity to wander into the strange land of cerium oxide and melanin. This work was only possible due to your guidance and seemingly endless “what does this mean??” questions. Your patience, knowledge, compassion, and encouragement has shaped me into the scientist I am today.

Dr. Annunziata and Dr. Neilson, thank you for all your help and feedback on my progress report, proposal, and this dissertation. Your questions have challenged me to think deeper about my project. Dr. Green, you have shaped how I approach teaching, advising, and being a female scientist (and mom). The influence of your support and reassurance cannot be overstated.

This work was written with the aid of coffee and music. For the latter, I owe deep gratitude to Lin Manuel Miranda (although he will likely never read this), whose soundtracks were on repeat non-stop for the last several months. Your words encouraged and inspired me, provided words for some unacknowledged emotions and fears, and made for great 3 AM dance parties. Also, “My Shot” is an excellent pre-dissertation defense pump-up/nerve-calming song. Thanks for that.

Kelly and Jacky (and Jared and Jonny of course): You are my Texas family. From day one, you made us feel like we belonged here. I cannot find words to explain how your friendship has enriched my life.

Samantha: You have a generous spirit, a brilliant mind, and so much passion for everything you do. Your presence touches so many of my memories of TCU. Between our coffee trips, vent-fests or parties depending on experiment progress, and naps while you held my newborn ("I'm not tired at all!"), your friendship kept me sane.

Coffer Group: My lab family. You have all had an enormous influence on this work. You have taught me, challenged me, inspired me, and provided me with friendship through this time. I am blessed to call you all colleagues as well as friends.

My parents: Thank you to my parents for raising me to be a strong, curious, intelligent woman. Thank you for your excitement, your advice, and your encouragement in all my endeavors over the last 29 years. I apologize for any grey hairs I gave you!

Elliott: Having you as a son may be one of the greatest gifts I've ever received. You have filled our house with laughter, total chaos, and limitless love. I'm inspired daily by your curiosity, passion, and wonder at life.

Finally, to Adam: You have been my rock. I still can't believe we've gotten to this point! Thank you for supporting my dream, no matter what life threw at us. You were with me through all of it: the expected, unexpected, good, and bad. You've moved half-way across the country, endured the grad school chaos and anxiety, and removed about 50,000 unnecessary commas from my writing. I truly could not have done this without you.

TABLE OF CONTENTS

LIST OF FIGURES

LIST OF TABLES

Chapter 1: Introduction

1.1. Cerium General Background

1.1.1. Abundance

The rare earth elements or lanthanides consist of the f-block elements from lanthanum to lutetium. Scandium and yttrium are frequently included due to similar chemical properties and presence in ore deposits, bringing the total number of rare earths to 17 (Table 1.1).[1] Lanthanide-containing ores are typically composed of several of the elements as a mixture. Since most of the lanthanides have similar solubilities in a range of solvents, acids, and bases, the elements were named “rare earths” due to the difficult process of isolation and purification of the individual elements.[2]

Table 1.1 *Rare earth elements with their assigned symbols and properties including their abundance the Earth’s crust in ppm, common oxidation states, and ionic radii.*[3]

Element	Symbol	Abundance (ppm)	Oxidation States	Ionic Radii (nm)
Lanthanum	La	39	La^{3+}	0.118
Cerium	Ce	66.5	Ce^{3+}, Ce^{4+}	0.114, 0.097
Praseodymium	Pr	9.2	Pr^{3+}, Pr^{4+}	0.114, 0.099
Neodymium	Nd	41.5	Nd^{3+}	0.114
Samarium	Sm	7.05	Sm^{3+}	0.109
Europium	Eu	2.0	Eu^{2+}, Eu^{3+}	0.125, 0.107
Gadolinium	Gd	6.2	Gd^{3+}	0.106
Terbium	Tb	1.2	Tb^{3+}, Tb^{4+}	0.105, 0.088
Dysprosium	Dy	5.2	Dy^{3+}	0.103
Holmium	Ho	1.3	Ho^{3+}	0.102
Erbium	Er	3.5	Er^{3+}	0.100
Thulium	Tm	0.52	Tm^{3+}	0.099
Ytterbium	Yb	3.2	Yb^{3+}	0.098
Lutetium	Lu	0.8	Lu^{3+}	0.097
Yttrium	Y	33	Y^{3+}	0.102

Despite the name, rare earths are relatively common in the earth's crust, with cerium most abundant with a crustal abundance of 66.5 ppm (Table 1.1). For reference gold, silver, and lead have abundances in the Earth's crust of 0.004, 0.075, 14 ppm, and 60 ppm respectively.[1]

1.1.2. Electron Configuration/Redox Activity

The 4f and 5d orbitals are very close in energy, so cerium utilizes both orbitals to minimize electron repulsion. As a result, elemental cerium has an electron configuration of [Xe] $6s^2 5d^1 4f^1$. The 4f electrons shield the 5d orbitals, so the heavier lanthanides typically have electron configurations of [Xe] $6s^2 4f^n$, with a few exceptions.[4]

During oxidation of cerium, the 6s electrons are removed first, followed by the 5d and the 4f electrons. Cerium can support two stable oxidation states: Ce^{3+} with an electron configuration of [Xe] $6s^0 5d^0 4f^1$, and Ce^{4+} which is isoelectronic with xenon.[4]

1.1.3. Synthesis and Crystal Structure of Cerium Oxide

Cerium is rapidly oxidized to CeO_2 (ceria) or Ce_2O_3 upon exposure to air or any oxygen containing atmosphere.[5] Cerium hydroxide or other oxygen-containing cerium salts (oxalates, nitrates, carbonates, etc.) also convert to cerium oxide upon heating in oxygen containing atmospheres. During this oxidation, cerium's valence electrons transfer to the 2p orbitals of the oxygen.[6]

Ce_2O_3 and CeO_2 stoichiometries are by far most stable, most commonly found, and therefore most studied. Cerium may be partially oxidized to Ce^{3+}, retaining its 4f electron localized on the cerium atom,[6] and forming Ce_2O_3 (Eqn 1.1).

$$2Ce(s) + \frac{3}{2}O_2(g) = Ce_2O_3(s)$$ (Eqn 1.1)[7-9]

$$Ce(s) + O_2(g) = CeO_2(s)$$ (Eqn 1.2)[7-9]

Since formation of CeO_2 only uses one cerium atom, its standard molar enthalpy of formation, $\Delta_f H_m^\circ$, is lower than the formation enthalpy of Ce_2O_3 (Table 1.2). At 298 K and standard pressure, Ce_2O_3 spontaneously reacts with gaseous oxygen to yield CeO_2 (Eqn 1.3).

$$Ce_2O_3(s) + \frac{1}{2}O_2(g) = 2CeO_2(s)$$ (Eqn 1.3)[7,9]

Table 1.2 *Thermodynamic data for oxidation of Ce(s) to Ce_2O_3(s) and CeO_2(s), and of Ce_2O_3(s) to CeO_2(s).*[10]

Reaction	$\Delta_f H_m^\circ$ (kJ/mol)	$\Delta_f S_m^\circ$ (J/mol)	$\Delta_f G_m^\circ$ (kJ/mol)
$2Ce(s) + \frac{3}{2}O_2(g) = Ce_2O_3(s)$	-1796.2	150.6	-1706
$Ce(s) + O_2(g) = CeO_2(s)$	-1088.7	62.3	-1024
$Ce_2O_3(s) + \frac{1}{2}O_2(g) = 2CeO_2(s)$	-371	-127.1	-342

CeO_2 favors a cubic fluorite structure with cerium atoms arranged in a face-centered cubic structure and oxygen atoms in the tetrahedral holes (Figure 1.1a).[11] Within this crystal structure, CeO_2 easily gains and loses oxygen as discussed in depth in Section 1.1.4, lowering the Ce^{4+}/Ce^{3+} redox potential. Ce_2O_3 crystallizes in a hexagonal crystal structure, with Ce ions bonded to seven oxygen neighbors, closer to four of the oxygens than the other three (Figure 1.1b).[12]

In nano-sized CeO_2, Ce^{3+} defects usually remain dispersed within the CeO_2 structure, with the Ce^{3+}/Ce^{4+} ratio of a specific sample controlled by factors including particle or

crystalline domain size[13] and the addition of dopants.[14] The substitution of Ce^{3+} for Ce^{4+} introduces oxygen vacancies, due to the difference in charge coupled with lattice strain from radii differences (Table 1.1).[15,35-39] The Ce^{3+}/Ce^{4+} ratio and resulting oxygen vacancy concentration is fundamental to the majority of CeO_2 chemical applications, and will be discussed more thoroughly in Section 1.1.6.

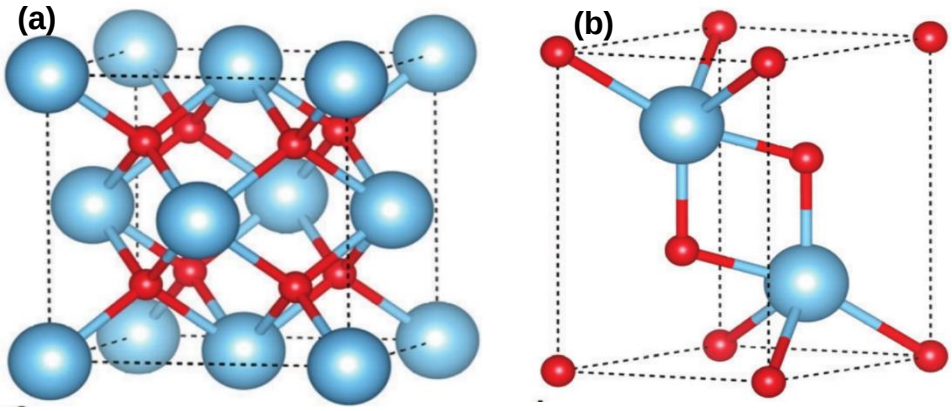

Figure 1.1 *Crystal structures of (a) CeO_2 and (b) Ce_2O_3. Blue spheres are cerium atoms while red spheres are oxygen atoms. Adapted from Reference [16].*

1.1.4. CeO_2 Redox Chemistry and Vacancy Formation

As discussed earlier, CeO_2 can gain and lose oxygen with the concurrent oxidation or reduction of neighboring cerium. For example, two Ce^{3+} ions of the surface of a large CeO_2 surface are accompanied by nearby oxygen vacancies to maintain charge balance. The 4f electron on each Ce^{3+} ion can transfer to the 2p orbital of an oxygen atom.[6] This oxidizes the Ce^{3+} to Ce^{4+}, binds the oxygen, and eliminates the oxygen vacancy. The capture of oxygen is reversible, as the electrons contributed by cerium can transfer from the O_{2p} orbital back to the Ce_{4f} orbital. The Ce^{4+} ion is reduced back to Ce^{3+}, and the oxygen is released to create an oxygen vacancy (Figure 1.2).

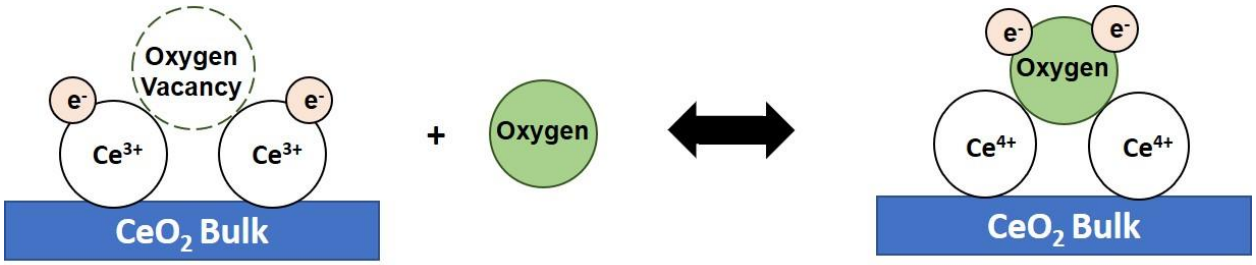

Figure 1.2 *Diagram of oxygen capture and release mechanism from CeO_2 surface. Left: Two Ce^{3+} ions with oxygen vacancy and 4f electrons. Right: Bound oxygen following Ce_{4f} to O_{2p} electron transfer, with oxidation from Ce^{3+} to Ce^{4+}.*

The capture and release of oxygen by CeO_2 can also be written as Equation 1.4 using Kröger-Vink notation, where Ce_{Ce}^{*} indicates a Ce^{4+} ion in the assigned fcc locations, O_O^*indicates an O^{2-} in the tetrahedral holes, with the charge due to the electron from Ce^{4+}.[17] Ce_{Ce}' indicates that the cerium remains in the original lattice space, but reduced to Ce^{3+}, and $V_{\ddot{O}}$ denotes the newly formed vacancy at the oxygen site.

$$2Ce_{Ce}^{*} + O_O^{*} \leftrightarrow 2Ce_{Ce}' + V_{\ddot{O}} + \frac{1}{2}O_2(g) \qquad \text{(Eqn 1.4)}$$

The Ce^{3+}/Ce^{4+} redox couple is also active in CeO_2 chemical reactivity with various reactive oxygen species (ROS), such as H_2O_2, $O_2^{\bullet-}$ and $OH^{\bullet}$.[18,19] The ROS oxygen is able to bind to both Ce^{3+} and Ce^{4+} sites on the CeO_2 by accepting or donating electrons to the cerium as necessary.

1.1.5. CeO_2 Crystallographic Planes

As this dissertation focuses exclusively on CeO_2-based morphologies, the following crystallographic discussion will focus on the fully oxidized structure. Three crystallographic planes are commonly observed, each with differing surface energies and activities in catalytic applications. Examples of exposed surfaces of each plane is shown in Figure 1.3, although the (111) and (200) planes can have multiple terminations.

The (111) index, or surface, is regarded as the most stable plane, and is commonly accepted to be terminated by oxygen anions.[20] The (220) plane is of intermediate stability, with stoichiometric termination. However, the (220) plane attracts a higher ratio of oxygen vacancies, increasing the surface energy relative to the (111) plane.[21]

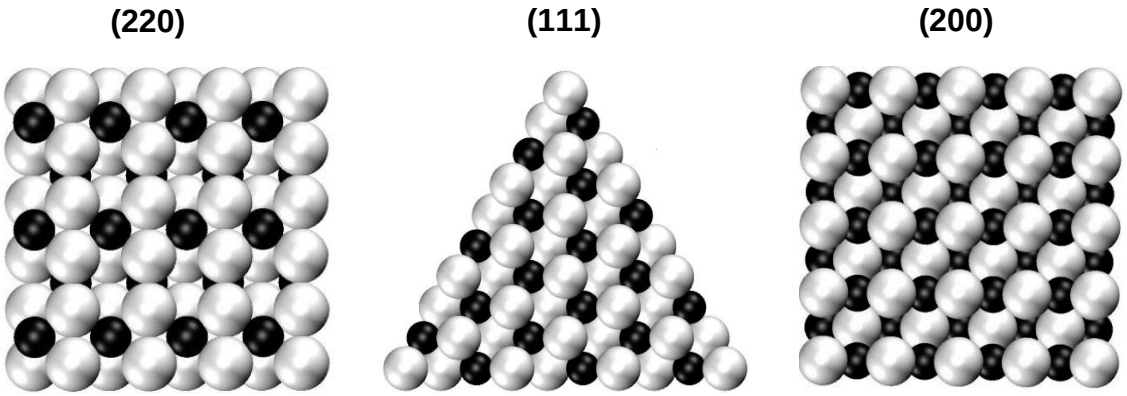

Figure 1.3 *CeO_2 surfaces of the (220), (111), and (200) crystalline planes. Black spheres represent cerium atoms and white spheres represent oxygen atoms. Adapted from Reference [12].*

The (200) surface is the least stable plane, with the highest surface energy. The two repeating layers, one with Ce^{4+} and the other with O^{2-}, results in charged layers and a dipole moment perpindicular to the surface. Simplified computational studies propose an O-terminated surface with half the oxygen removed to eliminate the dipole and reduce the surface energy.[21] Experimental analysis is divided, with some groups proposing Ce-terminated and others suggesting isolated CeO groups not incorporated into the crystal lattice.[21] Aberation-corrected high resolution TEM in an Argonne/Oak Ridge joint effort displayed surface termination by multiple species including O, Ce, and CeO.[12] Computationally, the differences between these terminations are small.[21]

1.1.6. Variation of CeO_2 Cubic Structure

Bulk CeO_2 has a lattice parameter of 0.5411 nm which increases with lattice strain.[22] The oxygen vacancies, Ce^{3+} defects, and addition of dopants can all influence the lattice parameter.

The first significant source of lattice strain are defects, most frequently oxygen vacancies on the particle surface. The absence of the anionic oxygen increases coulombic repulsion between the neighboring cationic cerium atoms. Oxygen vacancies also disrupt the balanced charge of the CeO_2 crystal structure, and requires reduction of two Ce^{4+} to Ce^{3+} to regain balance. The ionic radius of Ce^{3+} (0.114 nm) is significantly larger than that of Ce^{4+} (0.097 nm), further straining the crystal lattice and expanding the CeO_2 lattice (Figure 1.4).[23]

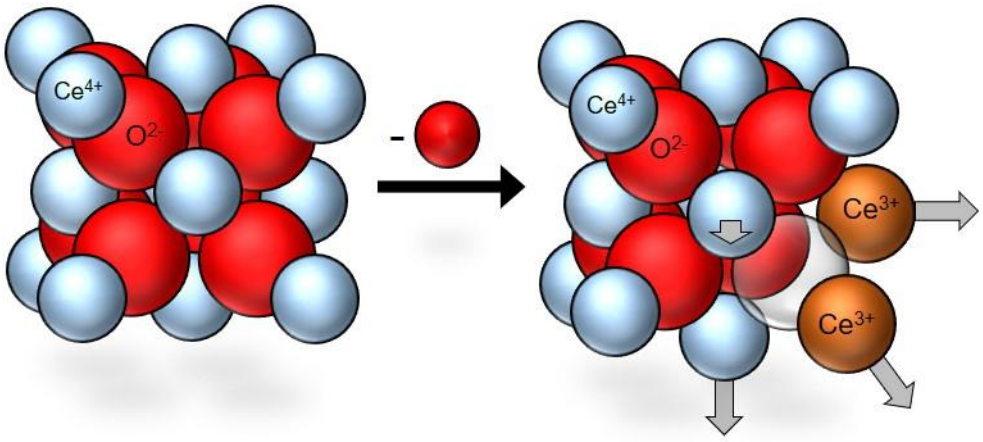

Figure 1.4 *Space filling model of one CeO_2 unit cell showing lattice expansion upon insertion of oxygen vacancy, with grey arrows indicating the movement of individual ions.*

Crystal defects often concentrate at the particle surface due to termination of the crystal structure and adsorption of hydroxyls and carbonates from the particle's surroundings. Oxygen vacancies also form near the surface of the particle due to oxygen

capture and release to the surroundings.[24] The impact of a single vacancy is diluted across the breadth of a large particle. However, due to an increased surface area:volume ratio, small particles cannot alleviate the lattice strain as efficiently as the larger particles, thereby increasing the lattice parameter.[23] Experimental results have shown that the particle size directly influences the lattice parameter by Equation 1.5, where Δa is the change in lattice parameter from the bulk measured in nm, and *D* is the particle size in nm.[14]

$$\Delta a = 0.031 D^{-0.4763} \qquad \text{(Eqn 1.5)}[14]$$

The inclusion of dopants also has significant implications for the crystal structure of CeO_2. Rare earth and transition metals are commonly used as dopants, substituting for the Ce^{4+} within the CeO_2 crystal structure. These dopants typically have ionic radii between Ce^{3+} and Ce^{4+} (Table 1.1), limiting the lattice strain due to radii difference. The dopants often have oxidation states of M^{3+}, as shown in Figure 1.5, and an oxygen vacancy is established to balance the resulting charge disparity.[25] Each oxygen vacancy within CeO_2 requires two M^{3+} cations for full charge balance, so a neighboring Ce^{4+} is reduced to Ce^{3+}. As a result, the dopants typically increase the size of the CeO_2 lattice.

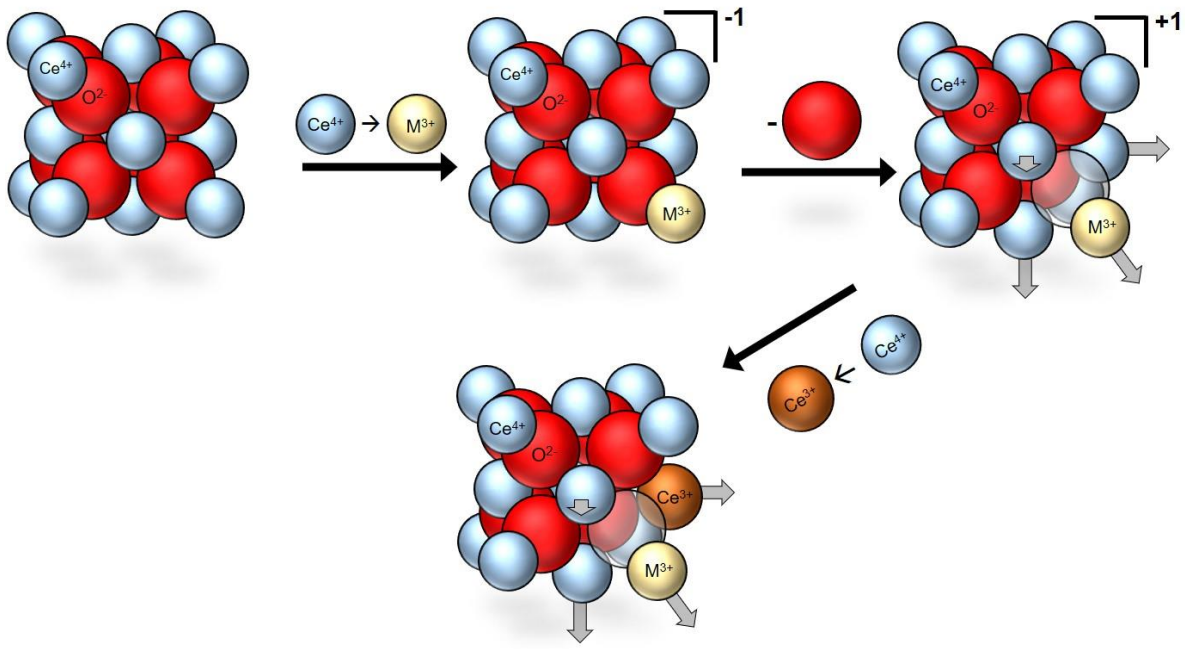

Figure 1.5 *Diagram of doping influence. A M^{3+} is substituted in a Ce^{4+} site, followed by formation of an oxygen vacancy, and finally reduction to Ce^{3+}. Gray arrows indicate movement of ions from original lattice position.*

Upon heating to high temperature in the absence of O_2, CeO_2 is reduced forming $CeO_{2-\delta}$, with the oxygen deficit increasing with annealing temperature to a maximum of $\delta=0.286$.[8] The lattice parameter also increases with annealing temperature until $\delta>0.286$, at which point the structure goes through a series of crystal structures before finally converting to the hexagonal Ce_2O_3.

1.1.7. Optical Properties

CeO_2 has a theoretical band gap of ~3.2 eV, corresponding to 390 nm, although the exact value varies based on particle size and Ce^{3+} concentration.[26] CeO_2 nanomaterials typically have an experimental band gap of 3.1-3.5 eV, or 400-350 nm, thereby making CeO_2 absorb in the UV region.[27] Due to the absence of valence electrons in Ce^{4+}, this absorbance is due to a charge transfer, with excitation of an electron from the O_{2p} valence

band to the Ce_{4f} conduction band.[28] However, a $4f^1 \rightarrow 5d^1$ transition of Ce^{3+} is in the same energetic region, complicating interpretation of the absorbance.[28]

The band gap of CeO_2 is primarily influenced by the Ce^{3+} concentration. The Ce^{3+} defects and O^{2-} vacancies within the CeO_2 lattice add energy levels below the CeO_2 conduction band.[29] The Ce^{3+} concentration is increased by either decreasing the particle size, through the addition of dopants, and irradiation using an electron beam.[30,31]

While the absence of Ce^{4+} valence electrons prevents fluorescence in defect-free CeO_2, small particles with high concentrations of Ce^{3+} defects frequently fluoresce with a range of excitation and emission wavelengths.[32,33] Some groups promote quantum confinement as the source of the fluorescence, but Ce^{3+}-associated defects is commonly accepted, with photoluminescence often used as an indicator of Ce^{3+} concentration within CeO_2 NPs.[32,34]

1.2. Synthesis

CeO_2 has been known in bulk form since 1803.[35] However, significant advances in the synthesis and characterization of nanomaterials brought new properties of CeO_2 to light with substantial implications for the chemical reactivity. As the size, Ce^{3+}/Ce^{4+} ratio,[20] and exposed crystalline planes[36] can all influence the chemical reactivity, extensive research has focused on controlled synthesis of a broad range of CeO_2 morphologies. Various CeO_2 morphologies have been synthesized through controlled precipitation, hydrothermal, sol-gel, surfactant-assisted, electrodeposition, and micellular methods, as well as ball-milling and other techniques. Several reviews have surveyed these methods and the resulting materials and due to the breadth of prior research, only the most relevant studies will be discussed.[5,13]

1.2.1. Precipitation

The most commonly studied morphologies arise from high yield procedures, especially those involving precipitation of cerium complexes such as cerium carbonate or cerium hydroxide. A series of Ce^{3+} and Ce^{4+} salts have been reacted bases such as NaOH, NH_4OH, and urea,[37,38] as well as other precipitating agents such as phosphates, carbonates, and H_2O_2. These reactions typically are carried out near room temperature. The advantage of the technique and the ease of introducing dopants is countered by significant product agglomeration in the absence of surface directing agents.[5]

Many surfactants or capping agents, such as poly-vinylpyrolidone (PVP) and hexadecyl trimethyl ammonium bromide (CTAB), have been added to reduce aggregation, control particle size, or encourage CeO_2 growth in unique morphologies. PVP has been used primarily as a capping agent, preventing aggregation and growth of small particles.[39] CTAB binds preferentially to the (111) plane, encouraging binding through the (200) planes to yield nanorods, wires, and tubes.[40] The products are often sintered to increase materials strength, density, grain size, and durability under high temperature applications.[37]

1.2.2. Hydrothermal Methods

Hydrothermal methods are slightly more complex routes to synthesize CeO_2 that utilize elevated temperatures and pressures to access higher energy morphologies unobtainable by lower temperature reactions. The hydrothermal approach has produce rods,[41,42] cubes,[43] wires,[44] tubes,[45] and polyhedral particles, as well as a number of other morphologies. A broad range of dopants have also been incorporated into such morphologies, including rare earth metals, transition metals, and alkaline earth metals.[5,46]

This flexibility and simplicity relative to templating methods described below makes hydrothermal procedures highly appealing for the rational synthesis of structured nanoceria.

Like the precipitation methods, hydrothermal reactions initiate with the reaction of cerium salts with precipitating agents, typically using bases such as NaOH, NH_4OH, or urea to precipitate cerium hydroxide species. This solution is then transferred and heated in a vessel stable under pressurization and heating. In principle, the precursor concentrations, precipitating agents, reaction temperature and duration, and any added surface directing agents drive the specific morphology and dimensions of the CeO_2.[5]

Cerium oxide and hydroxide nanomaterials frequently grow through a combination of two mechanisms: Ostwald Ripening (OR) and Oriented Attachment (OA). OR relies on dissolution and recrystallization of precipitates, due to the chemical equilibria controlled by reaction conditions.[47] Particles with higher surface area are gradually consumed and reprecipitated on larger particles, leading to particle growth (Figure 1.6). This mechanism frequently produces near spherical morphologies with high crystallinity and few defects due to the slow crystal growth.[48]

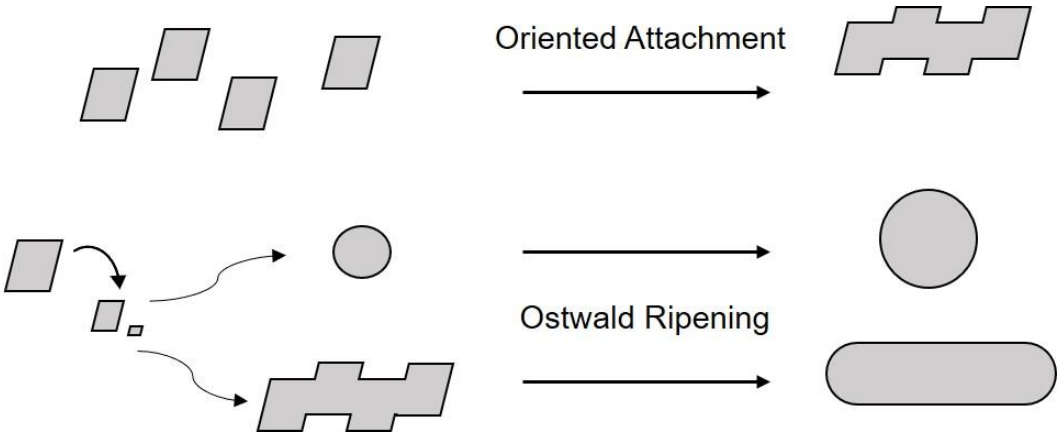

Figure 1.6 *Diagram of mechanism of nanomaterial growth through OA and OR.*

OA-based growth relies on interparticle attraction and fusion through a common crystallographic plane.[49] Surfactants and other surface directing agents are frequently added to the hydrothermal reaction mixtures, binding to specific planes and blocking fusion or the reprecipitation at those planes. Materials frequently grow through a combination of OA and OR, as particles fusing through OA form a rough morphology, followed by smoothing via OR.[49]

The commonly accepted mechanism for hydrothermal growth of CeO_2 starts with the combination of OA and OR growth of $Ce(OH)_3$ to form rods.[50] The presence of oxidizing agents such as dissolved O_2 or added NO_3^- oxidize small nuclei to CeO_2 (Figure 1.7).[51] Following the oxidation, the CeO_2 nuclei grow predominately through OA while the precipitates are $Ce(OH)_3$ followed by OA dominated growth following oxidation.

Despite the strengths of the hydrothermal method, it is accompanied by a few disadvantages. Hydrothermal reactions are typically run on smaller scales than simple precipitation reactions, and procedures often react overnight to reach the desired morphology. CeO_2 nanoparticles produced by the hydrothermal procedure often exhibit aggregation due to attraction of the oxide surfaces, although the addition of surfactants often alleviates this relative to precipitation methods and specialized reactors are required.[52]

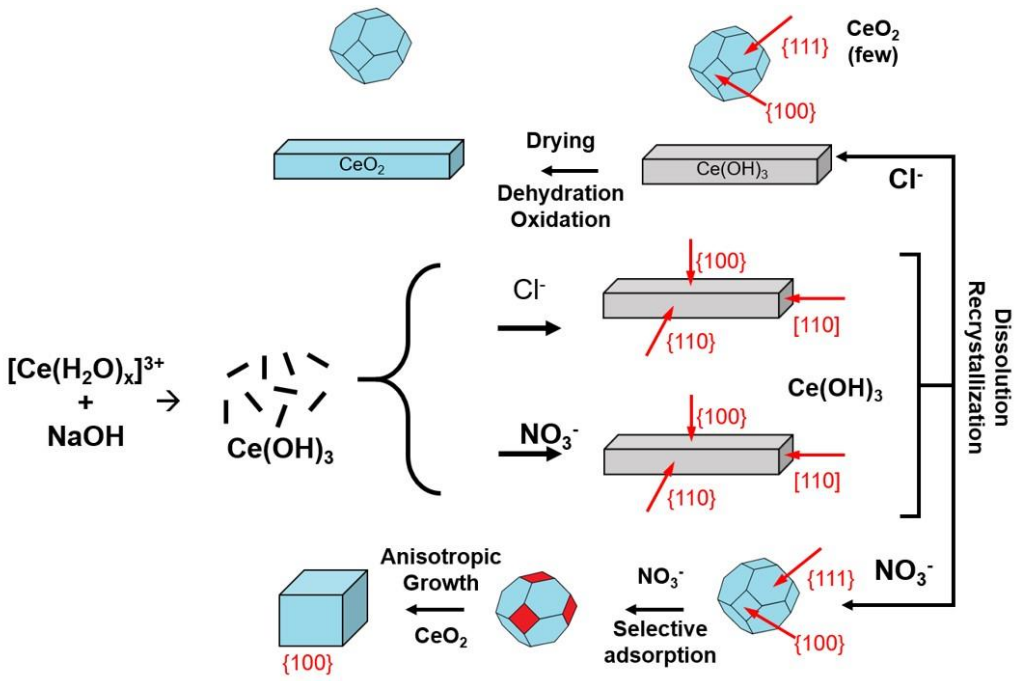

Figure 1.7 *Diagram showing the pathways to grow CeO_2 nanocubes, nanorods, and nanoparticles. Adapted from Reference [51].*

1.2.3. Templated Systems

The final approach to CeO_2 synthesis applicable to this dissertation is the use of templated materials to achieve specific morphologies. This approach enables the widest range of CeO_2 shape, limited only by the templates used. Templating techniques fall into two categories: hard or soft templating.

Hard templating techniques utilize solid structures to control the spatial growth of CeO_2, by loading or coating the template with cerium precursors, such as cerium hydroxide. Once loaded, the cerium precursor is oxidized to CeO_2 and the template is removed, typically through high temperature annealing or etching with acids or concentrated bases.[53,54,55]

One common hard templating route to CeO_2 formation is nanocasting, in which a $Ce(NO_3)_3$ solution is loaded into the pores of a mesoporous matrix, often mesoporous

silica.[56] Carbon nanotubes (CNTs) can be used to synthesize CeO_2 nanotubes. The CNTs are oxidized with nitric acid, creating a negatively charged surface to attract Ce^{3+}. NaOH is gradually added to precipitate $Ce(OH)_3$ particles on the surface of the CNT. Annealing oxidizes the $Ce(OH)_3$, fuses the CeO_2 particles to create a shell around the carbon nanotube, and remove the carbon template to leave CeO_2 nanotubes.[54,57] A similar approach using carbon or silica spheres, with the endpoint morphology of hollow CeO_2 nanospheres.[55,58] Anodic aluminum oxide membranes have also been used to synthesize CeO_2 nanotubes.[59]

Hard templating can also be used in conjunction with hydrothermal reactions to synthesize CeO_2 nanotubes. $Ce(OH)_3$ nanorods were synthesized through a hydrothermal reaction and exposed to air for a short time to oxidize the surface. The $Ce(OH)_3$ core was subsequently etched to yield the nanotube morphology.[60] $Ce(OH)CO_3$ nanorods aged in a basic solution followed by an acid wash produced thin walled, polycrystalline nanotubes, while a hydrothermal treatment of the same material led to smaller, monocrystalline nanotubes.[60]

Instead of using solid supports, soft template techniques use surfactants or micellular reactions to limit growth from Ostwald Ripening. These techniques sacrifice a slight degree of morphological control in exchange for increased yield. Like the hard template approaches, the soft template takes effort to remove,[61] although washing with solvents such as water, ethanol, or cyclohexane is often sufficient to remove the template.

A soft template example is the synthesis of ultrafine nanoparticles through reverse micellular synthesis. Aqueous cerium nitrate and NH_4OH were separately dispersed in a surfactant-cycloxhexane solution. The solutions were subsequently mixed, and due to

the micellular conditions the particle size was minimized to sub-5 nm.[62] Extended aging of sodium bis(2-ethylhexyl) sulfosuccinate based reverse micellular systems led to polycrystalline CeO_2 nanorods and nanowires, due to aggregation of small particles.[63]

1.2.4. CeO_2-Support Systems

Cerium oxide nanostructures are often coupled with noble metals or transition metal oxides to enhance catalytic activity, or for the addition of properties such as fluorescence or magnetism. These composites can incorporate CeO_2 as a small particle on a larger precipitate, or as the support for other nanocrystals.[8,64,65]

CeO_2 is frequently combined with Au nanoparticles for high-temperature catalytic applications. Au nanoparticles are deposited on CeO_2 particles by adding a pH 10 solution of $HAuCl_4$ to a suspension of CeO_2 nanoparticles, and can selectively oxidized CO to CO_2 even in the presence of H_2. Similar systems incorporating various CeO_2 morphologies decorated with small Pd, Pt, and various transition metal nanoparticles are also very commonly developed for catalysis.[64,66]

CeO_2 has also been used in conjunction with magnetic iron oxide. CeO_2 particles synthesized through a precipitation method were dispersed in a solution containing both Fe^{2+} and Fe^{3+}. Addition of NaOH precipitated magnetic Fe_3O_4 on the surface of the CeO_2 NPs.[67] The resulting CeO_2:Fe_3O_4 composite has been used for organic catalysis, with the magnetism useful in catalyst removal and recycling.[67]

CeO_2 has also been used in conjunction with carbon materials. Graphene, carbon nanotubes, and polymer nanofibers are common supports for CeO_2 nanoparticle deposition.[54,68] The combination of all these synthetic approaches allows CeO_2-

containing composites to have very elaborate designs, with multiple layers of several different noble metals and metal oxides deposited in multi-step synthetic procedures.[69]

1.2.5. Doping

Doping CeO_2 often contributes additional properties to CeO_2 nanomaterials, such as magnetism or fluorescence, useful in biological and optical applications.[70] The addition of a dopant can also improve CeO_2's catalytic or photocatalytic activity, thermal stability, or oxygen mobility. As mentioned in Section 1.1.6, CeO_2 is easily doped with other rare earth metals, due to the comparable size (Table 1.1), and first-row transition metals are also frequently used as dopants. Most methods to synthesize CeO_2 can be easily modified by adding the dopant to the cerium precursor, so long as precursors with similar counter-ions or alkoxides are available. However, differences in ionic radii, solution solubilities, and chemical activities can complicate the use of transition metals, and transition metals often phase separate at lower doping percentages than other rare earths.[71]

While a broad range of ions can be added to CeO_2, a few systems are particularly prevalent in the literature and/or relevant to this dissertation. Cerium doped zirconium oxide, or CSZ, is one of the most researched ceria-containing complexes, with applications in water splitting and solid oxide fuel cells. The addition of cerium improves the oxygen mobility and structure stability of the zirconium oxide.[72]

As previously discussed, CeO_2 has been doped by various lower-valent elements to improve the oxygen vacancy concentration of the material.[73,74] The incorporation of zirconium, yttrium, gadolinium, and samarium have been demonstrated to improve the oxide's oxygen mobility for use in solid oxide fuel cells.[75]

Some studies have demonstrated magnetic activity from CeO_2 nanoparticles, although this activity is very weak. Therefore, iron,[76] gadolinium,[77] and cobalt[78] have been incorporated into CeO_2 to enhance the chemical activity. Gadolinium has also been incorporated into CeO_2 particles for use as MRI contrast agents.[79]

The majority of rare earth elements have visible, near infrared (NIR), or infrared (IR) fluorescence emission and can contribute fluorescence to CeO_2 nanomaterials upon doping.[80] The addition of fluorescence from such dopants is applicable to biological applications, as the materials can be tracked for cellular uptake and distribution throughout the body.[70] Of particular interest to this work are trivalent rare earth ions (Ln^{3+}) fluorescing in the visible range (Eu^{3+}, Sm^{3+}) and NIR (Yb^{3+}, Nd^{3+}, Pr^{3+}, Er^{3+}, Ho^{3+}, Tm^{3+}). The mechanism of Ln^{3+}:CeO_2 fluorescence and specifics of fluorescence for each element will be further discussed in Chapter 6.

Various transition metals such as iron and cobalt have been investigated as dopants to enhance the photocatalytic activity of the material.[81,82] As discussed further in Section 1.3.6, the addition of these elements produce defects within the CeO_2 crystal lattice, which help reduce the optical band gap of CeO_2, improving the range of absorption by the material.[28] Furthermore, the defects can trap an excited electron and/or hole, influencing the life time of the excited state and subsequently the catalytic activity.[83]

1.3. CeO_2 Chemical Reactivity and Applications

The redox activity, catalytic and photocatalytic capabilities, and the optical properties of CeO_2 lend themselves to a broad range of applications. The following is brief discussion of select CeO_2 chemical reactivities and associated applications.

1.3.1. Enzyme Mimetic Chemistry

As previously discussed, CeO_2 nanomaterials are capable of adsorbing and releasing oxygen through oxidation and reduction of surface cerium atoms. Cerium oxide is also able to adsorb various radicals, such as H_2O_2, $O_2^{\bullet-}$ and $OH^{\bullet}$.[18] As a result, CeO_2 has been proposed to mimic enzymes such as superoxide dismutase (SOD) and catalase[84,19]. CeO_2 also scavenges other radicals such as nitric oxide radicals and mimics a number of other enzymes in this regard such as peroxidase, oxidase, and phosphatase.[85]

As described by Celardo *et al.*[84] and shown in Figure 1.8, the SOD-like activity of CeO_2 likely starts with $O_2^{\bullet-}$ binding to two Ce^{3+} atoms around an oxygen vacancy (Species 4). H_2O_2 is released following Ce^{3+} oxidation to Ce^{4+}, with addition of two protons from solution (Eqn 1.6). This process repeats for a second $O_2^{\bullet-}$, leaving two Ce^{4+} available to bind H_2O_2. The two Ce^{4+} are reduced to Ce^{3+} by binding H_2O_2, transferring two electrons and releasing $2H^+$ and O_2 (Eqn 1.7). The SOD activity of CeO_2 is increased with increasing Ce^{3+}/Ce^{4+} ratio, matching experimental results.[84]

$$O_2^{\bullet-} + Ce^{3+} + 2H^+ \rightarrow H_2O_2 + Ce^{4+} \qquad \text{(Eqn 1.6)}$$

$$H_2O_2 + 2\,Ce^{4+} \rightarrow +O_2 + 2H^+ + 2\,Ce^{3+} \qquad \text{(Eqn 1.7)}$$

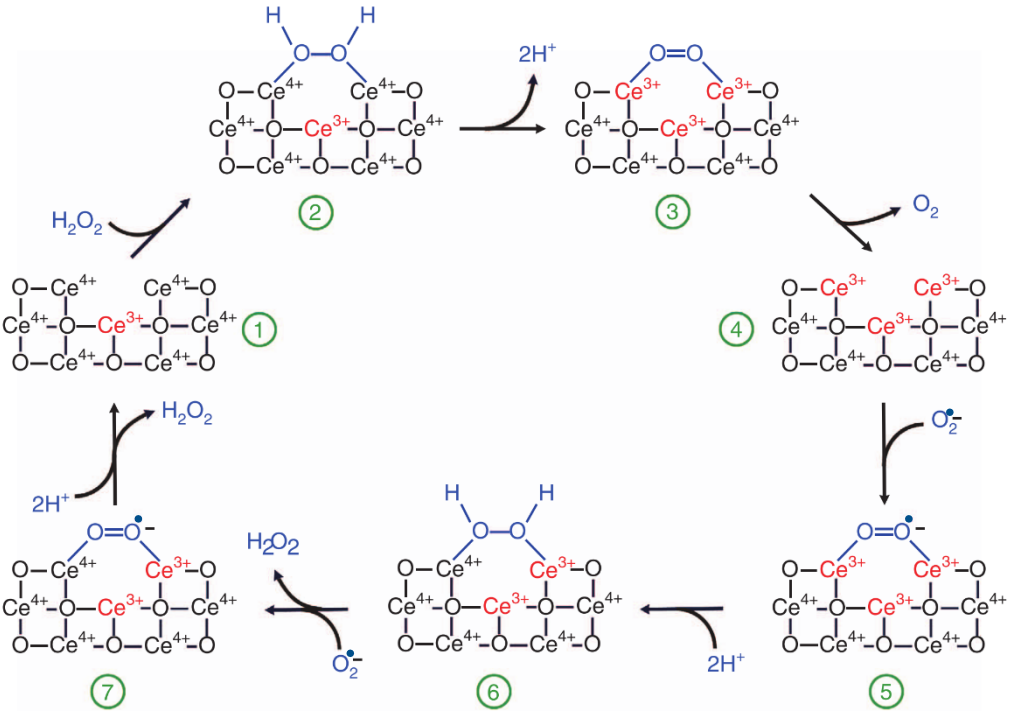

Figure 1.8 *Mechanism for the SOD-type CeO_2 catalytic cycle. Adapted from Reference [84].*

In contrast, the catalase activity of CeO_2 decreases with increased Ce^{3+} concentration.[86] H_2O_2 is able to bind to Ce^{3+} and is released as water following addition of two protons and oxidation of Ce^{3+} to Ce^{4+} (Eqn 1.8).[85] A second H_2O_2 then adsorbs to the two Ce^{4+} ions. Both Ce^{3+} are reduced to Ce^{3+}, and molecular oxygen is released along with two protons (Eqn 1.7).

$$H_2O_2 + 2Ce^{3+} + 2H^+ \rightarrow 2H_2O + 2Ce^{4+} \qquad \text{(Eqn 1.8)}$$

CeO_2 has also demonstrated significant activity against $OH^{\bullet}$ radicals derived from H_2O_2. The Ce^{3+} is reduced and undergoes a color change from white to orange. However, after sitting in the solution for two weeks, most of the Ce^{3+} is oxidized by dissolved oxygen back to Ce^{4+} to regenerate the original Ce^{3+}/Ce^{4+} ratio (Figure 1.9).[87]

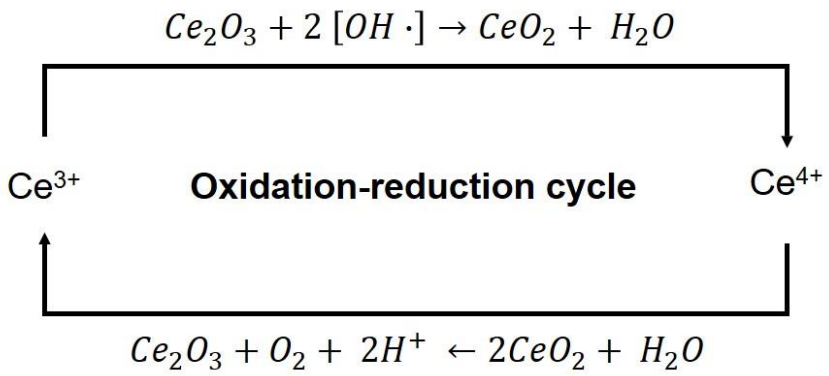

Figure 1.9 *Diagram showing full cycle for neutralization of hydroxyl radical by CeO_2. Adapted from Reference [87].*

The ability of CeO_2 to eliminate ROS, coupled with its self-regeneration and non-cytotoxicity[88] make it attractive for protective biological applications. Within cells, ROS has a protective role within biological systems but elevated concentrations cause oxidative stress and damage DNA.[89] This damage is linked to a series of medical diseases including cancer, cardiovascular disease, and potentially Alzheimer's.[88]

Enzymes such as SOD and catalase typically regulate the ROS within cells, but can become imbalanced by stresses including radiation treatments, infections, and exposure to pollutants.[90] CeO_2 has been used to either prevent or neutralize ROS species created during radiation treatments[88] and from post-surgical complications,[91] among other events.

In one study, CeO_2 nanoparticles reduced the risk of ischemic stroke following intestinal surgery.[91] Radicals are produced due to reduced blood flow, which leads to inflammation of the surrounding tissue. CeO_2 NPs implanted in the intestine tissue during surgery successfully exhibited post-surgical superoxide scavenging, based on reduced response from a Cytochrome C based biosensor, as well as suppressed inflammatory cytokines. The reduction in ROS accumulation lowered ROS-induced inflammation, and prevented ischemic stroke.[91]

CeO_2 nanoparticles also scavenged radicals produced during radiation for cancer treatment.[88] Within the neutral pH of healthy cells, the catalase and superoxide dismutase mechanism are both active, allowing the nanoparticles to assist cells with eliminating the radiation-created ROS. However, the acidic cancer cell environment suppressed the CeO_2 scavenging chemistry, particularly the catalase activity. As a result, treatment of cells with CeO_2 NPs protected only the healthy cells while the cancer cells were unaffected.[88]

1.3.2. Drug Delivery

The simpler drug delivery systems utilizing CeO_2 are based on electrostatic attraction of drugs to the CeO_2 surface. In one such drug delivery system, the anticancer drug doxorubicin is loaded onto negatively-charged CeO_2 particles.[92] The electrostatic attraction enables high loading percentages, and the particles gradually release the drug, reducing the burst effect of traditional delivery.

CeO_2 has also been used in more complicated systems, typically capitalizing on its pH-sensitive enzyme mimetic activity.[93,94] One approach uses CeO_2 nanoparticles coated with β-cyclodextrin to coat the mesoporous silica nanoparticles through a ferrocenyl linker.[95] In acidic environments, the CeO_2 oxidizes the ferrocenyl linker to a ferrocenium ion, which dissociates from the cyclodextrin, releasing the CeO_2 particle with loaded drug into the cell (Figure 1.10). Within healthy cells at neutral pH, CeO_2 NPs have radical scavenging activity, aiding the cell viability. However, the acidic environment of a cancer cell deactivates the catalase pathway, overproducing H_2O_2 and leading to cancer death.[95]

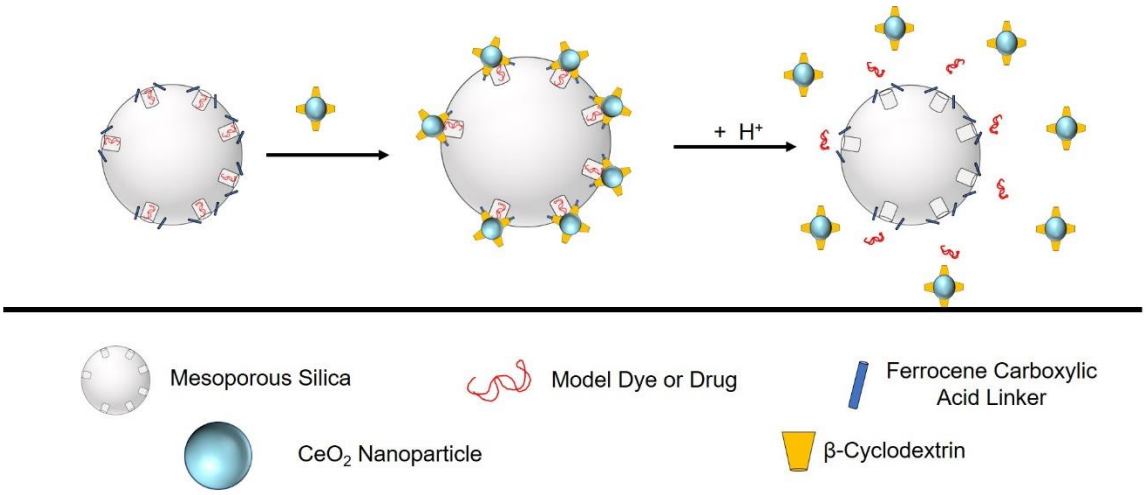

Figure 1.10 *Synthesis and release of model dyes or drugs from CeO_2-capped mesoporous silica nanoparticles. Adapted from Reference [95].*

1.3.3. Antibacterial Activity

CeO_2 nanostructures have also exhibited some antibacterial activity. CeO_2 nanocubes demonstrated activity against several strains of bacteria, attributed to cell membrane damage by the nanocubes.[96] However, other groups report very limited antibacterial activity with a variety of CeO_2 morphologies.[97,98] One major complication is fouling of the CeO_2 surface by components frequently found in biological systems, such as PO_4^{3-} groups which bind to surface cerium sites and block the Ce^{3+}/Ce^{4+} redox cycling.[99] A 2018 review of the antibacterial activity of CeO_2 particles, with a variety of particle sizes and synthetic protocols represented, concluded that the particles that do exhibit antibacterial activity adsorb to the bacterial wall and are reduced, resulting in oxidative stress on the bacteria.[34]

1.3.4. Sensors

Cerium oxide materials are often incorporated into sensors, capitalizing on the color change between Ce^{3+} and Ce^{4+}, the material's sensitivity to the P_{O_2} at elevated temperatures, and reactivity with radicals among other properties.[100,101]

For example, the Ce^{3+} defects and oxygen vacancies within CeO_2 enable oxygen transport, measurable as electrical conductivity. This allows measurement of the partial pressure of oxygen by CeO_2 films, with the conductivity directly proportional to the concentration of O_2.[101]

Cerium oxide has also been utilized within a glucose-sensing colorimetric assay due to the color change between Ce^{3+} and Ce^{4+}.[100] Upon immobilization of CeO_2 nanoparticles and glucose oxidase on filter paper, the addition of glucose and subsequent H_2O_2 production, the CeO_2 rapidly turns from white to dark orange depending on the concentration of glucose. Due to the self-regenerating capability of CeO_2 the color change is reversible, making the sensor reusable.

1.3.5. Photocatalysis

The band gap of CeO_2 (~3.2 ev, 380 nm) allows CeO_2 to absorb light, primarily in the UV range.[26] Upon absorption of a photon, electrons are excited to the conduction band while creating holes in the valence band, which forms an electron-hole pair. The holes can then react with dissolved OH^- ions forming $OH^{\bullet}$ radicals,[102] while the excited electrons can reduce adsorbed O_2, producing $O_2^{\bullet -}$ radicals.[28] Both of these radicals can decompose target dyes such as methylene blue[26] and rhodamine B,[28] or organic molecules such as formic acid and oxalic acid.[103] However, similar to ZnO and TiO_2, pure

CeO_2 can only utilize a small percentage of sunlight for photocatalysis, due to its band gap.

This can be partially mitigated by doping with transition metals. As previously discussed, dopants can add oxygen vacancies and subsequently reduce Ce^{4+} to Ce^{3+}. The presence of Ce^{3+} defects and oxygen vacancies red-shift the UV-Vis absorbance, reducing the optical band gap through the addition of energy levels between the valence and conduction bands (Figure 1.11).[26,104] The transition metals also contribute their 3d orbital energy levels, which lie between the CeO_2 conduction band and valence band.[105]

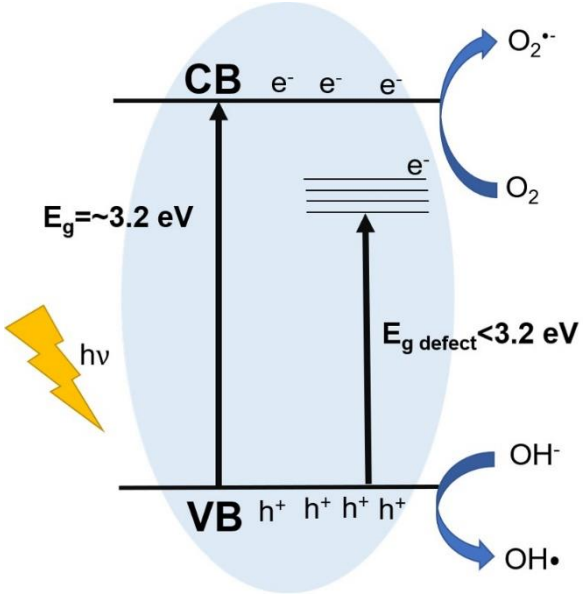

Figure 1.11 *Diagram of photoexcitation of electron within CeO_2, and formation of hydroxyl radical by reacting with holes in valence band.*

As a result, CeO_2 has been doped with transition metals or other rare earths, or decorated with small noble metal particles for photocatalytic degradation of dyes and organic compounds. For example, $Fe_{0.5}Ce_{0.5}O_2$ nanoparticles catalyzed 93% degradation of methylene blue, and completely mineralized congo red after four hours

using sunlight.[83] Doping CeO_2 nanorods with yttrium significantly improved the photocatalytic activity by increasing oxygen vacancy levels. These vacancies enhance the oxygen mobility, allowing transport of the charged pair to the surface to react with adsorbed species.[28]

The photocatalytic activity of CeO_2 is also dependent on the morphology. CeO_2 nanotubes synthesized from a $Ce(OH)CO_3$ precursor outperformed commercially available CeO_2 NPs and TiO_2 NPs (Degussa P25) in the rate of gas-phase degradation of benzene. The increased activity was attributed to the high aspect ratio of the nanotube, which may enable long-distance electron-hole separation, enabling increased $OH^{\bullet}$ and $O_2^{\bullet -}$ production.[106]

1.3.6. Solid Oxide Fuel Cells

One of the most highly researched applications for CeO_2 is in solid oxide fuel cells (SOFCs), as either doped CeO_2 or as a dopant within other oxide materials.[72,107] SOFCs operate at high temperatures (> 500 °C) to generate electricity from a variety of fuels including hydrocarbons.[108] Briefly, oxygen is reduced at the cathode to O^{2-}, transported through an electrolyte, and used to react with hydrogen in the fuel to produce water (Figure 1.12). The optimal electrolyte will have high thermal stability as well as high oxygen mobility in the applicable elevated reaction temperature.

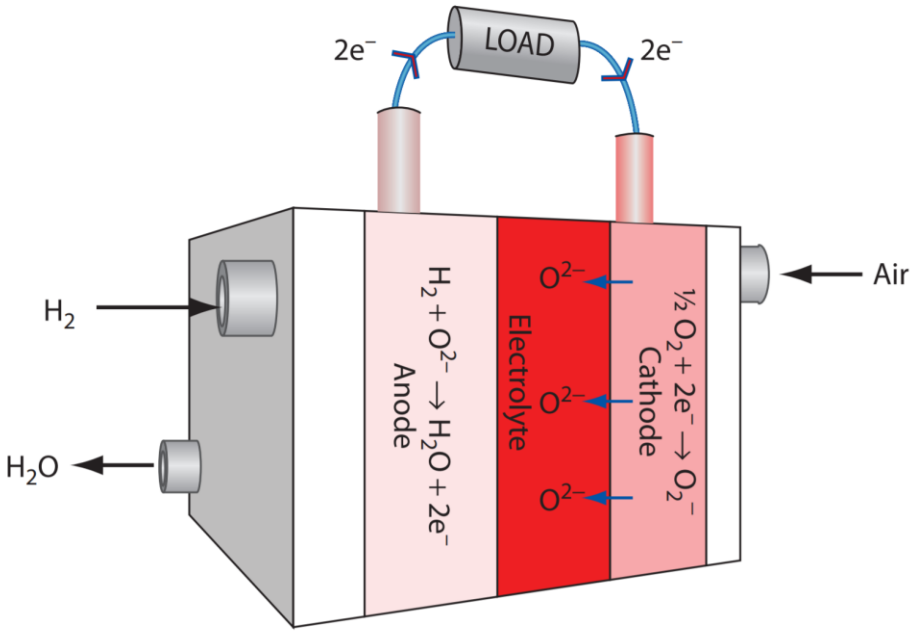

Figure 1.12 *Theoretical set-up of solid oxide fuel cell using H_2 as a fuel, with oxygen reduced, transported through an electrolyte, and reacted with hydrogen, creating an electric current in the process* [72]

Common electrolytes are typically ZrO_2-based, although CeO_2 has also shown promise due to its oxygen mobility. The larger ionic radius of cerium compared to zirconium results in a larger crystal unit, allowing more space for oxygen migration.[72] Furthermore, the crystal structure of CeO_2 is stable at elevated temperatures in the presence of oxygen.[73] Several other rare earth ions, such as Sm^{3+} and Gd^{3+}, have been doped into CeO_2 to further increase the number of oxygen vacancies, which increases the material's oxygen conductivity.[75]

1.3.7. Catalysis

While many of the aforementioned applications utilize cerium oxide's redox activity in a catalytic capacity, this is a very small portion of CeO_2's catalytic versatility. CeO_2 has potential uses in a very wide range of catalytic applications, ranging from high

temperature soot combustion catalysis[109] and steam reforming,[110] to room temperature, multicomponent one-pot organic syntheses.[111] Several of these uses are described below, with a brief description of CeO_2's contribution to the system.

CeO_2 has been commonly incorporated into three-way catalytic converters, which are responsible for purifying exhaust from combustion engines. These systems are multi-component, with some catalytic material targeting oxidization of CO and hydrocarbons, and another catalyst reducing nitrogen oxides.[112] The concentration of oxygen passed through the converter must be carefully controlled for both reduction and oxidation of the pollutants. At elevated temperatures, CeO_2 reversibly releases oxygen, transitioning between CeO_2 and reduced, sub-stoichiometric $CeO_{2-\delta}$ by Equation 1.9, where δ indicates the moles of $½O_2$ released.

$$CeO_2 \leftrightharpoons CeO_{2-\delta} + \delta\frac{1}{2}O_2 \qquad \text{(Eqn 1.9)}^{8,113}$$

Due to this oxygen storage capacity, it can support CO and hydrocarbon oxidation by releasing oxygen, and reduction of NO_x species by adsorbing oxygen.[114]

CeO_2 has been coupled with various noble metals for oxidation of volatile organic compounds, such as methane, ethanol, and benzene. Once again, CeO_2 is typically utilized as a support for other metals, such as Pt, Pd, and Cu.[8] In this situation, CeO_2 again acts as an oxygen supply, as well as an oxidizing agent due to reduction of Ce^{4+} to Ce^{3+}.

While less explored, CeO_2 has also been used in oxidation of organic molecules, such as alcohols, especially with use of Au/CeO_2 composites.[115] Other studies report CeO_2 oxidizing various alcohols and amines into imines.[116] CeO_2 has also been coupled with

magnetic iron oxide nanoparticles for a green, one pot synthesis of dihydropyridines, followed by magnetic removal of the catalyst.[67]

1.4. Project Overview

This research to be presented in this dissertation will focus on the synthesis, characterization, and uses of a new series of rare earth-doped CeO_2 nanomaterials. Chapters 2-4 cover the synthesis and characterization of Eu-doped CeO_2 (Eu-CeO_2) nanorods, nanocubes, nanowires, and nanotubes. The rods and cubes are synthesized by a hydrothermal protocol, following the Ostwald Ripening and Oriented Attachment mechanisms, respectively, as described in Section 1.2.2. The nanowires are synthesized by electrospinning networks of polymer nanofibers loaded with metal precursors, followed by annealing to remove the polymer template. Finally, the nanotubes are synthesized by depositing layers of Ce^{3+} and OH^- onto a ZnO nanowire assay, annealing to Eu-CeO_2, and etching the ZnO core.

As briefly mentioned in Section 1.2.5, doping CeO_2 with intrinsically-fluorescent ions such as Eu^{3+} can increase the Ce^{3+} concentration as well as add a strong fluorescence to the CeO_2. However, the Eu-CeO_2 nanorods as synthesized required annealing to activate the Eu^{3+} fluorescence. The mechanism of fluorescence quenching in the Eu-CeO_2 is discussed in Chapter 5. Subsequently, a series of other rare earths were doped into CeO_2 cubes, and investigated for fluorescence spanning the visible range into the near IR.

Finally, Chapter 6 discusses the interaction of various Eu-CeO_2 nanomaterials upon exposure to L-Dihydroxphenylalanine (L-Dopa), which is the precursor to melanin, a pigment in the skin.[117] The Eu-CeO_2 materials suppressed fluorescence associated with

L-Dopa derived melanin. However, the extent of this fluorescence suppression varied between CeO_2 materials. Materials with smaller crystalline domains and higher Ce^{3+} concentrations were significantly more active with L-Dopa than monocrystalline or heavily oxidized morphologies.

Chapter 2: Hydrothermal Synthesis of Eu-CeO_2 Nanorods

2.1. Overview

As previously mentioned in Chapter 1, CeO_2 nanomaterials have been synthesized through the precipitation and subsequent hydrothermal treatment of $Ce(OH)_3$.[50] Furthermore, a broad range of dopants have been introduced into the CeO_2 crystal structure within a variety of morphologies. The exposed crystallographic planes vary based on the morphology, with rods exposing (220) and (200), cubes exposing (200), and particles exposing (111) planes.[36,42] As a result, changing the morphology can significantly change the chemical reactivity of the material.

Incorporation of Eu^{3+} into CeO_2 nanomaterials increases oxygen vacancies and Ce^{3+} defects, as discussed in Chapter 1. This provides europium doped cerium oxide (Eu-CeO_2) materials with potential biological applications due to their radical and reactive oxygen species (ROS) scavenging activity. Several recent studies report enhanced Eu-CeO_2 nanoparticle activity against ROS compared to undoped CeO_2 particles,[118] with one study showing suppression of the ROS accumulation associated with intestinal ischemia.[91] Doping with Eu^{3+} may also add visible fluorescence to CeO_2 nanomaterials. As a result, no surface functionalization is necessary to track the materials within a biological system.

While some literature discusses Eu-CeO_2 spherical nanoparticle fluorescence and chemical activity,[119-121] research concerning Eu-CeO_2 nanorods is extremely limited with only one publication featuring the material. This earlier work describes using the material as a sensor, with Eu^{3+} fluorescence activated or suppressed by H_2O_2 and ascorbic acid, respectively.[122] However, only the Eu:Ce molar precursor ratio was varied to study the

impact on the Eu^{3+} fluorescence and Ce^{3+} defect concentration. The paper investigates annealing the nanorods to activate Eu^{3+} fluorescence, with the annealed nanorods displaying identical morphology to unannealed rods, according to TEM images in the main text. Some TEM images in the supplemental data contradict images in the main text and exhibit some morphological differences in the nanorods after annealing.[122]

Therefore, there is a need for a detailed analysis of the synthetic protocols and their effect on the photophysical properties of the Eu-CeO_2 nanorod product. This chapter specifically focuses on the synthesis of Eu-CeO_2 nanorods using a hydrothermal protocol, with other morphologies and techniques discussed in later chapters. Several reaction condition variables were altered for ideal control of the dimensions and morphology of the Eu-CeO_2 rods, including precursor concentrations and identities, reaction temperature, and reaction duration. Finally, select nanorod samples were annealed to analyze changes in the morphology and crystallinity of the rods. The annealing temperature and heating rate were varied to in an attempt to minimize the fusion of the nanorods.

Following the synthesis and morphological analysis of the rods and annealed rods, the cerium oxide products were analyzed using high resolution TEM lattice imaging and powder X-ray diffraction to confirm cubic fluorite CeO_2 crystal structure with negligible impurities and to determine relative crystalline domain sizes.

2.2. Introduction

2.2.1. Mechanism of Cerium Oxide Nanostructure Growth by Hydrothermal Chemistry

2.2.1.1. Nucleation

Ce^{3+} rapidly reacts with OH^- when mixed, and the resulting $Ce(OH)_3$ quickly reaches supersaturation due to its low solubility in water. The metal hydroxide subsequently precipitates, forming $Ce(OH)_3$ nuclei (Eqn 2.1).[22] Depending on solution conditions and the presence of oxidizing agents, these hydroxides may be stable or may oxidize to $Ce(OH)_4$ (Eqns 2.2, 2.3). The hydroxides can then dehydrate, forming Ce_2O_3 or CeO_2 (Eqns 2.4, 2.5, 2.6). Ce_2O_3 is unstable in air, and rapidly oxidizes to CeO_2 (Eqn 2.5).

$$Ce^{3+} + 3\,OH^- \rightarrow Ce^{III}(OH)_3 \quad \text{(Eqn 2.1)}[22]$$

$$Ce^{III}(OH)_3 \xrightarrow{O_2, OH^-} Ce^{IV}(OH)_4 \quad \text{(Eqn 2.2)}[123]$$

$$Ce^{4+} + 4\,OH^- \rightarrow Ce^{IV}(OH)_4 \quad \text{(Eqn 2.3)}[124]$$

$$2\,Ce^{III}(OH)_3 \rightarrow {Ce^{III}}_2O_3 + 3\,H_2O \quad \text{(Eqn 2.4)}[125]$$

$${Ce^{III}}_2O_3 \xrightarrow{O_2(g)} 2\,CeO_2 \quad \text{(Eqn 2.5)}[9]$$

$$Ce^{IV}(OH)_4 \rightarrow Ce^{IV}O_2 + 2H_2O \quad \text{(Eqn 2.6)}[124,125]$$

2.2.1.2. Crystal Growth

As discussed in Chapter 1, two predominant mechanisms for hydrothermal crystal growth are Ostwald Ripening (OR) and Oriented Attachment (OA). The two mechanisms reduce surface energy through elimination of high-energy surfaces.

Literature conflicts over the mechanisms controlling growth of the various CeO_2 morphologies, due to the sensitivity of the reaction products to precursor concentrations, basicity, temperature, and any added surface directing agents. The rods are often proposed to grow through the OR of $Ce(OH)_3$ followed by oxidation to CeO_2,[50] although some assign rod growth to OA.[126] In contrast, cubes are suggested to grow through the oxidation of nuclei to CeO_2 followed by OA.[51] This latter mechanism is discussed in more detail in Chapter 3.

Ostwald ripening, alternatively referred to as particle coarsening, was first introduced in 1896 by Wilhelm Ostwald.[47] The mechanism involves dissolution of small particles and their reprecipitation as larger particles, until an equilibrium is reached. This growth has been explained in the literature through a rate law (Eqn 2.7), where *r* is the average particle diameter at time *t*, r_o is the average initial particle size, and *k* is the rate constant.[127]

$$\bar{r}^3 - \bar{r}_o^3 = kt \qquad \text{(Eqn 2.7)}$$

The rate constant is further described by Equation 2.8, where γ is the precipitate-solution interfacial energy, V_m is the molar volume, $c_{r=\infty}$ is the solubility of a bulk-sized particle, D is the diffusion coefficient, R is the gas constant, and *T* is the reaction temperature.[127]

$$k = \frac{8\gamma D V_m^2 c_{r=\infty}}{9RT} \qquad \text{(Eqn 2.8)}$$

Pan *et al.* calculated the ideal Ostwald Ripening growth rate constants of several hydrothermal reactions leading to the nanorod morphology.[61] The calculated ideal rate constants were 10^{-8} to 10^{-10} $nm^3\,s^{-1}$ for CeO_2 growth and 10^{-2} to 10^{-3} nm^3s^{-1} for $Ce(OH)_3$

growth. Experimental growth rates were measured to be between 10^{-2} and 10^{-3} $nm^3\ s^{-1}$, matching the calculated ideal rates of OR-based growth of $Ce(OH)_3$.[61] The difference in rate constants may be attributed to the difference in bulk solubility of the two materials, with aqueous molar solubilities of $5.23 \times 10^{-12}\ {}^{mol}/_{L}$ for CeO_2 and $4.85 \times 10^{-6}\ {}^{mol}/_{L}$ for $Ce(OH)_3$.[61]

Nanorods were also synthesized and carefully washed in an presumably oxygen-free environment to prevent post-synthesis oxidation.[51] Powder XRD analysis of this sample confirmed that $Ce(OH)_3$ nanorods were the primary product of the hydrothermal reaction.

2.3. Methods and Materials

2.3.1. Materials

All reagents purchased were of analytical grade and used as received without further purification. Cerium (III) chloride heptahydrate ($CeCl_3$•7 H_2O), europium (III) nitrate hexahydrate ($Eu(NO_3)_3$•6 H_2O), and sodium hydroxide (NaOH) were purchased from Alfa Aesar. CeO_2 nanoparticles (<20 nm diameter) and ammonium cerium (IV) nitrate ($(NH_4)_2Ce(NO_3)_{6)}$ were purchased from Sigma Aldrich. Tribasic sodium phosphate dodecahydrate (Na_3PO_4•12 H_2O) was purchased from Mallinckrodt. Cerium (III) acetate hydrate ($Ce(C_2H_3O_2)_3$ and cerium (IV) t-butoxide were purchased from Gelest. Europium (III) chloride hexahydrate ($EuCl_3$•6 H_2O) was purchased from Strem. Cerium (III) nitrate heptahydrate ($Ce(NO_3)_3$•7 H_2O) was purchased from Acros Organics. Ethanol (95%, EtOH) was purchased from Pharmco-Aaper.

2.3.2. Standard Eu-CeO_2 Nanorod Synthetic Protocol

Eu-CeO_2 nanorods were synthesized by a modified procedure commonly used for CeO_2 nanorod synthesis.[42,51] Ce^{3+} and OH^- react and precipitate as $Ce(OH)_3$, followed by growth to nanorods in a hydrothermal reaction (Figure 2.1). The $Ce(OH)_3$ rods were subsequently washed and dried to oxidize the $Ce(OH)_3$ to CeO_2.

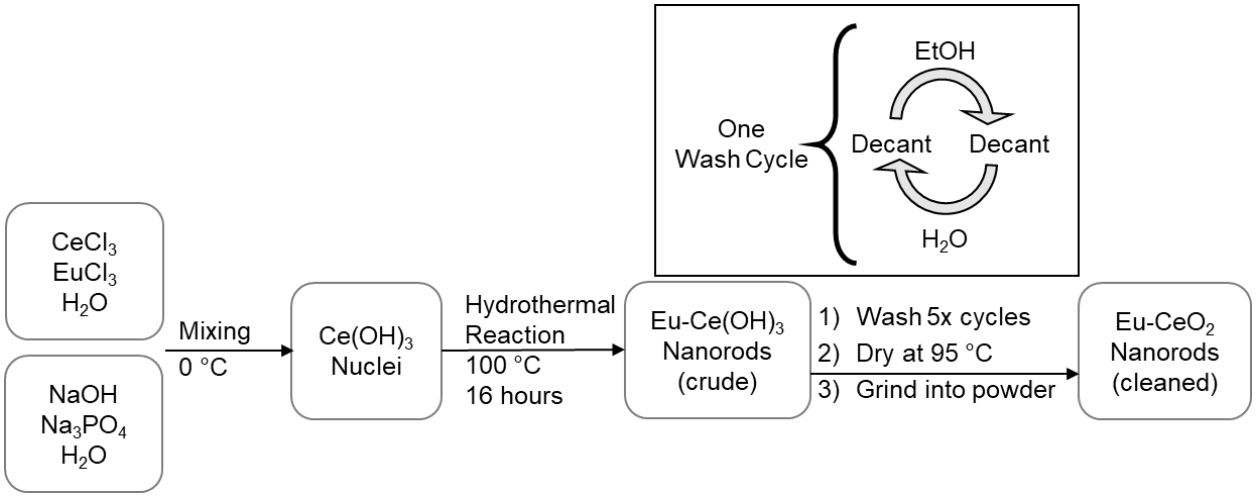

Figure 2.1 *Diagram of typical procedure for synthesis of Eu-CeO_2 nanorods.*

The standard synthesis of Eu-CeO_2 nanorods started with the reaction of 0.3 g $CeCl_3$ (44 mM) and 0.02 g $EuCl_3$ (3 mM) dissolved in 4.5 mL H_2O with 0.0187 g Na_3PO_4 (2.7 mM) dissolved in 13.9 mL of 2.5 M NaOH. The two solutions were mixed and rapidly stirred in an ice bath for 20 minutes, then transferred to a 50 mL Teflon screw-cap reactor. The reactor was placed in an electric oven held at 95 °C for 16 hours. Samples were washed three times with water and ethanol, dried at 95 °C, and ground into a powder. In subsequent experiments, these 'baseline' standard reaction conditions were followed by manipulation of the $CeCl_3$, $EuCl_3$, Na_3PO_4, and NaOH concentrations, cerium precursor

identity, reaction temperature, and reaction duration. The specific variations in the protocol are discussed in the relevant result sections.

The Eu^{3+} concentration within the CeO_2 materials is noted throughout this work using the convention described by Equation 2.9. The theoretical %Eu of a material is calculated using the molar concentrations of the precursor metals salts. The %Eu of a synthesized material is experimentally determined using the cerium and europium atomic percentages as detected by EDS as described in Section 2.3.6.

$$\%Eu = \frac{mM\ Eu^{3+}}{mM\ Eu^{3+} + mM\ Ce^{3+}} = \frac{at\%\ Eu}{at\%\ Eu + at\%\ Ce} \quad \text{(Eqn 2.9)}$$

A sample analyzed to have 10 at% Eu and 90 at% Ce would be referred to as 10% Eu-CeO_2.

2.3.3. Eu-CeO_2 Annealed Nanorod Synthesis

Annealed nanorods were produced from Eu-CeO_2 nanorods as synthesized above. The initial rods had 70 (± 21) nm lengths and 10 (± 3) nm diameters, with ~8 %Eu (Eqn 2.9). The ground nanorod powder was transferred to a quartz boat and placed in an electric oven. The rods were heated to 500-800 °C over the course of an hour, maintained at that temperature for 16 hours, then allowed to cool gradually to room temperature. The rods were then lightly ground to break apart any aggregates.

To test the effect of ramp rate and annealing time on nanorod morphology, samples were heated at 10 °C/min to 800 °C, held there for 2 hours, then allowed to cool gradually. This gave an annealing time of almost 3.3 hours, neglecting the cool down time.

2.3.4. Morphology and Size Characterization

The morphology of the Eu-CeO_2 nanorods was analyzed by Transmission Electron Microscopy (TEM) and High Resolution TEM (HRTEM) using a JEOL 2100 TEM operating at 200 kV. Samples were first sonicated in de-ionized water for 2 minutes, then a drop of the suspension was transferred to a carbon coated copper grid and allowed to evaporate prior to analysis. Nanomaterial dimensions were determined using ImageJ software, with a minimum of 90 nanorods sampled.

2.3.5. Nanomaterial Crystallinity

Powder X-ray Diffraction (XRD) data was acquired using a Philips XRG3100 in the 2Θ range from 10° to 80°, with step size of 0.02 degrees and step time of 20 seconds. Sample peak positions were compared to CeO_2 reference sample data from the National Institute of Standards and Technology (NIST), Standard Reference Material 674b.[128] Crystalline domain size (τ) in nanometers was determined from XRD spectra as applied to the Scherrer equation (Eqn 2.10). K is the shape constant, approximately 0.94 for spherical particles. λ is the wavelength of the incident x-rays (1.54178 Å for Cu $K_{a)}$, β is the full-width half-max of the CeO_2 (111) peak at approximately 31°. Finally, θ is the Bragg angle, or ½ the 2θ x-ray angle.

$$\tau = \frac{K\lambda}{\beta \cos(\theta)} \tag{2.10}$$

HRTEM was also used to analyze the crystalline domain size and exposed planes based on observed lattice spacings.

2.3.6. Elemental Composition

Elemental data was collected using a Gatan Energy Dispersive Spectroscopy Unit (EDS) attached to the JEOL 2100. Samples were analyzed for atomic percentage of O, Ce, and Eu using the K-shell of oxygen and L-shell of cerium and europium.

2.4. Results: Morphological Control of Eu-CeO2 Nanorods

2.4.1. Standard Synthetic Material

The primary product isolated using the initial synthetic conditions is Eu-CeO_2 nanorods with average length of 70 (± 20) nm and width of 10 (± 3) nm. A few larger dense aggregates are observed with the nanorods (Figure 2.2a, b). Some small nanoparticles grow on the surface of the Eu-CeO_2 nanorods (Figure 2.2c). The original reaction mixture turns a light pink during stirring, and purple-grey by the end of the hydrothermal reaction, indicating $Ce(OH)_3$ synthesis. After washing, the precipitates turn yellow-grey during washing from the partial oxidation of $Ce(OH)_3$. The final product following drying is a light yellow powder, indicating oxidation of $Ce(OH)_3$ to CeO_2. The standard reaction protocol has a theoretical yield of ~140 mg and actual yields around 130 mg, indicating that precipitation of Ce^{3+} to $Ce(OH)_3$ and finally CeO_2 is nearly complete.

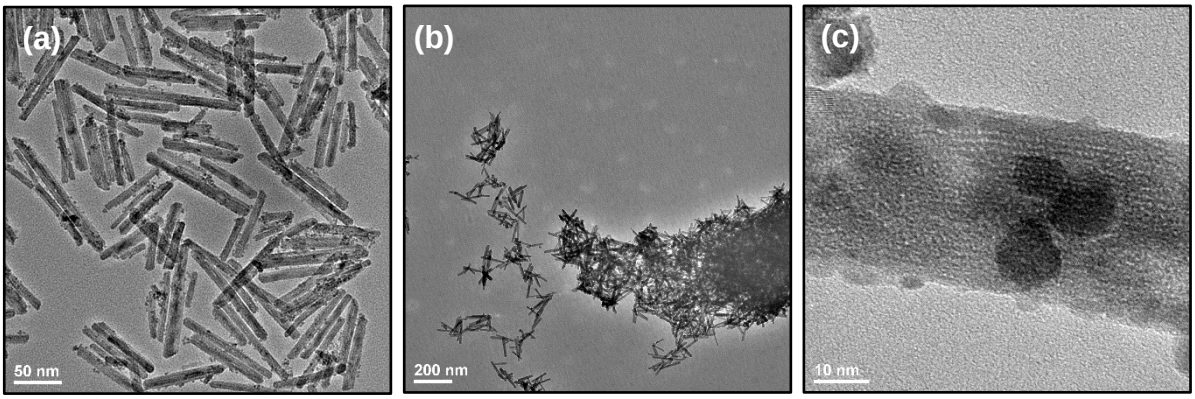

Figure 2.2 *TEM images of baseline Eu-CeO_2 nanorods showing: (a) distinct nanorod structure; (b) aggregates; and (c) small nanoparticles on surface of a given nanorod.*

2.4.2. Influence of $CeCl_3$ Concentration

As noted earlier in this chapter, following the mixing of Ce^{3+} with OH^-, $Ce(OH)_3$ rapidly reaches supersaturation and precipitates. By increasing the Ce^{3+} concentration, the rate of nucleation is enhanced, resulting in more numerous small particles. Conversely, a relatively lower Ce^{3+} concentration reduces the supersaturation and therefore the number of nuclei. As a result, increased Ce^{3+} concentrations typically yield more numerous but shorter rods than lower Ce^{3+} concentrations within the CeO_2 system.[41,126]

To probe this effect on Eu-CeO_2 nanorods, the $CeCl_3$ concentration was varied from 22 mM to 132 mM, with $EuCl_3$ adjusted to maintain a constant Eu:Ce molar ratio. Increasing the $CeCl_3$ concentration did gradually decrease the nanorod length, although large standard deviations slightly obscure the trend (Figures 2.3, 2.4a). The nanorod diameter is constant for all samples, other than an insignificant increase from 10 nm to 15 nm in the sample with a 22 mM $CeCl_3$ concentration (Figure 2.3, 2.4b). $Ce(OH)_3$ prefers anisotropic growth, often in the (220) direction, which may explain the minimal change in nanorod diameter.[51] As a result, variation of $CeCl_3$ concentration provides slight length manipulation independent of changes in width.

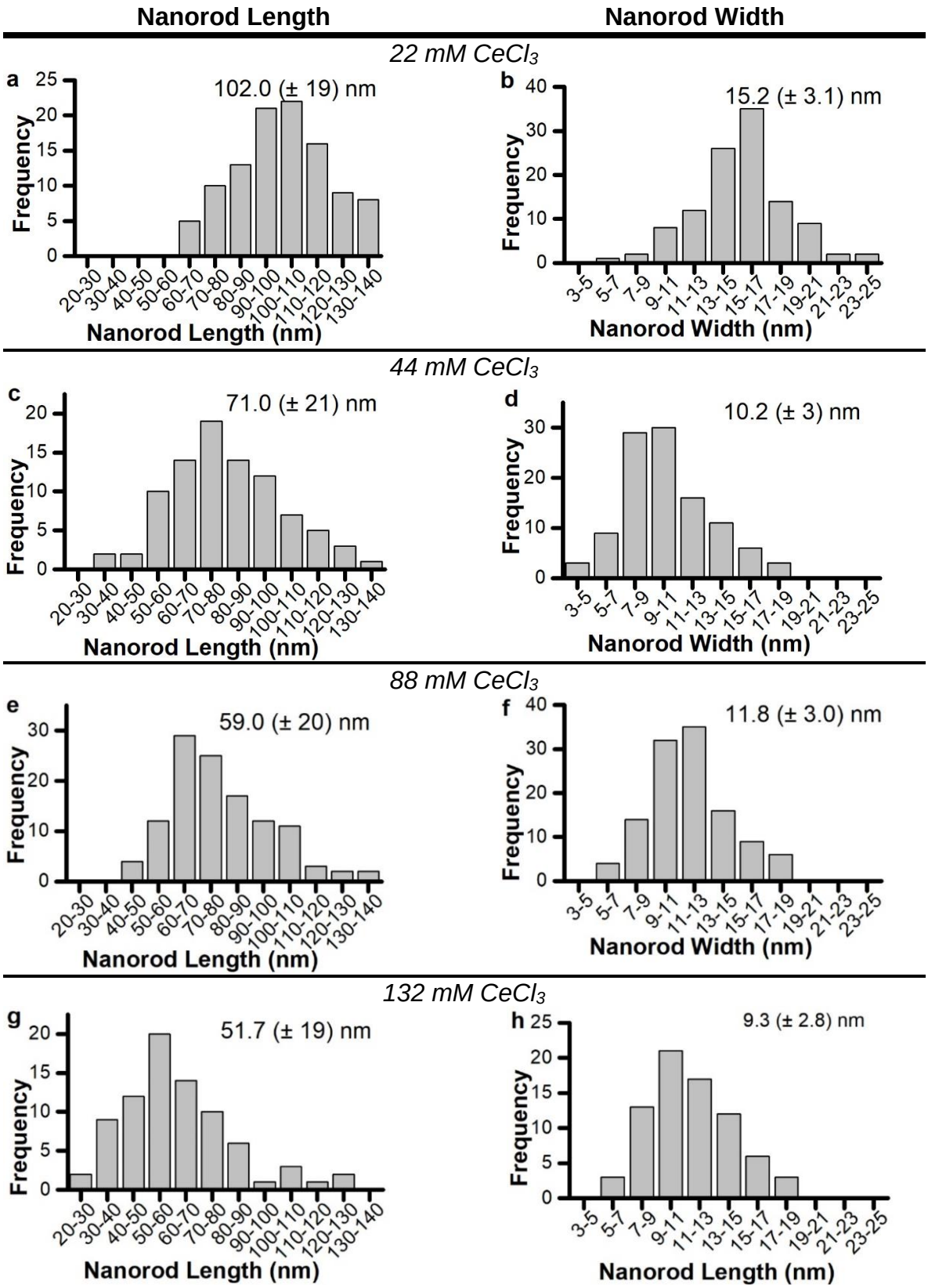

Figure 2.3 *Histograms of lengths and widths of Eu-CeO_2 nanorods using (a, b) 22 mM, (c, d) 44 mM, (e, f) 88 mM, and (g, h) 132 mM $CeCl_3$.*

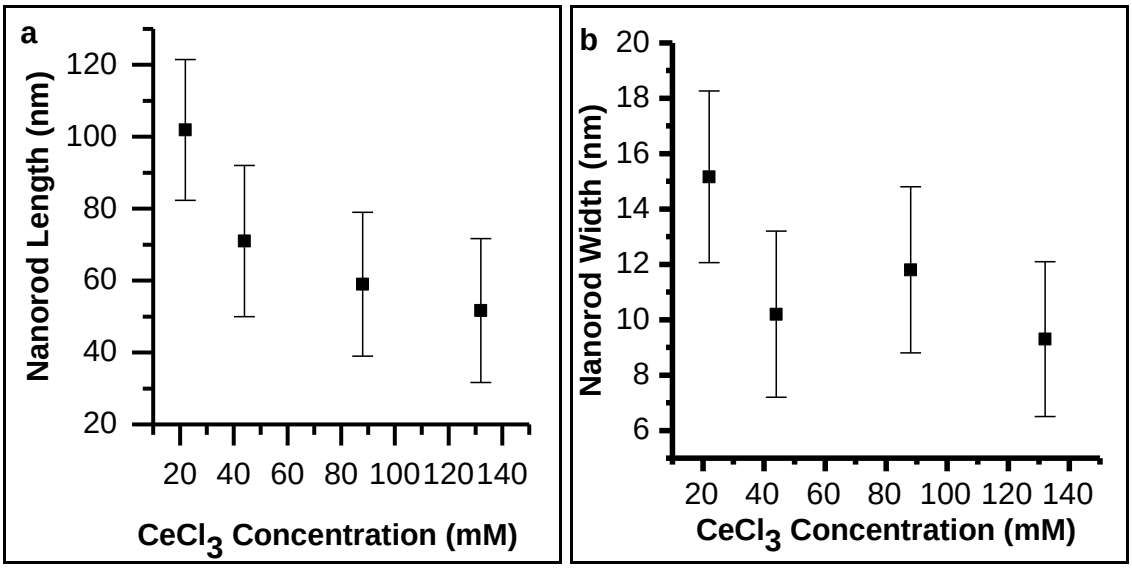

Figure 2.4 *Plot of nanorod (a) length and (b) width as a function of $CeCl_3$ concentration.*

2.4.3. Influence of Na_3PO_4 Concentration

Na_3PO_4 is required for nanorod growth in acidic-based hydrothermal reactions above 180 °C. It acts as a mineralizer, encouraging growth of $CePO_4$ and subsequent oxidation to CeO_2 in the absence of $Ce(OH)_3$ precipitation.[41,42,126,129]

In the absence of Na_3PO_4, nanorods are still formed, indicating that reaction with a lower temperature of 100 °C and with OH^-, Na_3PO_4 is not required for the anisotropic growth of $Ce(OH)_3$.[41] Increasing PO_4^- concentration significantly increases the nanorod width as well the standard deviation, although the length of the nanorods are not affected (Figures 2.5, 2.6).

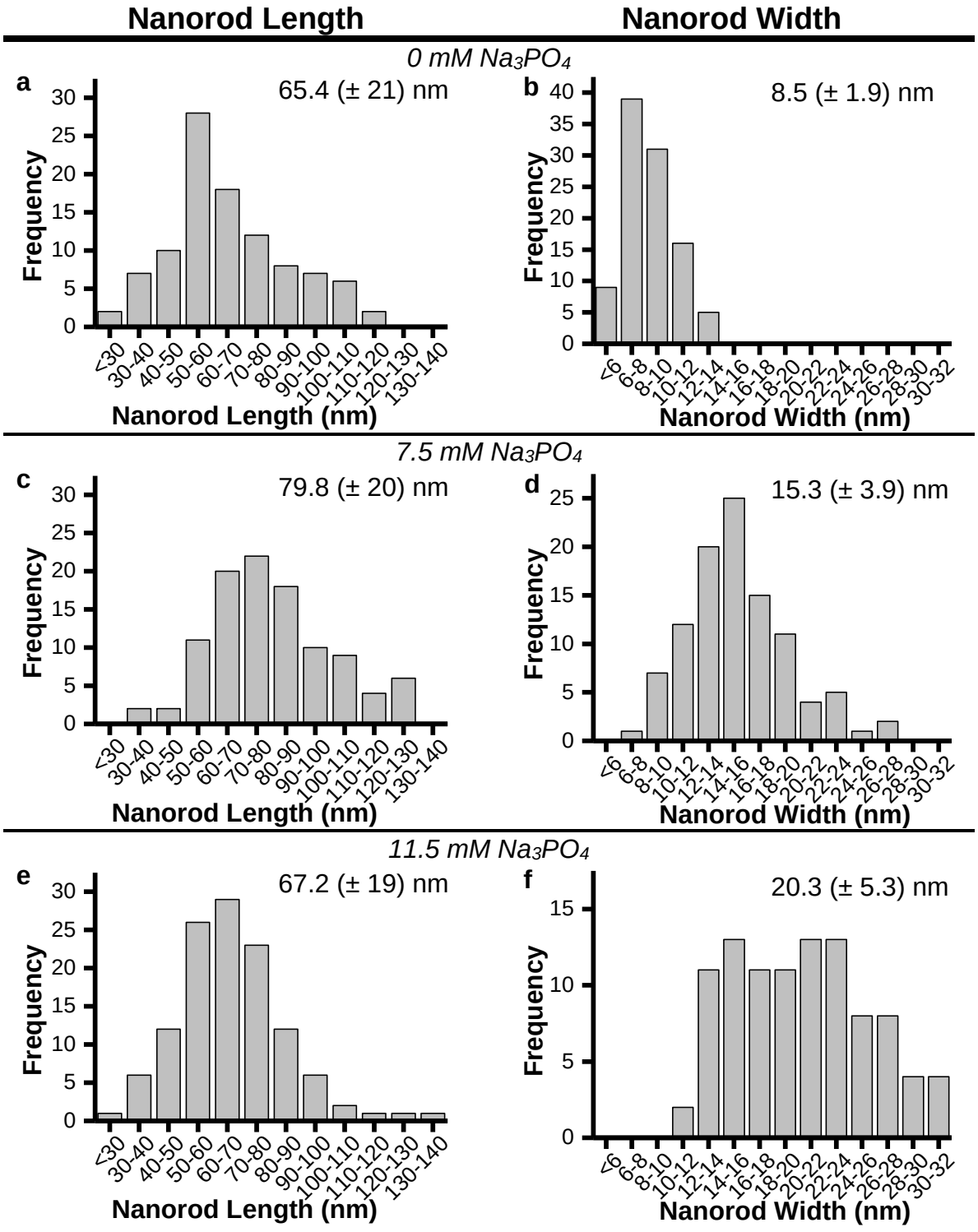

Figure 2.5 *Histograms of Eu-CeO_2 nanorods lengths and widths grown with (a, b) none, (c, d) 7.5 mM, and (e, f) 11.5 mM Na_3PO_4. Histograms for samples with 2.7 mM Na_3PO_4 are shown in Figures 2.4c,d.*

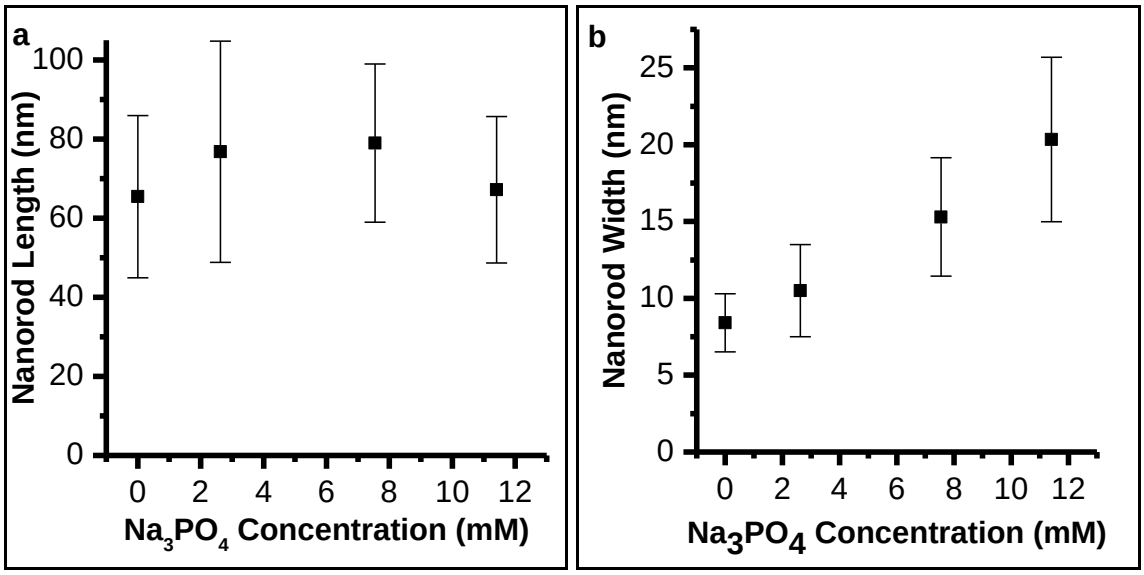

Figure 2.6 *Plot of Eu-CeO_2 nanorod (a) length and (b) widths relative to Na_3PO_4 concentration.*

Na_3PO_4 likely encourages the dissolution and recrystallization of $Ce(OH)_3$ and CeO_2 through competition with OH^-, thereby increasing the Oswalt Ripening in the system.[130] PO_4^{3-} therefore reduces the aspect ratio of the rods as Ostwald ripening favors spherical growth. However, the precipitation of $CePO_4$ is limited by the low concentration of PO_4^{3-} relative to the Ce^{3+} concentration. Given the extreme excess of OH^-, the minor $CePO_4$ precipitation is negligible relative to the precipitation of $Ce(OH)_3$.

2.4.4. Influence of $EuCl_3$ Concentration

Eu^{3+} had negligible influence on the morphology or size of the Eu-CeO_2 nanorods. Nanorods were insignificantly shorter in the absence of any $EuCl_3$ due to large standard deviation (Figure 2.7). The substitution of Ce^{4+} with Eu^{3+} increases O^{2-} vacancies for charge balance and causes strain from the substitution of the smaller Eu^{3+} ion.[131] The crystal lattice is subsequently expanded in principle, which may increase the size of the

nanorods. However, the relatively low concentration of Eu^{3+} presumably limits the extent of this expansion.

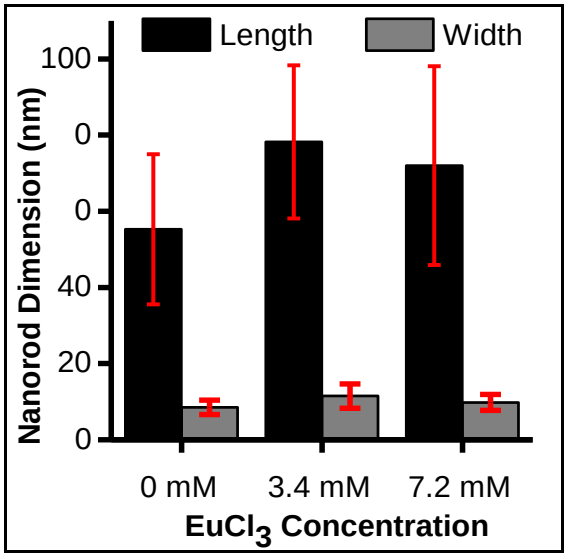

Figure 2.7 *Eu-CeO_2 nanorod width (gray) and length (black) with varying $EuCl_3$ precursor concentrations.*

2.4.5. Influence of Cerium Precursor Identity

The cerium precursor is also essential for morphological control of Eu-CeO_2 materials. Due to reduced solubility, the precipitation of $Ce(OH)_4$ from Ce^{4+} precursors would theoretically enhance the precipitation, while slowing OR growth. In the case of Ce^{3+}, different counter ions have also been proposed to act as surface directing agents, depending on their relative ease of dissociation from the $Ce(OH)_3$ surface or activity as oxidizing agents.[51,132]

To probe these effects, several cerium precursors were selected as detailed in Figure 2.8, featuring several counter ions as well as the Ce^{3+} and Ce^{4+} oxidation states. Commercially available CeO_2 nanoparticles were also included to check for oriented

attachment of CeO_2 during the hydrothermal reaction. All reactions were run at baseline conditions, with the precursor concentration set to a Ce^{3+} or Ce^{4+} concentration of 44 mM.

Nanorods are observed with all three Ce^{3+} salts (chloride, nitrate, acetate) (Figure 2.8a, b, c) with no significant size differences, indicating no influence of the counterions. However, no rods are observed with $(NH_4)_2Ce(NO_3)_4$ (Figure 2.8f) or cerium t-butoxide (Figure 2.8d). Instead, products isolated from reactions involving the Ce^{4+} precursors retain a morphology similar to that seen with $CeCl_3$ prior to any hydrothermal treatment (

Figure ***2.9***a). The commercially-obtained CeO_2 nanoparticles are very stable and retain their original morphology (Figure 2.8e). This indicates precipitation and nanorod growth occurs through $Ce(OH)_3$, with oxidation to Ce^{4+} preventing nanorod growth.

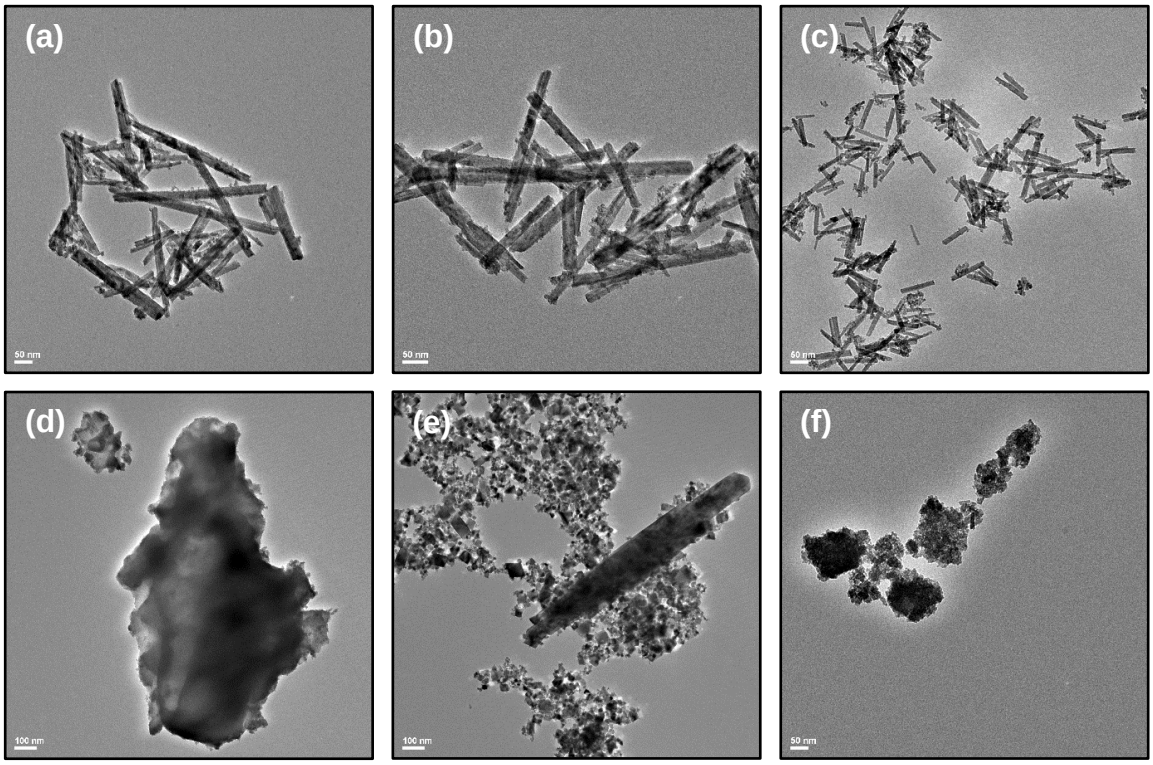

Figure 2.8 *TEM images of CeO_2 nanomaterials synthesized from (a) $CeCl_3$; (b) $Ce(NO_3)_3$; (c) $Ce(C_2H_3O_2)_3$; (d) Cerium (IV) t-Butoxide; (e) CeO_2 nanoparticles; and (f) $(NH_4)_2Ce(NO_3)_6$ at concentrations of 50 mM Ce^{3+} or Ce^{4+}.*

2.4.6. Influence of Reaction Time

The reaction time can also have a significant impact on the morphology of materials synthesized, particularly those based on growth through Oswald Ripening. Shorter reaction times are more likely to favor small particles as originally precipitated prior to the hydrothermal reaction. Prior research also reports shifts from polyhedral shapes to rods over the course of several hours, due to the slow Oswalt Ripening.[129]

Upon mixing the NaOH and $CeCl_3$ solutions for 10 minutes, large precipitates with no nanorod or polyhedral features are observed (

Figure ***2.9***a). After a 30-minute hydrothermal treatment, some nanorods are observed (

Figure ***2.9***b), although the majority of the product consists of dense aggregates. Once formed, the length and width of the observed nanorods do not increase with reaction time (

Figure ***2.9***, 2.10), indicating that the growth equilibrium is reached quickly. A relative reduction in the number and size of aggregates is observed with increasing reaction time, particularly over the first 10 hours (

Figure ***2.9***a-f).

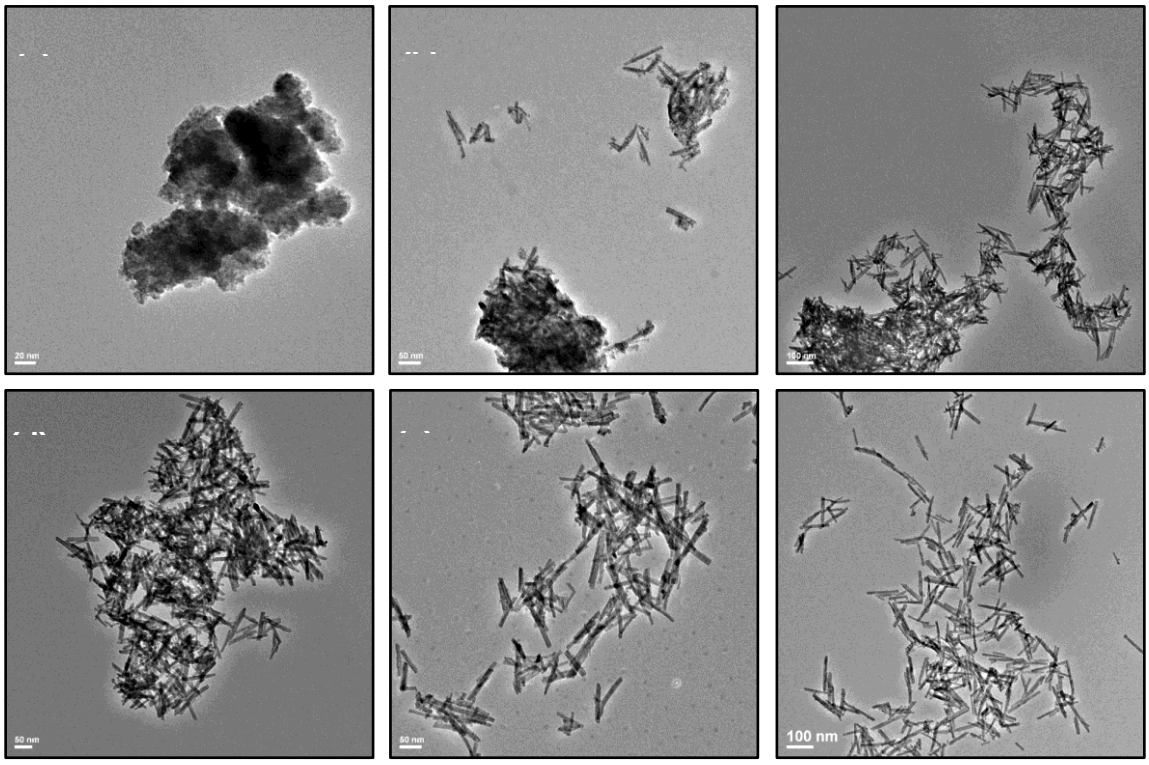

***Figure* 2.9** *TEM images of reaction products after (a) stirring only, (b) 30 min, (c) 1 hr, (d) 2 hr, (e)12 hr, and (f)16 hr hydrothermal reaction.*

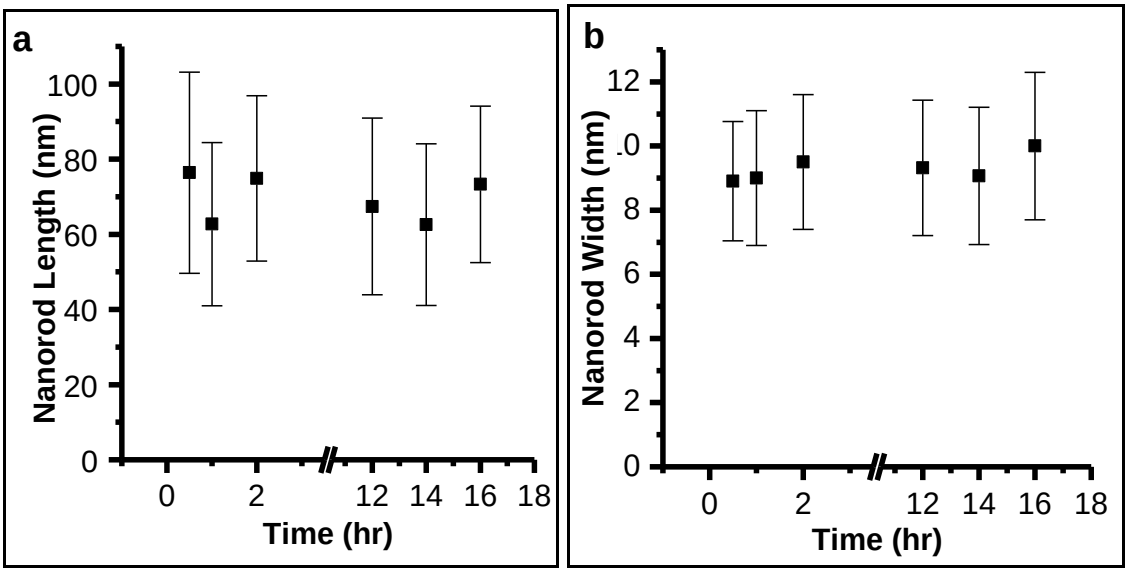

Figure 2.10 *Eu-CeO_2 nanorod (a) length and (b) widths when synthesized under various hydrothermal reaction durations.*

2.4.7. Influence of Reaction Temperature

The reaction temperature influences the aqueous solubility of the CeO_2 or $Ce(OH)_3$, and therefore the rate constant for OR. Higher temperatures also facilitate the oxidation of $Ce(OH)_3$ to CeO_2 by dissolved O_2 or NO_3^-.[50,51] Therefore, the reaction could either speed up due to accelerated OR, or slow down due oxidation of $Ce(OH)_3$.

Across the range tested, the hydrothermal reaction temperature had no impact on nanorod growth dimensions (Figure 2.11). This system produced nanorod morphologies at temperatures as low as 60 °C, significantly lower than the 100 °C to 220 °C typically used in the literature.[41,51]

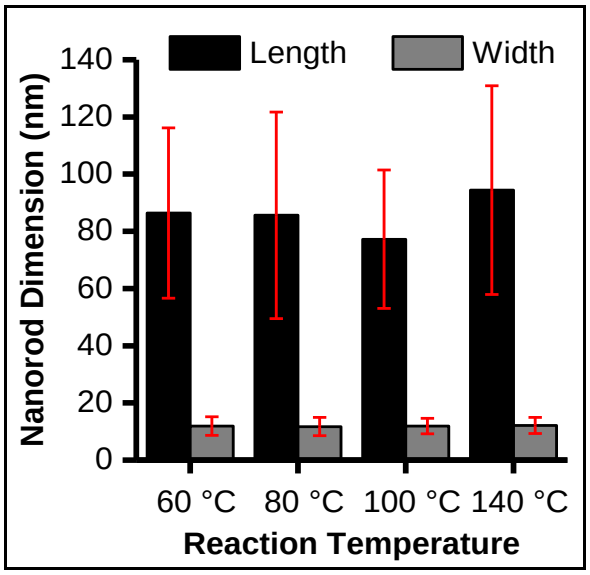

Figure 2.11 *Eu-CeO_2 nanorod lengths and widths when synthesized under various hydrothermal reaction temperatures.*

2.5. Results: Morphology of Eu-CeO_2 Annealed Nanorods

2.5.1. Influence of Annealing Temperature

The nanorods maintain the typical nanorod morphology following annealing temperatures of 400 °C to 700 °C (Figure 2.12a-e). Further annealing to 800 °C significantly shortened, thickened, and fused the nanorods (Figure 2.12f). Prior to 800 °C, the nanorods steadily reduce in length with heating (Figures 2.12g, 13**Figure 2.12**), although the deviation in length makes this reduction negligible. The shortening of the rods is consistent with sintering, as particles reduce their surface energy through minimization of surface area.

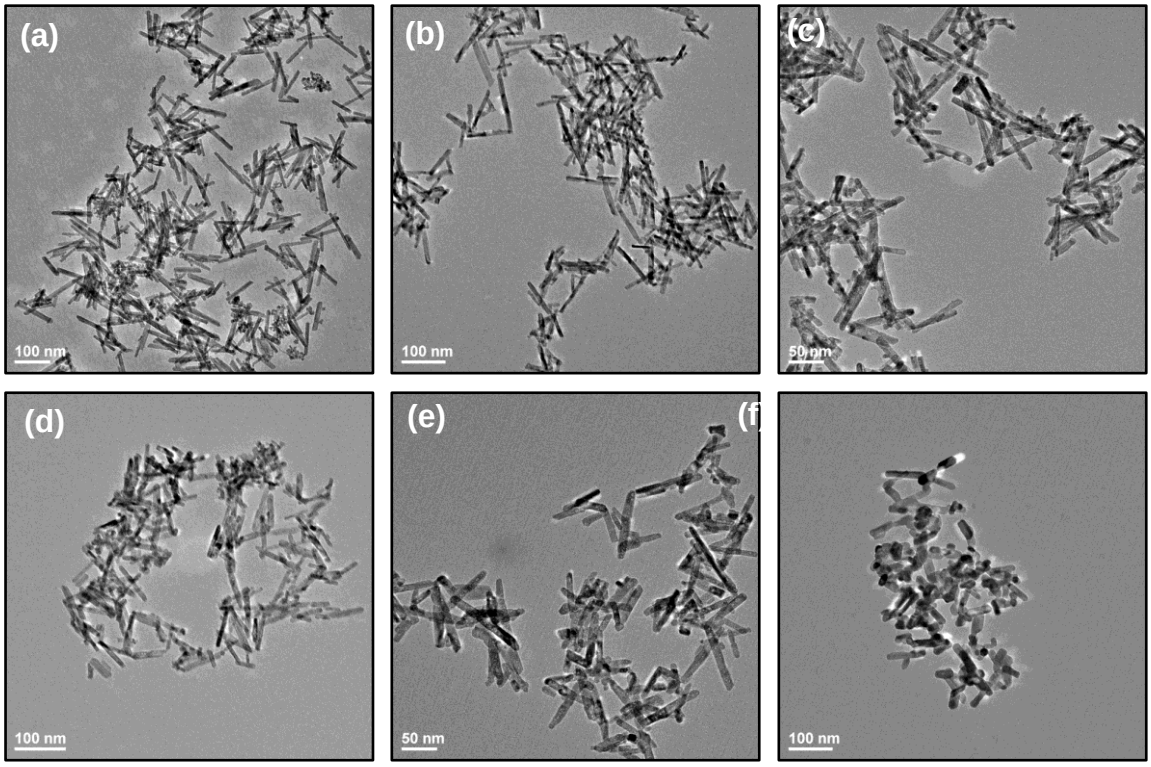

Figure 2.12 *TEM images of Eu-CeO_2 (a) unannealed, and annealed to (b) 400 °C; (c) 500 °C; (d) 600 °C; (e) 700 °C; and (f) 800 °C.*

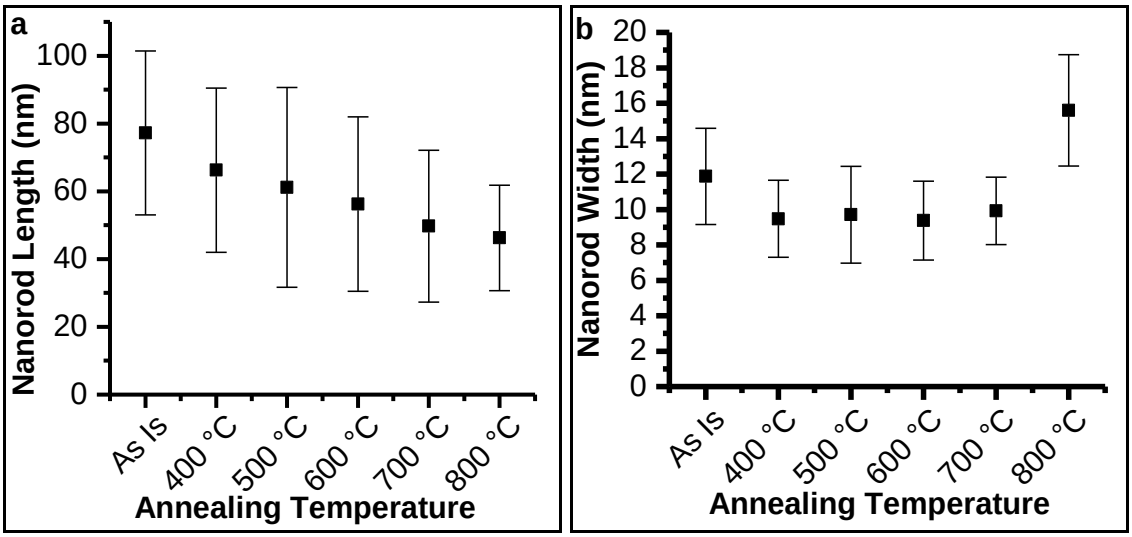

Figure 2.13 *Average Eu-CeO_2 nanorod (a) length and (b) width with increasing annealing temperature.*

2.5.2. Influence of Heating Rate and Annealing Duration

As mentioned in the overview (Section 2.1), a paper by Gao *et al.* reported annealed nanorods with no morphological change up to 900 °C by using a very slow annealing process. The nanorods in Section 2.5.1 were annealed by heating to 800 °C at 13 °C/min, holding steady for 16 hours, then gradually cooling. The Gao group used a heating rate of 10 °C/min, and started cooling after 2 hours annealing.

Unlike the Gao group, for the experiments completed in this dissertation slow annealing to 800 °C did not prevent the diminution of nanorod morphology, with significant shortening, thickening, and fusion between rods (Figure 2.14). The final length and width of the rods were 40.0 (± 24) nm by 14.0 (± 3) nm, similar to the nanorods annealed for a longer time and with a faster heating rate. Therefore, neither a gentle heating protocol or short annealing time will prevent a morphological change in the nanorods. This is contradictory to previously published research claiming annealing with no loss in morphology.[122]

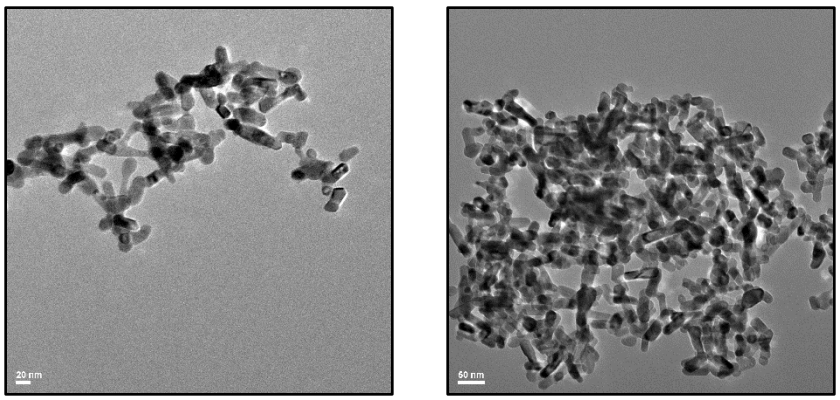

Figure 2.14 *TEM images of Eu-CeO_2 rods annealed to 800 °C using slow heating procedure and demonstrating same fusion as observed in faster protocol.*

2.6. Crystalline Properties of Eu-CeO_2 Nanorods

2.6.1. Analysis of Crystalline Domains by HRTEM

The Eu-CeO_2 nanorods and annealed nanorods were analyzed using HRTEM for crystallite size and orientation. The annealed nanorods were essentially monocrystalline, exhibiting lattice spacings associated with the (111) plane of CeO_2 (Figure 2.15c). As such, the crystalline domain size is assumed to match the dimensions of the annealed nanorods (Table 2.1).

The unannealed nanorods demonstrated a more complex crystallinity with small areas of multi-oriented crystalline domains. In Figure 2.15a one of the observed nanorods has one set of (111) CeO_2 lattice spacings running lengthwise on the outer edge of the nanorods and another orientation perpendicular to the nanorod width. This dual crystalline orientation is likely due to the oxidation mechanism. The surface of the Eu-CeO_2 nanorod is oxidized from hexagonal $Ce(OH)_3$ to cubic CeO_2 during the washing stage. However, the protected core may retain the hexagonal crystal structure until the solid is fully dried, and therefore may have a different crystal orientation.

The nanorods also frequently exhibit multiple lattice spacings, often with the (220) spacing perpendicular to the length of the nanorod, matching literature reports of growth in the [110] direction (Figure 2.15b).[36,42]

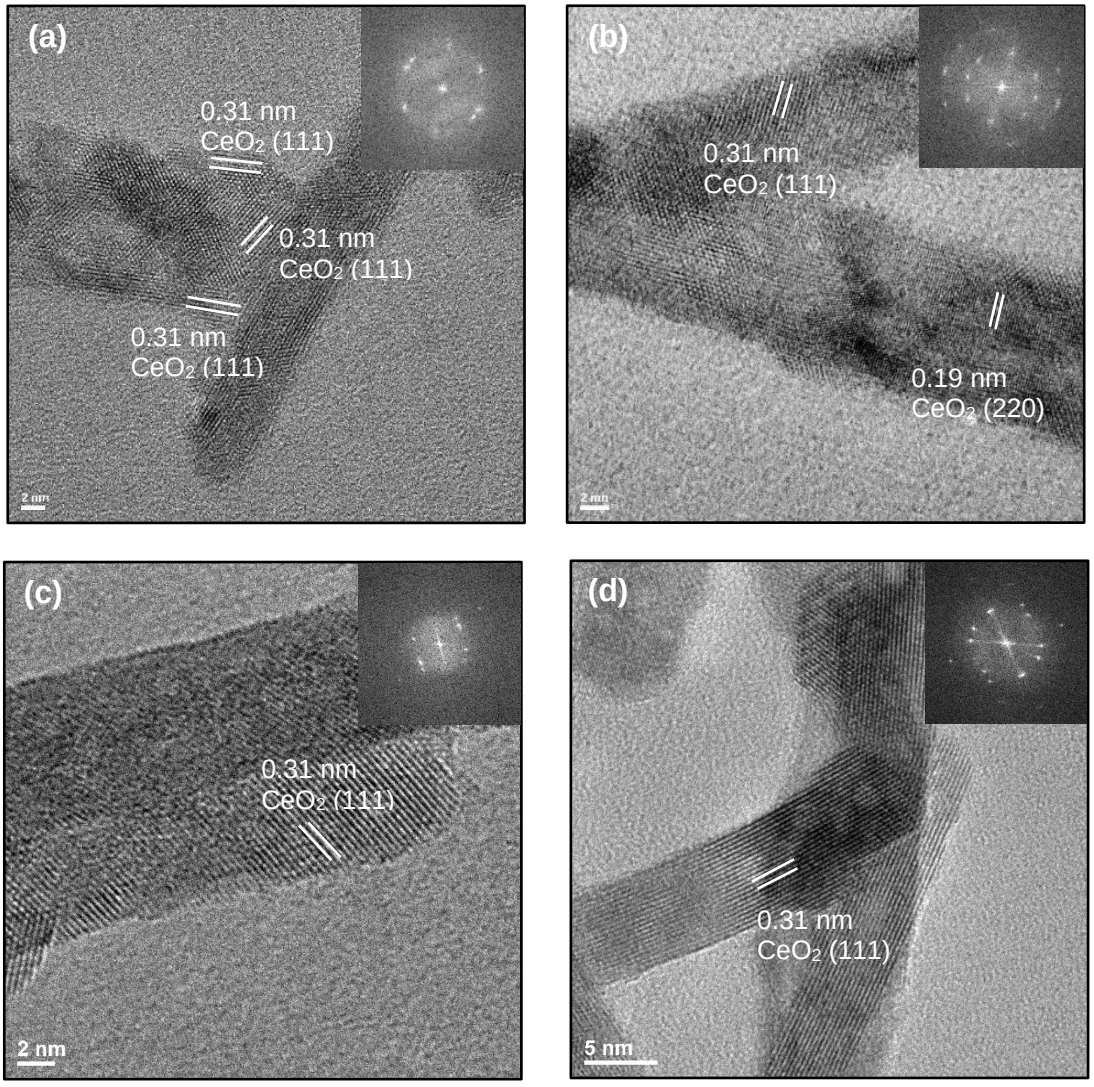

Figure 2.15 *HRTEM images of Eu-CeO_2 (a) nanorod polycrystallinity with different orientations of CeO_2 (111); (b) nanorod crystallinity with CeO_2 (111) and CeO2 (220) planes present; and (c,d) annealed nanorods showing monocrystallinity with CeO_2 (111) lattice spacing. Inset are FFT for each image.*

2.6.2. Crystalline Properties of Eu-CeO_2 Nanostructures by XRD Analysis

Nanorods prepared with 0 and 3.3 mM $Eu(NO_3)_3$ precursor concentrations corresponding to theoretical 0% and 7.7 %Eu concentrations, were analyzed using powder XRD. The Eu-CeO_2 nanorods annealed to 800 °C were also analyzed. Specific peak positions and assignments of the XRD spectra (Figure 2.16) are detailed in Table 2.1.

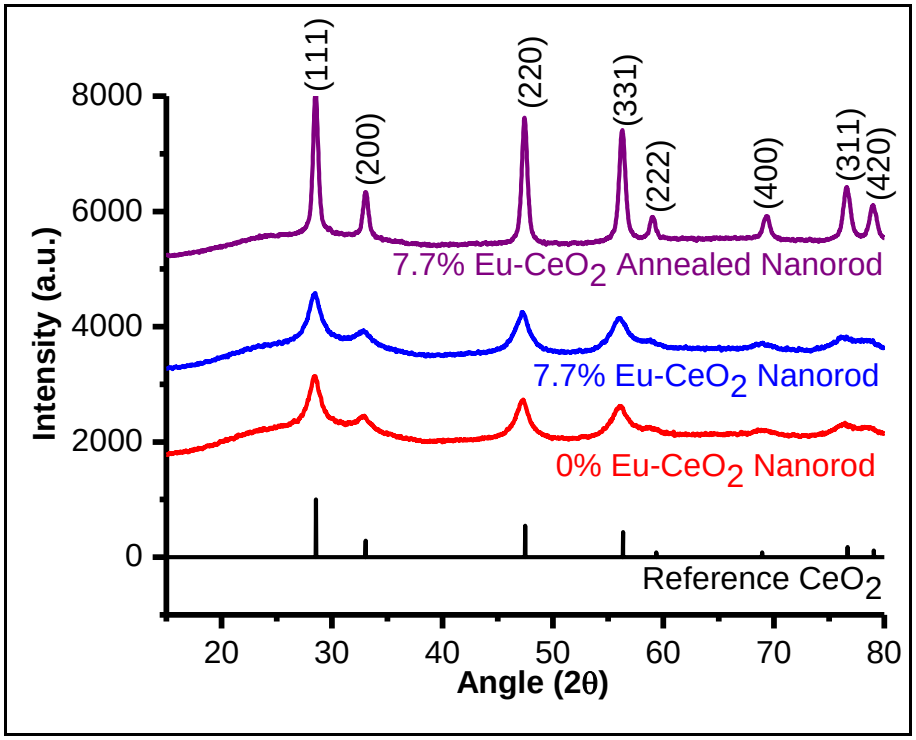

Figure 2.16 *XRD spectra of 0 and 7.7% Eu-CeO_2 nanorods, 7.7% Annealed Eu-CeO_2 nanorods, and reference CeO_2 from NIST.128*

All peaks are consistent with CeO_2 crystallized in a cubic fluorite structure. The absence of any peak near 2Θ of 19° indicates Eu^{3+} is incorporated in the CeO_2 lattice with no detectable formation of a Eu_2O_3 phase.[133] There are some minor shifts in peak position between the CeO_2 reference sample and the unannealed nanorods, with no difference in peak positions between the two unannealed samples. For instance, the

(111) peaks shifted from 28.54° to 28.48° and 28.46° for 0% and 7.7% respectively. This shift is minor and may be attributed to either measurement uncertainty, or to lattice strain and expansion from oxygen vacancies and Ce^{3+} defects as discussed in Chapter 1. Upon annealing, the increase of crystalline domain size coincides with removal of these defect sites and reduction of lattice strain. As a result, the majority of the annealed nanorod diffraction peaks are observed very close to the reference peaks.

Table 2.1 *Peak assignments in powder XRD for CeO_2, Eu-CeO_2 nanorods, and Eu-CeO_2 annealed nanorods, as compared to reference CeO_2.*[128]

Sample	CeO_2 Peak Assignments (2Θ)							
	(111)	**(200)**	**(220)**	**(331)**	**(222)**	**(400)**	**(311)**	**(420)**
Reference CeO_2	28.54	33.04	47.48	56.34	59.36	68.94	76.68	79.07
0% Eu-CeO_2 Nanorods	28.48	32.92	47.30	56.06	58.78	68.56	76.44	--
7.7% Eu-CeO_2 Nanorods	28.46	32.82	47.26	56.10	58.80	68.94	76.56	--
7.7% Eu-CeO_2 Annealed Nanorods	28.54	33.08	47.42	56.28	59.04	69.30	76.62	79.06

The unannealed nanorods have significant line broadening relative to the annealed rods, particularly the higher angle reflections which are nearly indistinguishable from the baseline. The crystalline domain, calculated through the Scherrer equation (Eqn 2.10) as detailed in Section 2.5.3, increases from ~6 nm to ~15 nm upon annealing (Table 2.2). which mirrors a shift from a polycrystalline material to monocrystalline observed under the TEM.

Table 2.2 *Full width half max (FWHM), calculated crystalline domain, and measured crystalline domain of nanorod samples.*

Sample	FWHM (2Θ)	XRD Crystalline Domain (nm)
0% Eu-CeO_2 Nanorods	1.44	6.26
7.7% Eu-CeO_2 Nanorods	1.44	6.05
7.7% Eu-CeO_2 Annealed Nanorods	0.58	15.65

However, this use of the Scherrer equation, (Eqn 2.10), only provides an estimate of the crystalline domain magnitude, due to two significant assumptions. The broadening in powder XRD can have three sources: the instrument (β_{inst}), the crystalline domain size (β_{size}), and strain (β_{strain}) as seen in Equation 2.11. β_{inst} should contribute equally to all spectra, reducing the calculated crystallite size evenly. The crystalline size was calculated for the (111), (220), and (331) planes with significant variation or trend found, indicating a minimal contribution from β_{strain}.[134]

$$\beta_{obs} = \beta_{inst} + \beta_{size} + \beta_{strain} \quad \text{(Eqn 2.11)}$$

Furthermore, the Scherrer constant (*K*), selected to be 0.94 for these calculations, is designated for spherical materials with cubic symmetry. However, while K can range from extremes of ~0.5 to ~2, values of ~0.9 are commonly used for cubic crystal structures.[135] As a result, the calculated values likely significantly underestimate the crystalline domain size, and only provide estimates of relative domain size magnitude.

2.7. Elemental Analysis by TEM EDS

Nanorod samples were first analyzed for contamination by counter ions in the reaction solution, namely sodium, phosphorus, and chloride. As observed in Figure 2.17, the EDS spectrum exhibits only cerium, europium, and oxygen signal, along with copper from the

TEM sample grid. Due to the small diameter of the rods, a silicon signal is occasionally observed in the EDS spectra near 1.8 keV as an artifact from the x-ray detector.

The atomic percent of Eu in the final nanorod product increases with increasing Eu^{3+} concentration in the reaction solution (Table 2.3). Additionally, the atomic percentage of oxygen decreases with increasing Eu^{3+}, corresponding to the predicted oxygen vacancies caused by the dopant.

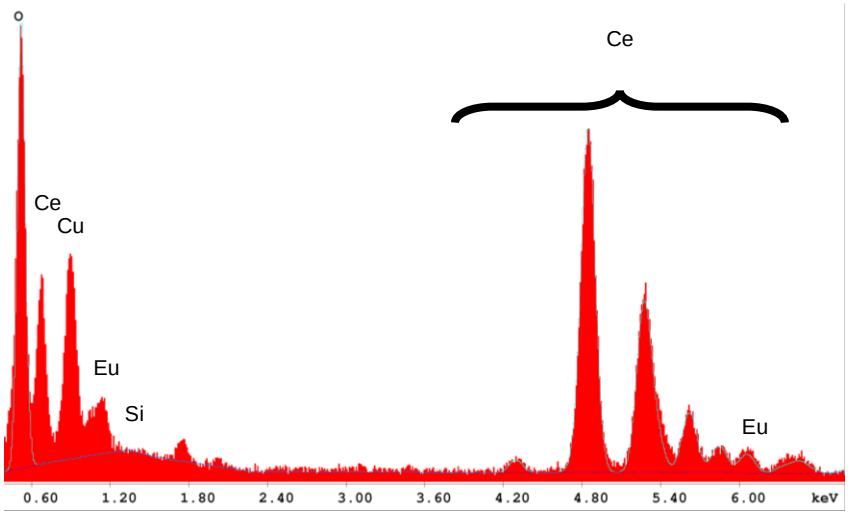

Figure 2.17 *Typical EDS spectrum for 7.7% Eu-CeO_2 nanorods. The series of peaks between 4.2 keV and 7 keV are attributed to CeL, except for Eu as marked at 5.8 keV.*

Table 2.3 *EDS data of at% O, Ce, and Eu for Eu-CeO_2 nanorods synthesized with a range of $EuCl_3$ concentrations.*

mM $EuCl_3$	Theoretical%Eu	At% O	At% Ce	At% Eu	%Eu
0	0	68.6 ± 2.9	31.2 ± 3.1	0.2 ± 0.3	0.9 ± 1
3.3	7.7	62.3 ± 1.9	34.6 ± 1.6	3.1 ± 0.3	8.2 ± 0.4
7.2	16.7	60.3 ± 5.7	33.4 ± 5.5	6.3 ± 0.5	16.1 ± 2

2.8. Conclusions

In this chapter Eu-CeO_2 nanorods were synthesized, and parameters for controlling the morphology and size were analyzed. The nanorod length was controlled through variation of $CeCl_3$ concentration in the range from 50 nm to 100 nm. The width was controlled by Na_3PO_4 concentration from 8 nm to 20 nm, providing a method for width control not previously reported in literature for CeO_2 nanorods. The europium content of the nanorods was also easily adjusted from 0 to 16 %Eu through the $EuCl_3$ concentration with limited influence on the nanorod morphology or size.

The influence of the various reaction parameters on the Eu-CeO_2 rod morphology are consistent with the mechanism in literature for the undoped system.[42,51] Eu-$Ce(OH)_3$ nuclei first precipitate, then grow by rapid Ostwald Ripening of Eu-$Ce(OH)_3$. Upon drying, the $Ce(OH)_3$ rods with a hexagonal crystal structure is quickly transformed to CeO_2 rods with a cubic fluorite crystal structure. This rapid change in crystal structure produces rods with numerous smaller multi-oriented crystalline domains in the nanorod core and decorating the surface. However, most rods also exhibit extended crystalline domains running the length of the rod.

Eu-CeO_2 nanorods could be converted to a monocrystalline rod morphology by heating above 500 °C. However, at temperatures above 700 °C, sintering of the rods began, with rod shortening and thickening. This research represents the first extensive investigation of Eu-CeO_2 nanorod synthetic mechanisms and dimensional control.

The variety of crystallinity, size, and doping in the nanorod and annealed nanorod systems prompt analysis of the resulting impact on Eu-CeO_2 chemical activity.

Furthermore, these two materials can also be compared to other morphologies synthesized and analyzed in the chapters that follow.

The complete integration of Eu^{3+} ions into the CeO_2 lattice enables further investigation of interesting chemistry due to the fluorescence capability of Eu^{3+} and introduction of oxygen vacancies. Furthermore, the relative absence of morphological or dimensional change with Eu^{3+} incorporation invites incorporation of other rare earths elements into the rod and cube morphology, as will be discussed in Chapter 5.

Chapter 3: Hydrothermal Synthesis of Eu-CeO_2 Nanocubes

3.1. Overview

Chapter 2 details the synthesis of europium-doped cerium oxide (Eu-CeO_2) nanorods and annealed nanorods. Eu-CeO_2 nanocubes are also synthesized through a hydrothermal reaction, similar to CeO_2 nanorods, but different reaction conditions have a significant impact on the growth mechanism. Just as Eu-CeO_2 nanorods are a relatively unexplored morphology, the literature of Eu-CeO_2 nanocubes is also very limited. The only current literature citation addressing Eu-CeO_2 nanocubes utilizes a microwave-assisted hydrothermal technique.[131] In this recent report, CeO_2 cubes were doped with up to 30% Eu^{3+} to analyze the influence of the europium on the nanocube morphology, crystallinity, oxygen vacancy concentration, and ease of reduction of Ce^{4+} by H_2. The europium was shown to distribute evenly through the nanocube with depleted oxygen near the surface, and lattice strain increasing with europium content. Doping the CeO_2 nanocubes above 10% Eu^{3+} leads to oxygen vacancy ordering and increased lattice strain, which may support surface oxidation at lower temperatures relative to undoped CeO_2 nanocubes.[131]

While this study on Eu-CeO_2 nanocubes was insightful, a few limitations invite further investigation to the nanocube synthesis. First, this study was focused only on the variations in the europium concentration and structure-associated impact, with no other synthetic parameters analyzed. Furthermore, microwaves are often utilized in conjunction with hydrothermal techniques, as the assistance can significantly shorten the reaction duration. The rapid heating affects the kinetics of the hydrothermal reaction, and frequently produces smaller nanomaterials relative to conventional heating.[136] Therefore, there is a need for an analysis of the synthetic parameters under conventional hydrothermal conditions and their influence on the structure and morphology of the Eu-CeO_2 nanocubes.

This chapter focuses on the synthesis of Eu-CeO_2 nanocubes by the precipitation of $Ce(OH)_3$, followed by a conventional hydrothermal reaction. Several reaction conditions, including precursor concentrations, cerium counter-ions, reaction temperatures, and reaction durations are analyzed for control over the morphology and dimensions of the product. The nanocubes were subsequently analyzed with HRTEM, powder XRD, and EDS to confirm cubic fluorite structure crystallization with negligible impurities and to determine the relative crystalline domain sizes compared to the nanorod samples of Chapter 2.

3.2. Introduction

At higher temperatures, growth through Ostwald Ripening (OR) as described in Chapter 2 is very slow, so most of the CeO_2 growth is through Oriented Attachment (OA). Higher temperatures facilitate oxidation of Ce^{3+} to Ce^{4+}, which reacts with OH^- to form $Ce(OH)_4$ rather than $Ce(OH)_3$ (Eqn 3.1).[39] $Ce(OH)_4$ can also be produced by oxidation of

$Ce(OH)_3$ in relatively high base concentrations and high temperature reaction conditions (Equations 3.1, 3.2).[123] Once produced, $Ce(OH)_4$ undergoes condensation and subsequent dehydration to produce CeO_2 nuclei (Equation 3.3).[43]

$$Ce^{4+} + 4\,OH^- \rightarrow Ce(OH)_4 \qquad \text{(Eqn 3.1)}^{39}$$

$$Ce(OH)_3 \xrightarrow{O_2, OH^-} Ce(OH)_4 \qquad \text{(Eqn 3.2)}^{123}$$

$$Ce(OH)_4 \rightarrow Ce^{IV}O_2 + 2H_2O \qquad \text{(Eqn 3.3)}^{43}$$

As a result, $Ce(OH)_3$ initially grows through the OR mechanism as described in Chapter 2 but is gradually oxidized during the dissolution step under the hydrothermal treatment (Figure 3.1). The rate of OR-based growth of CeO_2 is significantly slower than that of $Ce(OH)_3$, due to the reduced solubility of CeO_2.[61] Furthermore, the change in crystal structure from hexagonal $Ce(OH)_3$ to cubic CeO_2 suppresses the anisotropic growth as seen in the synthesis of $Ce(OH)_3$ rods.[137]

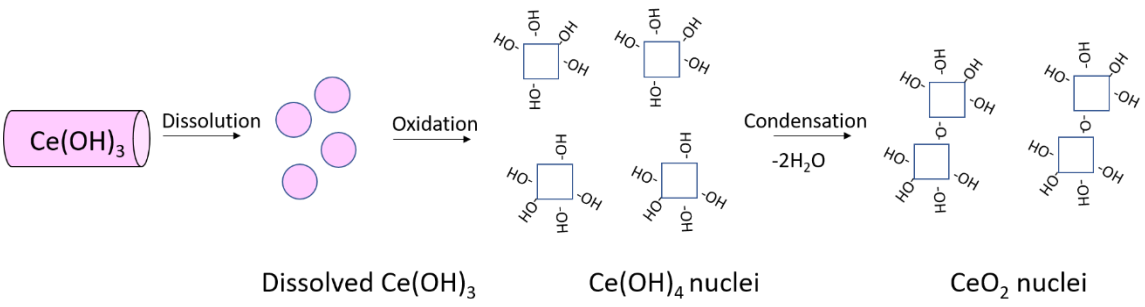

Figure 3.1 *Illustration of transition from rod-like $Ce(OH)_3$ growth to cubic $Ce(OH)_4$ by dissolution and oxidation, and finally condensation and dehydration to form CeO_2 nuclei.*

After oxidation, CeO_2 nuclei aided by Van der Waals forces,[131] collide and fuse along common crystallographic planes through condensation and dehydration of adsorbed OH^-.[52,138] Several ions and organic surfactants have been used as surface directors to control this process, such as NO_3^-,[51] oleic acid,[139] cetyltrimethylammonium bromide,[5] and

polyvinylpyrrolidone.[52] The charged surface directors bind selectively to the highest energy (200) plane of CeO_2, repelling each other during nuclei collisions to prevent particle fusion.[39] Surface hydroxyls of the CeO_2 nuclei typically interact with these larger polymers through hydrogen bonding, and steric hinderance preventing interactions between nuclei.[140]

The relative surface energies of the CeO_2 planes, (111) < (220) < (200), lead to strong adsorption of the surface directing groups on the (200) plane, as well as the (220) to a lesser extent. In systems with excess OH^-, CeO_2 nuclei are likely OH-terminated, even on the (111) planes. While negatively charged, hydroxides, unlike other surface directing agents, facilitate fusion through condensation and dehydration (Eqn 3.4).[141]

$$Ce^{4+} - OH + HO - Ce^{4+} \rightarrow Ce^{4+} - O - Ce^{4+} + H_2O \qquad \text{(Eqn 3.4)}^{141}$$

As a result, growth by fusion of (111) crystallographic planes is encouraged by the presence of OH^- and absence of other fusion-blocking groups (nitrates, surfactants, etc).[39] Particles continue growing through this mechanism until the concentration of fusion—blocking groups at remaining surfaces overcomes the energetically-favorable reduction in surface area. With the proper selection of surface directing agent and reaction conditions, this growth is completed when the cube is terminated with exposed (200) planes.[43]

3.3. Methods and Materials

3.3.1. Materials and Synthesis

All chemicals were purchased as described in Chapter 2 and used without further purification.

Doped cerium oxide nanocubes were synthesized by a modification of a well-established hydrothermal synthetic route to CeO_2 nanocubes (Figure 3.2).[50] To precipitate $Ce(OH)_3$, 0.4 g $Ce(NO_3)_3$ and 0.027 g $Eu(NO_3)_3$ dissolved in 6.6 mL H_2O were reacted with 13.3 mL of 15 M NaOH to give final concentrations of 46 mM Ce^{3+}, 3 mM Eu^{3+}, and 10 M OH^- respectively. The reaction mixture was rapidly stirred in an iced acetone bath at 0 °C for 20 minutes, then transferred to a 20 mL stainless steel-coated Teflon vessel. The reactor was placed in an oven and heated at 180 °C for 16 hours. After allowing the reactor to cool naturally, samples were washed five times with de-ionized water, dried at 95 °C, and ground into a powder. Precursor concentrations, reaction times, temperatures, and reactant concentrations were subsequently varied to probe relative influence on nanocube morphology, dimensions, and elemental composition.

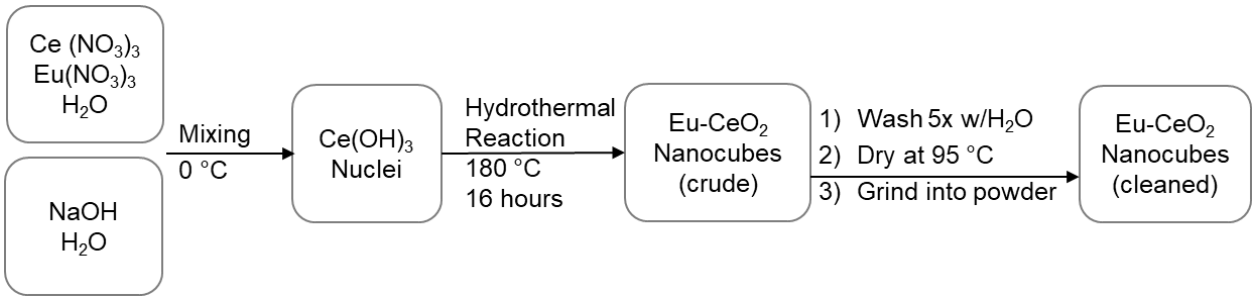

Figure 3.2 *Diagram of typical procedure for synthesis of Eu-CeO_2 nanocubes.*

3.3.2. Characterization

The reaction products were analyzed using the TEM, HRTEM, XRD, and EDS procedures described in Chapter 2.

Briefly, for TEM and EDS samples the solid product is sonicated in water, dispersed on a carbon coated copper grid, and analyzed at 200 kV in the TEM. Powder XRD

reflections are measured from 15° to 80° 2Θ, with a step size of 0.02° and step time of 20 seconds. Peak positions were compared to data published by NIST as made available online.[128] The crystalline domain size (τ) in nanometers was calculated using the FWHM (β) of the (111) reflection as applied to the Scherrer equation (Equation 3.5). The shape constant, k, was set to 0.94, the constant for spherical particles. 1.54178 Å was the incident x-ray wavelength, λ, from Cu $K_{a,}$ and θ is the Bragg angle, in this case ½ the (111) reflection 2θ angle.

$$\tau = \frac{K\lambda}{\beta \cos(\theta)} \qquad \text{(Eqn 3.5)}$$

3.4. Results: Nanocube Morphology

3.4.1. Standard Synthetic Protocol

Upon mixing the Ce^{3+} solution with OH^-, a light purple precipitate immediately forms, indicating formation of $Ce(OH)_3$. However, following the hydrothermal reaction, the precipitate is white, due to the conversion of $Ce(OH)_3$ to CeO_2. The precipitate maintains this white color through the washing and drying although off-white shades are occasionally observed, which may be due to minor defects in the CeO_2 lattice.

The primary product of the initial synthetic protocol is Eu-CeO_2 nanocubes with an edge length of 23.8 (±15) nm as measured by TEM imaging (Figure 3.3). The nanocubes cluster in small groups of nanocubes without the dense aggregates observed in the nanorods of Chapter 2. The theoretical yield of the standard synthetic protocol is 158 mg, assuming complete conversion of $Ce(NO_3)_3$ to stoichiometric CeO_2. The experimental yields are around 100 mg in a typical reaction.

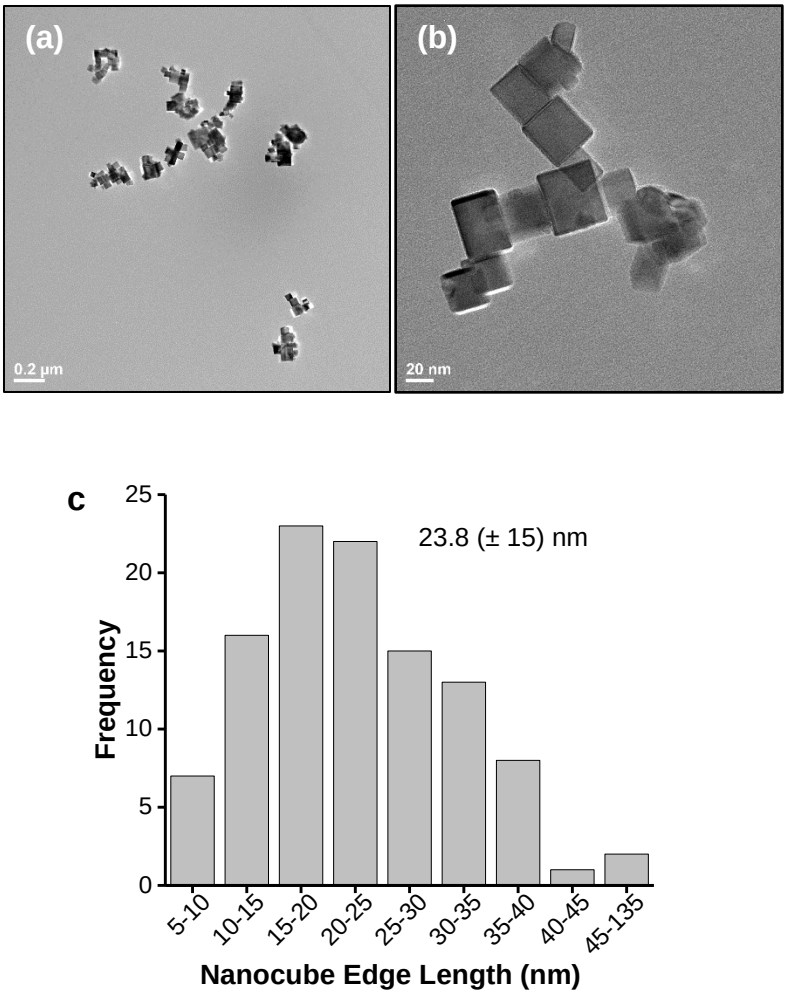

Figure 3.3 *TEM images of (a) several large clusters and (b) closer detail of one cluster, and (c) the histogram of nanocube edge length distribution.*

3.4.2. Influence of $Ce(NO_3)_3$ Concentration

The $Ce(NO_3)_3$ concentration affects the number and size of initial $Ce(OH)_3$ nuclei, with higher concentrations producing smaller and more numerous nuclei. In OR-based particle growth, increasing precursor concentrations result in more nuclei, and typically smaller final dimensions. However, in OA-based growth, increasing the number of nuclei increases the number of collisions between particles, increasing the probability of fusion and therefore producing larger particles.

To test the impact of the $Ce(NO_3)_3$, the concentration was varied from 18 mM to 112 mM. The concentration of $Eu(NO_3)_3$ was increased accordingly to maintain a consistent Eu^{3+}:Ce^{3+} precursor ratio across all samples. An insignificant increase in the nanocube edge length is observed from ~27 nm to ~40 nm (Figures 3.4, 3.5) upon increasing the $Ce(NO_3)_3$ from 18 mM to 112 mM. This contradicts the trend observed in the nanorods of Chapter 2, where increasing concentrations decreased the nanorod length, further implying growth is not primarily OR-based here.

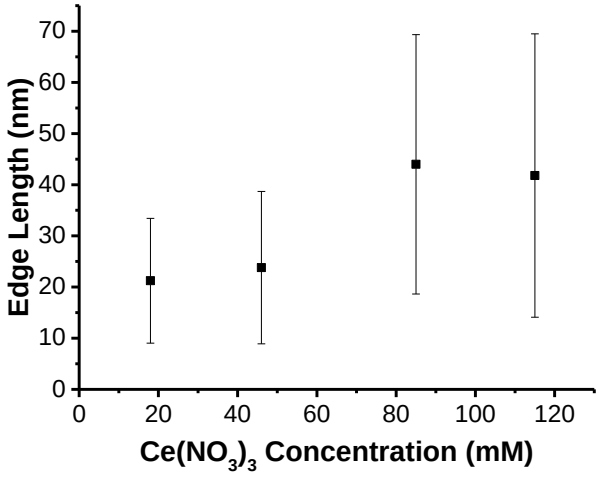

Figure 3.4 *Comparison of measured Eu-CeO_2 nanocube edge lengths with varying $Ce(NO_3)_3$ concentrations.*

The slight increase in edge length is matched with the standard deviation doubling from ~± 10 nm to ~± 22 nm. This larger deviation is primarily driven by the increase of cubes with edge lengths over 60 nm, as well as very large cubes with edge lengths of 100-200 nm. The increased frequency of these cubes at higher Ce^{3+} concentrations is likely due to the increased number of Eu-CeO_2 nuclei, which increase the collision frequency. High collision rates increase the likelihood of fusion between large cubes, explaining the nanocubes with edge lengths over 100 nm.

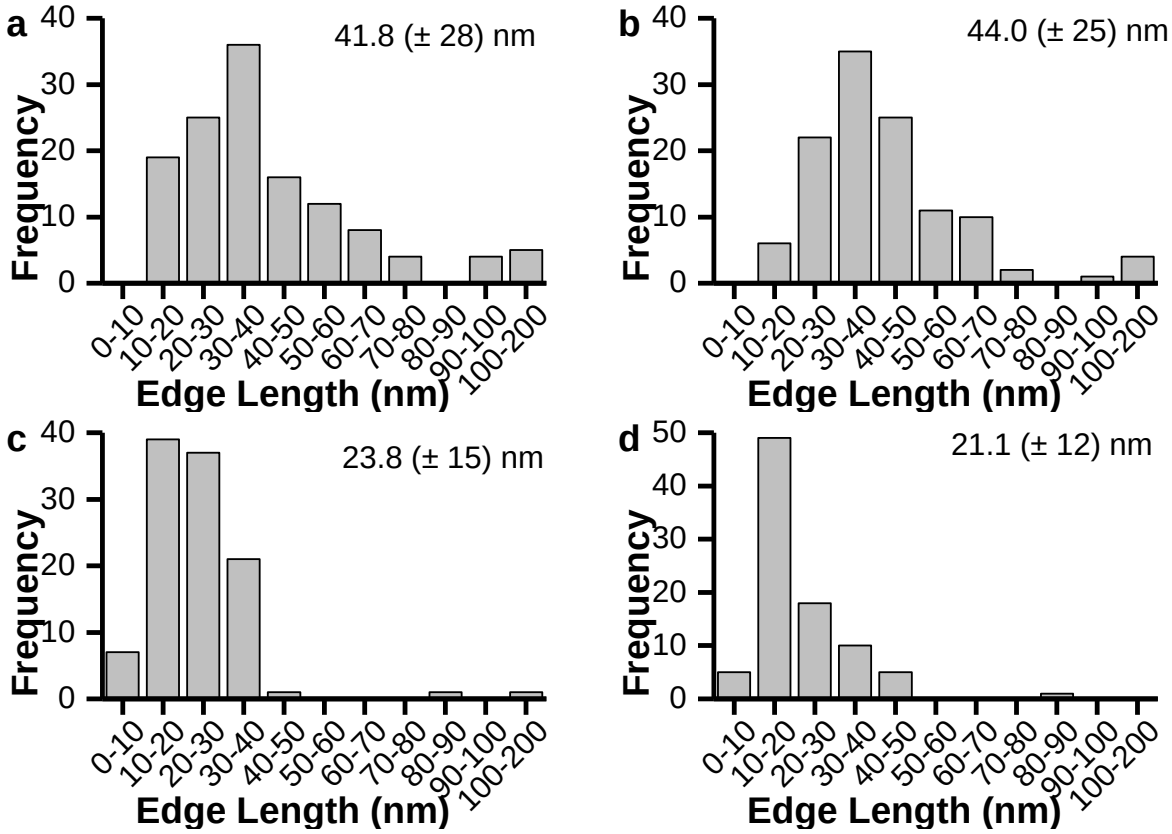

Figure 3.5 *Histograms of Eu-CeO_2 nanocube edge length with $Ce(NO_3)_3$ concentration of (a) 112 mM; (b) 84 mM; (c) 44 mM; and (d) 18 mM.*

Alternatively, assuming the rate of $Ce(OH)_3$ dissolution is constant and independent of precursor concentration, samples with higher Ce^{3+} concentrations will take longer to complete the dissolution-oxidation process. As illustrated in Figure 3.6, the CeO_2 nuclei produced at later time points may either attach to other nuclei produced at the same time, or onto larger, pre-established cubes. With lower concentrations of Ce^{3+}, this option is not available, due to the shorter dissolution-oxidation duration.

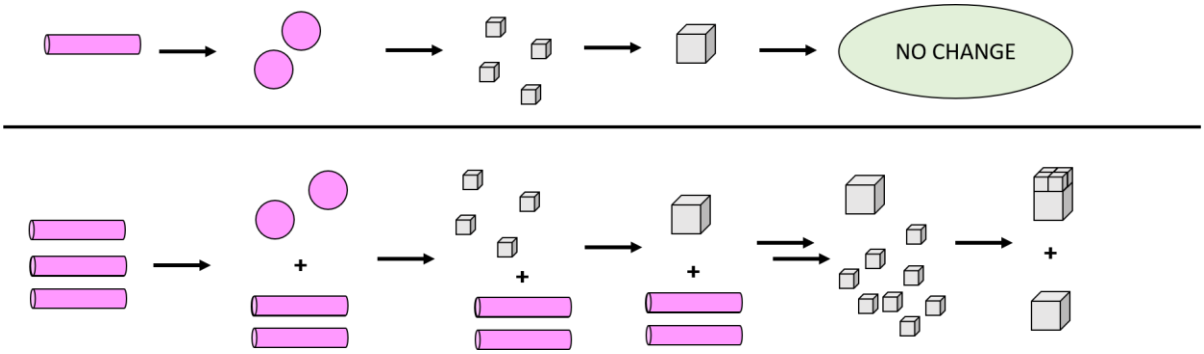

Figure 3.6 *Diagram of possible nanocube growth under (a) low and (b) high Ce^{3+} concentrations. Purple rods and spheres indicate $Ce(OH)_3$ species, while grey cubes indicate CeO_2 nuclei and cubes.*

3.4.3. Influence of $Eu(NO_3)_3$ Concentration

To probe the influence of $Eu(NO_3)_3$ on the morphology and elemental composition of the nanocubes, samples were synthesized using 112 mM $Ce(NO_3)_3$, varying the $Eu(NO_3)_3$ concentration from 0 mM to 7.6 mM. This range represents a %Eu:Ce ranging from 0% to 6.3%, as defined in Equation 3.6. No significant change in nanocube size was observed with the addition of $Eu(NO_3)_3$, indicating that the europium ion does not disrupt the nanocube growth mechanism under these conditions (Figure 3.7).

$$\%Eu{:}\,Ce = \frac{at\%\ Eu}{at\%\ Eu + at\%\ Ce} \qquad \text{(Eqn 3.6)}$$

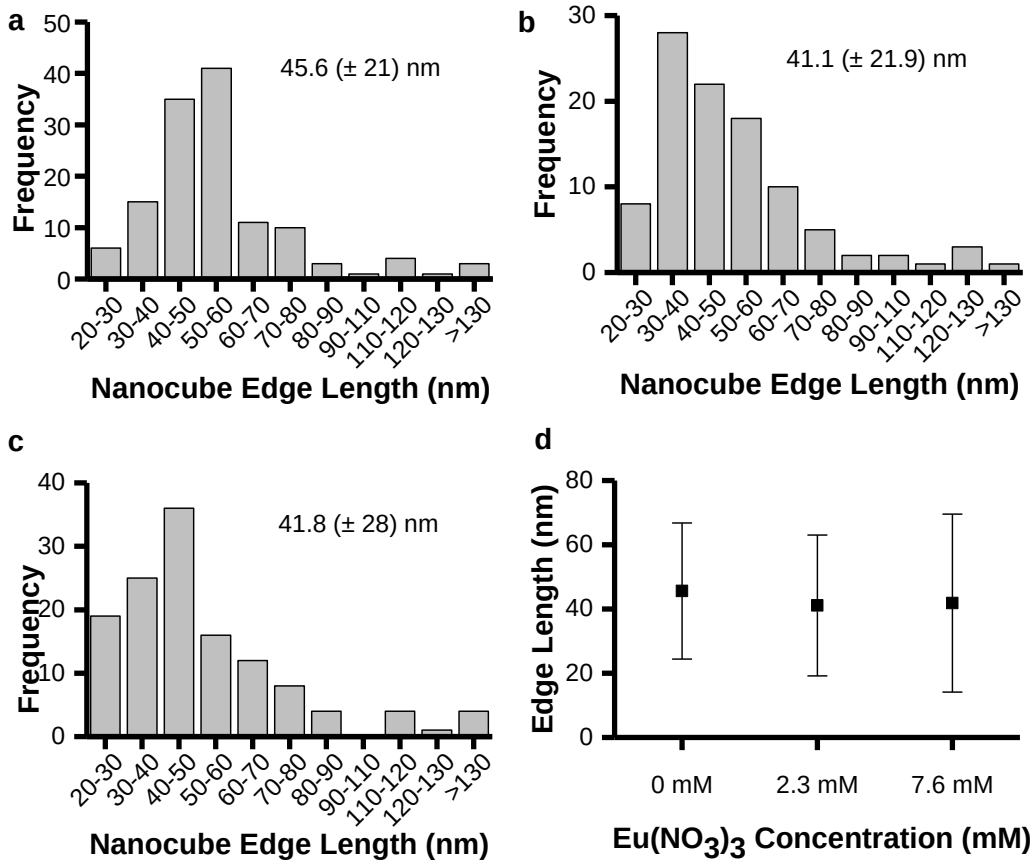

Figure 3.7 *Histograms of nanocube edge length with (a) 0 mM, (b) 2.3 mM and (c) 7.6 mM $Eu(NO_3)_3$ (d) a comparison between the three samples.*

3.4.4. Influence of NaOH Concentration

To probe the effect of hydroxide concentration on nanocube synthesis, the reaction concentration of NaOH was reduced from the original 10 M concentration to 7.5 M to 5 M. Across the range of $[OH^-]$ tested, no significant effect was observed on cube size (Figure 3.8). Most likely, the extreme excess of OH^- means even reducing the concentration in half does not influence the kinetics of nanocube growth.

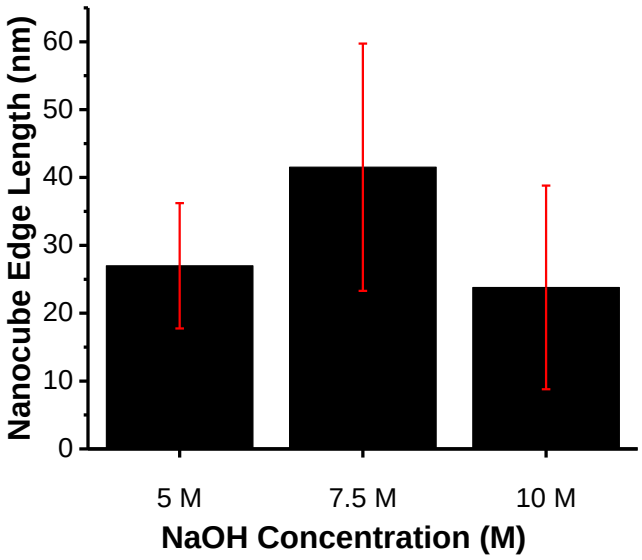

Figure 3.8 *Bar graph of nanocube edge length under different final NaOH concentrations.*

3.4.5. Influence of Ce^{3+} Precursor Counterion

Just as the Eu-CeO_2 nanorods in Chapter 2 require a cerium precursor with a Ce^{3+} oxidation state to produce a nanorod morphology, the Eu-CeO_2 nanocubes are sensitive to the cerium salt counter-ion. To test this hypothesis, the baseline synthetic protocol was followed, using $Ce(NO_3)_3$, $CeCl_3$, and $Ce(C_2H_3O_2)_3$ at 46 mM Ce^{3+}. Using $Ce(NO_3)_3$ produced Eu-CeO_2 nanocubes (Figure 3.9c), while $Ce(C_2H_3O_2)_3$ produced a mix of both Eu-CeO_2 nanorods and nanocubes (Figure 3.9b). However, upon the use of $CeCl_3$, high aspect ratio nanorods, or nanoneedles, with dimensions of 25.6 (± 7) nm by 413.5 (± 230) nm were the sole product (Figures 3.9a, 3.10c, d).[142] Furthermore, cerium acetate and nitrate precursors produced nanocubes with similar edge lengths (Figure 3.10a, b) of 31.3 (± 15) nm and 26.5 (± 9) nm respectively.

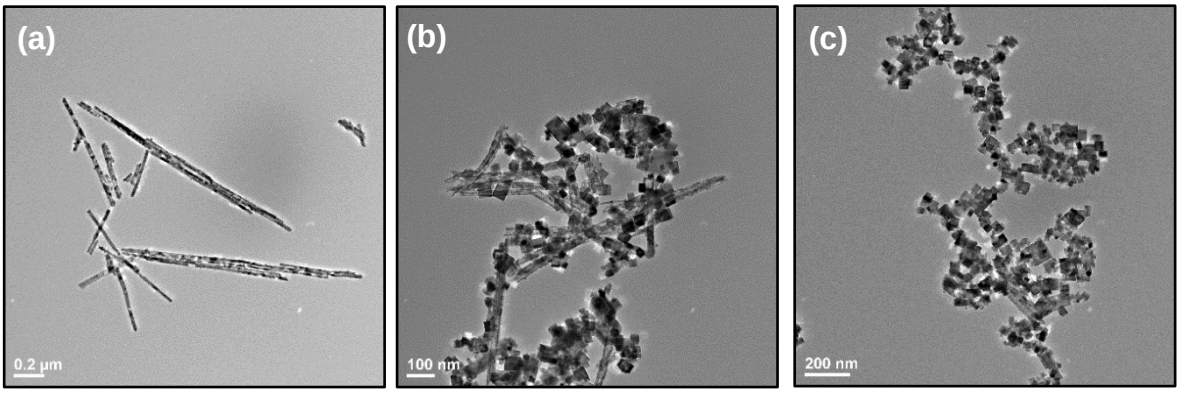

Figure 3.9 *TEM images of Eu-CeO_2 product using 46 mM (a) $CeCl_3$, $Ce(C_2H_3O_2)_3$, and (c) $Ce(NO_3)_3$.*

This dependence on the counter ion matches literature precedent with CeO_2 nanocubes.[51] The NO_3^- acts as an oxidizing agent with the increased temperature and $[OH^-]$, and a surface director by strongly adsorbing to the (200) plane as discussed in the introduction.[41,51] The Cl^- lacks the oxidizing power of the nitrate and is a weaker adsorber to the surface of CeO_2. As a result, the material remains in the form of $Ce(OH)_3$ and grows through OR.

The mechanism behind the mixed morphology observed in the presence of $CH_3CO_2^-$ has been less studied or understood. CeO_2 nanoparticles synthesized in an acetate buffer have shown acetate ions bound to surface Ce^{3+} sites even after washing.[143] The bound acetate ions may provide more surface directing capabilities than Cl^-, encouraging growth of nanocubes following oxidation by dissolved O_2. Since the acetate ions are not oxidizing agents, the acetate ions would not be as effective as nitrates at making cubes but could direct the particle growth more than Cl^-. Therefore, a mixed product of cubes and rods could form following oxidation by any dissolved O_2. However, more studies are required to determine the exact mechanism producing the mixed morphology.

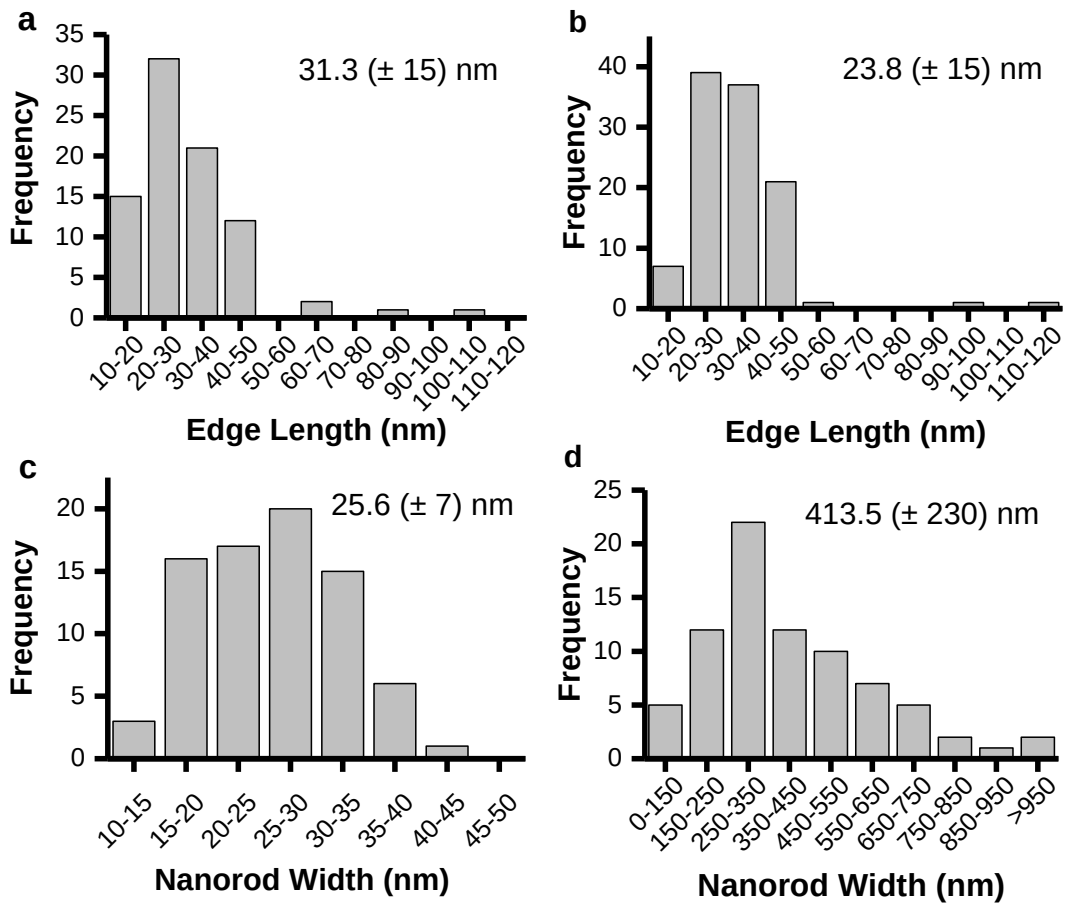

Figure 3.10 *Histograms of the nanomaterial dimensions, comparing (a) nanocubes from $Ce(NO_3)$, (b) nanocubes from $Ce(C_2H_3O_2)_3$, and (c, d) nanorods from $CeCl_3$.*

3.4.6. Influence of Reaction Temperature

The hydrothermal reaction temperature was varied to test the influence on the CeO_2 produced, with samples synthesized at temperatures ranging from 100 °C to 200 °C. As the hydrothermal temperature increases, oxidation of $Ce(OH)_3$ to CeO_2 species is more energetically attainable.[42] $Ce(OH)_3$ is also less soluble at lower temperatures, slowing the rate of dissolution/recrystallization. This leads to a transition from OR-based growth to OA-based growth with increasing temperatures, with the product morphology transitioning from rods to cubes.

This was observed, as at 100 °C only nanorods were observed (Figure 3.11a). At 120 °C some small particles were observed with the rods (Figure 3.11b), but 140 °C was the transition temperature at which a mixture of rods and cubes were observed (Figure 3.11c). Samples synthesized at 180 °C and above consisted only of nanocubes (Figure 3.11d, e). No significant difference was seen in edge length of cubes synthesized, independent of the reaction temperature (Figure 3.12).

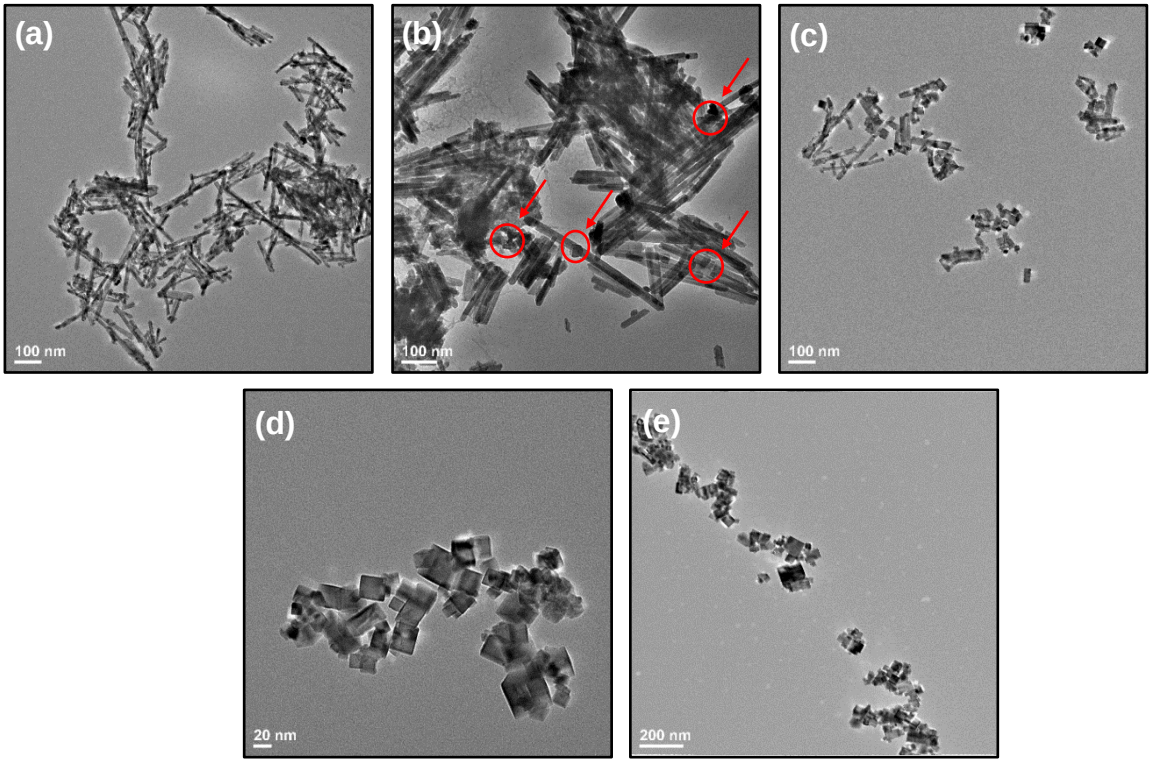

Figure 3.11 *TEM images of Eu-CeO_2 product morphologies at (a) 100 °C, (b) 120 °C, (c) 140 °C, (d) 180 °C, and (e) 200 °C. The red circles and arrows in (b) indicate small particles growing.*

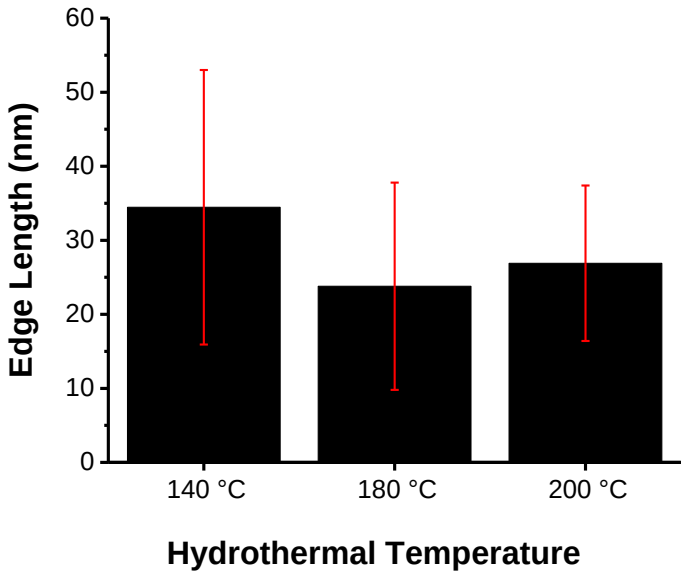

Figure 3.12 *Eu-CeO_2 nanocube edge lengths at reaction temperatures from 140 °C to 200 °C.*

3.4.7. Influence of Reaction Time

To test the effect of the hydrothermal reaction duration, a series of reactions were stopped at specific time points, rapidly cooled to room temperature, and subsequently washed and dried. All samples were slightly off-white in color immediately after their removal from the reactor. However, the 1.5-hour sample turned grey then dark yellow during washing, and finally to a light yellow after drying. This tracks the color change seen in the rod synthesis described in Chapter 2, with product present as $Ce(OH)_3$ after the hydrothermal reaction, and only converting to CeO_2 after drying. Samples grown for 4 hours maintain their white color through the washing process, suggesting complete oxidation to CeO_2 by that time.

TEM analysis of the product morphologies supports this hypothesis. After 1.5 hours the product consists of nanorods, while after 24 and 48 hours the product consists only of nanocubes (Figure 3.13). The four-hour sample contains both rods and cubes, with only a portion of the rods have presumably been consumed and transformed to cubes.

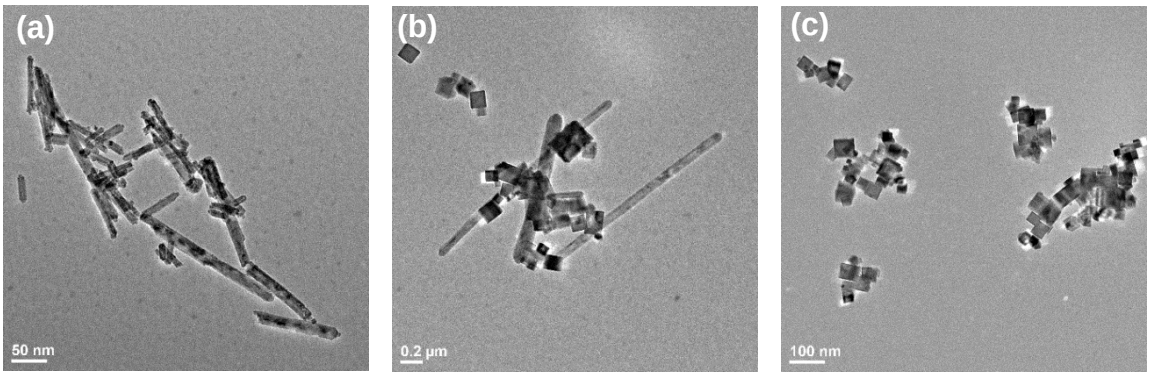

Figure 3.13 *Eu-CeO_2 product as synthesized at 180 °C for (a) 1.5 hr, (b) 4 hr, and (c) 48 hr using 46 mM $Ce(NO_3)_3$.*

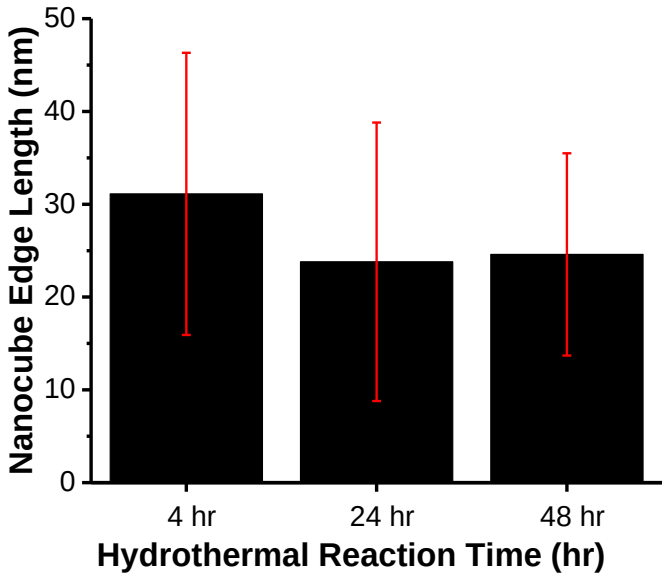

Figure 3.14 *Eu-CeO_2 nanocube edge lengths as synthesized with 4, 24, and 48 hours hydrothermal reaction time.*

3.5. Crystalline Properties of Eu-CeO_2 Nanocubes

3.5.1. Analysis of Crystalline Domains by HRTEM

Following synthesis, the nanocubes were also analyzed for crystallinity using HRTEM. All cubes appear monocrystalline, with crystal lattice spacings spanning the entire length of the cube. Most of the nanocubes exhibited lattice spacings matching the d-spacing of CeO_2 (200). However, a portion of the cubes had lattice spacings matching d-spacing of (111). This indicates that most but not all most cubes have exposed (200) planes. Lattice spacings from one cube often extended into an adjacent cube, as seen in Figure 3.15a. This extended crystallinity is often observed with oriented attachment, as particles fuse along a common crystallographic plane with a slight offset between particle edges.[48]

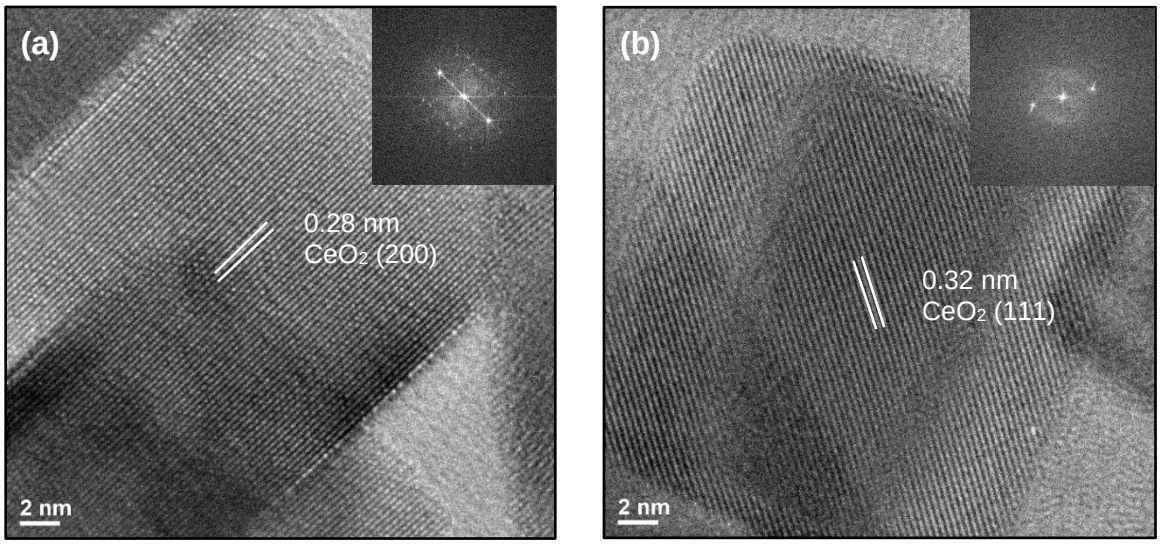

Figure 3.15 *HRTEM images showing lattice spacings of Eu-CeO_2 nanocubes with lattice spacings matching (a) CeO_2 (200) and (b) CeO_2 (111). Inset are FFTs for each image.*

3.5.2. Crystalline Properties of Eu-CeO2 Nanocubes by XRD Analysis

Nanocubes with a theoretical Eu:Ce at 6.3% Eu were analyzed by powder XRD (Figure 3.16). All peaks are consistent with CeO_2 crystallized in a cubic fluorite crystal structure (Table 3.1). The absence of any peak near 2Θ of 19° indicates that the europium stays incorporated in the CeO_2 lattice, with no detectable formation of a Eu_2O_3 phase.[133]

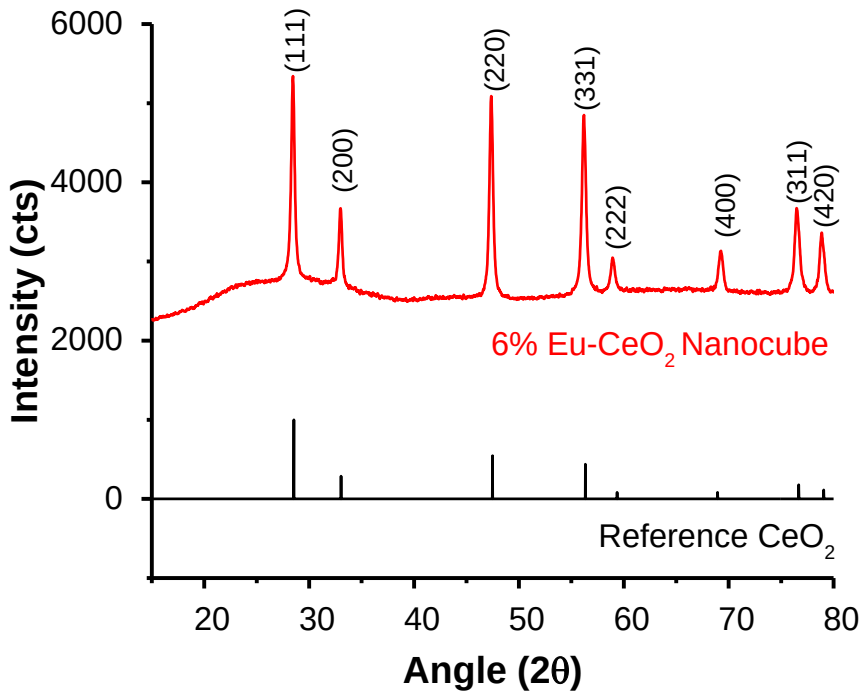

Figure 3.16 *XRD spectra of 6% Eu-CeO_2 nanocubes and reference cubic fluorite CeO_2 peaks as published by NIST in red and black respectively.*[128]

Table 3.1 *Peak assignments in powder XRD for 6% Eu-CeO_2 nanocubes, as compared to annealed and unannealed 7% Eu-CeO_2 nanorods from Chapter 2, and the reference CeO_2 peaks from NIST.*[128] *The nanocube peaks are highlighted for emphasis.*

Sample	CeO_2 Peak Assignments (2Θ)							
	(111)	**(200)**	**(220)**	**(331)**	**(222)**	**(400)**	**(311)**	**(420)**
Reference CeO_2	28.54	33.04	47.48	56.34	59.36	68.94	76.68	79.07
6.3% Eu-CeO_2 Nanocubes	28.46	32.98	47.42	56.20	58.92	69.26	76.98	78.86
7.7% Eu-CeO_2 Nanorods	28.46	32.82	47.26	56.10	58.80	68.94	76.56	--
7.7% Eu-CeO_2 Annealed Nanorods	28.54	33.08	47.42	56.28	59.04	69.30	76.62	79.06

The monocrystallinity observed in TEM is consistent with the intense, narrow peaks observed in the XRD spectrum of the Eu-CeO_2 sample. The crystalline domain size of these nanocubes was calculated using the (111) plane reflection using the Scherrer equation and compared to the annealed and unannealed nanorods (Chapter 2) in Table 3.2. The nanocubes had the largest crystalline domain size, compared to the nanorod, annealed nanorod, and nanowire samples, likely due to the attachment of cubes through a common crystallographic plane.

The assumptions concerning calculation of the domain size, as discussed in analysis of nanorod crystallinity in Chapter 2, Section 2.6.2, are still applicable concerning the nanocubes. The measured FWHM may increase due to broadening from the instrument while the *K* factor used in the Scherrer equation is intended for spheres, not cubes. Therefore, the calculated crystalline domain sized values significantly underestimate the crystalline domain size and can only be used to estimate the magnitude of crystal domain sizes.

Since the nanocubes are monocrystalline, the Eu-CeO_2 cubes likely have fewer Ce^{3+} defects and oxygen vacancies. The larger crystalline domains alleviate disruptions caused by defects within the nanocube due to delocalization of the strain. As a result, most of the nanocube reflections are slightly closer to the reference CeO_2 peaks, with the exception of the (400) and (311) reflections. For instance, the (220) peak was located at 47.48° and 47.42° in the reference CeO_2 and nanocubes, respectively, but shifted to 47.26° in the nanorod sample. The higher angle (400) peak was at 68.94° for the reference CeO_2 as well as the nanorods but shifted to 69.26° for the nanocube sample. However, significant broadening in the nanorod sample likely contributes some uncertainty to the peak position of that sample. Out of the three materials, annealed Eu-CeO_2 nanorods match the reference CeO_2 closest, as annealing removes more defects and alleviates more strain than the cubes.

Table 3.2 *Full width half max (FWHM) and calculated crystalline domain of Eu-CeO_2 nanocubes (highlighted), compared to 7.7% Eu-CeO_2 unannealed and annealed rods.*

Sample	FWHM (2Θ)	XRD Crystalline Domain (nm)
6.3% Eu-CeO_2 Nanocubes	0.38	22.53
7.7% Eu-CeO_2 Nanorods	1.44	6.05
7.7% Eu-CeO_2 Annealed Nanorods	0.58	15.65

3.6. Elemental Analysis by TEM EDS

The nanocubes were analyzed for the presence of contaminants from the reaction solution, primarily sodium. Based on the EDS spectra (Figure 3.17), the nanocubes were comprised only of cerium, europium, and oxygen. Similar to the nanorod samples, the measured ratio of Eu:Ce matched the precursor molar ratio, increasing as expected with

increasing Eu^{3+} ratio. Unlike the nanorod system, the oxygen concentration did not show any notable trend (Table 3.3).

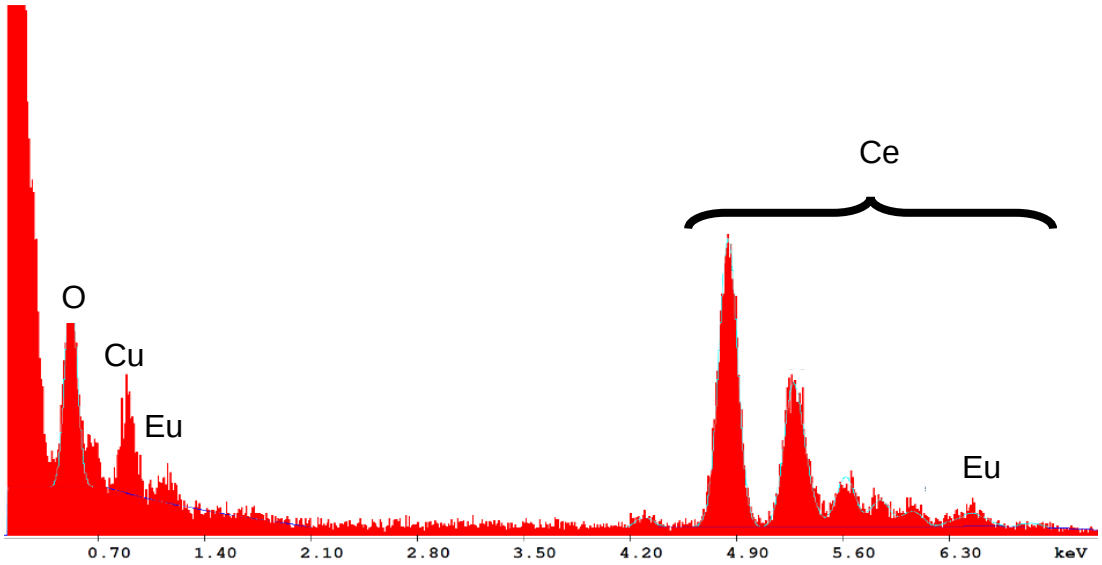

Figure 3.17 *Typical EDS spectrum for 6% Eu-CeO_2 nanocubes. The series of peaks between 4.2 keV and 7 keV are attributed to CeL, except for Eu as marked at 5.8 keV.*

Table 3.3 *EDS data of at% O, Ce, and Eu for Eu-CeO_2 nanorods synthesized with a range of $Eu(NO_3)_3$ concentrations.*

mM $Eu(NO_3)_3$	Theoretical at% Eu:Ce	At% O	At% Ce	At% Eu	At%Eu:Ce
0	0	64.9 ± 6.4	34.9 ± 6.7	0.2 ± 0.2	0.6 ± 0.8
2.3	2.0	54.8 ± 2.9	44.4 ± 2.9	0.8 ± 0.3	1.7 ± 0.6
7.6	6.3	55.5 ± 2.7	40.8 ± 2.5	3.4 ± .85	8.0± 1.68

3.7. Conclusions

This chapter discussed the synthesis of Eu-CeO_2 nanocubes by a conventional hydrothermal protocol. While Bezkrovyni *et al.*[131] did explore the synthesis of Eu-CeO_2 nanocubes, this procedure was assisted by microwave radiation. Furthermore, studies were limited to variations in the Eu^{3+} concentration to determine the dopant's influence

on the reducibility and crystal structure of the nanocube.[131] Therefore, a more thorough analysis of the parameters controlling the Eu-CeO_2 structural features was necessary.

Several synthetic parameters were varied to probe their influence over the size and morphology of the Eu-CeO_2 nanocubes. Unfortunately, none of the parameters investigated demonstrated significant edge length control, with all samples measuring between 24 nm and 50 nm on average. However, the choice of Ce^{3+} precursor counter-ion provides morphological control with $CeCl_3$ producing large, high aspect ratio nanorods and $Ce(NO_3)_3$ producing nanocubes. In addition, europium concentration of the nanocubes was easily adjusted from 0 to 6 at% Eu:Ce through the $EuCl_3$ concentration with no influence of nanocube morphology or size.

The influence of reaction temperature, time, and cerium precursor counter ion all support the general mechanism proposed in the literature for the undoped system. Eu-$Ce(OH)_3$ nuclei first precipitate during the reaction of Ce^{3+} precursors with NaOH. During the hydrothermal reaction, the nuclei initially grow by rapid Ostwald Ripening, growing in a nanorod morphology due to the hexagonal crystal structure of Eu-$Ce(OH)_3$. However, the dissolution step of the Ostwald Ripening can be disrupted by oxidation of the small nuclei, under specific reaction conditions. At temperatures above 140 °C, nitrate ions oxidize the dissolved Eu-$Ce(OH)_3$ to CeO_2 nuclei (Figure 3.1). These small nuclei then grow by an OA-based mechanism.[5,51] This gradually converts the Eu-$Ce(OH)_3$ nanorods to Eu-CeO_2 nanocubes.

The nanocubes were monocrystalline as observed by HRTEM, with lattice spacings indicating exposed (200) CeO_2 planes, as well as some (111) CeO_2 planes. The XRD spectrum confirmed the cubic fluorite structure of the nanocubes, with minor lattice strain

at higher reflections. The cubes have common characteristics with both the unannealed and annealed Eu-CeO_2 nanorods. The cubes and annealed rods have similar monocrystallinity, but as judged by their non-white color and XRD peak shifts, the cubes and annealed rods have more crystalline defects than the annealed nanorods. Furthermore, both the nanocubes and unannealed rods expose (111) and (200) planes, while the annealed nanorods expose (111) planes.

So far, a series of three Eu-CeO_2 morphologies have been synthesized with varying lattice strain, defect concentrations, and exposed planes. This variety of structural properties leads to comparison of the chemical reactivity of the various Eu-CeO_2 materials, as discussed in Chapter 7. In addition, the successful integration of Eu^{3+} into a nanocube with no impact on morphology or size of the nanocube, produces a material with Eu^{3+} fluorescence, variable oxygen vacancy concentrations, and leads to the incorporation of other rare earth ions as discussed in Chapter 6.

Chapter 4: Synthesis of Eu-CeO_2 Nanowires by Electrospinning

4.1. Overview

Chapters 2 and 3 discussed the synthesis of Europium-doped Cerium Oxide (Eu-CeO_2) nanorods and nanocubes. This chapter focuses the use of electrospinning as a templating procedure to synthesize Eu-CeO_2 and Yttrium-doped CeO_2 (Y-CeO_2) nanowires.

CeO_2 nanowires are often investigated for use in sensors,[144] fuel cells,[75] and other catalytic applications.[145] CeO_2 nanowires have been electrospun using polymers such as polyvinylpyrrolidone (PVP), polyvinyl alcohol (PVA), and polyvinyl butyral (PVB) to establish a polymer template. Metal salts are dissolved into the polymer solution, which is subsequently electrospun. Annealing the resulting fibers removes the polymer template, leaving CeO_2 in the nanowire morphology.[146-148] The electrospun CeO_2 nanowires have been doped by several ions, such as Ni^{2+}, Gd^{3+}, and Y^{3+} by adding the appropriate metal precursor to the electrospinning solution.[148-150]

The previously published study on Y^{3+} doped CeO_2 (Y-CeO_2) electrospun nanowires was limited in its scope to synthetic protocol, influence of Y^{3+} on the nanowire diameter and XRD properties.[148] Similarly, only one paper has reported Eu-CeO_2 nanowires, also synthesized by electrospinning using a PVP polymer template.[146] The study covered only the effect of varying the $Eu(NO_3)_3$ concentration on the optical properties of the nanowires. No mention is made of the effect of annealing on nanowire diameter, and the reported Eu-CeO_2 nanowires appear more nanoribbon-like than nanowire in terms of morphology.

More research is needed concerning the synthesis of the Eu-CeO_2 nanowire morphology with thorough characterization of the crystallinity, elemental composition, and diameter control of the nanowires. Determining which parameters are useful for diameter control is also essential for any application of the Eu-CeO_2 nanowires. For example, reducing the diameter of the nanowires may improve their catalytic activity due to an increase in surface area.

In this chapter, Y-CeO_2 and Eu-CeO_2 nanowires are synthesized by the: (i) adsorption of the Ce^{3+}, Eu^{3+}, and Y^{3+} ions to the PVP template assisted by a sol-gel reaction; (ii) electrospinning the metal-polymer solution to produce a metal-polymer nanowire composite film; and (iii) annealing to remove the polymer template. A general procedure for doped CeO_2 nanowire fabrication was developed, using Y^{3+} as the dopant. Experimental parameters evaluated in these experiments including electrospinning voltage, pump speed, electrode distance, and solvent concentrations were analyzed for influence on nanowire morphology and elemental composition. Eu-CeO_2 nanowires were subsequently synthesized through slight adjustments to the Y-CeO_2 synthetic procedure. A select number of parameters were then varied to control the Eu-CeO_2 nanowire diameter and europium concentration.

The Eu-CeO_2 nanowires were then analyzed with HRTEM and powder XRD to confirm CeO_2 cubic fluorite crystal structure and to determine the crystallite domain size relative to the previously synthesized Eu-CeO_2 nanomaterials. EDS was used to detect any impurities and to determine the concentration of Eu^{3+} within the nanowires.

4.2. Introduction

Electrospinning at its most basic level utilizes a strong electric field to draw fibers from a polymer solution to a collector, producing a polymer nanofiber mat. The procedure has been used to produce fibers since 1934, with a renewed interest increasing significantly in the early 2000s.[151] Manipulation of the operational parameters and the electrospinning solution properties can drastically change the nanofiber size and morphology. More complex electrospinning protocols can produce core-sheath fibers, porous fibers, or fibers decorated with nanoparticles.[152-154] This versatility has led to medicinal,[155-157] optical,[158] energy-based,[151,159] and catalytic applications.[160,161]

4.2.1. Electrospinning Polymer Nanowires

In a typical electrospinning procedure, a polymer solution or melt is injected from a needle into a high electric field. The electric field induces repulsive electrical charges on the surface of the Taylor cone, eventually overwhelming the surface tension of the polymer solution.[162-164] The tip of the cone forms a jet, which is pulled to a collector. The instability of the electrical charge causes the jet to whip as it moves from the syringe nozzle to the collector, which stretches and thins the jet. The solvent evaporates as the jet flies to the collector, depositing solid polymer fibers. (Figure 4.1).

The stability of the electrospinning process is very sensitive to several parameters including operational conditions (i.e. electrospinning voltage, pump speed) and intrinsic solution properties (i.e. viscosity, conductivity). By tuning these conditions, polymer nanowires can be produced with diameters ranging from nanometers to microns.[160] However, if a parameter is changed too much, the electrospinning system cannot produce

homogenous nanowires and either introduces beads into the fibers, creates short and broken nanowires, or electrosprays a film instead of wires.[165]

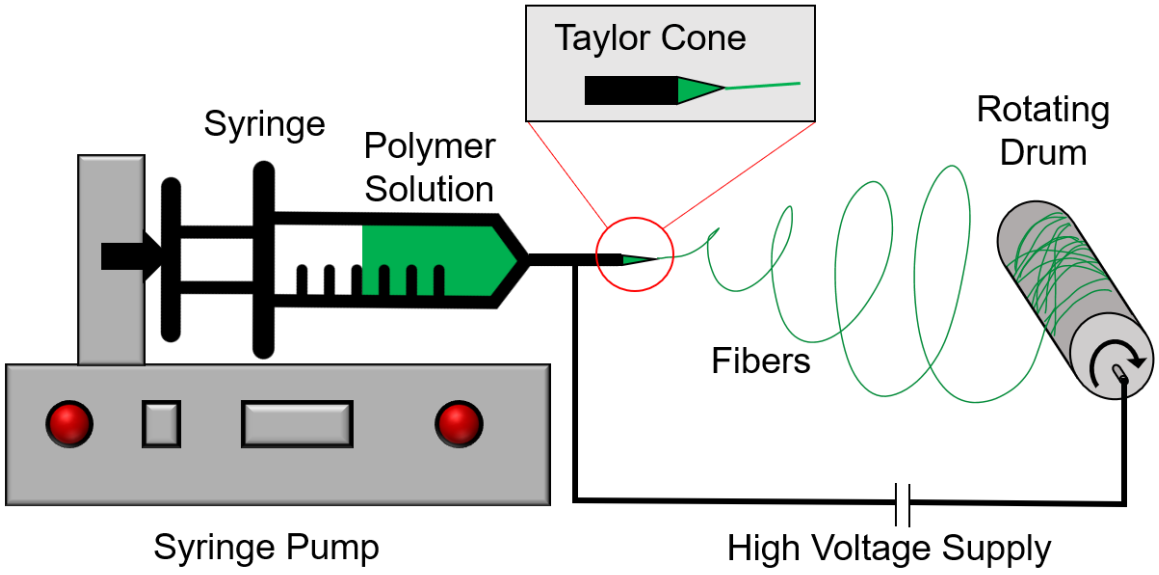

Figure 4.1 *Diagram of electrospinning system, with an illustration of a Taylor cone as the inset.*

For example, the solution viscosity is partially controlled by the choice of polymer, its molecular weight and its concentration.[163] Within certain limits, the viscosity contributed by the polymer counters the effects of surface tension, allowing nanowires to form. Increasing the solution viscosity within this range produces nanowires with larger diameters.[5] If the polymer concentration is too high, the solution will be too viscous to electrospin. Conversely, electrospinning solutions with polymer concentrations below the minimum concentration produces beads strung on thin fibers.[166] As the polymer concentration and associated solution viscosity continues to decrease, the viscosity cannot overcome the surface tension and the solution electrosprays droplets instead of fibers. [165]

Extensive research and numerous reviews have covered the controlled synthesis of polymer nanofibers.[160,167,168] A large number of natural and synthetic polymers, such as polyvinylpyrollidone (PVP), polyethylene oxide, and collagen have been used in electrospinning.[163,169-171] The polymer is typically chosen for its solubility and viscosity properties as well as for properties useful in the desired application, such as biodegradability for use in drug delivery systems.

The solvent is also selected to manipulate the viscosity, surface tension, conductivity, and solubility of the polymer. Common electrospinning solvents include methanol, ethanol, water, chloroform, and dimethylformamide.[160] Some electrospinning systems also utilize a di-solvent system, which may either improve solubility of additives to the electrospinning solution such as metal precursors, or induce phase separation leading to porous nanofibers.[155]

4.2.2. Electrospinning as Templates for Nanowire Formation

While polymer fibers have numerous applications,[172,173] they can also be used a template during the electrospinning event for eventual formation of nanowires such as metal oxides and nitrides.[174] Typically, metal alkoxides react with each other in a sol-gel reaction, before being combined with the templating polymer.[168,175] This sol-gel polymer hybrid is then electrospun to yield polymer nanowires with the sols well-distributed. The polymer template is removed by annealing which also fuses the sols, which retain the nanowire morphology.

In this work, $Ce(NO_3)_3$ is used as the source of cerium for electrospinning. When dissolved in aqueous solutions, Ce^{3+} ions are solvated as $Ce(H_2O)_x^{3+}$, with x=9 most common.[176] The water can be deprotonated to form a hydroxyl, which undergo

condensation with another Ce-OH species to form Ce-O-Ce bonds and water (Eqns 4.1, 4.2).[177,178] Dopant salts can be added to the solution and are concomitantly hydrolyzed and condensed with the cerium to ideally produce a sol of evenly distributed metal-oxo species. However, in non-aqueous, aprotic solvent systems, hydrolysis in the absence of an alkoxide progresses very slowly.[178] Therefore, at least some of the lanthanide ions are likely present as hydrated M^{3+} ions.

$$Ce(H_2O)_9{}^{3+} \rightarrow Ce(H_2O)_{9-x}(OH)_x{}^{(3-x)+} + xH^+ \quad \text{(Eqn 4.1)}[177]$$

$$2\,Ce(H_2O)_8(OH)^{2+} \rightarrow Ce(H_2O)_8{}^{2+} - O - Ce(H_2O)_8{}^{2+} + H_2O \quad \text{(Eqn 4.2)}[178]$$

PVP has been used as a capping agent during the synthesis of cerium oxide in several synthetic techniques, including precipitation and hydrothermal techniques.[179,180] Cerium, either as hydrated Ce^{3+} and Ce^{4+} ions, or as CeO_2 sols, adsorb to the PVP through the carbonyl oxygen due to electrostatic attraction. Upon drying during electrospinning, the cerium ions are captured within the polymer (Figure 4.2).[179] A slow annealing process oxidizes the adsorbed Ce^{3+} and Eu^{3+} to Eu-CeO_2, while gradually decomposing the polymer template, enabling fusion between particles while retaining the nanowire morphology.[174]

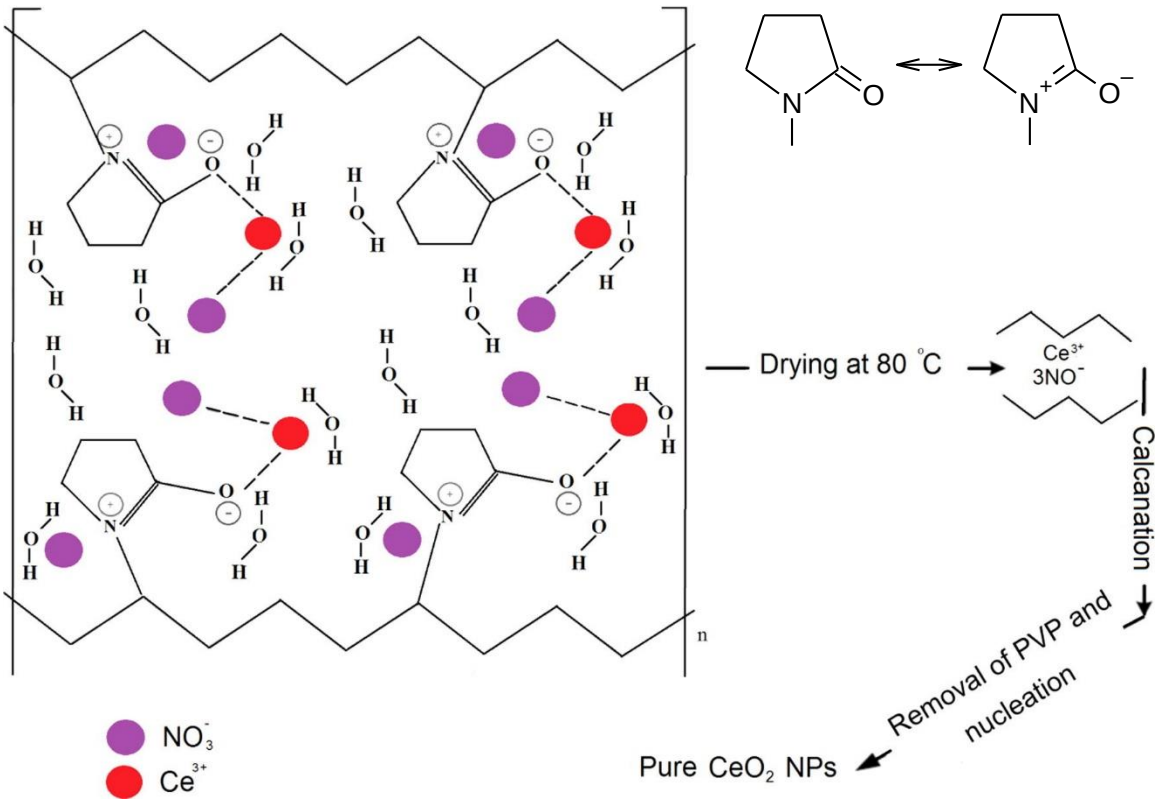

Figure 4.2 *Possible interaction of $Ce(NO_3)_3$ with PVP, with Ce^{3+} adsorbing to PVP oxygens, being encapsulated by the polymer during drying, then oxidation to CeO_2 with removal of PVP. Adapted from Reference [179].*

4.3. Methods and Materials

4.3.1. Materials

All purchased chemicals were of analytical grade and used as received without further purification unless otherwise noted. Polyvinylpyrrolidone (PVP, M_w~1,300,000), dimethylformamide (DMF), methanol (MeOH), and yttrium nitrate hexahydrate ($Y(NO_3)_3 \bullet 6H_2O$) were purchased from Sigma Aldrich. Acetone was purchase from Pharmco. MeOH and DMF were dried and stored with molecular sieves. PVP was heated to 95 °C for 24 hours and stored in a desiccator. All other chemicals were purchased as described in Chapter 2 and used without further purification.

4.3.2. Synthesis of Y-CeO_2 and Eu-CeO_2 Metal-Polymer Composite Nanowires

The Y-CeO_2 and Eu-CeO_2 were synthesized by a sol-gel reaction, followed by electrospinning to produce metal-polymer composite nanowires (Figure 4.3). The polymer template was subsequently removed through a two-step annealing process.

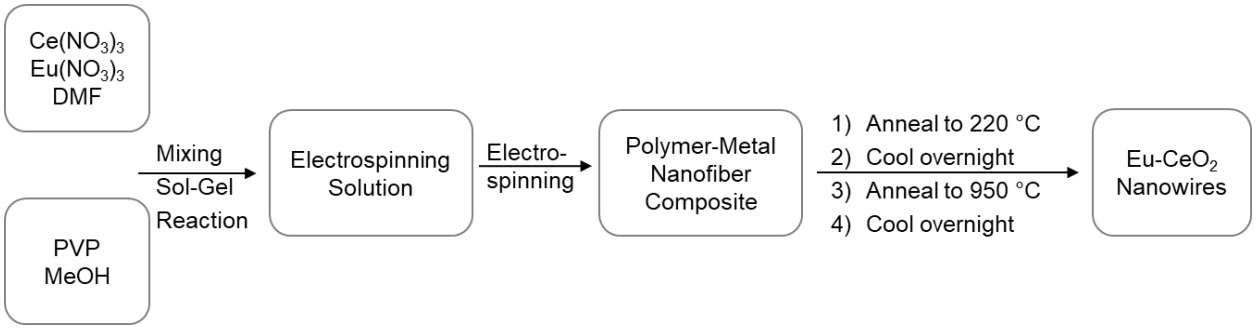

Figure 4.3 *Diagram of typical procedure for synthesis of doped CeO_2 nanowires, using Eu-CeO_2 nanowires as an example.*

To synthesize Y-CeO_2 nanowires, PVP was dissolved in MeOH while $Ce(NO_3)_3$ and $Y(NO_3)_3$ were dissolved in DMF. Eu-CeO_2 nanowires were synthesized by the same procedure, substituting $Eu(NO_3)_3$ for $Y(NO_3)_3$, and slight modifications in the precursor concentrations. Table 4.1 details the specific mass and wt % for each precursor used in the synthesis of Y-CeO_2 and Eu-CeO_2 nanowires. The concentration of Y^{3+} or Eu^{3+} within a specific sample is indicated by its atomic percentage, disregarding oxygen. This percentage is calculated by Equation 4.3, using europium as an example.

$$\%Eu = \frac{at\%\ Eu}{at\%\ Ce + at\%Eu} \qquad \text{(Eqn 4.3)}$$

Table 4.1 *Concentrations of the electrospinning precursors, listing both the mass used and the resulting wt %.*

	g PVP *(wt%)*	g MeOH *(wt%)*	g $Ce(NO_3)_3$ *(wt%)*	g $M(NO_3)_3$ *(wt%)*	g DMF *(wt%)*
Y-CeO_2	0.2 *(10.1%)*	1.0 *(50.6%)*	0.2 *(10.1%)*	0.026 g $Y(NO_3)_3$ *(1.4%)*	0.55 *(27.8%)*
Eu-CeO_2	0.25 *(8.1%)*	1.5 *(48.7%)*	0.3 *(9.8%)*	0.03 *(0.9%)*	1.0 *(32.5%)*

The DMF and MeOH solutions were combined and rapidly stirred using a vortex mixer for 20 seconds until any visible precipitates dispersed, then gently shaken for 10 minutes to release any air bubbles. The solution was transferred to a syringe, which was connected to a long cannula terminated with a 1", 16-gauge metal nozzle. The polymer was injected at a speed of 0.8 mL/hr into an electric field with a voltage of 20 kV for a minimum of 15 minutes. A rotating drum covered with aluminum foil was placed 12 cm from the syringe tip and used as the counter electrode.

4.3.3. Oxidation to Y-CeO_2 or Eu-CeO_2 nanowires

To remove the polymer template, the metal-polymer nanowire films were removed from the collecting drum and sandwiched between two quartz plates. In the first step, the films were gradually heated to 220°C over the course of 3 hours, held at that temperature for 16 hours, then gradually cooled to room temperature over 5 hours. Once cooled, the quartz plates and nanowire films were transferred to a tube furnace and heated to about 950 °C over the course of 5 hours, maintained at that temperature for 16 hours, then cooled to room temperature over 6 hours.

Unless otherwise noted, the remainder of this work will use the term *nanowires* or *annealed nanowires* to specify the oxidized, polymer-free material, while the term

nanowire composite or *unannealed* nanowires will refer to as-synthesized electrospun samples still containing the polymer template.

4.3.4. Characterization of Nanowires

The annealed nanowires were analyzed for morphology and dimensions by TEM at 200 kV. A 1 mm^2 piece of the annealed film was sonicated in acetone for 5 minutes, a drop of the suspension added to a carbon-coated copper grid and allowed to dry prior to use in the TEM.

Scanning Electron Microscopy (SEM) was used to examine the macroscopic morphology of the annealed and unannealed nanowire films, as well as detect nanowire defects such as beading or nanowire breakage. To prepare the samples, the annealed and unannealed nanowires were attached to a stainless-steel thimble using carbon tape, and sputter-coated to 7 nm thickness using a gold or gold-palladium target.

Crystallinity was measured by HRTEM and powder XRD as described in Chapter 2, with the annealed nanowires ground lightly prior to the XRD measurement. Powder XRD reflections were measured from 15° to 80° 2Θ, with a step size of 0.02° and step time of 20 seconds. The peak positions were compared to data published by NIST as made available online.[128] The crystalline domain size (τ) in nanometers was calculated by the Scherrer equation (Eqn 4.4) using the FWHM (β) of the (111) reflection as discussed in Chapters 2 and 3.

$$\tau = \frac{K\lambda}{\beta \cos(\theta)} \qquad \text{(Eqn 4.4)}$$

The elemental composition and mapping was acquired on a Gatan X Energy Dispersive Spectroscopy Unit (EDS) attached to the JEOL 2100. Samples were analyzed

for atomic percentage of O, Ce, Y and Eu, as applicable, using the K-shell of oxygen and L-shell of cerium, yttrium, and europium.

4.4. Results: Y-CeO_2 Nanowires

The initial optimization and diameter control studies focused on Y^{3+}-doped CeO_2, with possible applications with regard to thermal conductivity. As the lab focus shifted to biological applications, Eu^{3+} was used as a dopant for its fluorescent capabilities. Based on the results from the Y-CeO_2 system, select experimental parameters were manipulated to obtain control over %Eu and nanowire diameter. The Y-CeO_2 system will be discussed to explain the selection of parameters applied to the Eu-CeO_2 system.

First, a set of parameters were established that produced a homogenous nanowire sample with no production of beads or films, referred to as the *standard synthetic protocol* or *baseline condition*. Solution concentrations and electrospinning apparatus conditions were then varied to test their effect on the electrospinning process and Eu-CeO_2 morphology and dimensions.

4.4.1. Y-CeO_2 Nanowires: Non-influential Parameters

1.1.1.1. Flow Rate

At high flow rates, the solvent is unable to evaporate before the jet reaches the collector, resulting in beading, ribbons, or fusion of neighboring fibers.[172] With slower flow rates, the polymer template wires may theoretically decrease in diameter,[175] although in other studies the flow rate has had no influence.[181] At even slower rates, the mass flow is too low to maintain a stable jet, resulting in short, broken fibers.[182]

To probe the influence of the flow rate, the pump speed was varied to determine the range in which nanowires can be produced. The voltage and electrode distance were kept constant at 20 kV and 12 cm, respectively. Nanowires are produced with pump speeds between 0.5 mL/hr and 2 mL/hr, but with this increase in pump speed the diameter only decreases nominally from 181 (± 38 nm) to 165 (± 26 nm) at 2 mL/hr (Figure 4.4c).

1.1.1.2. Electrode Distance

According to some sources, an increased distance between the collector and the syringe nozzle decreases the nanowire diameter as the longer distance allows more whipping and therefore more thinning of the jet.[172] Other studies report no significant difference, just a reduction in beading due to improved solvent evaporation.[183]

To probe the influence of the electrode distance, the syringe was moved until the limits of nanowire production were detected. The voltage and pump speed were kept constant at 20 kV and 0.8 mL/hr, respectively. Within the limit of the Eu-CeO_2 electrospinning system (12 cm to 21 cm), the nanowire diameter increases insignificantly from 165 (± 32 nm) to 208 (± 33 nm) upon increasing the electrode distance from 12 cm to more than 15 cm. There is no continued increase in nanowire diameter up to the limit at 21 cm (Figure 4.4b).

1.1.1.3. Electrospinning Voltage

A minimum voltage is required for to build up enough charge to overcome the surface tension. Above this threshold, the diameter of polymer nanowires typically decreases with electrospinning voltage.[184]

To probe the influence of the electrospinning voltage, the upper and lower limits of the nanowire-producing voltage were determined. The pump speed and electrode distance were kept constant at 0.8 mL/hr and 12 cm, respectively. Within the range of 14.2 kV to 26 kV, nanowire diameters are consistently ~160 (±20) nm (Figure 4.4a).

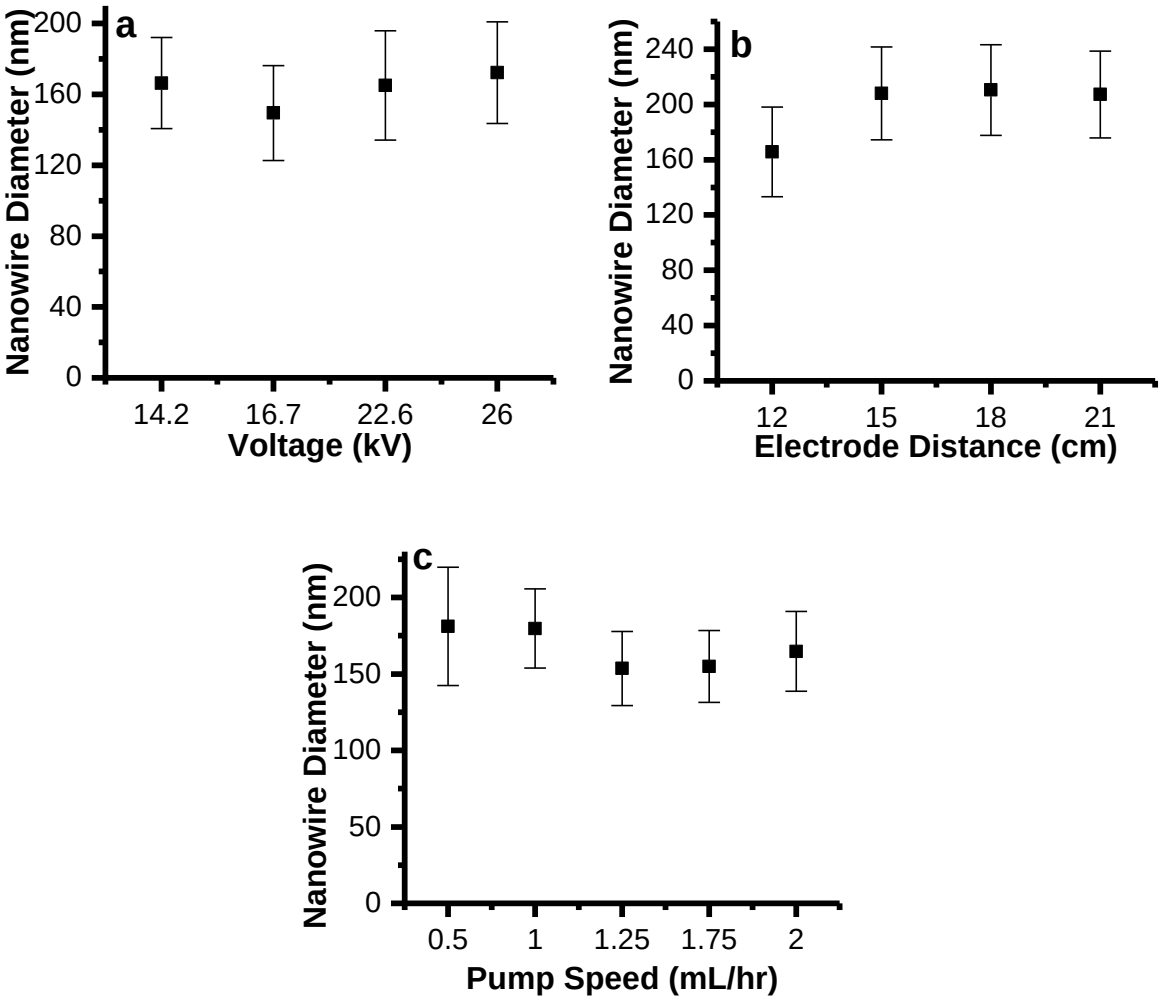

Figure 4.4 *Plots showing the relationship of Y-CeO_2 nanowire diameters to (a) electrospinning voltage, (b) distance from syringe tip to electrode, and (c) electrospinning pump speed.*

4.4.2. Y-CeO_2: Influential Parameters

The precursor concentrations have a significant influence on the stability of the Taylor cone, and therefore on the produced nanowires. Increasing PVP concentrations and $Ce(NO_3)_3$ concentration both increase the nanowire diameter, while additional MeOH and DMF decrease the diameter.

1.1.1.4. PVP Concentration

As described in Section 4.2.1, the polymer concentration is one of the major controlling factors of the electrospinning viscosity. High polymer concentrations may cause fusion between nanowires or prevent electrospinning altogether.[165] As the concentration is decreased, the solution viscosity reduces, leading to thinner nanowires. At very low polymer concentrations, the surface tension over-rides the charge repulsion, resulting in bead formation.[155,166]

The annealed nanowire morphology is stable with PVP concentrations of 7.7 wt% to 12.8 wt%, with diameters ranging from 156 nm (± 31 nm) to 413 nm (± 87 nm) (Figure 4.5a). Below 7.6 wt% PVP the solution sprays to form a film, while PVP content above 15.4 wt% results in composite nanowires fusing together before annealing.

1.1.1.5. $Ce(NO_3)_3$ Concentration

The influence of $Ce(NO_3)_3$ is slightly more complex than that of PVP. The addition of metal salts may decrease the unannealed nanowire diameter, due to the addition of metal ions to the solution and the resulting increase in surface charge build up and Columbic repulsion. However, prior research with TiO_2 nanowires[181] and CeO_2 nanowires[175] suggest that, despite any influence the sol-gel or metal salt have on the unannealed

nanofibers, increasing the metal:PVP loading produces larger nanowire diameters after removing the polymer template.

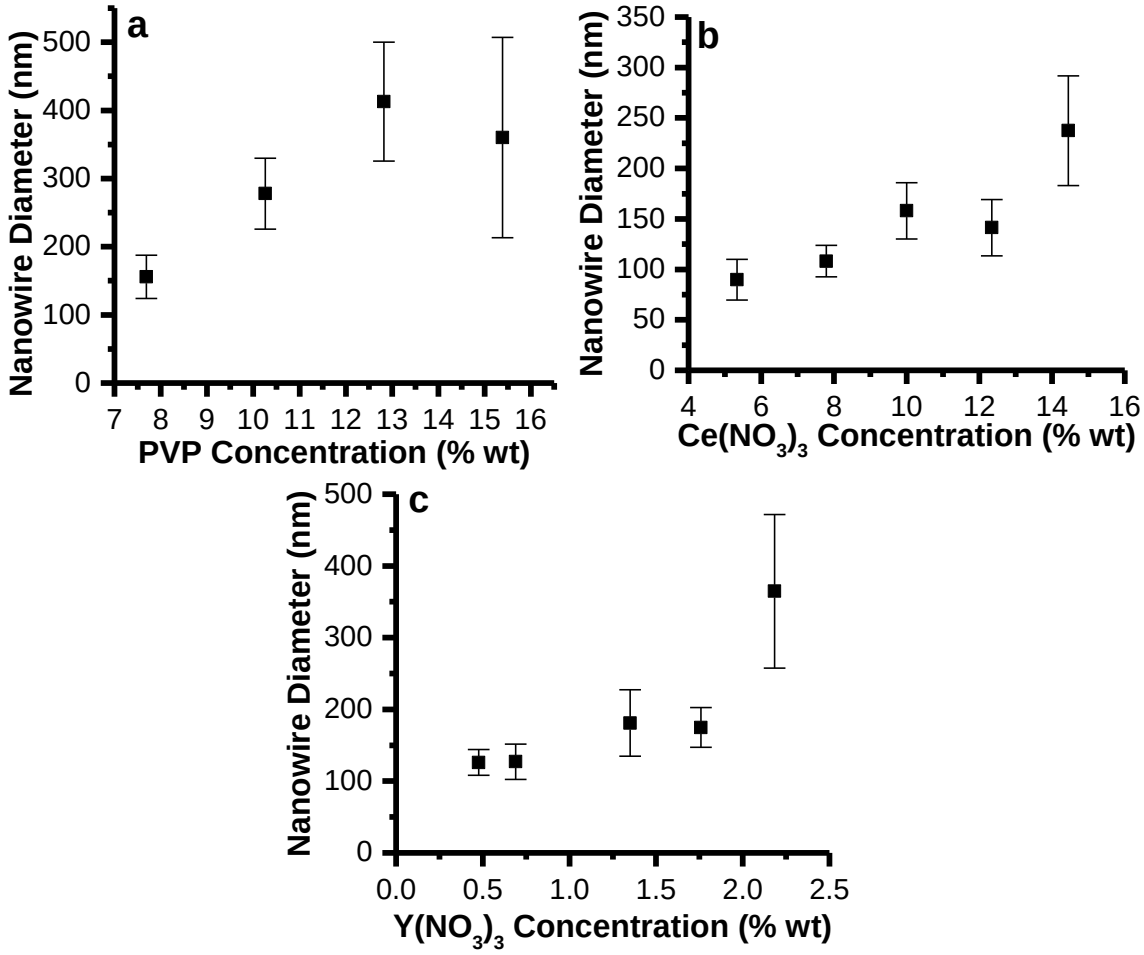

Figure 4.5 *Plots of the relationship between Y-CeO_2 nanowire diameter and (a) PVP concentration, (b) $Ce(NO_3)_3$ concentration, and (c) $Y(NO_3)_3$ concentration.*

To investigate this, the $Ce(NO_3)_3$ concentration was varied to find the upper and lower limits of stable nanowire production. Upon increasing from 5.33 wt% to 14.45 wt% of $Ce(NO_3)_3$, the average nanowire diameter increases from 90 nm (± 20 nm) to 237 nm (± 54 nm) (Figure 4.5b). This matches the literature precedent that the increase in loading of metal:PVP dominates the $Ce(NO_3)_3$ influence on the nanowire diameter, not the increase in ion concentration.

1.1.1.6. $Y(NO_3)_3$ Concentration

The influence of $Y(NO_3)_3$ was also probed by varying the concentration from 0.48 wt% to 2.2 wt% $Y(NO_3)_3$. Within the range of 0.48 wt% to 1.8 wt% $Y(NO_3)_3$, the nanowire diameters increase negligibly from 126.1 (± 18) nm to 174.8 (± 27) nm. However, a further increase 2.2 wt% significantly increased the nanowire diameter to 364.7 (± 107) nm (Figure 4.5c). The large diameter increase coupled with the large standard deviation is likely due to fusion of several nanowires, but the cause of the fusion in this particular sample is undetermined.

1.1.1.7. Solvent Concentrations

The use of a mixed solvent system was necessary for electrospinning of Y-CeO_2 nanowires. PVP and $Ce(NO_3)_3$ immediately precipitate as a white polymeric clump when combined within a single solvent, regardless of the order of addition, temperature, or concentration. However, dissolving $Ce(NO_3)_3$ in one solvent and PVP in the other, then mixing the two solutions prevents this precipitation. Some white precipitates are seen immediately upon combining the two solutions, but quickly disperse upon mixing.

The physical properties of the electrospinning solvent play a significant role in the final size and morphology of electrospun nanowires. In particular, the surface tension, electrical conductivity, viscosity, boiling temperature, and dipole moment of the solvent contribute to stability of the Taylor cone and deposition of nanowires.[169,185] . The density, surface tension, viscosity, conductivity, and dipole moment of MeOH and DMF are listed in Table 4.2.

Increasing the DMF concentration could reduce the nanowire diameter, due to DMF's dipole moment and electrical conductivity relative to MeOH.[186] However, DMF's higher boiling point and surface tension would increasing the likelihood of beading or breakdown of nanowire morphology during electrospinning.[169]

Table 4.2 *Physical properties of DMF and MeOH, measured at either 20 °C or 25 °C.*[169,185]

Solvent	Boiling Temp. (°C)	Density (g/mL)	Electrical Conductivity at 25 °C (S /m^{-1})	Abs viscosity 25 °C (mPa*s)	Dipole Moment (D)	Surface tension at 20 °C (mN/m)
DMF	153	0.948	6.0×10^{-6}	0.82	3.8	35
MeOH	64	0.791	5.5×10^{-6}	0.60	1.7	22.6

1.1.1.8. MeOH and DMF concentrations

Adding more of either solvent to the electrospinning solution will reduce the solution viscosity as to the increased solvent volume dilutes the polymer. As a result, the unannealed nanowire diameter is expected to decrease with addition of either MeOH or DMF, leading to smaller annealed nanowires. This was tested by varying the mass of DMF or MeOH utilized while keeping all other operation parameters and solution masses ($Ce(NO_3)_3$, PVP, $Y(NO_3)_3$, and other solvent) constant.

When MeOH is increased from 0.6 g to 1.6 g (37.3 to 61.3 wt%), the nanowire diameter decreases from 212 (± 41) nm to 109 (± 20) nm, shown in Figure 4.6a. Similarly, increasing the DMF from 0.5 g to 0.8 g (25.9 wt% to 35.9 wt%), decreases the nanowire diameter from 201 (± 45) nm to 87 (± 15) nm as shown in Figure 4.6b.

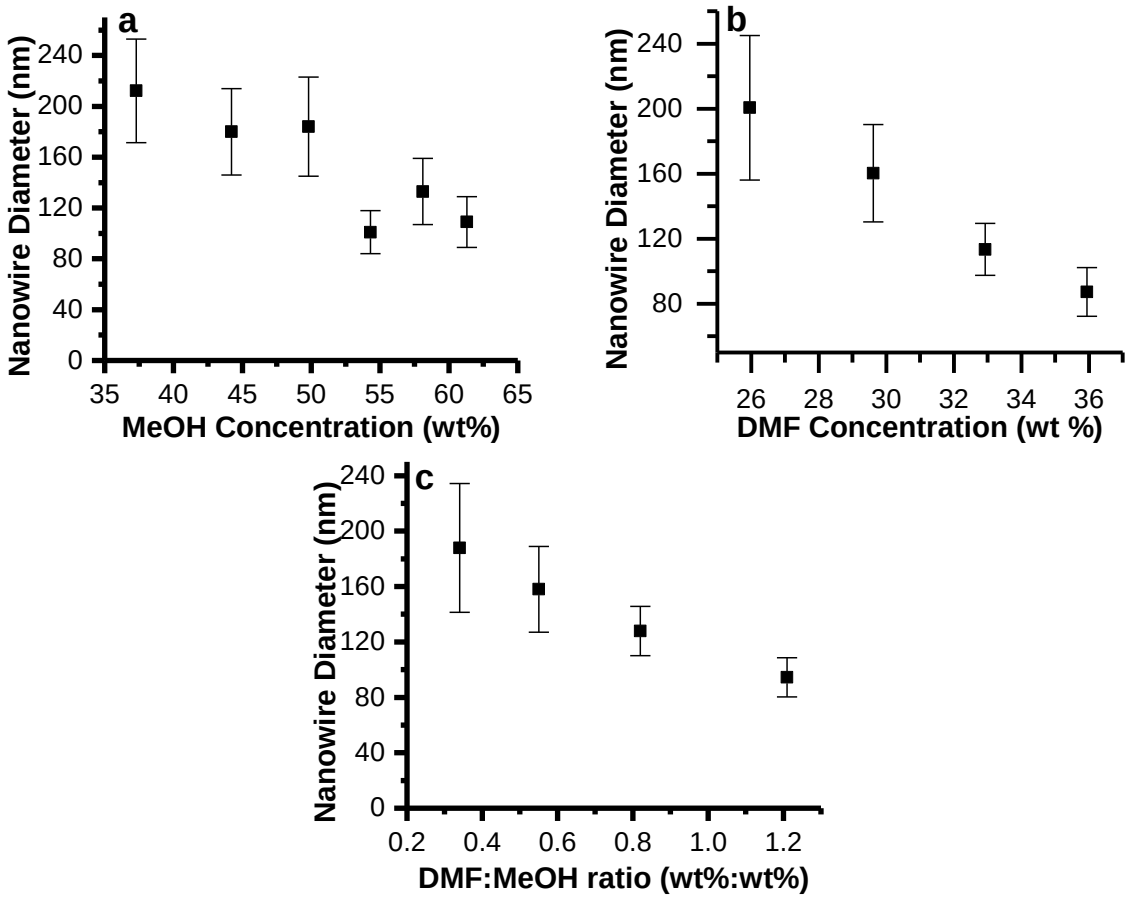

Figure 4.6 *Plots showing relationship of nanowire diameter to (a) MeOH concentration, (b) DMF concentration, and (c) DMF:MeOH mass ratio.*

1.1.1.9. DMF:MeOH ratio

Increasing the DMF:MeOH ratio should make the electrospinning denser and more viscous, and increase its dipole moment and conductivity. Increasing the DMF:MeOH ratio would also decrease the volume of a DMF/MeOH solution of a given mass, increasing the PVP concentration and further increasing the solution viscosity. Increased viscosity tends to increase nanowire diameter, while increasing the surface tension often introduces beading.[169] However, solutions with higher dipole moments and electrical conductivities tend to produce thinner nanowires due to charge repulsion within the solution.[186]

To evaluate the overall trend, the DMF:MeOH wt % ratio was varied from 0.34 to 0.55, while keeping the total weight of solvent constant at 1.55 g. As the DMF portion increases, the nanowire diameter decreases from 188 (± 46) nm to 95 (± 14) nm (Figure 4.6c). This implies that the increase in surface tension and viscosity is countered by the increase in charge separation upon increasing the DMF concentration.

1.1.1.10. Sonication Time

The sonication time and solvent prior to TEM sample preparation were also analyzed for nanowire length control. The nanowire length decreases from 1692 (± 1663) nm with 1 minute of sonication to 855 (± 538) nm after 60 minutes sonication time, although the standard deviation makes the length difference insignificant (Figure 4.7). The standard deviation did consistently, and significantly, decrease with sonication time, indicating an increased homogeneity in nanowire dimensions. The majority of the reduction in standard deviation was completed by 5 minutes, so samples are only sonicated for five minutes.

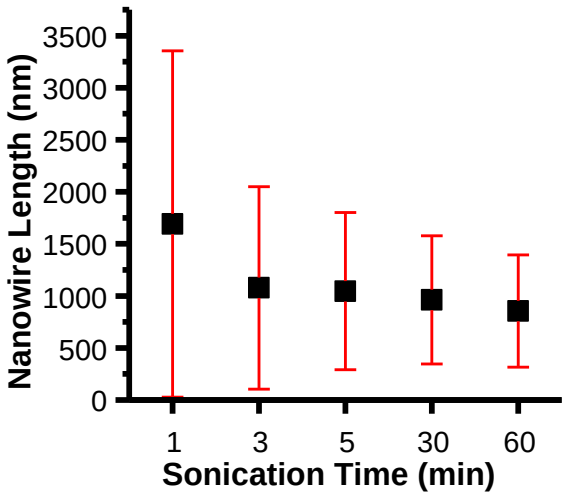

Figure 4.7 *Plot of Y-CeO_2 nanowire length after various sonication times.*

4.5. Results: Eu-CeO_2 Nanowires

4.5.1. Standard Synthetic Protocol

SEM and TEM analysis were used as complimentary techniques to characterize both annealed and unannealed nanowires. SEM imaging allows analysis of large areas of the fiber networks and avoids damage of the PVP template both during sonication, and by the high energy beam used in the TEM. However, the 3-D nature of non-sonicated networks can complicate accurate diameter measurement from SEM images. Conversely, since the sonicated networks are nearly 2-D, TEM is better suited for analysis of nanowire diameters. High resolution TEM also provides essential information about the microstructure of the nanowires.

As seen in SEM images in Figure 4.8a, the unannealed nanowires form an interlocking network with no nanowire alignment. The nanowires are affected by minimal beading and demonstrate no significant nanowire breakage even with wire lengths easily exceeding 10 microns. This network is maintained after removing the PVP template and oxidizing the Ce^{3+} and Eu^{3+} to form Eu-CeO_2 nanowires (Figure 4.8b).

Following analysis by SEM images, the annealed nanowires were also analyzed in by TEM imaging. The nanowires synthesized from the baseline protocol described in Section 4.3.3 have an average diameter of 99 (±17) nm and remain in small networks of inter-connecting nanowires (Figure 4.9a). The extended networks seen under SEM analysis are broken by the sonication of the sample during preparation for the TEM. Under higher magnification, the individual Eu-CeO_2 nanoparticles comprising a given nanowire are clearly observable, fused together to form the nanowire morphology. (Figure 4.9b).

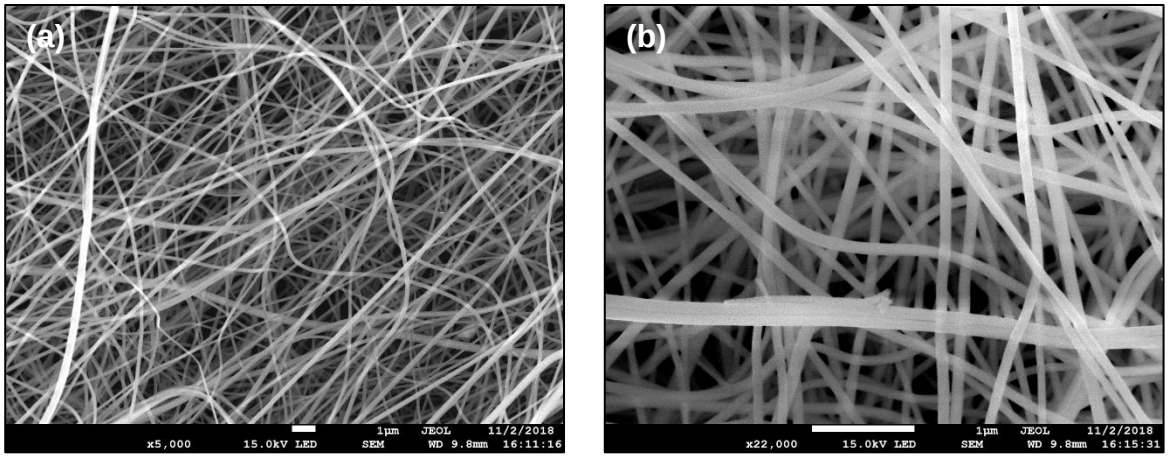

Figure 4.8 *SEM images of (a) unannealed nanowire network and (b) Eu-CeO_2 nanowires following polymer removal by annealing. These samples were not synthesized by the standard synthetic protocol, but still exhibit the microscopic network morphology.*

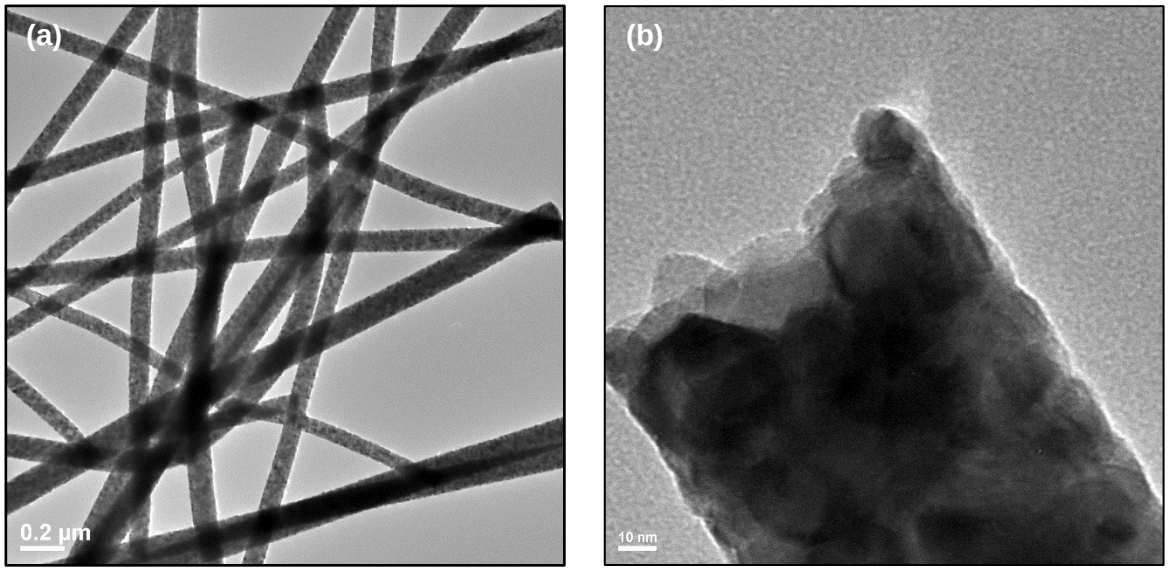

Figure 4.9 *TEM images of Eu-CeO_2 (a) network of nanowires, and (b) individual Eu-CeO_2 nanoparticles fused into nanowires.*

The theoretical yield of the Eu-CeO_2 nanowires would be 100 mg, assuming complete conversion of $Ce(NO_3)_3$ to stoichiometric CeO_2. However, a significant quantity of nanowires do not collect on the foil during electrospinning due to the jet whipping, or remain adhered to the aluminum foil. The electrospinning and annealed protocol is less

efficient than the hydrothermal protocols, with experimental yields typically about 15 to 20 mg for one reaction.

4.5.2. Influence of DMF Concentration

The DMF concentration was used to control the Eu-CeO_2 nanowire diameter, based on the results of the Y-CeO_2 nanowire system. Within the Y-CeO_2 system, manipulation of the DMF concentration provided a larger range of nanowire diameters, and was more linear than the MeOH, providing the best overall control out of the three solvent parameters.

Within the Eu-CeO_2 system, a similar trend is seen upon increasing the DMF concentration, again due to the increasing conductivity and dielectric constant. The Eu-CeO_2 nanowire diameter decreases from 282 nm (± 86 nm) to 99 nm (± 17 nm) with an increase in the wt % DMF from 25% to 33% (Figure 4.10).

4.5.3. Influence of the $Eu(NO_3)_3$ concentration

The concentration of $Eu(NO_3)_3$ was selected to control the %Eu, in a manner similar to that of the Y-CeO_2 system where the concentration of $Y(NO_3)_3$ did not influence the Y-CeO_2 nanowires below 2.2 wt% $Y(NO_3)_3$. $Eu(NO_3)_3$ was varied from 0 to 2.0 wt %, which corresponds to 0 to 12.7 at% Eu. No significant difference is observed in the diameter across this range (Figure 4.11). The influence of $Eu(NO_3)_3$ on the elemental composition of the nanowires is discussed later in Section 4.

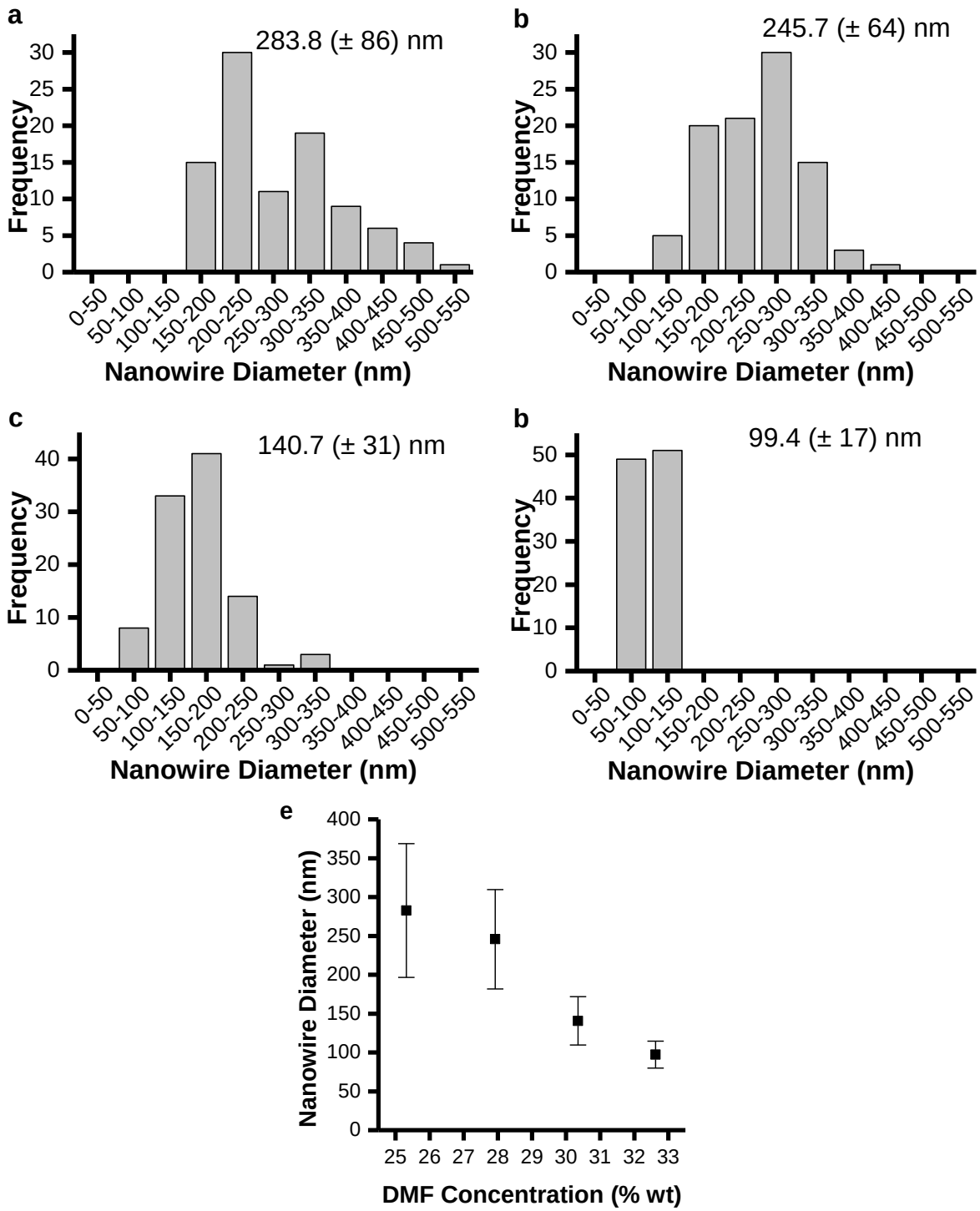

Figure 4.10 *Histograms of Eu-CeO_2 nanowires with DMF concentrations of (a) 25.3 wt%, (b) 27.9 wt%, (c) 30.4 wt%, and (d) 32.6 wt%, and (e) the plot showing nanowire diameter dependence on DMF concentration.*

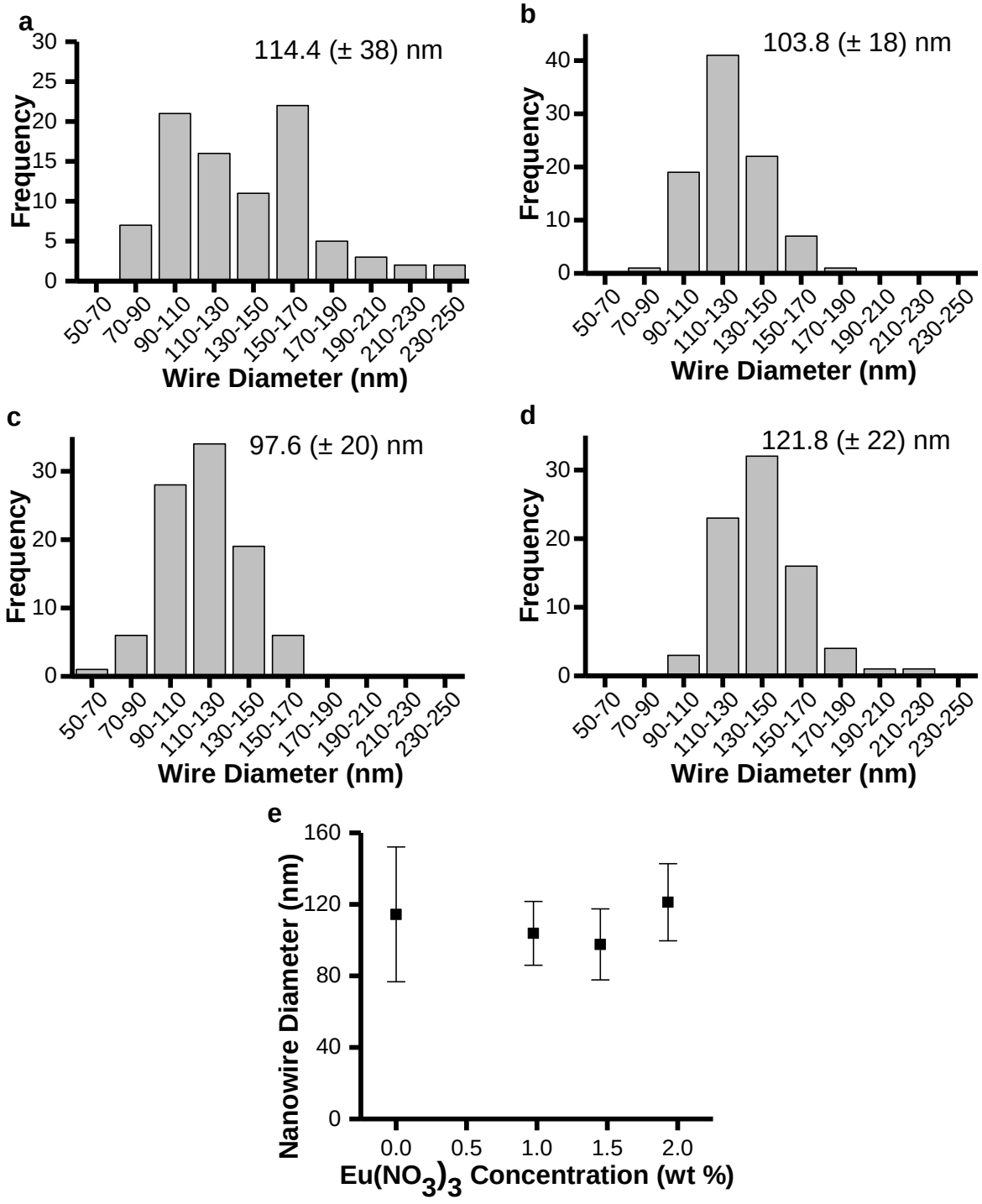

Figure 4.11 *Histograms of Eu-CeO_2 nanowire diameters with wt% $Eu(NO_3)_3$ of (a) 0 wt%, (b) 0.9 wt%, (c) 1.5 wt%, and (d) 2 wt% $Eu(NO_3)_3$.*

4.6. Crystalline Properties of Eu-CeO_2 Wires

4.6.1. Analysis of Crystalline Domains by HRTEM

The Eu-CeO_2 nanowires were analyzed for their crystallinity by HRTEM. As mentioned previously, the individual particles comprising the Eu-CeO_2 nanowires are readily apparent in HRTEM, and measure about 40 nm in width. The thickness of the nanowires leads to significant absorption of the electron beam, preventing lattice spacing measurements along most of the nanowire. Some edges of the nanowires along with small protrusions are thin enough to enable lattice spacing measurement. These individual particles appear to be monocrystalline and expose (111) planes (Figure 4.12), although (220) and (200) lattice spacings are also occasionally observed. Since the nanowires are composed of numerous, monocrystalline particles, the nanowires as a whole are polycrystalline.

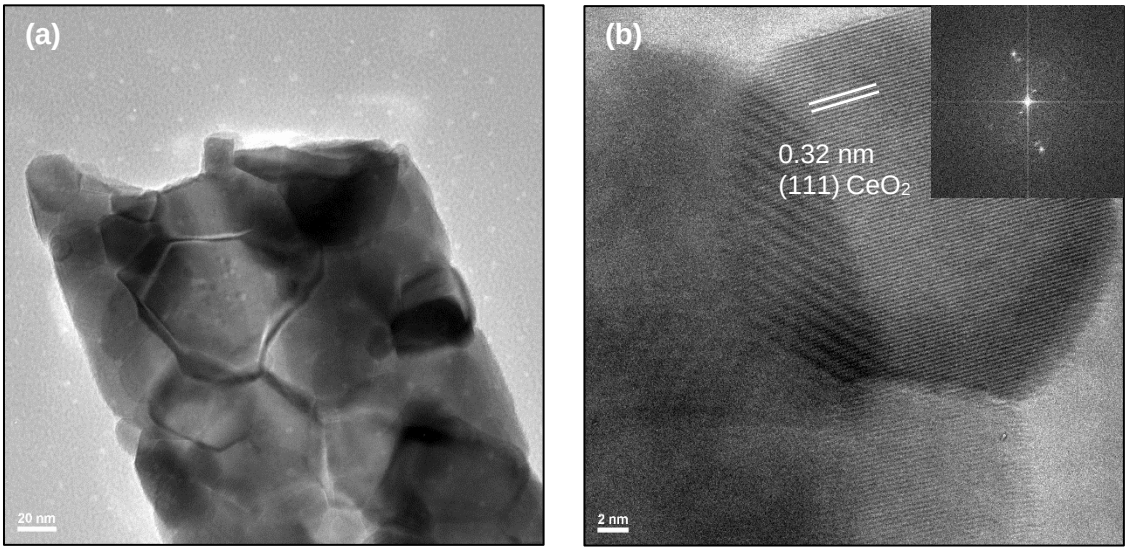

Figure 4.12 *HRTEM images of (a) Eu-CeO_2 nanoparticles assembled into nanowire morphology, and (b) protruding Eu-CeO_2 nanoparticle with lattice spacing matching (111) CeO_2, with FFT inset.*

4.6.2. Crystalline Properties of Eu-CeO_2 Nanowires by XRD Analysis

The 8.5% Eu-CeO_2 nanowires were analyzed by powder XRD. All peaks are consistent with CeO_2 crystallized in a cubic fluorite crystal structure (Figure 4.13) and with the other Eu-CeO_2 nanomaterials discussed in Chapters 2 and 3.

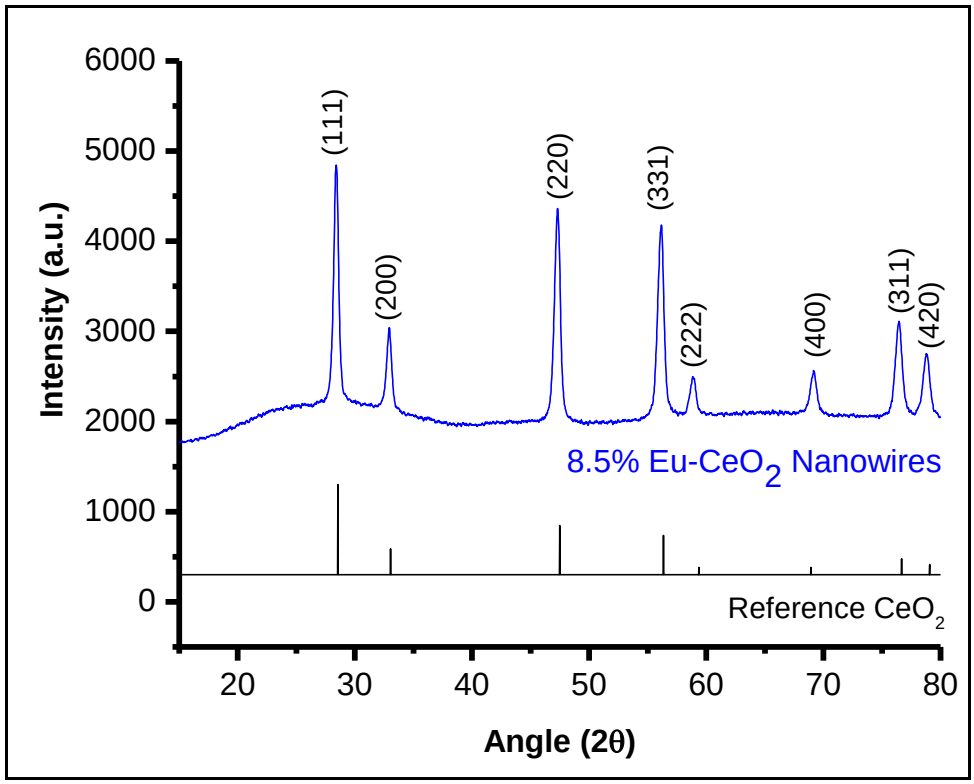

Figure 4.13 *XRD spectra of 8.5% Eu-CeO_2 nanowires (blue) and reference cubic fluorite CeO_2 peaks as published by NIST (black).*[128]

The specific peak positions and assignments to CeO_2 planes are highlighted in green in Table 4.3, along with the assignments from the rods and cubes in Chapters 2 and 3. When comparing the annealed rods, unannealed rods, and nanowires to the reference CeO_2 material, the nanowires have peak positions closer to the unannealed nanorods than to the annealed nanorods or reference CeO_2. For example, the (222) reflection has a reference peak at 59.36°, the annealed rods are slightly shifted to 59.04°, while the

unannealed rods and nanowires are shifted to 58.80° and 58.84° respectively. This trend is consistent with increased lattice strain in the nanowires compared to nanorods annealed to similar temperatures. The lattice strain is possibly caused by slightly higher Eu^{3+} concentration relative to the nanorods, or by defects originating from the polymer calcination step in the process.

Table 4.3 *Peak assignments in powder XRD for 8.5% Eu-CeO_2 nanowires and comparison to nanocubes, nanorods, annealed nanorods, and reference CeO_2 as presented in Chapters 2 and 3. The nanowire peaks are highlighted for emphasis.*

Sample	CeO_2 Peak Assignments (2Θ)[128]							
	(111)	**(200)**	**(220)**	**(331)**	**(222)**	**(400)**	**(311)**	**(420)**
Reference CeO_2	28.54	33.04	47.48	56.34	59.36	68.94	76.68	79.07
8.5% Eu-CeO_2 Nanowires	28.40	32.92	47.3	56.18	58.84	69.16	76.46	78.78
6.3% Eu-CeO_2 Nanocubes	28.46	32.98	47.42	56.20	58.92	69.26	76.98	78.86
7.7% Eu-CeO_2 Nanorods	28.46	32.82	47.26	56.10	58.80	68.94	76.56	--
7.7% Eu-CeO_2 Annealed Nanorods	28.54	33.08	47.42	56.28	59.04	69.30	76.62	79.06

The crystallinity observed in the HRTEM is consistent with the strong, sharp peaks observed in the XRD spectrum. The crystalline domain size was calculated using the Scherrer equation (Eqn 4.4, Section 4.4.3), and compared to the annealed nanorods, unannealed nanorods, and nanocubes in Table 4.4. The calculated crystalline domain size increases as unannealed nanorods<annealed nanorods<nanowires<nanocubes. The average size of the individual particles that comprise the nanowires are slightly larger than the nanocubes, measuring ~40 (± 11) nm and ~25 (± 9) nm respectively. However, nanocubes are often fused together, combined within one crystallographic domain.

Two factors may contribute to the underestimation of the crystalline domain size as calculated in Table 4.4. As noted in Section 2.6.2 of Chapter 2, instrumental broadening has not been removed, although this should be consistent across all samples. In addition, the K factor used in the Scherrer equation is intended for isolated spherical particles, not the pseudo-spherical particles that comprise the Eu-CeO_2 nanowires. Therefore, the calculated crystalline domain sized values likely underestimate the true crystalline domain size and can only be used to estimate its magnitude.

Table 4.4 *Full width, half maximum of Eu-CeO_2 nanomaterials as determined using (111) peaks and calculated through Scherrer equation. The nanowires are highlighted in green.*

Sample	FWHM (2Θ)	XRD Crystalline Domain (nm)
8.5 % Eu-CeO_2 Nanowires	0.5	17
6.3% Eu-CeO_2 Nanocubes	0.38	22
7.7% Eu-CeO_2 Nanorods	1.44	6
7.7% Eu-CeO_2 Annealed Nanorods	0.58	16

4.7. Elemental Analysis by TEM EDS

The elemental composition of the nanowires was analyzed using EDS through TEM. Unlike the nanorods and nanocubes, the synthesis of Eu-CeO_2 nanowires does not require elements such as sodium or phosphorus, which are more likely to contaminate the material than carbon or nitrogen. However, EDS was still utilized to check for any stray contaminations from the syringe or silicon plates used during annealing.

Cerium, oxygen, europium, carbon, copper, and silicon were the major elements present in the EDS spectra (Figure 4.14). The carbon and copper signals are due to the carbon-coated copper grid used for TEM analysis. The very weak silicon signal may be

due to either slight contamination from the plate during annealing or from an artifact within the EDS system.

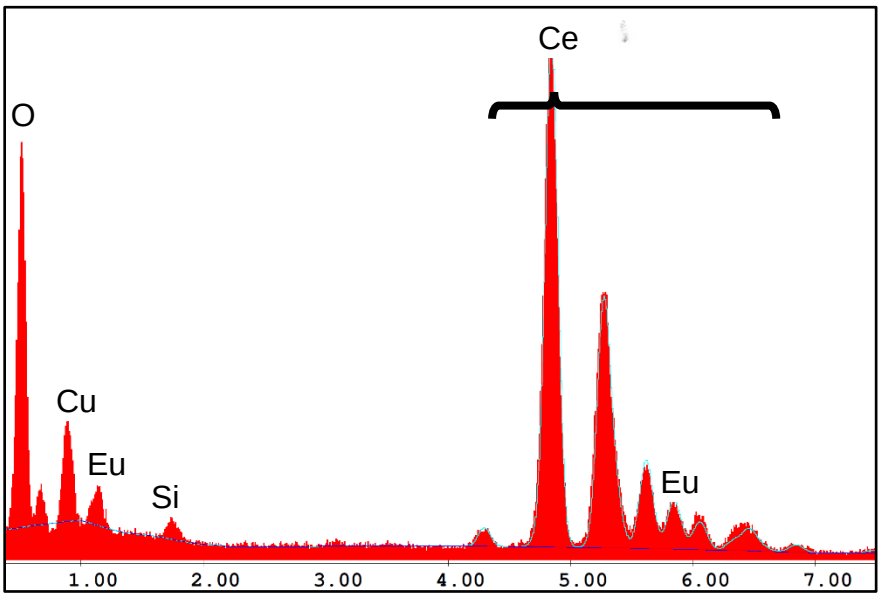

Figure 4.14. *EDS spectrum of 8.5 % Eu-CeO_2 nanowires.*

4.7.1. Control of Dopant Concentration with $Eu(NO_3)_3$

The %Eu concentration as defined by Equation 4.3 and restated below was controlled through manipulation of the $Eu(NO_3)_3$ precursor. By increasing the wt% $Eu(NO_3)_3$ from 0 to 2 wt%, the theoretical %Eu increased to a maximum to 12.7 %Eu. The %Eu measured by EDS matched well with the theoretical molar ratio in the precursors as determined by Equation 4.3 and shown in Table 4.5. However, a ~1 at% europium is detected in samples with no $Eu(NO_3)_3$. This is likely due to residual electrospinning solution sticking to the cannula despite repeated washings with acetone and water.

$$\%Eu = \frac{at\%\ Eu}{at\%\ Ce + at\%Eu} \qquad \text{(Eqn 4.3)}$$

Table 4.5 *Elemental composition of nanowires with varying %Eu as controlled by wt% $Eu(NO_3)_3$, with oxygen, cerium, and europium concentrations as determined by EDS.*

Wt% $Eu(NO_3)_3$	Theoretical %Eu	At% O	At% Ce	At% Eu	%Eu
0	0	51.5 ± 1.7	47.5 ± 1.7	1.0 ± 0.2	1.8 ± 0.17
1.5	8.9	57.1 ± 1.2	39.0 ± 0.7	3.9 ± 0.6	8.5 ± 0.49
2.0	12.7	51.2 ± 1.1	41.8 ± 1.3	7.0 ± 0.3	14.4 ± 0.8

4.7.2. Analysis of Elemental Distribution by EDS Mapping

The elemental distribution within individual samples was analyzed by EDS mapping. Cerium, oxygen, and europium are all very evenly distributed throughout the nanowire, with no observable segregation of elemental constituents throughout the nanowire, as seen in Figure 4.15.

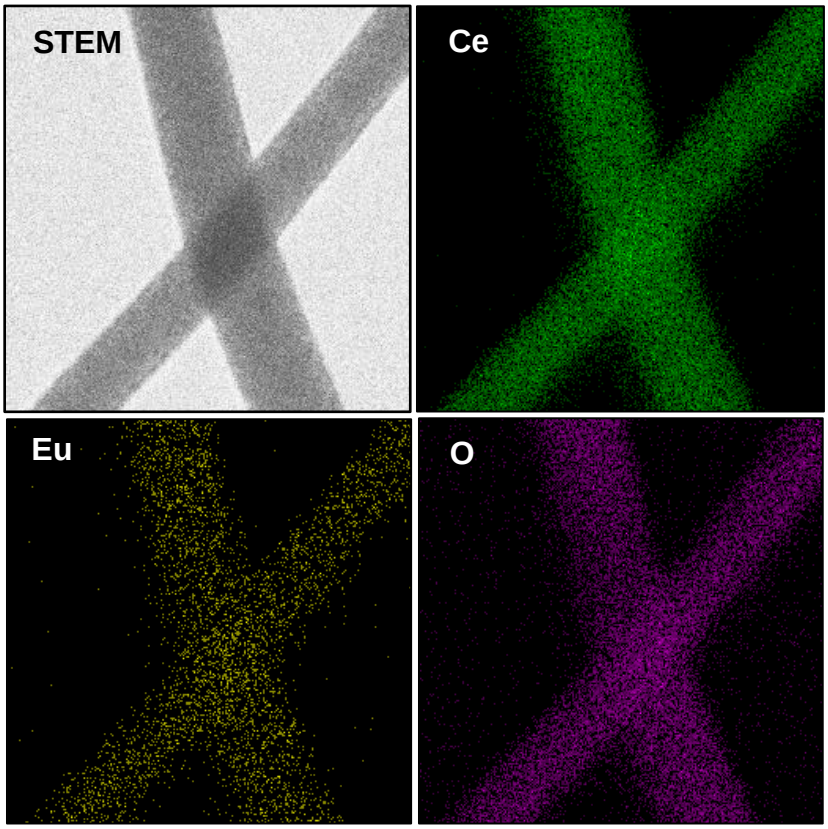

Figure 4.15 *STEM image and EDS mapping images of cerium (green), europium (yellow), and oxygen (magenta) in Eu-CeO_2 nanowires.*

4.8. Conclusions

This chapter describes the details of an electrospinning protocol producing Y-CeO_2 nanowires with controllable nanowire diameter, and Eu-CeO_2 with controllable nanowire diameter and europium concentration. The synthesis proceeds through dispersion of Ce^{3+} and Ce^{4+} using a sol-gel-assisted process, in a viscous polymer solution. Electrospinning this solution produced cerium-loaded polymer fibers, which can be carefully annealed to produce the doped CeO_2 nanowires.

The Y-CeO_2 system was more thoroughly investigated to establish the parameters controlling the nanowire size and elemental composition. Specifically, the operational parameters (voltage, electrode distance, pump speed) had a minimal influence, while parameters controlling the solution's intrinsic properties (solvent concentration, PVP concentration, metal salt concentration) were more important for diameter control. Y-CeO_2 nanowires were synthesized with diameters ranging from 400 nm down to 80 nm by manipulation of these parameters. However, the intrinsic fluorescence of europium prompted the adjustment from Y-doped to Eu-doped nanowires.

The Eu-CeO_2 nanowire diameter and europium concentration were both controlled using parameters indicated in the Y-CeO_2 system. The DMF concentration controlled the Eu-CeO_2 nanowire diameter, which could be tuned between ~280 and ~100 nm by increasing the DMF concentration due to increases in the solution conductivity and dielectric constant. The europium concentration in the nanowires could also be tuned by changing the $Eu(NO_3)_3$ precursor concentration, and nanowire samples with measured 2 to 14 %Eu were synthesized with no influence on the nanowire diameter.

The produced nanowires were comprised of smaller monocrystalline particles fused together, typically with exposed (111) CeO_2 planes. As a result, the crystalline domain size for nanowires as estimated through XRD was smaller than the nanocubes, comparable to the annealed nanorods, and significantly larger than the unannealed nanorods discussed in Chapters 2 and 3. The XRD spectrum confirmed the CeO_2 cubic fluorite structure, with some peak shifts comparable to those seen in the unannealed nanorods.

The controlled doping of Eu^{3+} into the CeO_2 morphology, with no significant change in the nanowire morphology, produces another morphology with potential Eu^{3+} fluorescence. The fluorescence of the Eu-CeO_2 nanowires as well as the Eu-CeO_2 materials from Chapters 2 and 3, will analyzed in Chapter 6.

Eu-CeO_2 annealed nanorods, unannealed nanorods, nanocubes, and nanowires have now been synthesized, with lattice strain, exposed planes, defect concentration, and crystalline domain size varying between the samples. The relative chemical reactivity of these four morphologies are compared in Chapter 7. Specifically, experiments are discussed probing the interactions of the Eu-CeO_2 materials with L-dihydroxyphenylalanine (L-Dopa), a precursor for the synthesis of melanin. Due to their structural differences, the extent of L-Dopa adsorption varies significantly between the four morphologies.

Chapter 5. Synthesis and Characterization of Eu-CeO_2 Nanotubes

5.1. Overview

Chapters 2, 3, and 4 covered in depth the manipulation of pre-existing synthetic techniques to prepare europium-doped variations of non-porous CeO_2 nanoscale morphologies. In contrast, Chapter 5 describes initial studies of the novel use of spin-coating steps combined with successive ionic layer adsorption on a ZnO nanowire array to make europium-doped cerium oxide (Eu-CeO_2) nanotubes.

Nanotube morphologies offer a significantly higher surface area relative to other 1-D structures with similar dimensions, with a wide range of uses including drug delivery, photocatalysis, and sensing.[187] Tubes with large inner cavities, pores, and/or openings may be loaded with drugs or various nanoparticles. For example, magnetic iron oxide particles have been loaded into or grown within carbon nanotubes, contributing a magnetic component to the nanotubes.[188,189] Nanotubes have also been used as a drug delivery vector, with drugs either loaded either inside the nanotube's cavity or attached to its outer surface.[187,190,191]

The combination of CeO_2 catalytic activity, Eu^{3+} fluorescence, and the nanotube's high surface area motivates the synthesis of Eu-CeO_2 nanotubes as a possible drug delivery platform. While a number of studies have led to various CeO_2 nanotube-based morphologies, most of these techniques require long reaction times, expensive templates, or produce tubes in mixed morphologies or limited to small inner cavities. The technique detailed in Chapter 5 overcomes a number of these faults through the use of a ZnO nanowire array as a sacrificial template.

The sacrificial ZnO nanowires are grown on a silicon substrate, with controllable dimensions as previously reported.[192] A thin Eu-$Ce(OH)_3$ shell is grown on the ZnO nanowires by successive layer by layer deposition of Eu^{3+}/Ce^{3+} and OH^-.

The Eu-$Ce(OH)_3$ shell is oxidized to Eu-CeO_2 by annealing, and the ZnO core is etched to complete the fabrication of the nanotubes. Two etching procedures are also compared in an attempt to maximize nanotube adhesion to the substrate without affecting the nanotube morphology. This synthesis produces a polycrystalline Eu-CeO_2 nanotube morphology of relatively high porosity, with large inner diameters and lengths as controlled by manipulation of a sacrificial ZnO template.

5.2. Introduction

Several approaches have been used to synthesize CeO_2 nanotubes, hydrothermal reactions, loading into porous membranes, and coating carbon nanotubes or ZnO nanowires.[11,45,54,60,106,193,194] However, no Eu-CeO_2 nanotubes have been reported in the literature to date.

The synthesis of CeO_2 nanotubes has been reported using various hydrothermal procedures, due to increased yield and simpler experimental protocols compared to other approaches. In the first reported nanotube synthesis, nanotubes were synthesized through aging a reaction of $Ce(NO_3)_3$ with NH_4OH for 45 days.[11] The produced nanorods had very small inner cavities (<10 nm inner diameter) and the procedure is very time inefficient. Oxygen-free hydrothermal reactions have also produced nanotube morphologies, with significant aggregation of the tubes.[195] Yet another group manipulated the hydrothermal conditions to selectively oxidize the nanotube surface. This oxidation minimized dissolution of the CeO_2 shell, but due to Ostwald Ripening, the $Ce(OH)_3$ core

dissolved and reprecipitated on the shell.[61] Alternatively, the outer surface of $Ce(OH)_3$ has been oxidized by exposure to air, and the inner $Ce(OH)_3$ core etched away using H_2O_2, producing nanotubes with ~15 nm inner diameters and ~5 nm wall thickness.[45]

Templates have also been utilized to synthesize CeO_2 nanotubes. CeO_2 can be electrochemically grown within porous membranes, such as anodic alumina oxide (AOT) membranes,[193] although AOT membranes are expensive relative to templates such as ZnO or carbon nanotubes. Carbon nanotubes (CNTs) are frequently used as a support to grow CeO_2 nanoparticles, which can be fused to make a CeO_2 shell.[54] Nitric acid is used to induce a negative charge on the CNT surface, which aids adsorption of Ce^{3+} ions. NaOH is added to precipitate $Ce(OH)_3$ nanoparticles, which oxidize and fused together while the CNT is removed by annealing.[54] The produced nanotubes are polycrystalline with a high surface area, but are very long and twisted which may hinder efficient tube loading. Furthermore, the nanotube diameter is largely dependent on the CNT inner diameter. In this particular study, the CeO_2 nanotubes have relatively small inner cavities, with inner diameters of 15-30 nm.

Zinc oxide (ZnO) nanowires have also been used as templates, due to their ease of etching. $Ce(OH)_3$ shells have been grown on ZnO nanorods by successive ionic layer adsorption. In this technique, OH^- was first adsorbed to the ZnO nanord surface by dispersion and sonication of the ZnO rods in an NaOH solution.[53] The hydroxide-terminated and coated rods were recollected and washed, then dispersed in an $Ce(NO_3)_3$ solution. The Ce^{3+} ions adsorb to the surface of the ZnO rod, aided by electrostatic attraction to the hydroxide. Gradually, the alternating layers build up a $Ce(OH)_3$ shell (Figure 5.1). The ZnO core was then etched using HCl to produce CeO_2 nanotubes.

However, this procedure required extensive hands-on labor, with 20 five-minute sonication-assisted depositions of Ce^{3+} and OH^-, washing and centrifuging with EtOH between deposition.

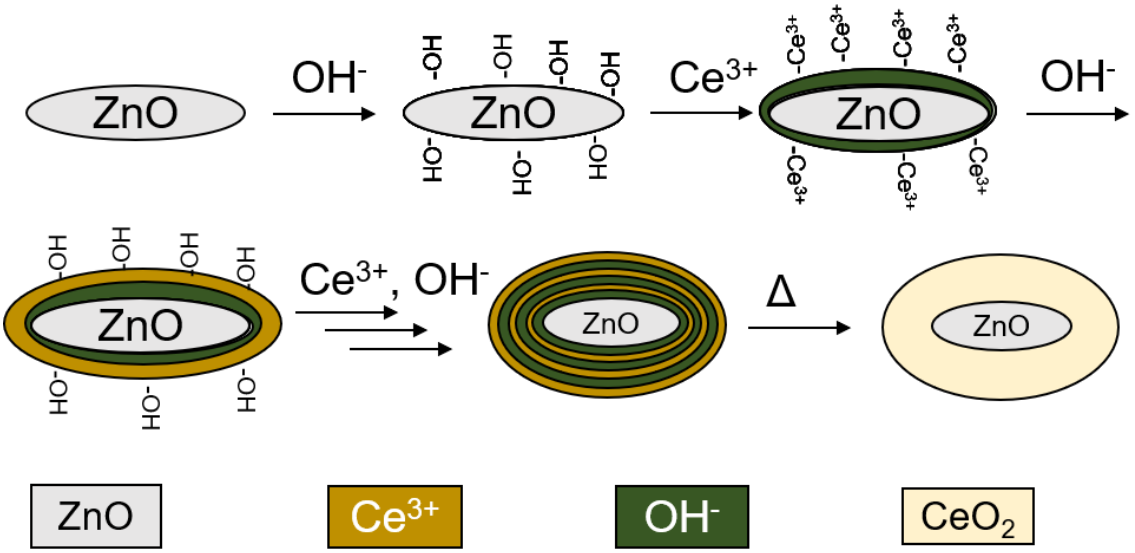

Figure 5.1 *Diagram showing the layering of Ce^{3+} and OH^-, which convert to CeO_2 with heat to give a CeO_2-ZnO core shell structure.*

Hua *et al.* used successive ionic layer adsorption by growing ZnO nanowires on a substrate. The ZnO/substrate was repeatedly dipped in Ce^{3+} and OH^- solutions, separated by a H_2O washing dip.[196] The only reported dimension is an inner diameter of 20 nm. The nanotube wall thickness and nanotube lengths were measured as ~20 nm and 1 μm, respectively, based on provided images. These nanotubes have a high aspect ratio, with thick walls compared to a relatively thin inner cavity.

Finally, a hydrothermal procedure was utilized to deposit CeO_2 on a ZnO nanowire array. As the CeO_2 precipitated, released hydrogen ions increased the acidity of the solution, gradually etching the ZnO core.[197] While this protocol is very simple, the product

was limited to very large (inner diameter ~400 nm) nanotubes, with no control over any nanotube dimensions.

The system discussed in this chapter combines layer-by-layer deposition with ZnO nanowire arrays grown on a substrate and addresses several of the issues previously mentioned. The ZnO provides a very cost-efficient templating system, unlike membrane based templates. Manipulation of the ZnO synthetic conditions provides control over the ZnO nanowire lengths and diameters, which in turn controls the nanotube inner diameter and lengths. The use of spin-coating eliminates the necessity for repeated washing and centrifugation in the sonication approach.

5.3. Methods and Materials

5.3.1. Reagants

All materials purchased were of analytical grade, and used as purchased with no further purification. Zinc acetate dihydrate ($Zn(C_2H_3O_2)_2 \bullet 2H_2O$) was purchased from Mallickrodt. Zinc nitrate ($Zn(NO_3)_2 \bullet 6H_2O$) and hexamethylenetetramine (HMTA) were obtained from Sigma Aldrich. Concentrated hydrochloric acid (HCl) was purchased from BDH, and absolute ethanol (EtOH) was purchased from Pharmco. All other reagents were purchased as described in Chapters 2, 3, or 4.

5.3.2. Synthesis of ZnO Core Nanowires

Single crystal silicon wafers were used as the substrate for the ZnO nanowire growth, Eu-$Ce(OH)_3$ deposition and oxidation, and finally ZnO core etching.

Prior to ZnO nanowire growth, substrates were cut to approximately 12 mm by 12 mm. The wafers were then washed by sonicating in 10% HCl for 45 minutes, and acetone for 45 minutes, before drying using N_2.

ZnO seeds were synthesized by a protocol commonly utilized in our lab.[192] 12.5 mL of 0.01 M $Zn(C_2H_3O_2)_2$ in methanol (MeOH) were combined with 6 mL of 0.03 M NaOH in MeOH and diluted with MeOH to a total volume of 40 mL. The reaction was heated at 60 °C for 2 hours while the solution turned from cloudy to clear.

Two to three drops of the seed solution were added to a clean wafer, allowed to dry for 30 seconds, and excess solution removed by spinning at 3000 rpm for 20 seconds. This was repeated a second time. The wafers were then annealed at 260 °C for 40 minutes. This entire process was repeated a second time.

ZnO wires were grown on the seed coated wafers using 50 mL of 0.08 M solutions of $Zn(NO_3)_2$ and HMTA each. Wafers were positioned upside down in a specifically design rack (Figure 5.2), and the reaction container covered with a watch plate to reduce evaporation. The nanowires grew for two to seven hours, with the reaction solution replenished with fresh $Zn(NO_3)_2$ and HMTA every 3 hours. The wafers were rinsed with de-ionized water, and any ZnO grown on the back or sides was wiped off with a Kimwipe. The final ZnO nanowire-coated silicon substrate is referred to as a ZnO/Si substrate.

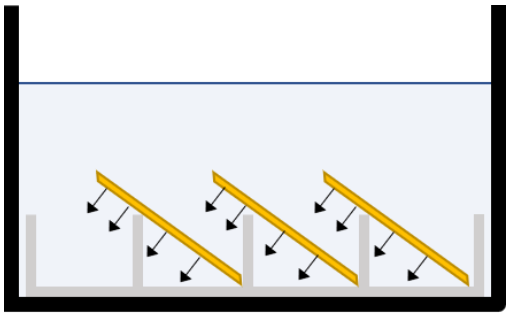

Figure 5.2 *Diagram of system to grow ZnO nanowires. The large glass beaker (black) holds a small glass rack (gray). The substrates (orange) are placed with the ZnO seed layer facing down. ZnO nanowires grow in the direction of black arrows.*

5.3.3. Deposition and Oxidation to Eu-CeO_2/ZnO Core-Shell Structures

A Eu-$Ce(OH)_3$ shell was grown on the ZnO nanowires through repeated deposition of Ce^{3+} and OH^- on the ZnO/Si substrates. To start, the ZnO-coated substrates were washed using EtOH and spun at 3000 rpm for 20 seconds. The OH^- solution was composed of 0.05 M NaOH in absolute ethanol. The Ce^{3+} solution was composed of 0.05 M $Ce(NO_3)_3$ and 0.005 M $Eu(NO_3)_3$ dissolved in absolute ethanol.

The ZnO nanowire film was first completely coated with about 4-5 drops of NaOH. After drying for ~10 seconds, the excess solution was removed by spinning at 3000 rpm for 30 seconds. The wafer was washed with spin-coating 95% EtOH, and the process repeated using the Ce^{3+} solution instead of OH^-. The second EtOH wash constitutes the end of one deposition cycle (Figure 5.3a) with the typical synthetic protocol utilizing 21 deposition cycles. The samples were annealed to 500 °C for 1 hour after depositing $^1/_3$ and $^2/_3$ of the total cycles. Once all cycles had been completed the samples were annealed to 600 °C overnight as the final annealing treatment (Figure 5.3b). Samples at this point, consisting of ZnO nanowires coated with Eu-CeO_2, are referred to as Eu-CeO_2/ZnO nanowires.

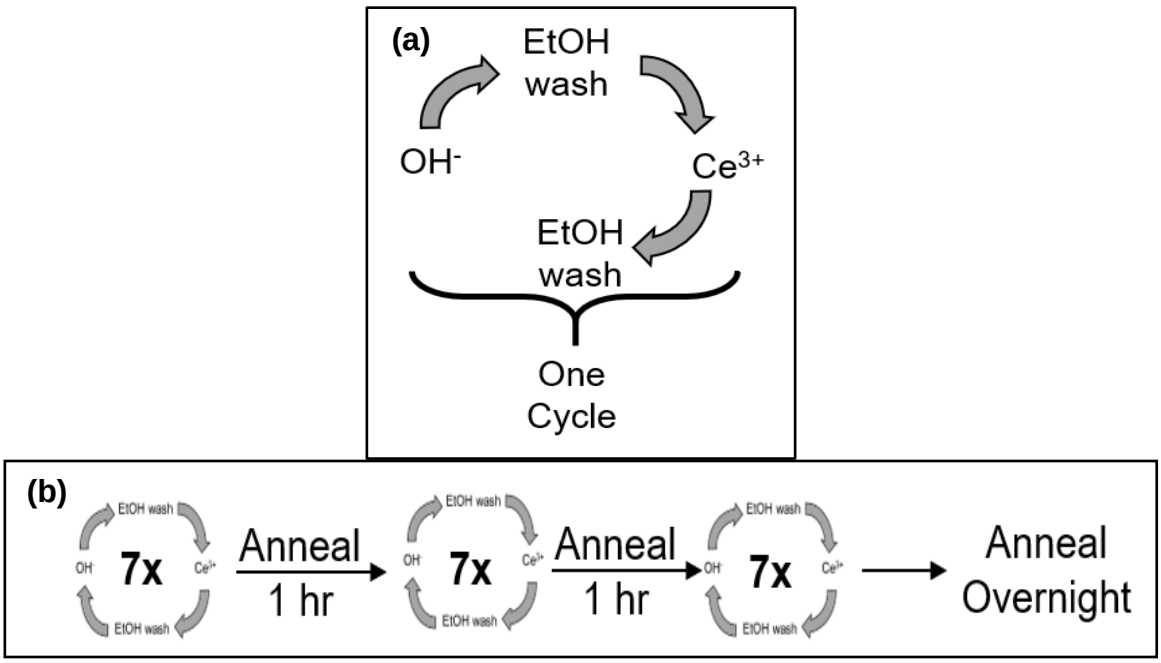

Figure 5.3 *Diagrams of the process to deposit the Eu-CeO_2 shell on ZnO nanorods. (a) illustrates the steps that make up an individual deposition cycle while (b) illustrates the deposition and annealing procedure.*

5.3.4. Removal of ZnO Core

Following the Eu-CeO_2 deposition, the ZnO core is etched by one of two methods: wet etching using 10% HCl, or gas phase etching using NH_4Cl at 450 °C – 500 °C.

5.3.4.1. <u>HCl solution etch</u>

After the samples were annealed overnight at 600 °C, about 10 drops of 10% aqueous HCl were added to coat the surface of the Eu-CeO_2/ZnO nanowires. After 20 minutes, the acid and any detached nanotubes were pipetted off and stored in a microcentrifuge tube, and fresh HCl was added to the substrate. This was repeated for a total of 3 etch cycles, with all HCl and detached nanotubes combined in the centrifuge tube. The surface was then washed with DI H_2O by the similar procedure, with the water washing added to the HCl washings.

Detached nanotubes were isolated from the HCl and H_2O washings by centrifuging at 7000 rpm for 10 minutes, removing the supernatant and adding fresh DI H_2O. This was repeated until the supernatant was no longer acidic by pH paper.

5.3.4.2. NH_4Cl Etching

NH_4Cl etching used a quartz tube reactor heated by an open-ended furnace. Samples were placed in a small ceramic boat with the Eu-CeO_2/ZnO side facing up. About 20 mg of NH_4Cl was loaded into a second boat. Helium gas was used as the carrier, with a flow rate of 180 sccm. The two boats were inserted into the quartz tube, with the NH_4Cl-loaded boat positioned at the front edge of the furnace, and the sample-loaded boat was positioned in the center of the furnace, as shown in Figure 5.4. A mineral oil-containing bubbler was added to the exhaust end of the quartz tube. The quartz tube was heated to a minimum of 400 °C for 3 hours and allowed to cool gradually.

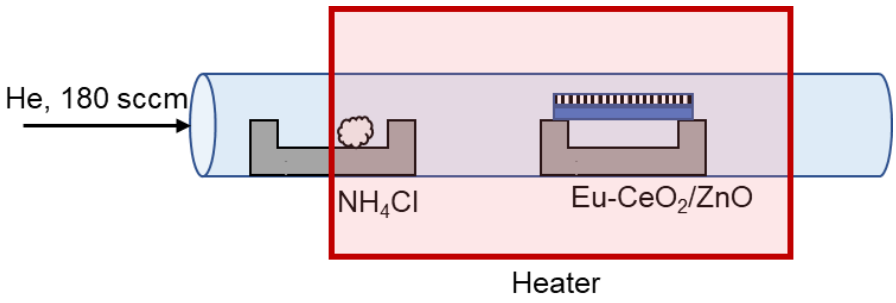

Figure 5.4 *Diagram of the NH_4Cl set up, with gas flowing from left to right, first encountering the NH_4Cl, then the Eu-CeO_2 sample.*

5.3.5. Characterization

SEM analysis was used to check the morphology of the ZnO nanowires prior to Eu-CeO_2 deposition and to calculate their length and width. The ZnO nanowires were imaged while attached to the substrate with no sputtered metal coating and using 15 kV

accelerating voltage. To measure the nanowire length, a silicon substrate with ZnO nanowires was broken down the middle. A small piece of carbon tape attached the broken wafer to a creased piece of copper foil as illustrated in Figure 5.5, with the broken edge facing up. The bottom fold of the copper foil was then attached to the SEM thimble with a second piece of carbon tape.

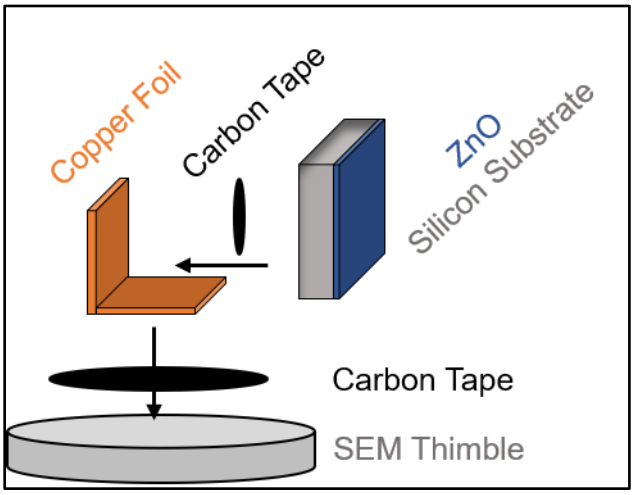

Figure 5.5 *Illustration of sample preparation for SEM cross-sectional analysis of ZnO nanowires.*

SEM imaging was also used to analyze the morphology of the tubes after Eu-CeO_2 deposition and ZnO core etching. The samples were etched again if >3 at% zinc was detected after analysis through SEM-EDS.

The etched Eu-CeO_2 nanotubes were analyzed by TEM for morphology and nanotube dimensions. HRTEM was used to detect the crystalline planes and domains of the nanotubes, while EDS was used to analyze the elemental composition. To prepare the TEM sample, nanotubes delaminated during the etching procedure were suspended in DI H_2O, and 1-2 drops of the suspension added to a carbon-coated copper grid. Adhered

tubes were gentle scraped off of the substrate using a spatula. The TEM grid was subsequently brushed against the surface, picking up the loosened tubes.

5.4. Results: ZnO Nanowire Growth and Eu-CeO_2 Deposition

5.4.1. ZnO Nanowire Growth

ZnO nanowires of various dimensions were grown by submersion of the ZnO seed-coated silicon wafers in HMTA bath for 2, 5, and 7 hours. SEM images show relatively consistent nanowire morphology and diameter across the entire substrate for each sample (Figure 5.6), with a few areas with larger nanowires. The ZnO nanowire length and diameter directly correlate with the growth time, with the wire lengths and diameters increasing with reaction time. Table 5.1 details the ZnO nanorod width and length with increasing growth time, also plotted in Figure 5.8, while Figure 5.7 provides the SEM images of the cross-section and surface view of each ZnO nanowire sample.

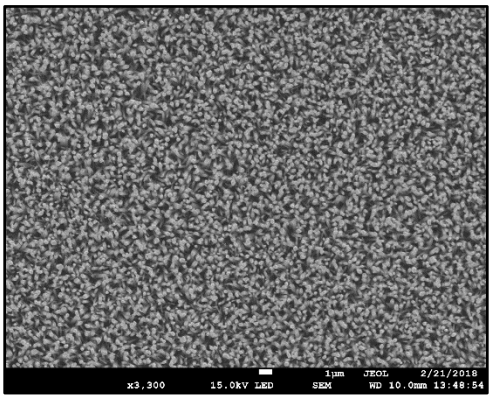

Figure 5.6 *SEM image of typical ZnO nanowire array after growth, demonstrating the even growth observed across most of the substrate.*

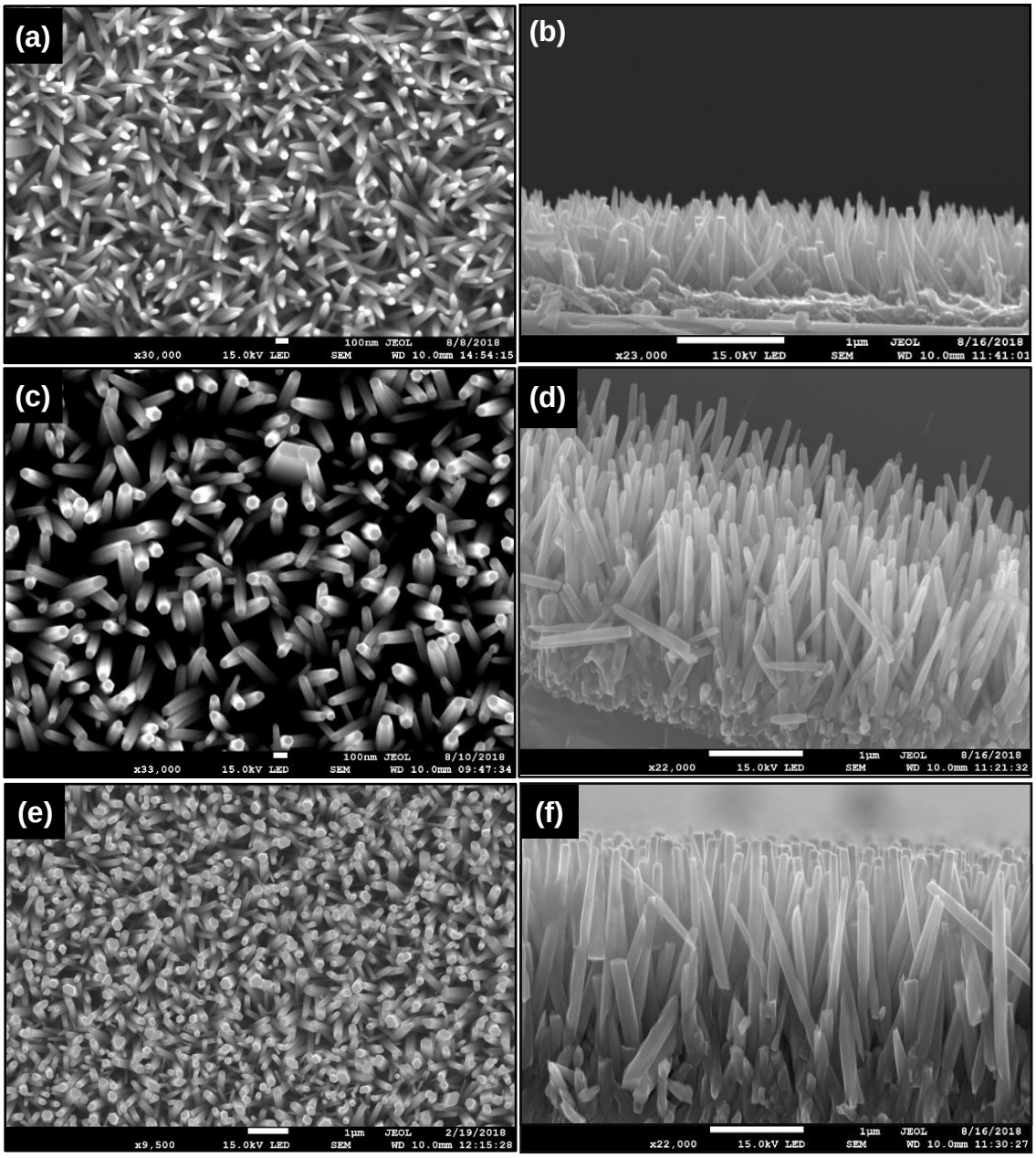

Figure 5.7 *SEM images ZnO nanowire grown for (a, b) 2hrs (c, d) 5 hours, and (e, f) 7 hours (left: plain view; right: cross-section view).*

Table 5.1 *ZnO nanowire lengths and widths as the reaction time increases from 2 hr to 7 hr.*

	2 hr	5 hr	7 hr
Width (nm)	50.5 (± 11.8) nm	82.9 (± 18) nm	218 (± 57) nm
Length (nm)	685 (± 137) nm	1068 (± 149) nm	1874 (± 240) nm

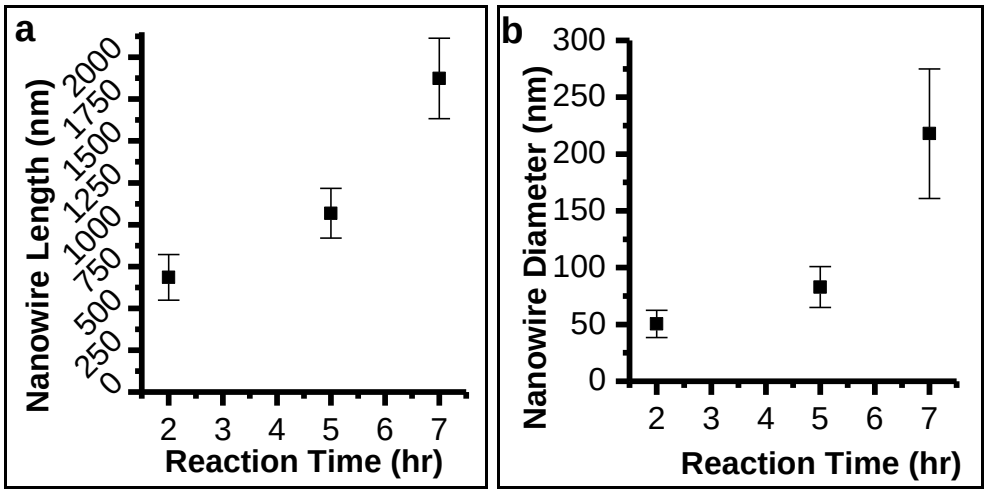

Figure 5.8 *Plots of increasing ZnO nanowire (a) length and (b) width, relative to increasing growth times.*

5.4.2. Results: Eu-CeO_2 Deposition on ZnO Nanowires

SEM images show the Eu-CeO_2/ZnO nanowires after Eu-CeO_2 deposition and prior to ZnO etching in Figure 5.9. No significant precipitates are observed, suggesting the $Ce(OH)_3$ coated only the ZnO nanowire and the washing process is sufficient to remove excess reagent. The flattened rods in Figure 5.9c are likely due to compression from tweezers.

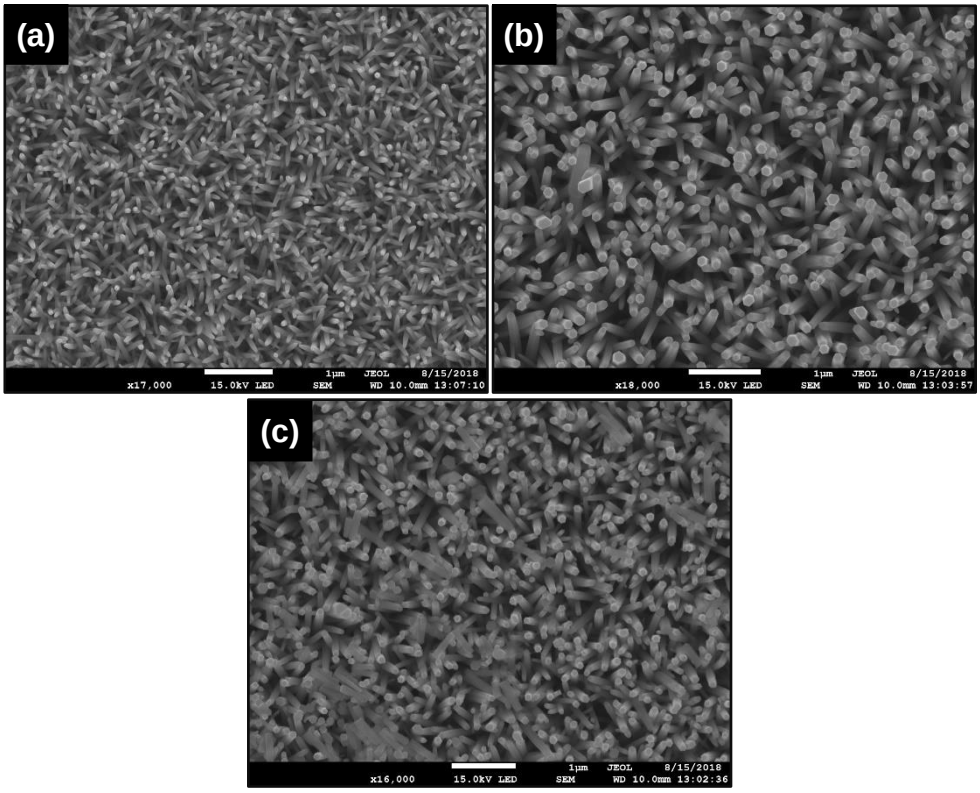

Figure 5.9 *SEM images of Eu-CeO_2/ZnO nanowires, with ZnO nanowires grown for (a) 2hr, (b) 5 hr, and (c) 7 hr.*

5.5. Results: Eu-CeO_2 Tubes Post Etch

Following etching, the vast majority of Eu-CeO_2 nanotubes delaminate, leaving the substrate mostly bare of product. Occasionally, small areas of nanotubes remain adhered, allowing SEM analysis of the etched product (Figure 5.10). Both the delaminated and attached nanotubes are washed after etching, so TEM analysis on the detached tubes was complimented by SEM imaging of the attached tubes.

A theoretical yield cannot be calculated, but silicon nanowires synthesized by the same substrates typically yield ~200 µg of nanotubes. Due to delamination, a measurable quantity of Eu-CeO_2 nanotubes has yet to be isolated.

5.5.1. Morphology: SEM imaging

Following ZnO etching, the nanotubes that remain adhered appear to be fully etched under SEM analysis, with darker cores relative to edges indicating void space within the nanotube (Figure 5.10 a-c).

Some portions of the nanotubes also partially delaminate and rotate by 90° to lie flat on the substrate. This provides a cross-section view, and shows the nanotubes extend from a larger film (Figure 5.10d). This is likely due to Eu-$Ce(OH)_3$ coating any space between the base of the ZnO nanowires.

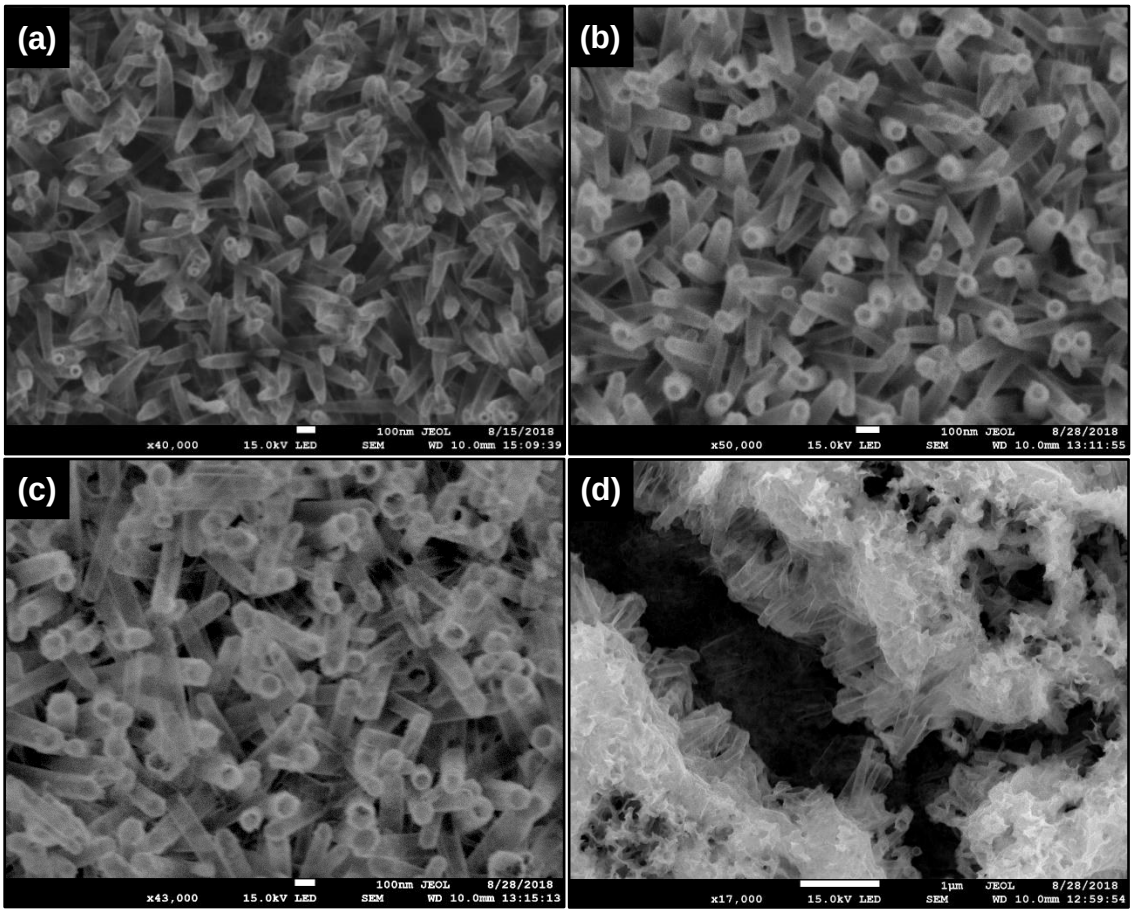

Figure 5.10 *TEM images of Eu-CeO_2 nanotubes after removing the ZnO core using 10% HCl. ZnO cores grown for (a) 2h, (b)5 hr, and (c) 7 hr. Also shown in (d) are nanotube films delaminated and rotated on the substrate.*

5.5.2. Morphology: TEM Imaging

The etched nanotubes were also analyzed by TEM imaging, facilitated by the tubes very thin walls and tendency to delaminate. TEM images allow better analysis of nanotube fracturing, non-nanotube precipitates, or extensive nanotube aggregation that may happen in solution, relative to SEM images. Furthermore, use of the nanotubes for applications such as heterogeneous catalysis or drug delivery typically require dispersion into solution.

TEM images in Figure 5.11 demonstrate the typical morphologies of the nanotubes synthesized using different sizes of ZnO templates. Most nanotubes have well defined, but thin edges, with a curved cap on one end and an opening the size of the tube inner diameter on the other end. The nanotubes form both dense aggregates (Figure 5.11b, f, i), as well as dispersed individual tubes (Figure 5.11g). Some nanotubes also exhibit long tails lacking the definition of a nanotube edge porous film-like morphology and (Figure 5.11e). Precipitates were observable in most samples, likely from shattered nanotubes or uneven precipitation around a ZnO nanowire.

The inner diameter of the Eu-CeO_2 nanotubes typically varies based on the ZnO nanowire diameter. By adjusting the template diameter from ~50 nm to ~200 nm, the nanotube inner diameter increases from ~45 nm to ~140 nm. Similarly, the nanotube length increases from ~310 nm to ~670 nm upon lengthening the ZnO nanowires from ~670 nm to 1 μm with ZnO growth times of 2 and 5 hours, respectively. 700 nm appears to be the limit for Eu-CeO_2 nanotube lengths under these conditions, as using the longer ZnO wires grown for 8 hours does not translate to longer Eu-CeO_2 nanotubes (Table 5.2).

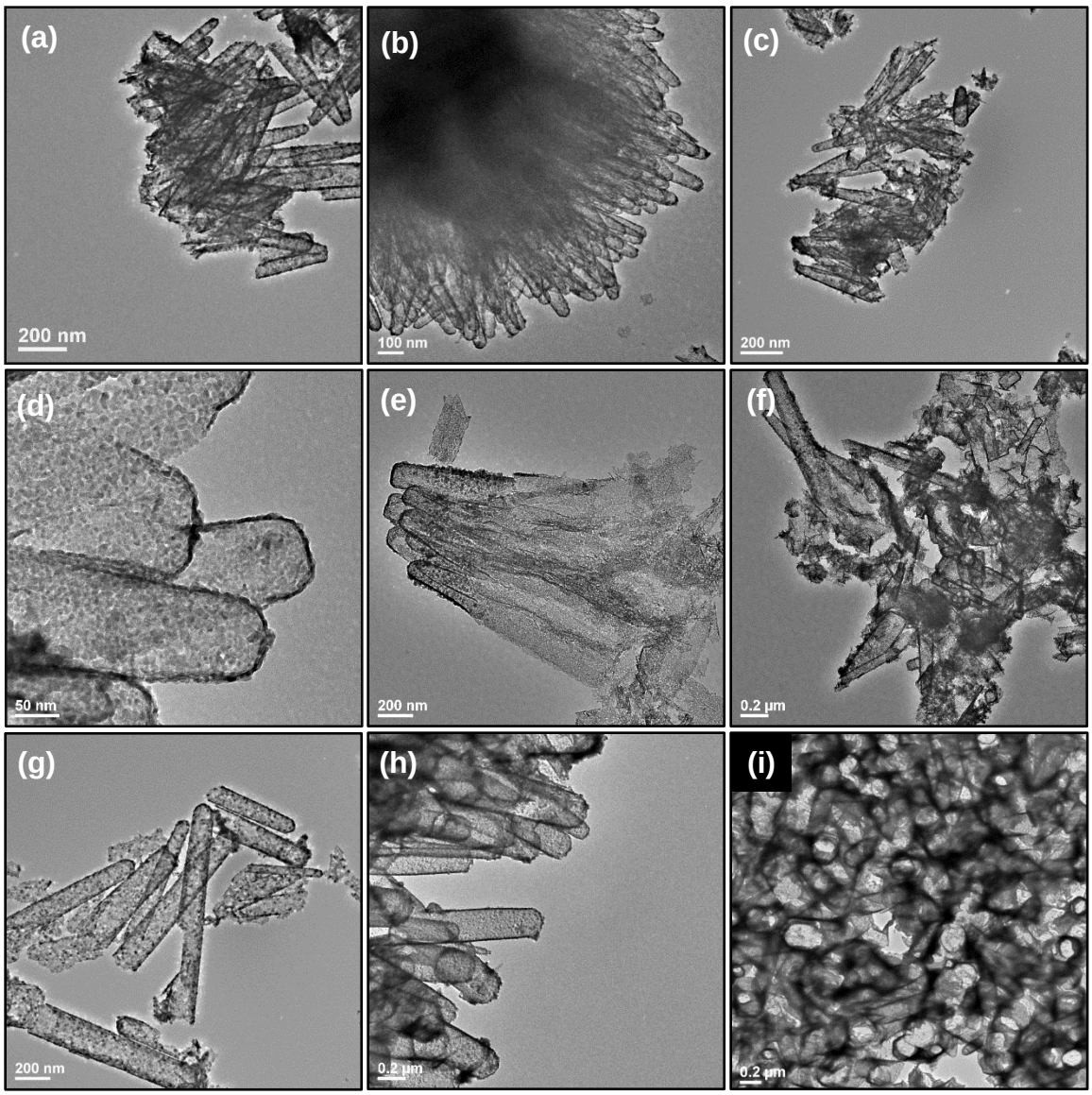

Figure 5.11 *TEM images of Eu-CeO_2 nanorods synthesized using ZnO nanowire arrays grown for (a-c) 2 hr, (d-f) 5 hr, and (g-i) 7 hr.*

The Eu-CeO_2 wall thickness increases ~8 nm to ~20 nm as the nanotube inner diameter increases from ~47 nm to ~140 nm (Table 5.2). Thick nanotube walls likely provide more structural stability than the thinner ones, which is required to stabilize large inner cavities. Therefore, large nanotubes with thin walls may disintegrate prior to TEM analysis.

Table 5.2 *Eu-CeO_2 nanotube length, inner diameter, and wall thickness as determined by TEM imaging. ZnO nanowire dimensions are included shaded in gray for comparison.*

ZnO Growth Time	2 hours	5 hours	7 hours
ZnO Width (nm)	54 (± 11)	83 (± 18)	218 (± 57)
Eu-CeO_2 Inner Diameter (nm)	47 (± 12)	83 (± 24)	139 (± 56)
ZnO Length (nm)	667 (± 135)	1012 (± 147)	1884+/-204
Eu-CeO_2 Length (nm)	311 (± 77)	669 (± 221)	673(± 328)
Eu-CeO_2 Wall thickness (nm)	8 (± 2)	16 (± 4)	20 (±6)

5.5.3. Influence of etching technique on Eu-CeO_2 Nanotube morphology

Since CeO_2 is inert to dilute acids, a simple 10% HCl etch is theoretically the simplest method to removing the ZnO core. However, this process requires several washings to remove the etched Zn^{2+}. The Eu-CeO_2 nanotubes attach to the Si substrate through the ZnO nanowires, so rapid etching and watching to remove the ZnO shell causes most of the nanotubes to delaminate. The delaminated tubes can be washed by centrifugation and decanting but this process is time consuming and likely reduces the overall yield of synthesized nanotubes.

Gas-phase etching by NH_4Cl was tested to avoid this delamination. NH_4Cl reacts with ZnO under heat to form $Zn(NH_2)Cl$, which can evaporate at elevated temperatures (Eqns. 5.1-5.3).[192] As the ZnO core is etched over several hours, with no agitation as present in a solution etch, this gas phase protocol may be less disruptive for the nanotube array.

$$NH_4Cl(s) \xrightarrow{\Delta} NH_3(g) + HCl(g) \quad \text{(Eqn 5.1)}$$

$$2HCl(g) + ZnO(s) \rightarrow ZnCl_2(s) + H_2O(g) \quad \text{(Eqn 5.2)}$$

$$ZnCl_2(s) + NH_3(g) \rightarrow Zn(NH_2)Cl(g) + HCl(g) \quad \text{(Eqn 5.3)}$$

The NH_4Cl etch was tested on Eu-CeO_2/ZnO composites using both 50 nm and 200 nm diameter ZnO nanowires. These samples can be compared to nanotubes synthesized using a similar ZnO template, but etched using HCl as discussed in Section 5.5.1 and shown in Figure 5.11a-c. While the NH_4Cl etch does still yield nanotubes, the elevated temperature significantly influences the morphology of the tubes (Figure 5.12).

The nanotube inner diameter is significantly smaller with the gas etch, ~26 nm, compared to the wet etch, ~47 nm (Table 5.3). The smaller inner cavity is likely due to sintering of the CeO_2 as the ZnO core is removed, leading to core collapse facilitated by the elevated temperature required for the NH_4Cl etch. Occasionally a second NH_4Cl etch is necessary to fully remove the ZnO core. The nanotube morphology further deteriorates under the second etch, with several nanotubes appearing to fuse (Figure 5.12c).

As discussed in Section 5.5.2, increasing the ZnO nanowire diameter from 50 nm to 200 nm increased the resultant nanotube inner diameter from ~47 nm to ~140 nm, and the nanotube wall thickness from ~8 nm to ~20 nm, when etched using HCl. The larger nanotubes were etched using NH_4Cl to probe if the thicker walls contributed any stability to the nanotube morphology, preventing the pore collapse observed in the smaller nanotubes. However, due to the larger ZnO core, two to three NH_4Cl etches are required. As seen in nanotubes using 50 nm ZnO nanowires, the repeated calcinations cause fusion and core collapse of the nanotube morphology.

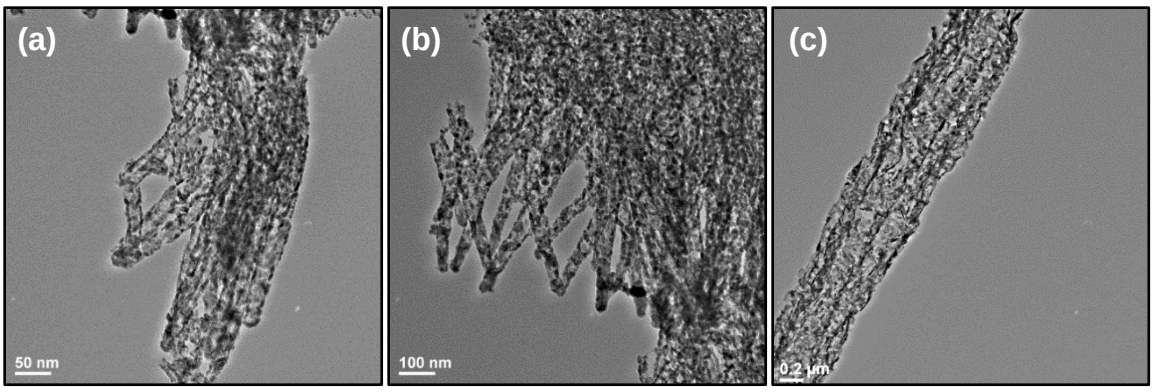

Figure 5.12 *TEM images of Eu-CeO_2 nanotubes following (a, b) one NH_4Cl etch and (c) two NH_4Cl etches.*

Despite the fused morphology, the extent of sample delamination was checked through SEM imaging. While some Eu-CeO_2 product does remain on the substrate following an NH_4Cl etch, the tubes aggregate into large clumps connected by string-like Eu-CeO_2 bundles (Figure 5.13). As a result, the NH_4Cl etch is not favorable for growth of the Eu-CeO_2 nanotubes with large inner cavities as seen with the HCl etch.

Table 5.3 *Lengths, widths, and inner diameters of Eu-CeO_2 nanotubes with ZnO etched by NH_4Cl and HCl techniques. ZnO template measurements included for comparison.*

	ZnO	**HCl**	**NH_4Cl**
Diameter (nm)	55.6 (± 20)S	47.2 (± 12.1)	26.0 (± 7.3)
Length (nm)	~670*	396 (± 140)	375 (± 92)
Eu-CeO_2 Wall thickness (nm)	-----	11.0 (± 2.7)	9.7 (± 2.1)

**The cross-section of this particular template was not analyzed, but as the diameter is consistent with samples in Section 5.4, a comparable length is also assumed.*

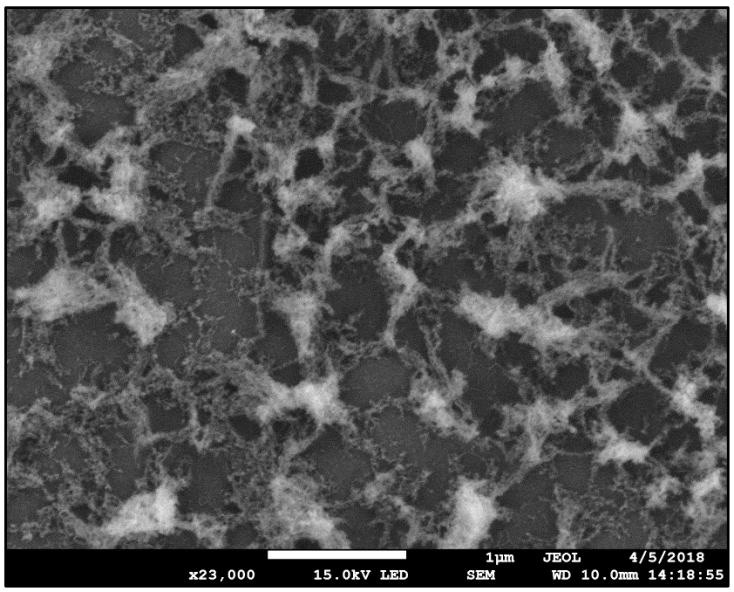

Figure 5.13 *SEM image showing the Eu-CeO_2 morphology on an Si substrate following the NH_4Cl etch.*

5.6. Results: Eu-CeO_2 Tube Crystallinity by HRTEM analysis

The low yield on the nanotubes as well as their delamination during etching prevented analysis of the samples through powder XRD. However, the samples could still be analyzed using HRTEM. As seen in Figure 5.14a, the nanotube wall is composed of small Eu-CeO_2 nanoparticles. Very small gaps, indicated by red arrows, suggest the nanotube wall is porous, which could be useful for loading and release small molecules from the nanotube.

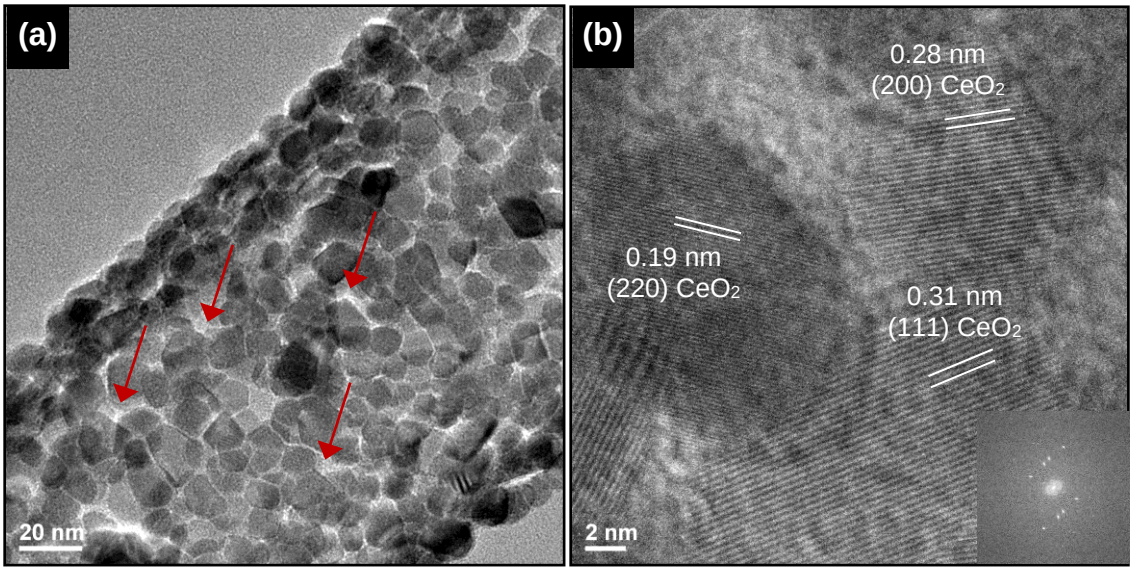

Figure 5.14 *HRTEM images of Eu-CeO_2 nanotubes showing (a) small nanoparticles fused together, with voids as indicated by red arrows, and (b) lattice spacing showing all three CeO_2 planes, with FFT inset.*

Under high magnification, lattice fringes of the individual particles indicate monocrystallinity within a single ptotal splinarticle. However, the nanotubes overall are polycrystalline, with each particle exposing different CeO_2 planes in different orientations (Figure 5.14b).

5.7. Elemental Analysis by TEM EDS

TEM EDS was utilized to analyze the elemental composition of the Eu-CeO_2 nanotubes, detect any contamination, and check the completeness of the ZnO etch. The EDS spectra for etched nanotubes indicates a zinc contamination below 3 at%, and typically around 1 at%. Any samples with a zinc concentration above 3% were considered incompletely etched and processed through a second HCl etch and wash prior to reanalysis. Other than zinc, the EDS spectra did not indicate any contamination, with only peaks due to oxygen, cerium, europium, and zinc observed (Table 5.4), with copper due to the sample holder (Figure 5.15).

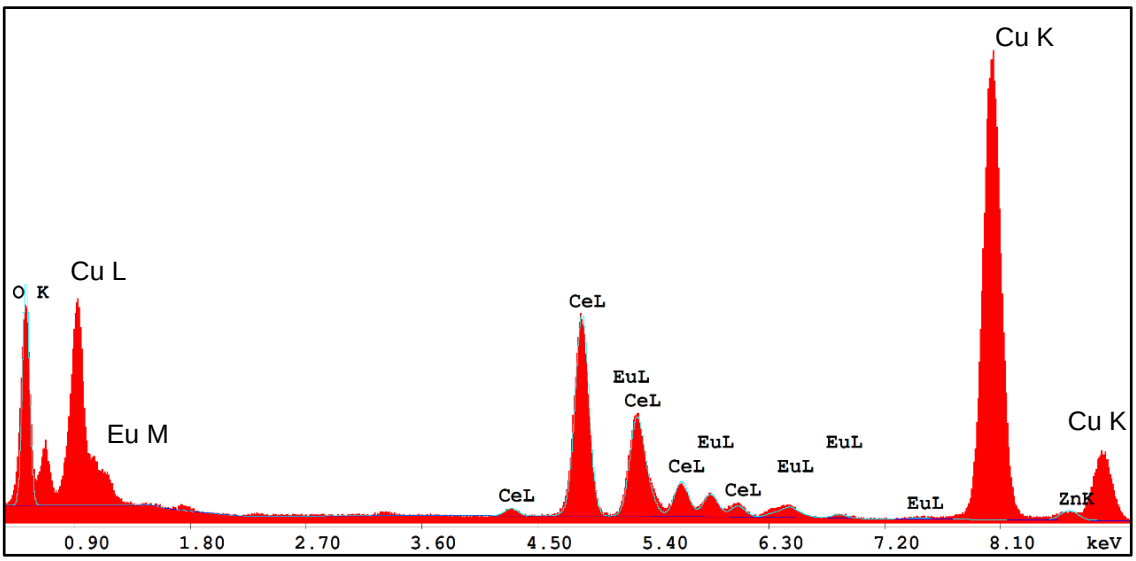

Figure 5.15 *Typical EDS spectrum for an etched Eu-CeO_2 nanotube, with only the expected elements observed.*

Table 5.4 *Elemental composition of etched Eu-CeO_2 nanotube as calculated by TEM EDS both with and without zinc.*

	At% O	At% Ce	At% Eu	At% Zn
Without Zn	57.6	37.9	4.5	---
With Zn	56.7	37.4	4.5	1.4

The nanotubes were also analyzed using EDS line scan mode to confirm the nanotube morphology. The two peaks in Figure 5.16b indicate the edges of the nanotube, where the nanotube curvature increased the signal intensity due to sample thickness. The lower intensity between the two peaks is consistent with thin nanotube walls between two edges.

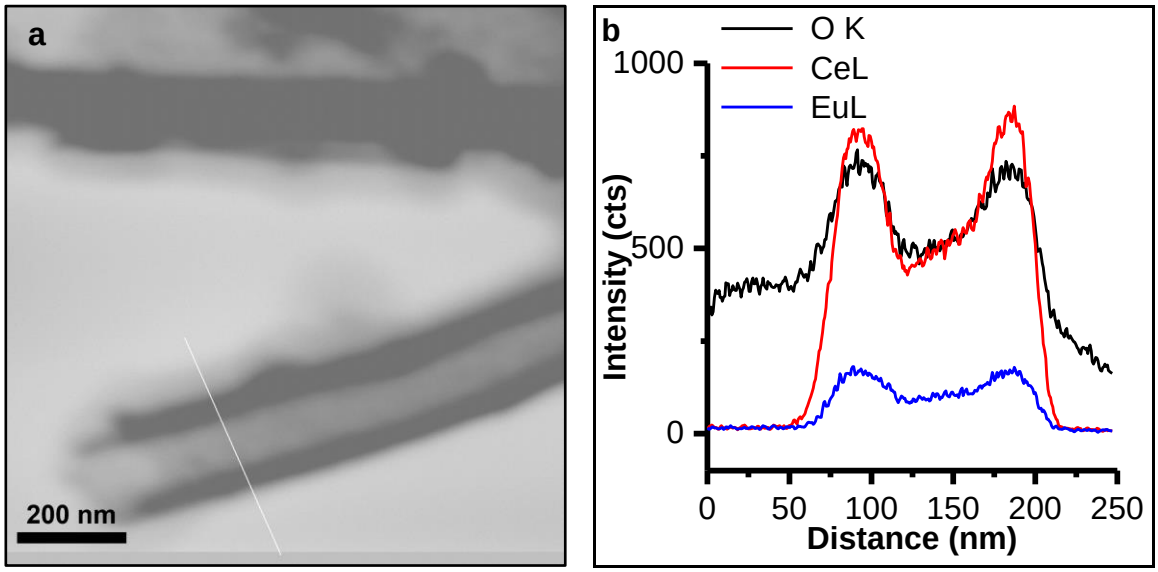

Figure 5.16 *Line scan for Eu-CeO_2 from an 8-hour ZnO growth with (a) STEM image of nanotube with line scan in white, and (b)intensity of O, Ce, and Eu across the nanotube.*

5.8. Conclusions

In this chapter, Eu-CeO_2 nanotubes were synthesized through repeated deposition of Ce^{3+}/Eu^{3+} and OH^- on a sacrificial ZnO nanowire template. The dimensions of the nanotubes were easily controlled by the ZnO core as manipulated by the ZnO nanowire growth time.

An increase in approximate ZnO nanowire diameter from 50 nm to 200 nm produced Eu-CeO_2 nanotubes with approximate inner diameters of 50 nm to 150 nm. The Eu-CeO_2 nanotube wall thickness increases from ~8 nm to ~ 20 nm with this increase in inner diameter, as thick walls are likely necessary to stabilize the larger nanotubes. Increasing the template wire length from about 670 nm to about 1000 nm also increased the nanotube length from about 300 nm to about 670 nm.

A persistent problem is nanotube delamination during etching, so two etching techniques were evaluated for their influence on nanotube morphology and delamination.

The Eu-CeO_2 product did remain on the substrate following the NH_4Cl etch, but with significant fusion and loss of the desire nanotube morphology. Therefore, HCl is the better etching approach of the two, with ongoing efforts focusing on minimization of delamination.

The produced Eu-CeO_2 nanotubes were comprised of small, monocrystalline crystallites, fused together with numerous voids. As a result, the nanotubes were polycrystalline with the desired high surface area. Elemental analysis indicated nearly complete removal of the ZnO core, as only a trace of Zn remained after etching. The nanotubes are doped with Eu^{3+}, as determined by EDS although XRD analysis is necessary to confirm Eu^{3+} incorporation into the CeO_2 lattice.

This approach to a CeO_2-based nanotube morphology does have a relatively poor yield given the time required for synthesis, exacerbated partially due to the delamination complication. Due to the limited sample availability, the Eu-CeO_2 nanotubes are not included in the discussion of Eu^{3+} fluorescence of Chapter 6, or in the discussion of the Eu-CeO_2 interaction with L-Dopa in Chapter 7. Future efforts should focus on both improving the yield and reducing the processing time per substrate.

Despite the low yield, this work represents the first synthesis of Eu-CeO_2 nanotubes. The manipulation of nanotube dimensions by changing the ZnO nanowire template allows synthesis of nanotubes with sub-micron lengths, but with large inner diameters not typically seen in most previous CeO_2 nanotube methods. No attempt has been made yet to synthesize Eu-CeO_2 tubes using ZnO nanowires with diameters less than 50 nm or lengths less than 500 nm, so even smaller nanotubes may be possible. The large nanotube cavity, coupled with the high surface area, porous nature, and potential

fluorescence from Eu^{3+} make this morphology promising for catalysis or for loading with drugs for biological applications.

Chapter 6: Fluorescence of Rare earth-doped CeO_2 Nanomaterials

6.1. Overview

The first five chapters of this dissertation discussed the synthesis of several europium-doped cerium oxide (Eu-CeO_2) nanomaterial morphologies. In Chapter 6, the differences in the Eu^{3+} fluorescence associated with these various CeO_2 host morphologies are discussed. The mechanisms controlling the fluorescence suppression and activation in the nanorod morphology are also discussed. Finally, several rare earth-doped CeO_2 nanocubes were synthesized and analyzed for visible or near infrared (NIR) fluorescence.

The Eu^{3+} fluorescence is strongly influenced by the surrounding crystal structure, due to the symmetry-sensitive nature of select Eu^{3+} fluorescent transitions.[198] Europium fluorescence within a CeO_2 host has been previously investigated, with the nanoparticle morphology most thoroughly studied.[120,199-202] As mentioned in Chapter 4, Eu-CeO_2 nanowires/nanoribbons have been synthesized with varying Eu^{3+} concentrations. Increasing the concentration of Eu^{3+} initially intensified the Eu^{3+} fluorescence up to a concentration of 0.62 Eu at %, after which the fluorescence was quenched.[203]

Eu-CeO_2 annealed nanorods have previously been investigated as possible sensors, with the Eu^{3+} fluorescence quenched through reduction of the surface Ce^{4+} by ascorbic acid.[122] This emission is proposed to proceed through excitation of the CeO_2 host by the $O^{2-} \rightarrow Ce^{4+}$ charge transfer, followed by nonradiative relaxation and energy transfer to the Eu^{3+} dopants.[202] The reduction of Ce^{4+} to Ce^{3+} by ascorbic acid was suggested to minimize the excitation of this charge transfer band, suppressing fluorescence.[122] These rods were synthesized at a much higher pH, which may influence the oxidation of Ce^{3+} to Ce^{4+} during the hydrothermal reaction.

While Eu-CeO_2 nanocubes have been synthesized,[131] no data is available on their fluorescence, nor has there been any comparison in this particular property between the nanorods, nanocubes, nanowires, or annealed nanorods described in Chapters 2-4.

Out of the discussed morphologies, the CeO_2 nanocubes were evaluated as hosts for other fluorescent rare earth dopants due to strong fluorescence from Eu-CeO_2 nanocubes, their small dimensions, and the high synthetic yield relative to the other morphologies. Rare earth ions fluorescing in the NIR have promise in bioimaging, as light in the NIR region has improved transmission and therefore greater penetration within biological tissues relative to light in the UV-VIS range.[70] Four of the rare earth ions gave either visible or near-IR fluorescence in the CeO_2 nanocube host: neodymium (Nd^{3+}), ytterbium (Yb^{3+}), erbium (Er^{3+}), and samarium (Sm^{3+}).

6.2. Introduction

6.2.1. Theory of Fluorescence

Prior to fluorescent emission of light, a molecular or material must first absorb a photon and promote an electron into an excited state. The lattice first relaxes through vibrational energy levels within the excited state, releasing energy through non-radiative relaxation. The electron then relaxes back to the original energy state, releasing a photon lower in energy than the absorbed photon as shown in Figure 6.1.[204]

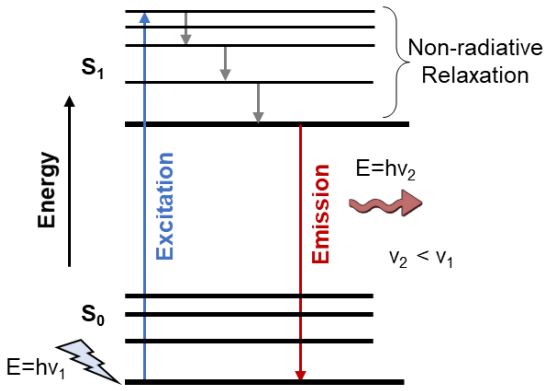

Figure 6.1 *Simplified diagram showing the electron excitation from S_0 to S_1, vibrational non-radiative relaxation within S_1, and emission of energy through fluorescence.*

6.2.2. CeO_2 Fluorescence

Ce^{4+} is isoelectronic with Xenon with no 4f or 5d electrons available for 4f-4f or 5d-4f fluorescent transitions. Upon forming the CeO_2 crystal, Ce^{4+} has demonstrated a strong $O_{2p} \rightarrow Ce_{4f}$ ligand-to-metal charge transfer (LMCT) process.[205] Due to this transition, most CeO_2 materials have a broad and strong absorbance between 300 and 400 nm.[32] As this transition is located in the UV region and is the only transition available to Ce^{4+} within the CeO_2 lattice, most CeO_2 nanomaterials are not intrinsically fluorescent in the visible region.

The presence of Ce^{3+} defects within the crystal structure has been suggested to contribute visible fluorescence to CeO_2. First, Ce^{3+} does have the electron configuration of $[Xe]6s^0 5d^0 4f^1$, and therefore has 4f-4f and 4f-5d transitions available for fluorescence.[80] More importantly, the presence of Ce^{3+} within a CeO_2 lattice produces defects that have energies within the CeO_2 band gap[33,132,206] Therefore, these sites can absorb and emit light at lower energies compared to the $O_{2p} \rightarrow Ce_{4f}$ charge transfer transition.

The energy level of the defects is partially influenced by the concentration and distribution of defects within the CeO_2 lattice.[201] For instance, reducing the CeO_2 particle size increases the Ce^{3+} defect concentration, as discussed in Chapter 1.[14,134] The Ce^{3+} ions and corresponding oxygen vacancies create trap sites in the band gap of small CeO_2 nanoparticles, introducing lower energy transitions relative to the $O_{2p} \rightarrow Ce_{4f}$ charge transfer and red-shifting the fluorescence into the visible region.[33]

Furthermore, the variety of Ce^{3+}, and oxygen defects of different geometries results in trap sites of varying energy.[32] As the wavelength of incident light increases, the excited electron is limited to lower-energy trap sites. Therefore, one nanoparticle sample could emit at multiple wavelengths by exciting into different energy defect sites (Figure 6.2). However, traps frequently serve as sites of non-radiative relaxation, which may significantly weaken the emission intensity of associated fluorescence.[207]

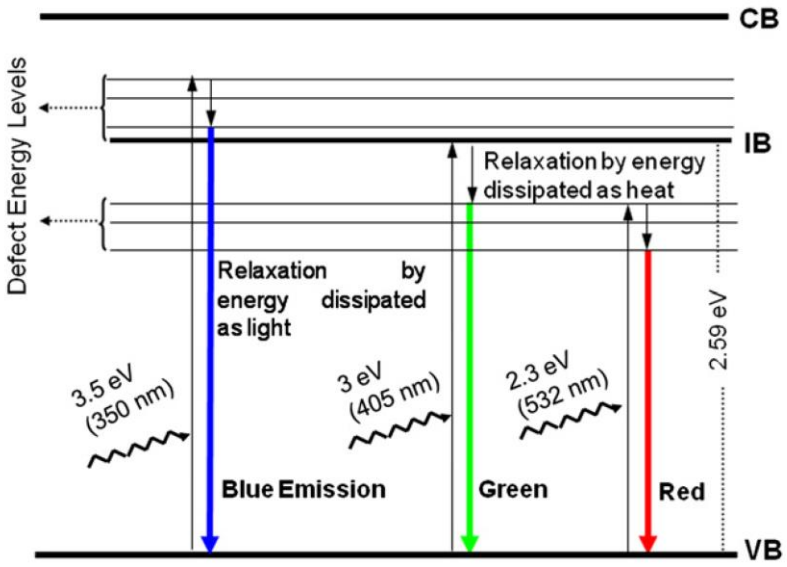

Figure 6.2 *Diagram of reported CeO_2 nanoparticle emission facilitated by defects in the CeO_2 crystal lattice. Lower energy excitations pump into lower energy trap sites and subsequently red-shifted fluorescence.*[32]

None of the materials synthesized in Chapters 2-5 exhibited intrinsic visible fluorescence as undoped CeO_2. Therefore, the materials were doped with other emissive rare earth ions with visible fluorescence.

6.2.3. Russell Saunders Terms

Russell Saunders term symbols are frequently used to facilitate clear descriptions of electronic energy states and optical transitions. These terms are written as $^{2S+1}L_J$, where L is the total orbital angular momentum, S is the total spin angular momentum, and J is the total angular momentum.[208] The term symbol describes the overall electron configuration for one specific energy state.

For example, Eu^{3+} has an electron configuration of $[Xe]4f^6$. In the ground state, Eu^{3+} has 6 unpaired electrons, giving it a total spin angular momentum of 3, a spin multiplicity (2S+1) of 7, a total orbital angular momentum of 3 (notated as “F”), and a total angular momentum of 0. Therefore, the ground term symbol of Eu^{3+} is $^7F_0$. The relaxation from the first excited state with two paired electrons, $^5D_0$, to the ground state is written $^5D_0 \rightarrow {}^7F_0$.

6.2.4. Rare Earth Fluorescence

With a few exceptions, rare earths or lanthanides typically oxidize to the trivalent charge, Ln^{3+}, with electron configurations of $[Xe]6s^04f^x$ (x=0-14). The Ln^{3+} free ions have well-defined energy levels (Figure 6.3), but undergo additional splitting from coulombic splitting, spin orbital coupling, and finally splitting due to the crystal field or Stark splitting, similar to the splitting seen in transition metal d-orbitals Figure 6.4.[80] As a result, all of the Ln^{3+} ions have at least one potential transition available for fluorescence, with the emission spanning from the UV to the IR.

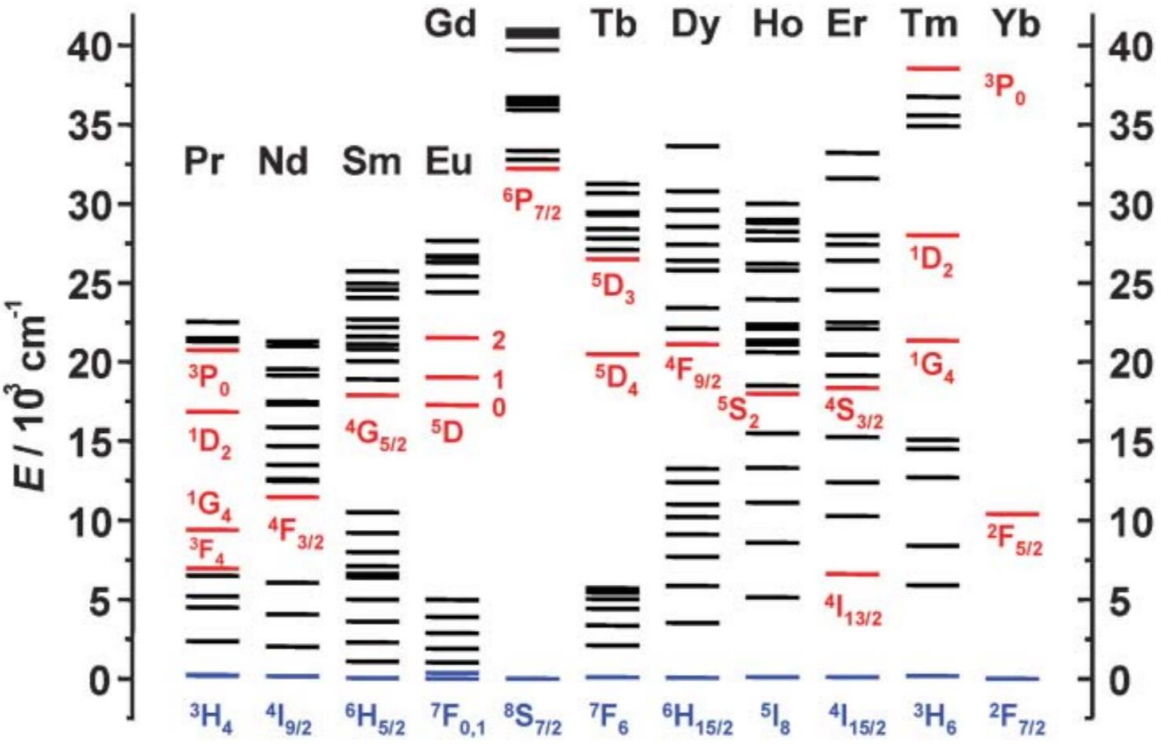

Figure 6.3 *Energy diagram of the energy levels of hydrated Ln^{3+} ions. Ground state levels highlighted in blue, while main luminescent levels are in red.*[209]

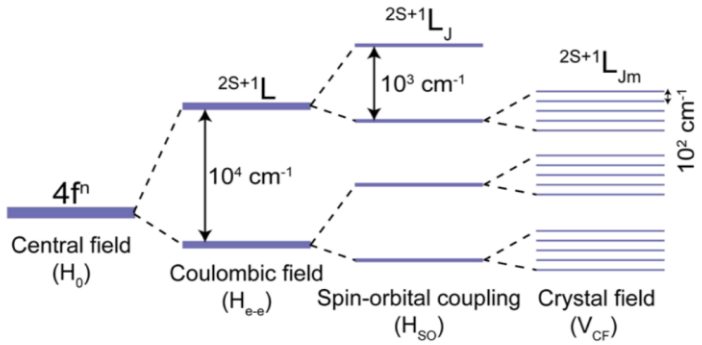

Figure 6.4 *Simplified diagram of the splitting of a general Ln^{3+} orbital.*[210]

The lanthanides can be optically active through 4f-4f and 4f-5d transitions, as well as through charge transfer between the metal and a ligand as seen with Ce^{4+}.[80] The 4f-4f transition emission is very sharp, while the other two transitions typically have broader

signals. The 4f-5d transitions are usually higher energy relative to the other two, often optically active in the UV or deep UV region, and are not discussed in this work.[80]

The 4f-4f transitions can be categorized as either magnetic dipole (MD) or electronic dipole (ED) transitions, based on which part of the electromagnetic wave the excited atom interacts with.[211] Laporte selection rules as applied to atoms or molecules with an inversion center forbid electronic transitions which maintain symmetry, including 4f-4f ED transitions.

Within a crystal field, the excited states often mix with empty 5d orbitals of opposite parity, breaking the symmetry to allow the transition. The ion is then able to absorb or emit through the ED transition, frequently at similar intensities as the MD transitions.[212]

6.2.5. CeO_2 as a host for Ln^{3+}

Since the Ln^{3+} f-f transitions are forbidden, fluorescence following direct excitation of Ln^{3+} is often very weak due to poor absorption.[213] Rare earth ions have been doped into a number of crystalline structures, host-to-Ln^{3+} energy transfer to overcome the poor absorbance and subsequently enhancing the fluorescence.[70,214] Doping Ln^{3+} ions into a host also protects the ions from quenching by the surrounding environment.

CeO_2 has been used to host several other rare earths to enhance their fluorescence.[215-218] The intense and broad charge transfer from O_{2p} to Ce_{4f} is efficient in transferring energy from the CeO_2 host to the excited energy level of the doped Ln^{3+}.[219]

6.2.6. Eu^{3+} and Hypersensitive Fluorescence

Most, but not all, of the Ln^{3+} ions have ED transitions that are particularly sensitive to the symmetry of their environments due to their dependence on the breaking of symmetry.

These transitions, frequently called *hypersensitive transitions*, can provide insight to their local environment, as the emission is quenched in more symmetrical environments.[220]

The $^5D_0 \rightarrow {}^7F_1$ transition is a MD transition, and therefore is insensitive to the local environment.[198] However, the $^5D_0 \rightarrow {}^7F_2$ transition is a *hypersensitive* ED transition, and is significantly suppressed in highly symmetric environments. The use of the *asymmetry ratio* (Eqn 6.1), a comparison of the integrated area of the two transitions, is well established and frequently used in structural analysis of Eu^{3+}-containing systems. Higher R_{21} values correspond with insertion of the Eu^{3+} ion into more asymmetric structures. The inverse is also typically accepted: low R_{21} values suggest more symmetric environments around the Eu^{3+} site.

$$R_{21} = \frac{I_{^5D_0 \rightarrow {}^7F_2}}{I_{^5D_0 \rightarrow {}^7F_1}} \qquad \text{(Eqn 6.1)}$$

6.2.7. Eu-CeO_2 Fluorescence

Eu^{3+} has been doped into several CeO_2 materials, including particles,[199] wires,[203] and cubes.[131] The europium ions typically substitute into the Ce^{4+} site within the cubic fluorite CeO_2 crystal structure[201] and are theoretically surrounded by oxygen anions in an octahedral geometry.[221] This highly symmetrical environment around the Eu^{3+} atom suppresses the $^5D_0 \rightarrow {}^7F_2$ transition, in turn lowering the R_{21} ratio. Disruption of the CeO_2 lattice by Ce^{3+} or oxygen vacancies removes the inversion symmetry about the Eu^{3+} centers, allowing fluorescence through the hypersensitive peak and increasing the asymmetry ratio.[222] An example of oxygen vacancies breaking the inversion symmetry about the Eu^{3+} is illustrated in Figure 6.5b, while Figure 6.5c shows asymmetry from a Ce^{4+}-Eu^{3+}-Ce^{3+} system.

Eu-CeO_2 systems are prone to quench Eu^{3+} fluorescence through non-radiative relaxation. The oxygen vacancies within CeO_2 can also quench the Eu^{3+} fluorescence from Eu-CeO_2 nanomaterials, as discussed by Kumar *et al*.[199] Surface hydroxyls in particular have been indicated as fluorescence quenchers, partially due to their presence coating the surface of nanomaterials.[25]

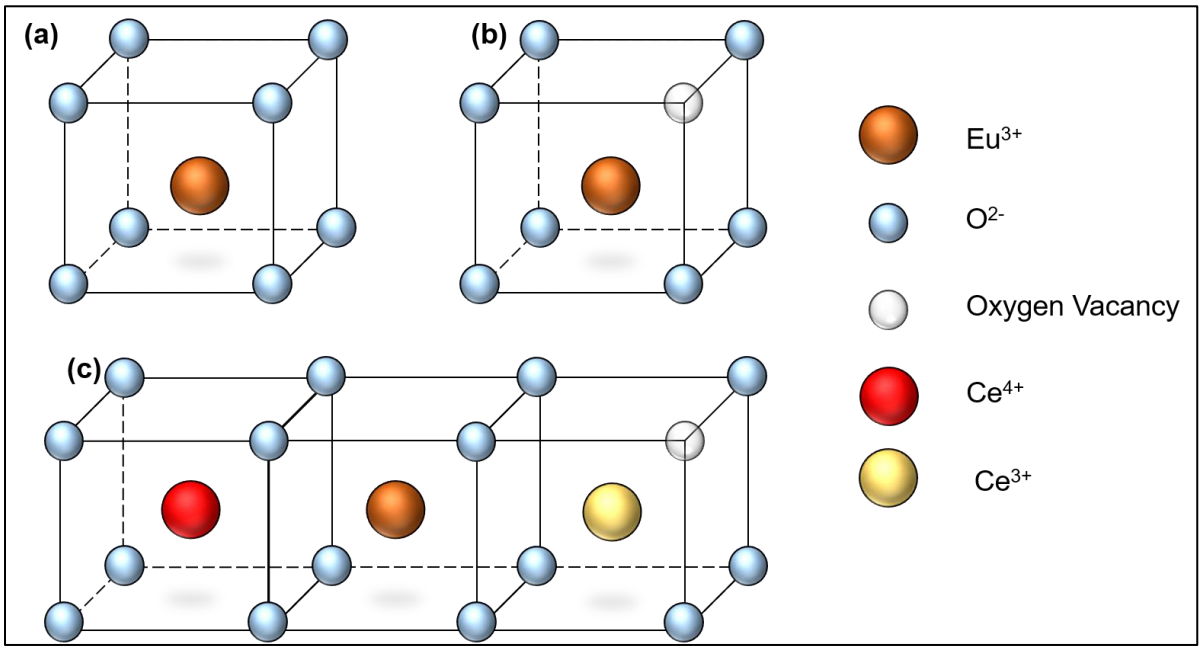

Figure 6.5 *Illustration of various Eu^{3+} environments, including (a) Eu^{3+} in perfect O_h symmetry, (b) Eu^{3+} with asymmetry from O^{2-} vacancy, and (c) Eu^{3+} with asymmetry from Ce^{3+} defect sites. Adapted from Reference [119].*

Finally, in addition to sensitivity in transition intensity, the Eu^{3+} $^5D_0 \rightarrow {}^7F_2$ and $^5D_0 \rightarrow {}^7F_2$ peaks can split. The $^5D_0 \rightarrow {}^7F_1$ transition at 590 nm typically remains a single peak within cubic structures, splitting into more peaks within other crystal structures.[198] The $^5D_0 \rightarrow {}^7F_2$ transition can also split, indicating multiple structural environments, although thorough quantification of this splitting is complicated and still under investigation.[119]

6.3. Methods and Materials

6.3.1. Materials

All chemicals purchased were analytical grade and used as purchased with no further purification.

Neodymium nitrate hexahydrate ($Nd(NO_3)\bullet 6H_2O$), erbium nitrate pentahydrate ($Er(NO_3)_3\bullet 5H_2O$), gadolinium chloride hexahydrate ($GdCl_3\bullet 6H_2O$), and samarium nitrate hexahydrate ($Sm(NO_3)_3\bullet 6H_2O$) were purchased from Sigma Aldrich. Praseodymium nitrate hexahydrate ($Pr(NO_3)_3\bullet 6H_2O$) was purchased from GTI Laboratory Supplies. Holmium nitrate hexahydrate ($Ho(NO_3)_3\bullet 6H_2O$) and thullium acetate tetrahydrate ($Tm(C_2H_3O_2)_3\bullet 4H_2O$) were purchased from Chem Craft. Ytterbium nitrate pentahydrate ($Yb(NO_3)_3)\bullet 6H_2O$) was purchased from Ventron.

All Eu-CeO_2 materials were synthesized as described in Chapters 2, 3, and 4.

6.3.2. Synthesis and Morphological Characterization of Ln-CeO_2

Ln-CeO_2 nanocubes were synthesized by minor modifications of the procedure detailed in Chapter 3. Briefly, 0.4 g $Ce(NO_3)_3$ was dissolved in 6.6 mL H_2O, with the appropriate rare earth salt added in 1 at% to 10 at% Ln^{3+} concentrations, as defined in Equation 6.2. This solution was reacted with 13.3 mL of 15 M NaOH to give final concentrations of 46 mM Ce^{3+}, 0.46-4.6 mM Ln^{3+}, and 10 M OH^- respectively. The reaction mixture was rapidly stirred in an iced acetone bath at 0 °C for 20 minutes, transferred to a 20 mL stainless steel-coated Teflon vessel, and heated at 180 °C for 16 hours. After allowing the reactor to cool naturally, samples were washed with water, dried

and ground into a powder. No parameters other than the rare earth concentration were manipulated.

The Ln^{3+} concentration within the CeO_2 materials within this chapter is described using the convention established in Chapter, *Section 2.3.2,* and is restated as Equation 6.2. Briefly, the theoretical %Ln of a material is calculated using the molar concentrations of the precursor metals salts. The atomic %Ln of a synthesized material is experimentally determined using the cerium and europium atomic percentages as detected by EDS.

$$\%Ln = \frac{mM\ Ln^{3+}}{mM\ Ln^{3+} + mM\ Ce^{3+}} = \frac{at\%\ Ln}{at\%\ Ln + at\%\ Ce} \qquad \text{(Eqn 6.2)}$$

Fluorescent nanocubes were analyzed by TEM, HRTEM, and EDS as described in Chapter 2. The morphology and elemental composition of non-fluorescent samples was not investigated.

6.3.3. Dry Powder Fluorescence Measurements and Imaging

The Eu-CeO_2 nanomaterials were excited at a wavelength of 370 nm using a mercury lamp equipped with a ±5 nm bandpass filter. Fluorescence images were taken on a Nikon fluorescence microscope and fluorescence spectra was recorded by an Ocean Optics spectrometer interfaced to the above microscope. Fluorescence was acquired with a 100 ms integration time, unless otherwise noted.

6.3.4. UV-Vis absorbance and visible fluorescence measurements

UV-VIS spectra were collected using an Agilent Technologies Cary 60 UV-Vis spectrometer in the range from 800 nm to 200 nm. Fluorescence spectra were collected

on a Shimadzu RF-5301PC Spectrofluorometer, with excitation at 375 nm, measuring emission from 400 nm to 700 nm, and using slit widths of 5 mm.

Three mg of 8 at% Eu-CeO_2 nanocubes were suspended in 5 mL of DI H_2O to make a stock solution. The stock solution was diluted until the peak absorbance was below 1.4. The diluted solution (400 µL stock + 5 mL DI H_2O) had a nanocube concentration of 44 µg CeO_2/mL and was used to analyze the UV-Vis absorbance and visible fluorescence of all suspended nanocubes.

6.3.5. NIR fluorescence and UV-VIS-NIR Fluorescence Mapping

All excitation-emission mapping, as well as near-IR fluorescence data was collected on a Horiba Nanolog using 80 µg/mL solutions of doped CeO_2 nanocubes. Emission spectra for NIR-emitting cubes was measured between 900 and 1600 nm, with excitation wavelengths from 340 nm to 700 nm and monochromator slit widths of 14.5 mm.

2-D mapping experiments of the NIR-emitting cubes (Nd-CeO_2 and Yb-CeO_2) varied the excitation wavelength from 330 nm to 700 nm. Emission was measured from 900 nm to 1600 nm with 14.5 nm slit widths for NIR-emitting cubes. The excitation wavelength was measured in 15 nm increments with 100 s integration time.

2-D mapping experiments of the visible-emitting Sm-CeO_2 nanocubes scanned excitation wavelengths at a 5 nm increments from 350 nm to 500 nm. Emission was measured from 530 nm to 645 nm, with an integration time of 0.4 s per 5 nm excitation increment.

6.4. Results: Eu^{3+}-associated fluorescence

6.4.1. Fluorescence of 8% Eu-CeO_2 nanomaterials

~8 at% Eu-CeO_2 nanorods, annealed nanorods, nanocubes, and nanowires as determined by EDS analysis were analyzed for Eu^{3+} fluorescence using a mercury light source with a bandpass filter centered at 370 nm.

While the emission spectrum of the unannealed nanorods does exhibit peaks matching Eu^{3+} fluorescence, the intensity of the unannealed nanorod emission is less than 1% of the other materials. (Figure 6.6) The activation of fluorescence in the nanorods will be discussed further in Section 6.4.3.

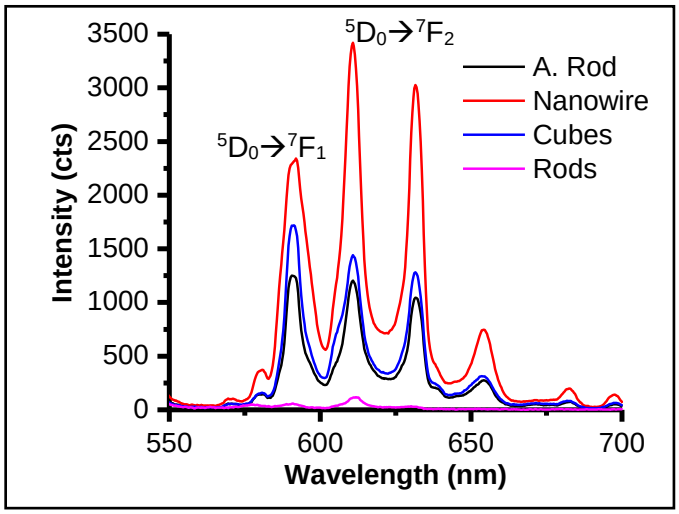

Figure 6.6. *Fluorescence spectra of Eu-CeO_2 nanomaterials upon excitation at 375 nm. Acquisition time for rods was 400 ms.*

The nanocubes, nanowires, and annealed nanorods all display strong red fluorescence (Figure 6.7b-c), associated with emission through three dominant emission peaks which match previously reported Eu^{3+} fluorescence of Eu-CeO_2 materials (Figure 6.6). The peak at 590 nm can be assigned to the $^5D_0 \rightarrow {}^7F_1$ MD transition, while 610 nm and 630 nm originate from the $^5D_0 \rightarrow {}^7F_2$ ED transition.[122,199] These three peaks are

consistently present throughout most of the Eu^{3+} fluorescent samples, except low %Eu nanowires and nanocubes as discussed in Sections 6.4.2 and 6.4.4.

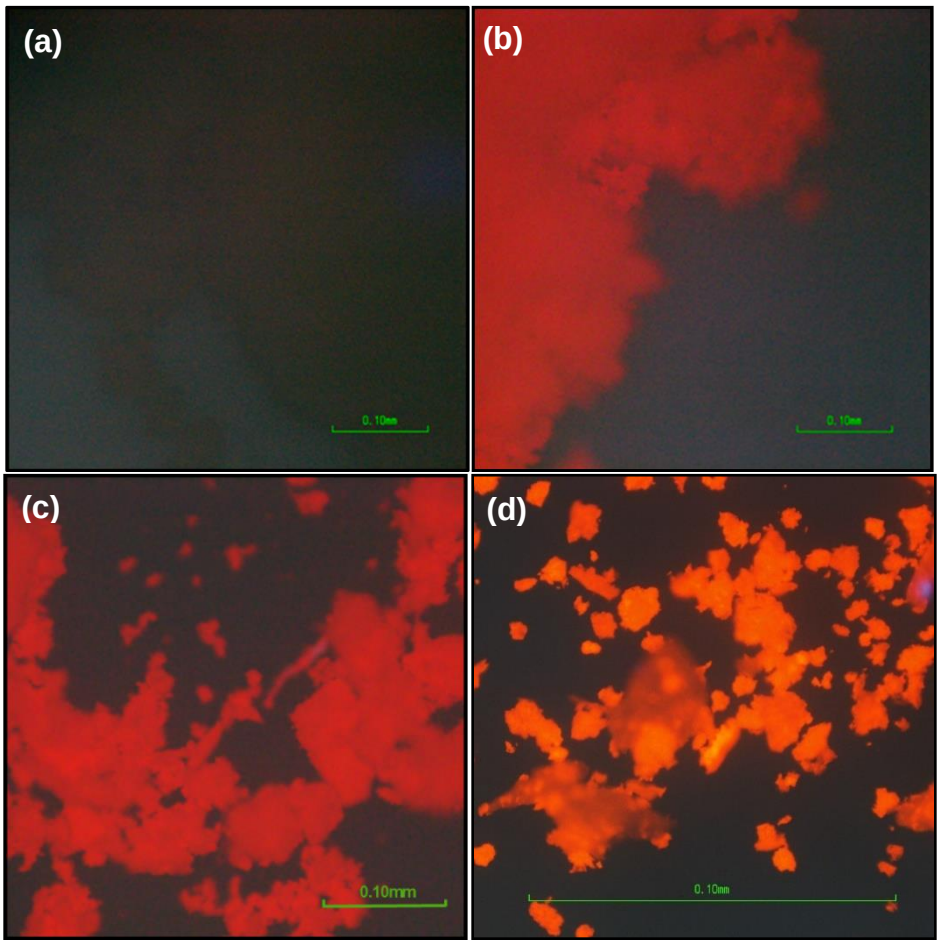

Figure 6.7 *Visual fluorescence with λ_{ex}=370 nm of 8% Eu-CeO_2 (a) nanorods, (b) annealed nanorods, (c) nanocubes, and (d) nanowires (orange tint is an artifact of white balance on camera).*

The asymmetry ratios of the nanomaterials were calculated using the spectra in Figure 6.6 and are summarized in Table 6.1. The unannealed nanorods had a significantly higher asymmetry ratio of 2.5, although this value may have significant error due to the nanorod's very weak fluorescence intensity.

Table 6.1 *Calculated asymmetry ratios for 8% Eu-CeO_2 nanomaterials.*

	Annealed Nanorod	Nanowires	Nanocubes	Nanorods
Asymmetry Ratio	1.97	2.15	1.82	2.54

The other three materials had ratios ranging from 2.15 to 1.82, with higher asymmetry exhibited in the annealed nanomaterials than the nanocubes. This may be due to the nanocube's larger crystalline domain size (~22 nm), compared to the annealed materials size (~16 nm). Crystal edges have more vacancies and defects than the bulk crystal structure, due to the termination of the lattice.[121] Therefore, Eu^{3+} ions near a crystal surface are in more asymmetric environments than ions in the bulk. Due to the larger domains in nanocubes, Eu^{3+} ions are less likely to be near the crystal edge and more likely to be in sites of higher symmetry, decreasing the asymmetry ratio relative to the annealed morphologies.

6.4.2. Eu^{3+} fluorescence in Eu-CeO_2 Nanowires

As Fang *et al.* discussed, the fluorescence from Eu-CeO_2 nanowires with low Eu^{3+} concentration is dominated by the MD transition at 590 nm and very weak emission through the hypersensitive transition at 600 and 630 nm.[203] Increasing the Eu^{3+} concentration gradually increased the emission intensity at 600 nm and 630 nm. While Eu^{3+} initially substitutes into the symmetric Ce^{4+} site (Figure 6.5a), oxygen vacancies and Ce^{3+} concentrations increase with increasing Eu^{3+}. As shown in Figure 6.5b and c, these defects break the inversion about the Eu^{3+} site, increasing the asymmetry around the emitting atom, and allowing fluorescence through the hypersensitive transition.[119] In the experiments described in this section, Eu-CeO_2 nanowires were synthesized with 100 nm

diameters as described in Chapter 4, with the theoretical at% Eu varying from 0.0% to 14.4 % Eu.

Slight contamination in the 0% Eu-CeO_2 nanowires introduces very weak fluorescence and fluorescence imaging shown Figure 6.8a suggests only random nanofibers contain emissive Eu^{3+}. Further increasing the Eu^{3+} concentration to 4.7% improves the homogeneity of the Eu^{3+} fluorescence within the Eu-CeO_2 film (Figure 6.8b). However, samples with 8.5 and 14.4% Eu exhibit the most consistent fluorescence, with strong Eu^{3+} fluorescence across the entire film (Figure 6.8c,d).

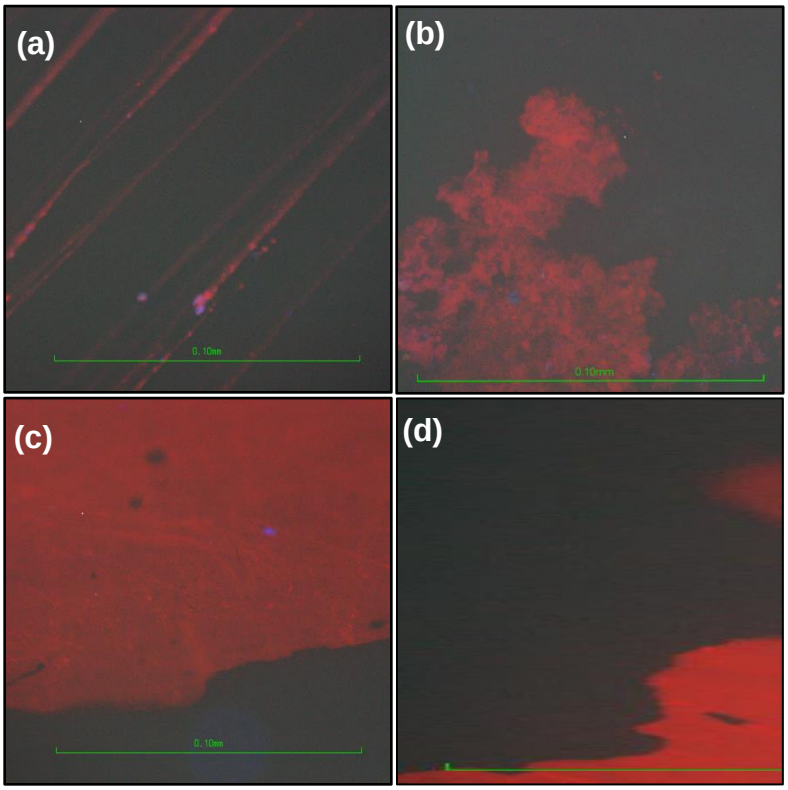

Figure 6.8 *Images of fluorescence emitted from Eu-CeO2 with experimental Eu at% of (a) 1.8%, (b) 4.7% (c) 8.5%, (d) 14.4% as determined by TEM-EDS.*

The relative intensity of the fluorescence images is consistent with the corresponding fluorescence spectra, as seen in Figure 6.9a. Increasing the %Eu from 1.8% to 8.5%Eu

consistently increases the intensity of the Eu^{3+} fluorescence. Further addition of Eu^{3+} to 14.4 %Eu only intensified the fluorescence at 590 nm by 8%. Normalizing the fluorescent signal to the intensity at 590 nm highlights the change in the $^5D_0 \rightarrow {}^7F_2$ intensity with increasing %Eu (Figure 6.9b). This is matched by the asymmetry ratio, which increases steadily with increasing %Eu (Figure 6.9c).

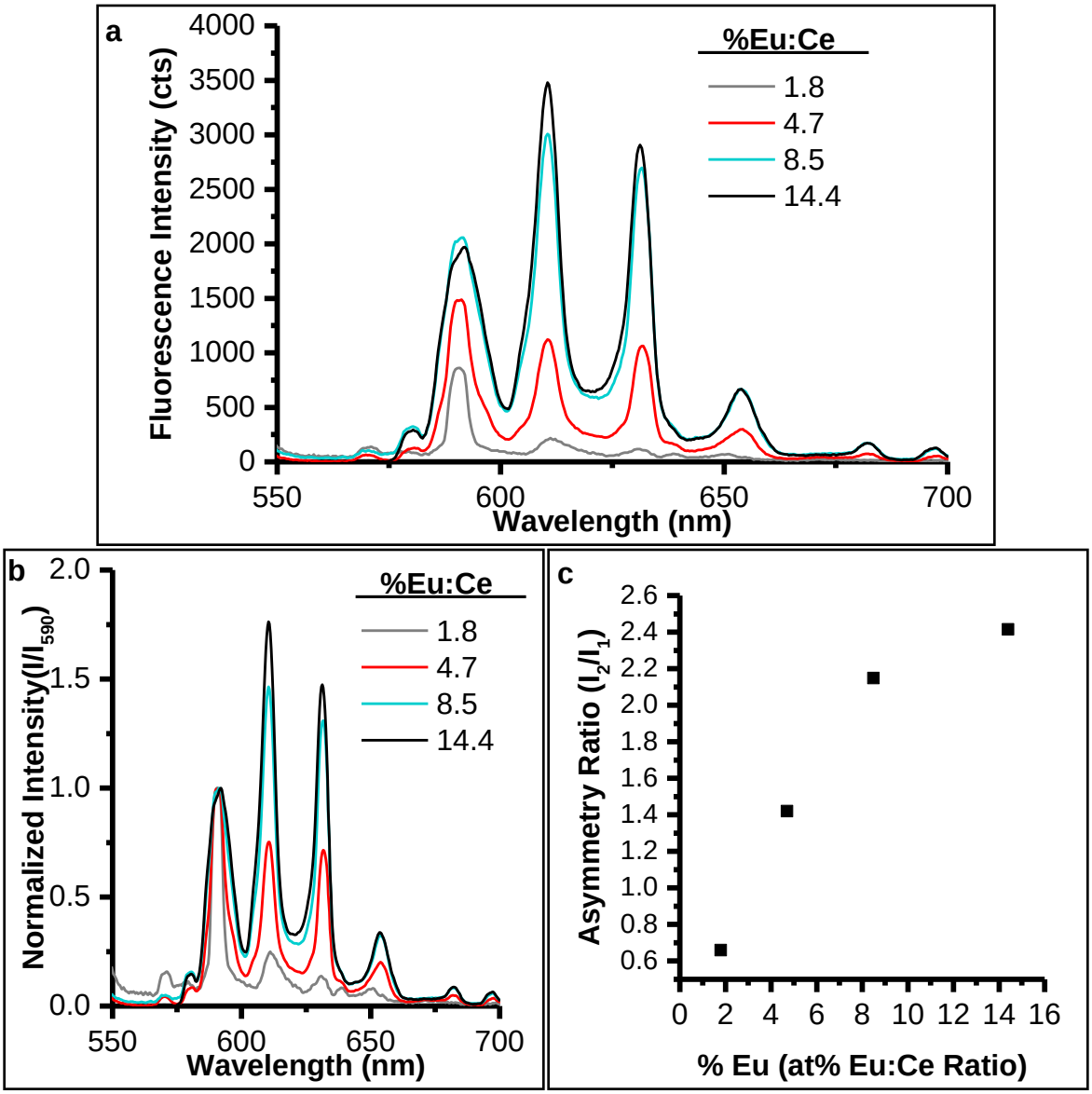

Figure 6.9 *(a) Emission spectra of Eu-CeO_2 nanowires with varying %Eu, (b) same spectra normalized to the intensity at 590 nm, and (c) plot of asymmetry ratio related to the measured %Eu.*

6.4.3. Eu^{3+} fluorescence in Eu-CeO_2 Nanorods

The as-synthesized Eu-CeO_2 nanorods do not intrinsically fluoresce. The Eu^{3+} fluorescence was activated by heating above 400 °C. Figure 6.10 demonstrates the activation of Eu^{3+} fluorescence in nanorods as a function of temperature, with onset of weak fluorescence at 400 °C, and intensity of fluorescence strengthening with increasing annealing temperature.

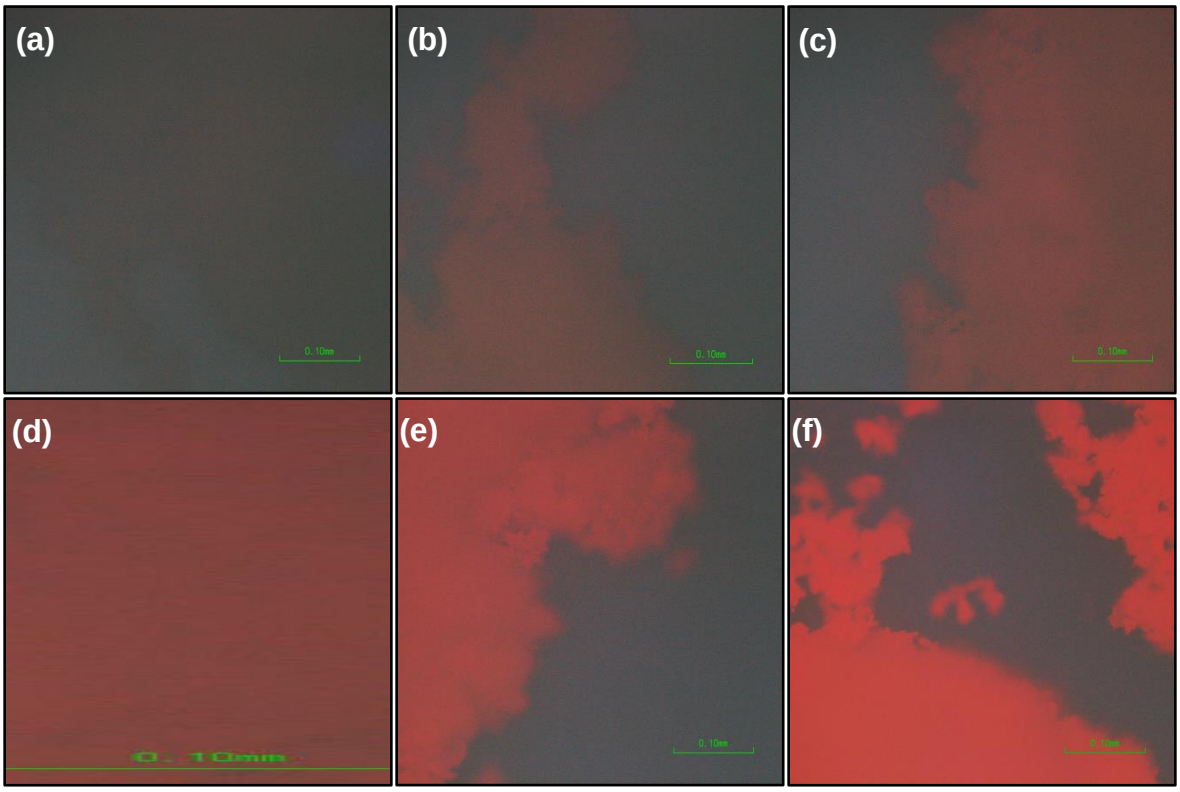

Figure 6.10 *Fluorescence images as annealing temperature increases. Samples include (a) unannealed nanorods and nanorods annealed to (b) 400 °C, (c) 500 °C, (d) 600 °C, (e) 700 °C, and (f) 800 °C.*

Once again, this increase in visual fluorescence is also seen in the fluorescence spectra (Figure 6.11a). The unannealed nanorods exhibit a very weak intensity through the hypersensitive $^5D_0 \rightarrow {}^7F_2$ transition, indicating that the minor Eu^{3+} fluorescence emitted is originating from a site with asymmetry. With increasing temperatures, the MD transition

at 590 nm rapidly strengthens. The peaks at 610 and 630 nm also intensify and are broad peaks relative to the signal observed in the nanowires. Fluorescence spectra of samples annealed between 400 °C and 600 °C even suggest an additional, weak emission slightly red-shifted from the $^5D_0 \rightarrow {}^7F_2$ transition at 610 nm. This shoulder is not easily observed in the unannealed sample due to weak fluorescence intensity, but may indicate an additional site of asymmetry that is removed as the nanorods are annealed.

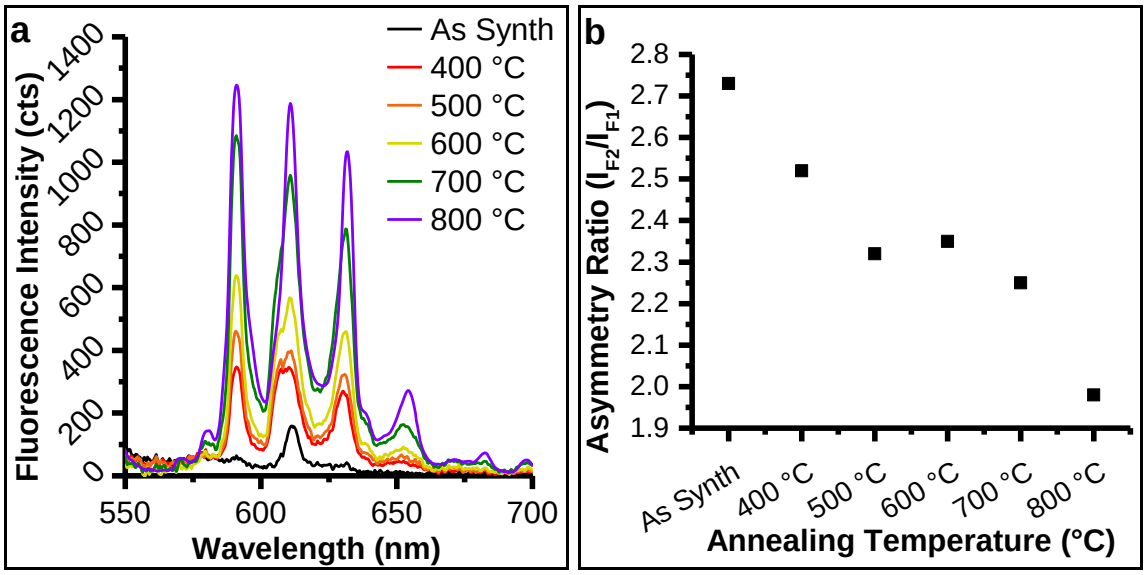

Figure 6.11 *(a) Fluorescence spectra of Eu-CeO_2 nanorods with excitation at 375 nm following annealing at temperatures up to 800 °C, and (b) calculated asymmetry ratio for Eu-CeO_2 nanorods as annealing temperature increases.*

The asymmetry ratio decreases from 2.73 to 1.95 after unannealed rods were heated to 800 °C. In samples with visibly detectable emission (400 °C to 800 °C) the asymmetry ratio only decreases by about 0.3 (Figure 6.11b). While the ratio does decrease with increasing annealed temperature and fluorescence intensity, the emitting Eu^{3+} ions in annealed nanorods remain in sites of high asymmetry. This asymmetry is likely due to oxygen vacancies and Ce^{3+} from Eu^{3+} doping, since the 8 at% Eu-CeO_2 nanowires, nanocubes, and nanorods annealed to 800 °C all have comparable asymmetry ratios.

The initial reduction in asymmetry from ~2.7 to ~2.3 upon annealing to 500 °C is consistent with elimination of fluorescence quenching species. Functional groups, such as surface hydroxyls, are known quenchers of lanthanide fluorescence, including emission from Eu^{3+}.[223] Due to the synthetic procedure, the nanorod morphology is coated in surface hydroxyls. Annealing removes surface hydroxyls from CeO_2 nanomaterials which explains the reduction in Eu^{3+} emission quenching.[199]

However, the Eu-CeO_2 nanocubes still strongly fluoresce, despite having a significant coating of surface hydroxyls. The nanorods remain as $Ce(OH)_3$ until oxidation to CeO_2 during washing, which may have trapped $Ce(OH)_x$ defects within the nanorod. In contrast, the nanocubes are oxidized to CeO_2 *in situ*, and likely have few internal hydroxyl species. The internal hydroxyl species may be responsible for the Eu^{3+} fluorescence quenching in the nanorod samples and are likely removed during annealing.

Last, annealing removes crystal defects such as oxygen vacancies from the nanorods, and greatly expands their crystalline domain size from 6 nm to almost 16 nm, similar in size to the nanowire sample. Crystal defects often act as sites for recombination of excited electron-hole pairs, thereby reducing the fluorescence emission intensity.[199]

Most likely, the Eu^{3+} fluorescence is activated due to a combination of these factors.

6.4.4. Eu^{3+} fluorescence in Eu-CeO_2 nanocubes

Finally, the Eu^{3+}-associated fluorescence in the nanocube morphology was tracked as the %Eu was increased from 0 %Eu to 8 %Eu. The 0% Eu sample is missing any Eu^{3+} fluorescence as expected and is not included in further discussion in this section.

Unlike the nanorods and nanowires, the nanocubes exhibit very strong red fluorescence at minimal concentration of europium, as seen in Figure 6.12. Furthermore, the nanocubes are much smaller than the nanowires, with edge lengths of ~25 (± 10 nm) versus nanowires, which are ~100 nm thick and microns long. Due to their small size, the nanocubes disperse in water with significantly reduced scattering compared to the nanowire samples. The strong fluorescence and reduced scattering enable measurement of the nanocube fluorescence while suspended in solution, unlike the wires and rods which were measured as dry powders using a mercury light source fixed at 370 nm.

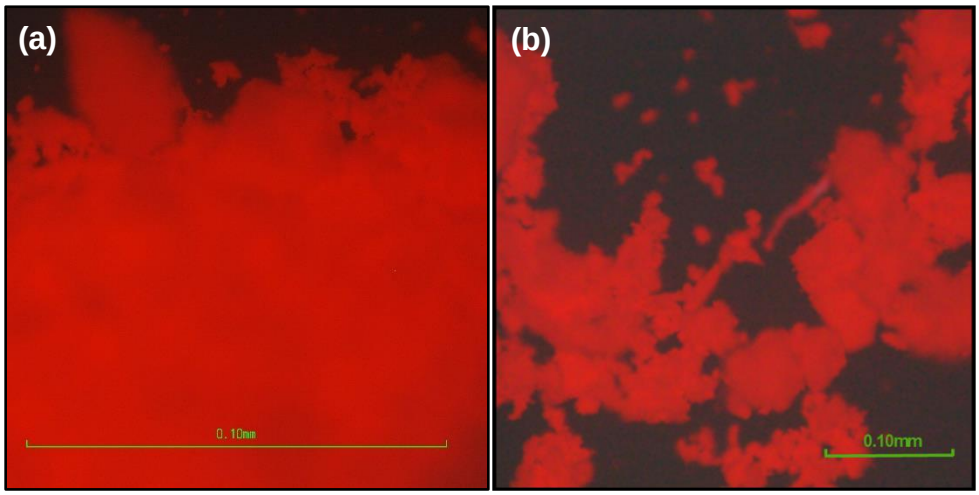

Figure 6.12 *Fluorescence image of CeO_2 nanocubes with (a) 1% and (b) 8% Eu^{3+}.*

The fluorescence spectra of the cubes follow the trends observed in the Eu-CeO_2 nanowires. At Eu^{3+} low concentrations, the hypersensitive peak at 610 nm and 630 nm is significantly suppressed relative to the insensitive transition at 590 nm. Upon increasing the %Eu, the hypersensitive peaks are activated (Figure 6.13a). This trend is indicated in the asymmetry ratio, with low asymmetry calculated in low Eu% samples, and significantly higher asymmetry with higher %Eu doping (Figure 6.13b).

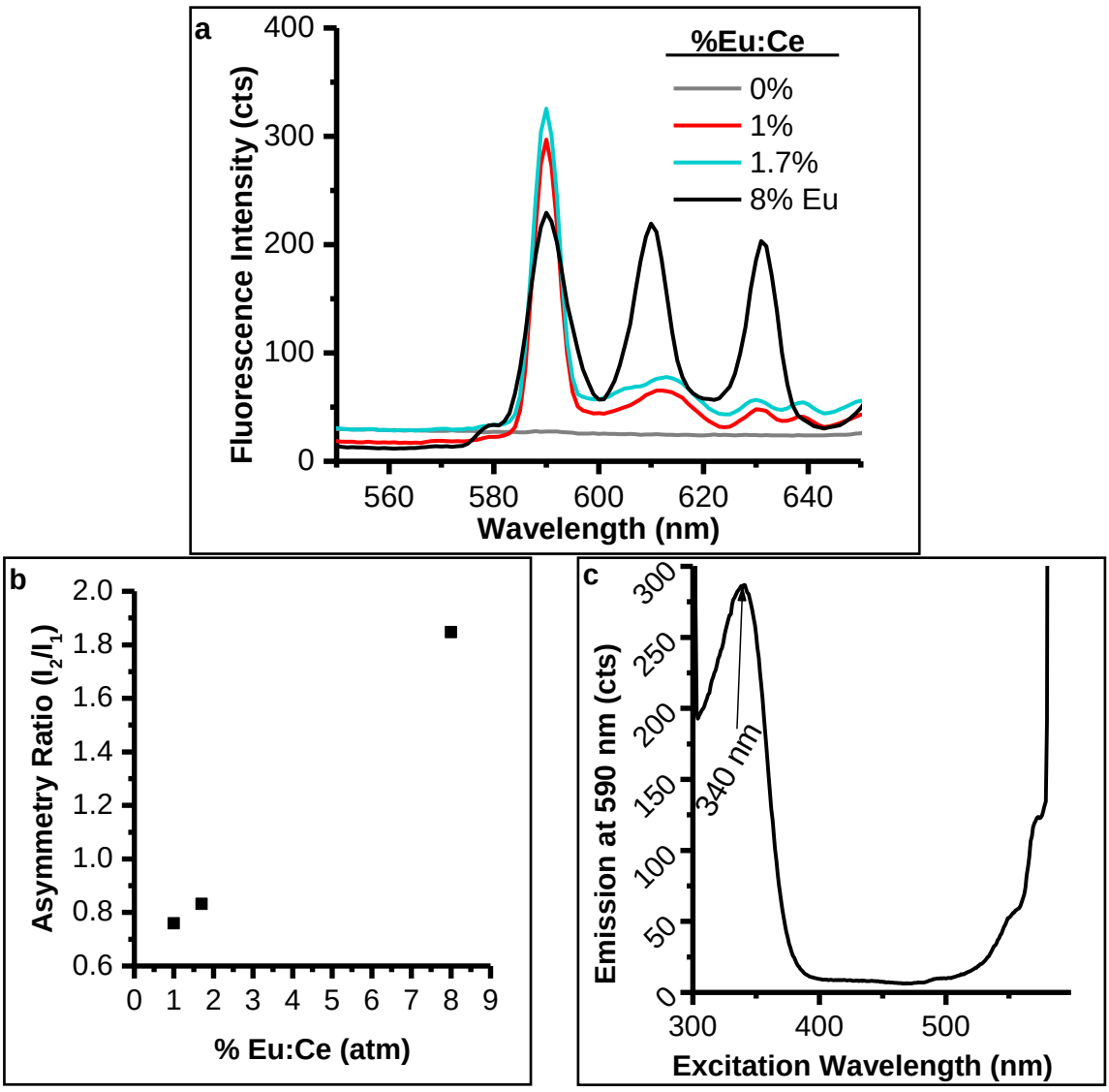

Figure 6.13 *Plots of fluorescence from Eu-CeO_2 nanocubes. (a) Fluorescence spectra of nanocubes with 0%, 1%, 2%, and 8% Eu, with excitation at 340 nm, (b) asymmetry ratio relative to measured %Eu, and (c) excitation scan of 2% Eu-CeO_2, measuring emission at 590 nm.*

Finally, the 2% Eu-CeO_2 nanocubes were used to measure the excitation spectrum. While tracking the emission at 590 nm associated with the $^5D_0 \rightarrow {}^7F_1$ MD transition, only one broad band is observed, spanning the 300-400 nm region (Figure 6.13c). This region is associated with the Ce_{4f}-O_{2p} charge transfer transition, as mentioned earlier. However, several transitions, such as the charge transfer from oxygen to Eu^{3+} are located near this

region.[224] Most likely, after the CeO_2 host is excited through the charge transfer, some energy is released through non-radiative relaxation, and the remainder of the energy from the excited electron transfers non-radiatively to the Eu^{3+}. The excited Eu^{3+} electron then drops back to the ground state, emitting a photon characteristic of the Eu^{3+} fluorescence (Figure 6.14).

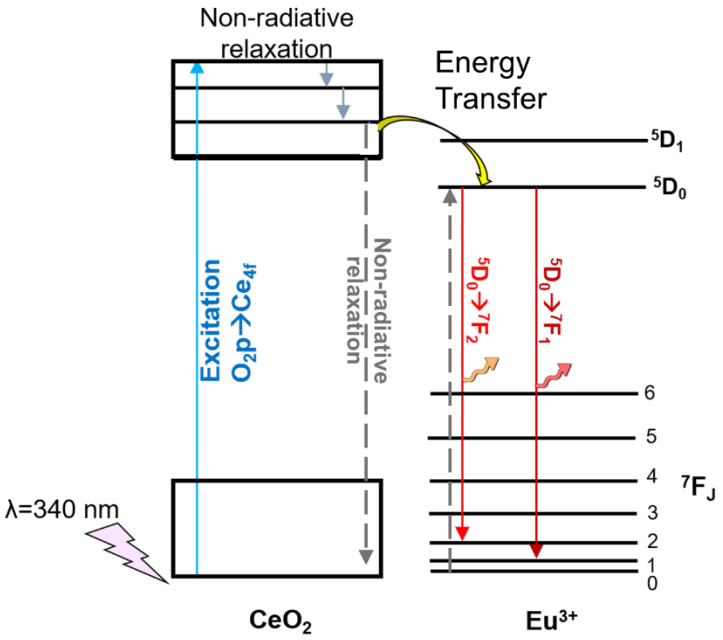

Figure 6.14 *Diagram of likely mechanism of Eu3+ fluorescence, as sensitized by CeO2.*

6.5. Rare Earth-doped CeO_2 Nanocube Fluorescence

Due to the strong Eu^{3+} fluorescence observed in the CeO_2 nanocube morphology without requiring fluorescence activation, other Ln^{3+} dopants were tested for fluorescence within this specific morphology. Pr-CeO_2, Nd-CeO_2, Sm-CeO_2, Eu-CeO_2, Gd-CeO_2, Ho-CeO_2, Er-CeO_2, Tm-CeO_2, and Yb-CeO_2 were all synthesized, although only materials with detectable fluorescence were analyzed by TEM and subsequently discussed in this chapter.

The nanocubes were doped with 1, 5, or 10 Ln at% (Eqn 6.2). The cubes were subsequently tested for visible and NIR fluorescence. Table 6.2 lists the theoretical dopant concentrations synthesized and indicates the presence and range of any observed fluorescence.

$$Ln^{3+}\ at\% = \frac{at\%\ Ln^{3+}}{at\%\ Ln^{3+} + at\% Ce^{3+}} \qquad \text{(Eqn 6.2)}$$

Table 6.2 *Summary of rare earths doped into CeO_2, including dopant concentrations and any observed fluorescence.*

	Theoretical At%	Fluorescence	Vis, NIR
Pr^{3+}	1, 10	☒	
Nd^{3+}	1, 5, 10	☑	NIR
Sm^{3+}	1	☑	Vis
Eu^{3+}	0, 1, 2, 8	☑	Vis
Gd^{3+}	10, 20	☒	
Ho^{3+}	1, 10	☒	
Er^{3+}	1, 5, 10	☑	NIR (weak)
Tm^{3+}	1, 10	☒	
Yb^{3+}	1, 5, 10	☑	NIR

6.5.1. Nanocube Morphology and Elemental Composition

Fluorescent nanocube materials were analyzed by TEM and EDS for their morphology, dimensions, and elemental composition. All samples display morphologies very similar to the Eu-CeO_2 nanocubes discussed in Chapter 3, so only one TEM image is included per dopant (Figure 6.15). All five samples have edge lengths measuring between 25 and 35 nm, once again comparable to the Eu-CeO_2 nanocube morphology (Figure 6.16). Manipulation of the Ln^{3+} precursor concentration matches well with the

measured Ln^{3+} concentration by EDS, and elemental data for the samples is detailed in Table 6.3**.**

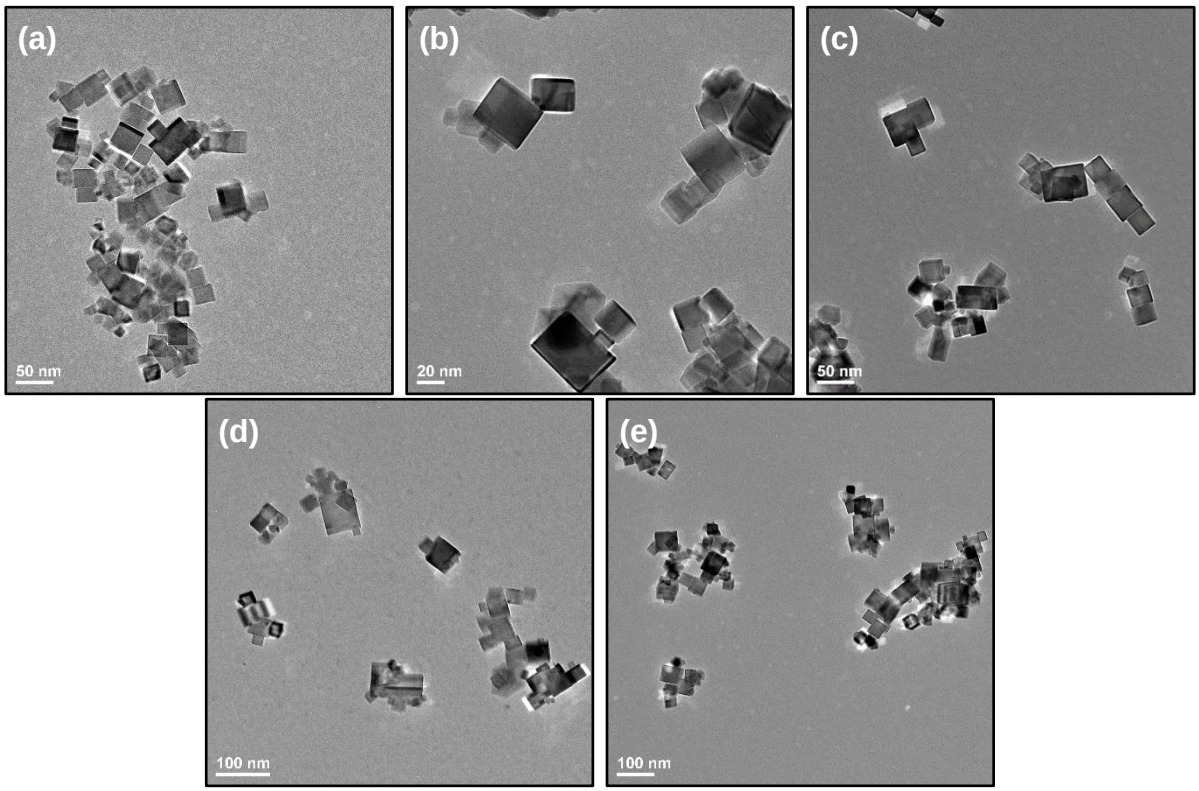

Figure 6.15 *TEM images of the fluorescent nanocubes (a) 10% Er-CeO_2, (b) 2.5% Yb-CeO_2, (c) 5% Nd-CeO_2, (d) 10% Sm-CeO_2, and (e) 8% Eu-CeO_2 nanocubes.*

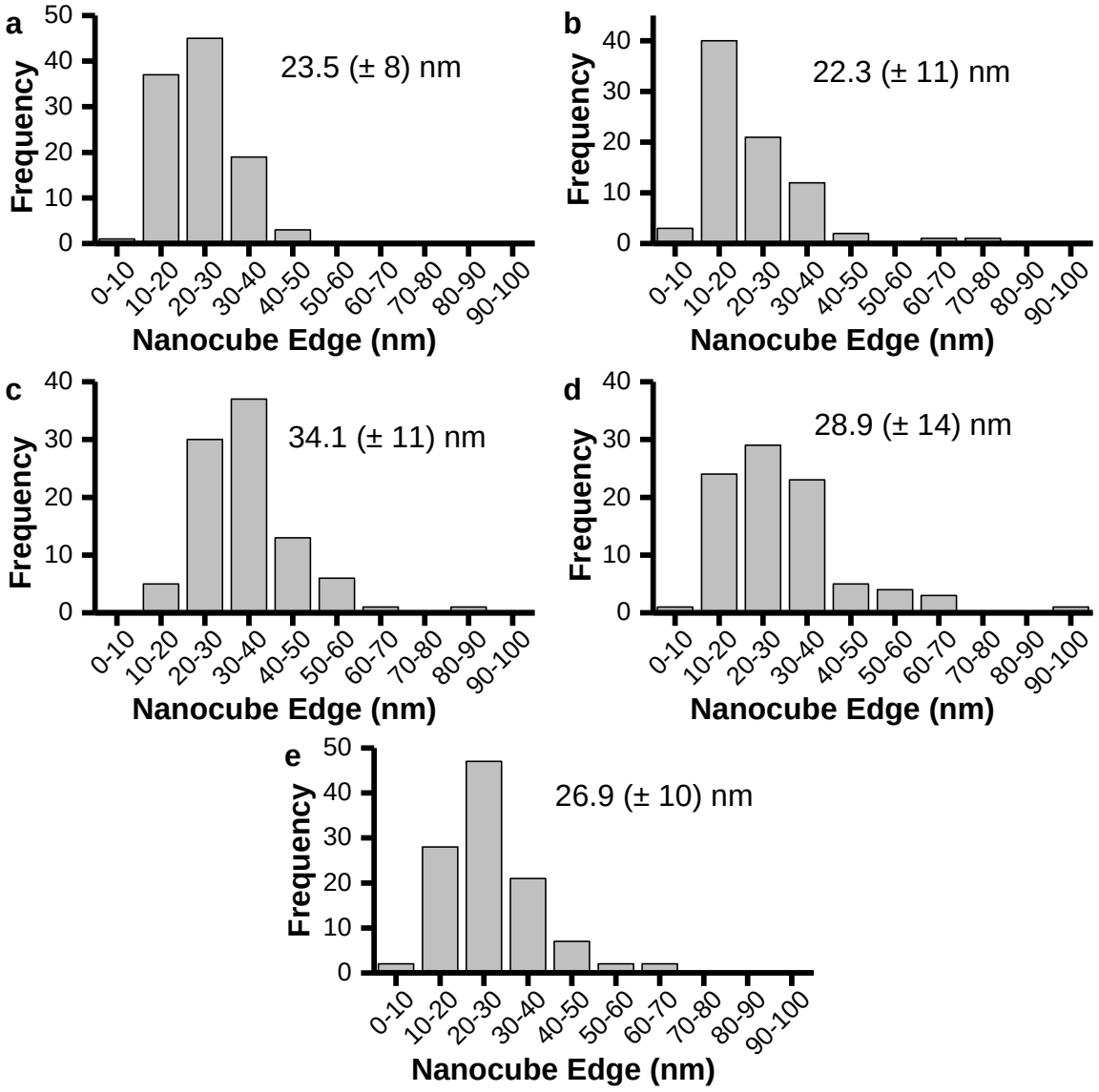

Figure 6.16 *Histograms of edge lengths in nanocubes made of (a) 10% Eu-CeO_2, (b) 5% Yb-CeO_2, (c) 5% Nd-CeO_2, (d) 10% Sm-CeO_2, and (e) 8% Eu-CeO_2.*

Table 6.3 *Elemental details for Ln-CeO_2 nanocubes as analyzed by EDS.*

	At% O	At% Ce	At% Ln	At% Ln	At%Ce
10%Er-CeO_2	59.4 ± 13.5	22.8 ± 7.7	2.5 ± 0.6	10.0 ± 1.1	90.0 ± 1.1
5% Yb-CeO_2	56.2 ± 3.0	42.0 ± 2.6	1.8 ± 0.5	4.0 ± 0.8	96.0 ± 0.8
5% Nd-CeO_2	64.4 ± 1.9	33.8 ± 1.9	1.8 ± 0.6	5.3 ± 0.4	94.7 ± 0.4
10% Sm-CeO_2	80.3 ± 1.1	17.1 ± 1.2	2.6 ± 0.2	10.0 ± 4.4	90.0 ± 4.4
8 % Eu-CeO_2	55.5 ± 2.7	40.8 ± 2.5	3.4 ± .85	8.0± 1.68	92.0± 1.68

6.5.2. UV-Vis Absorbance and Emission

The Ln-CeO_2 nanocubes were first analyzed for their absorption in the UV-Vis range. All samples were dominated by a broad transition tentatively assigned to the O_{2p}-Ce_{4f} charge transfer band (Figure 6.17). Upon normalizing the spectra for absorbance maxima, the Yb-CeO_2 and Eu-CeO_2 samples show a blue-shift of up to 30 nm (Figure 6.17b). This shift may be due to charge transfer from lattice oxygen to the lanthanide dopants or differences in Ce^{3+} concentration and distribution within the cubes.[206]

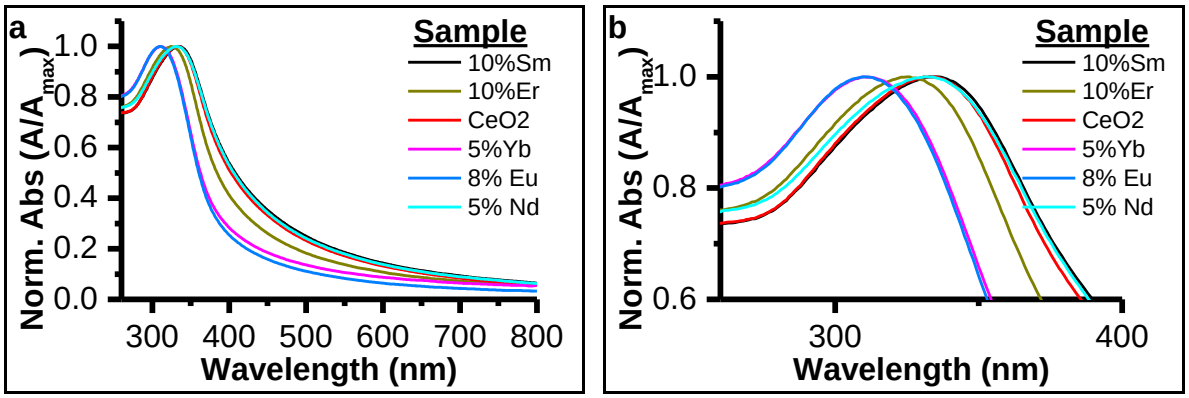

Figure 6.17. *UV-VIS of doped and undoped CeO_2 nanocubes both (a) normalized peak absorbance and (b) enlarged peak absorbance.*

The visible fluorescence of these nanocubes were also measured, with excitation through the Ce_{4f}-O_{2p} charge transfer band at 340 nm. As seen in Figure 6.18a, the only nanocubes with fluorescence in the visible range were Eu-CeO_2 and Sm-CeO_2. The fluorescence spectra of Eu-CeO_2 and Sm-CeO_2 from 550 nm to 700 nm are shown in

Figure 6.18b and c. The Sm-CeO_2 nanocube fluorescence is consistent with the expected Sm^{3+} transitions, with emission at 560 nm, 572 nm, and 589 nm assignable to the $^4G_{5/2} \rightarrow {}^6H_{5/2}$ transition, and the emission at 616 nm assignable to the $^4G_{5/2} \rightarrow {}^6H_{7/2}$ transition.[225]

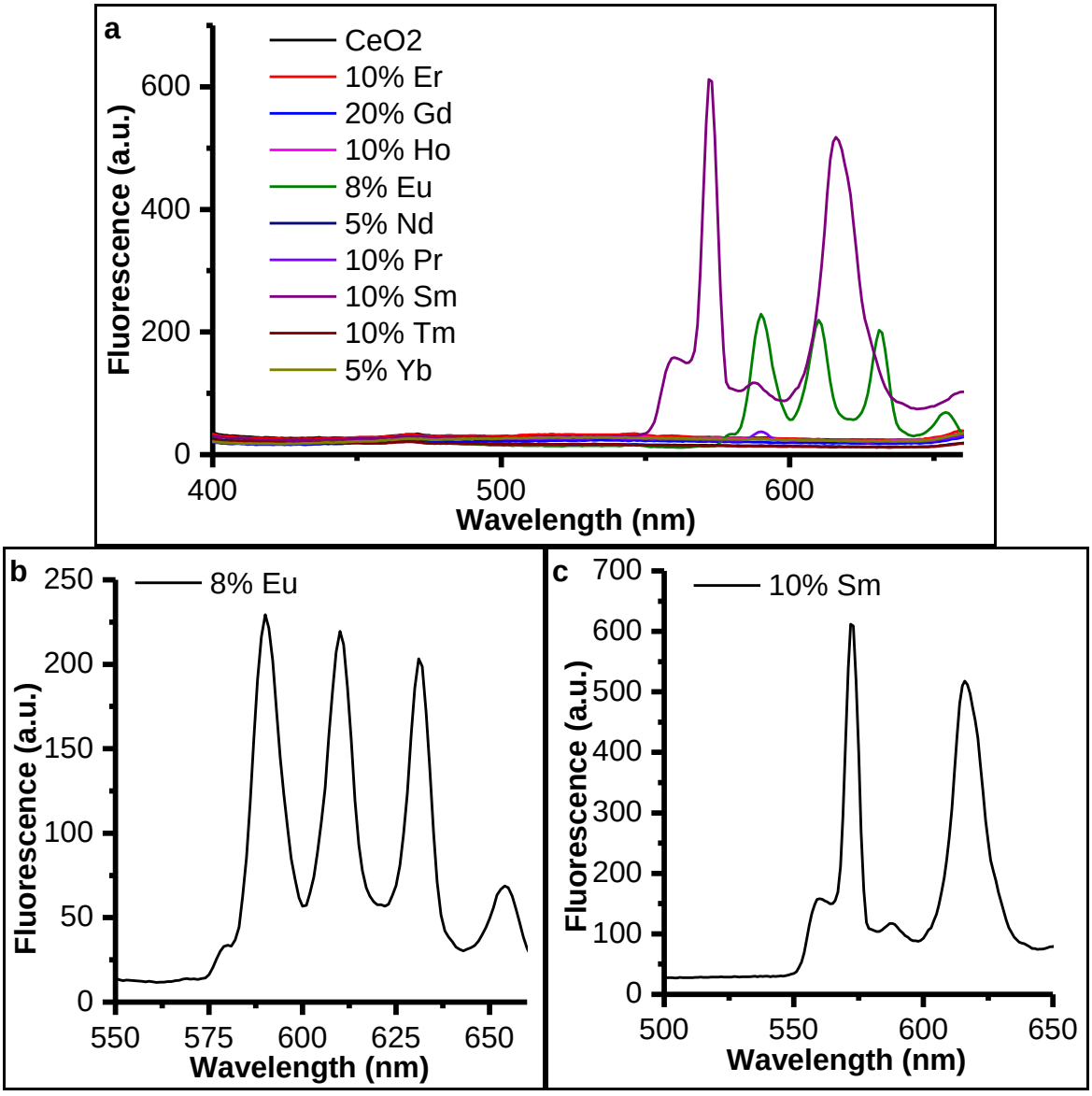

Figure 6.18 *Visible fluorescence of the doped and undoped CeO_2 nanocubes with excitation at 340 nm with (a) emission spectra of all Ln^{3+}-CeO_2 samples (b, c) enlarged spectra of Eu-CeO_2 and Sm-CeO_2 respectively.*

The emission properties of Sm-CeO_2 nanocubes were also evaluated by an emission-excitation 2-D mapping experiment. In this measurement, the excitation wavelength is increased incrementally while the emission is measured at each increment. As seen in Figure 6.19, the Sm-CeO_2 fluoresced strongly, indicated by the red and green color in the map, upon excitation between 340 nm and 380 nm. This matches the sample's UV-Vis absorbance maximum shown in Figure 6.17a. No other transitions are observed within this range, indicated by the blue background. Sm^{3+} is not being directly excited but presumably sensitized through the CeO_2 host, analogous to the Eu-CeO_2 cubes.

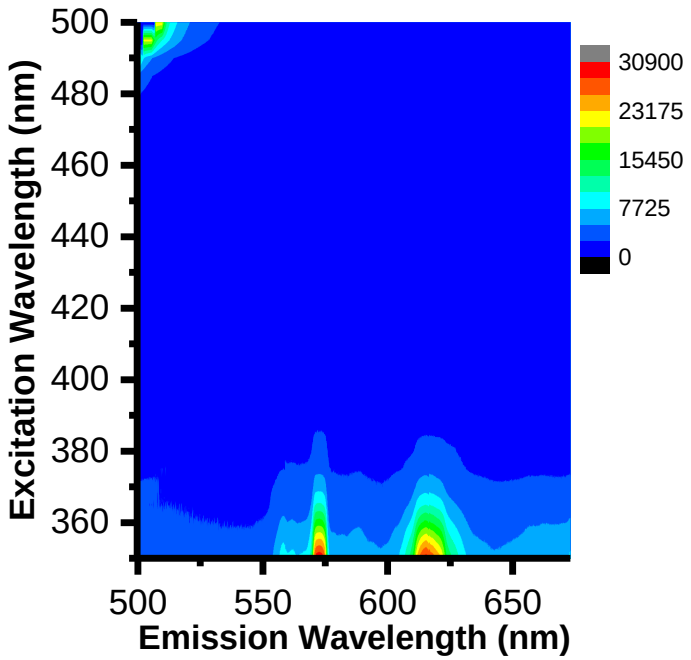

Figure 6.19 *Excitation-emission map of Sm-CeO_2 in visible region, measuring excitation from 340 nm to 500 nm and emission from 500 nm to 700 nm.*

6.5.3. Near IR Fluorescence

The Ln-CeO_2 nanocubes were also tested for fluorescence in the NIR region. Out of the dopants listed in Table 6.2, only three dopants emitted in this region when added to

CeO_2 nanocubes: Er^{3+}, Nd^{3+}, and Yb^{3+}. Table 6.4 lists the excitation wavelengths, emission wavelengths, and likely assignments for these transitions.

The fluorescence of the Nd-CeO_2 and Yb-CeO_2 samples was first probed by incrementally increasing the excitation wavelength from 330 nm to 700 nm, while measuring the emission from 850 nm to 1600 nm (Figure 6.20). Both samples emit upon excitation near 340 nm, as observed in the Sm-CeO_2 and Eu-CeO_2 nanocubes discussed in Section 6.5.1. The nanocubes also emit through a second excitation near 650 nm, albeit with significantly lower intensity.

Table 6.4 *Observed fluorescence excitations and emissions, with assignments to transitions as possible.*[198,209,225,226]

	$\lambda_{ex,A}$	$\lambda_{ex,B}$	$\lambda_{em\#1}$ (nm)	$\lambda_{em\#2}$ (nm)	$\lambda_{em\#3}$ (nm)
Yb^{3+}	350 nm	640 nm	1034	968	
Transition	$O_{2p} \rightarrow Ce_{4f}$ CT	Undetermined	$^2F_{5/2} \rightarrow {}^2F_{7/2}$	$^2F_{5/2} \rightarrow {}^2F_{7/2}$	
Nd^{3+}	350	640	1080	900	
Transition	$O_{2p} \rightarrow Ce_{4f}$ CT	Undetermined	$^4F_{3/2} \rightarrow {}^4I_{13/2}$	$^4F_{3/2} \rightarrow {}^4I_{9/2}$	
Er^{3+} peaks	340		956	1007	1520
Transition	$O_{2p} \rightarrow Ce_{4f}$ CT		$^4I_{11/2} \rightarrow {}^4I_{15/2}$	$^4I_{11/2} \rightarrow {}^4I_{15/2}$	$^4I_{13/2} \rightarrow {}^4I_{15/2}$
Sm^{3+} peaks	340		560, 572, 589	616	
Transition	$O_{2p} \rightarrow Ce_{4f}$ CT		$^4G_{5/2} \rightarrow {}^6H_{5/2}$	$^4G_{5/2} \rightarrow {}^6H_{7/2}$	
Eu^{3+} peaks	340		590	610	630
Transition	$O_{2p} \rightarrow Ce_{4f}$ CT		$^5D_0 \rightarrow {}^7F_1$	$^5D_0 \rightarrow {}^7F_2$	$^5D_0 \rightarrow {}^7F_2$

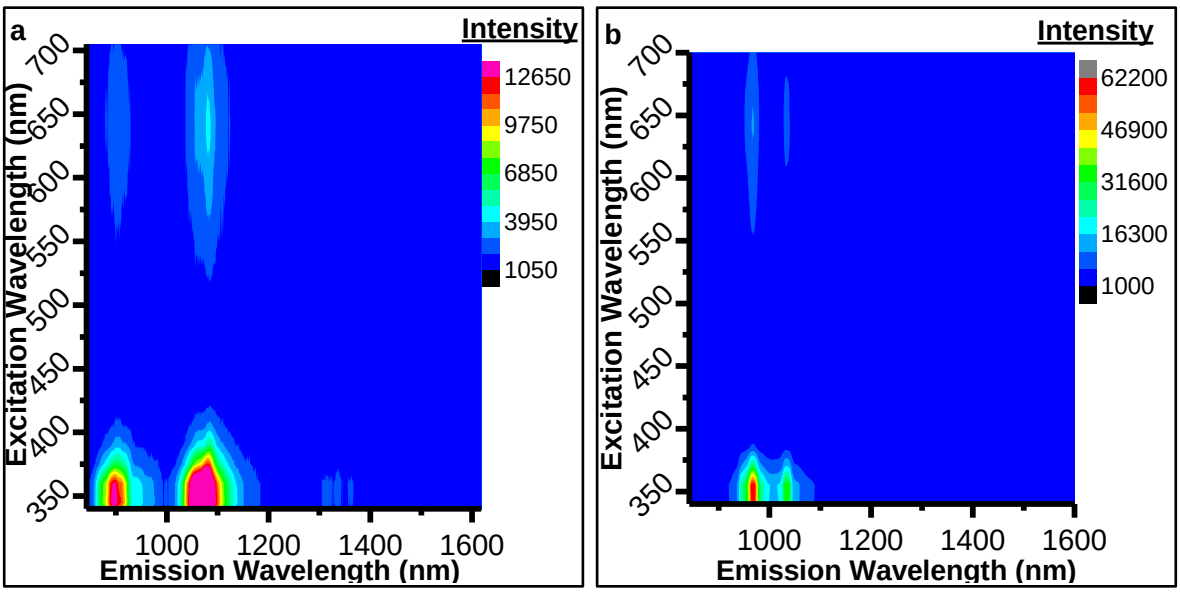

Figure 6.20 *Excitation-emission scans of (a)Nd-CeO_2 nanocubes and (b) Yb-CeO_2 nanocubes with increasing intensity indicated by shifts from blue to red colors.*

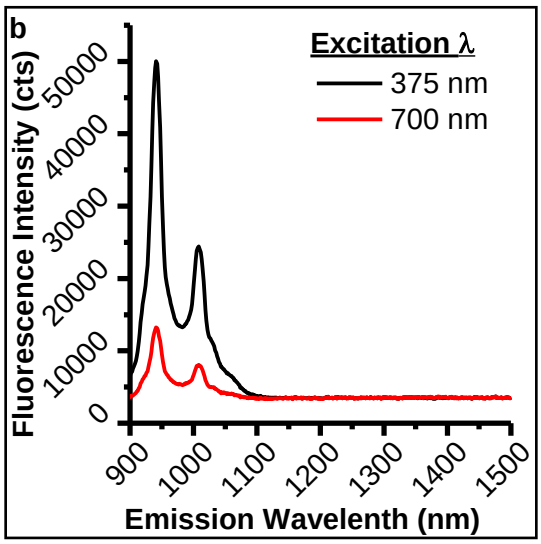

Figure 6.21 compares the emission spectra of the Yb-CeO_2 and Nd-CeO_2 nanocubes upon excitation at 375 nm and 700 nm. To maintain consistency with the Sm-CeO_2 and Eu-CeO_2 nanocube analysis in Section 6.5.1, the Yb-CeO_2 and Nd-CeO_2 nanocubes were excited at 375 nm despite their stronger emission at 340 nm. The 700 nm excitation wavelength was chosen to probe the cube's potential for imaging in the NIR.

Upon exciting at 375 nm, the Nd-CeO_2 and Yb-CeO_2 nanocubes fluoresce intensely at NIR wavelengths assignable to transitions of the Ln^{3+} dopant (Table 6.4). Specifically, the Yb-CeO_2 nanocubes emit strongly at 1070 nm and slightly weaker at 895 nm (

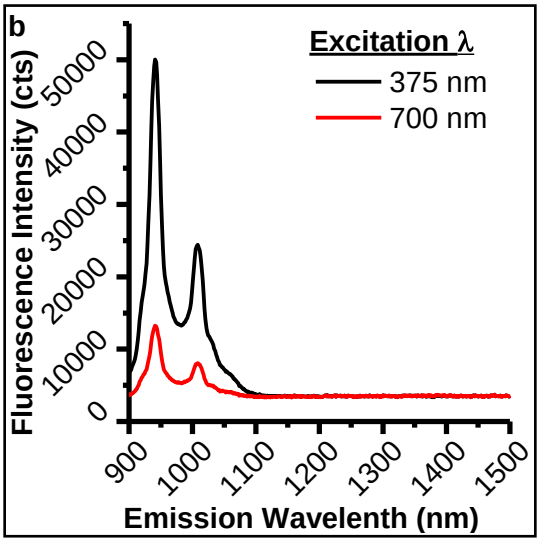

Figure 6.21a), due to splitting of the Yb^{3+} $^2F_{5/2}$ → $^2F_{7/2}$ transition.[227] Nd-CeO_2 nanocubes also fluoresce strongly with the primary peak at 1035 nm with a second emission peak at 968 nm (

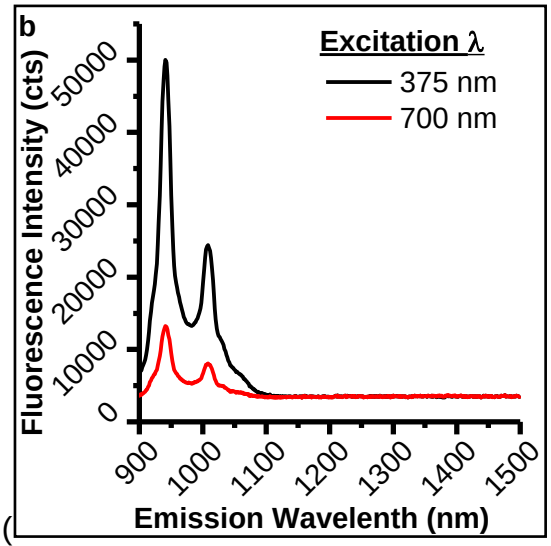

Figure 6.21b), assignable to the Nd^{3+} $^4F_{3/2}$ → $^4I_{13/2}$ and $^4F_{3/2}$ → $^4I_{9/2}$ transitions, respectively.[80]

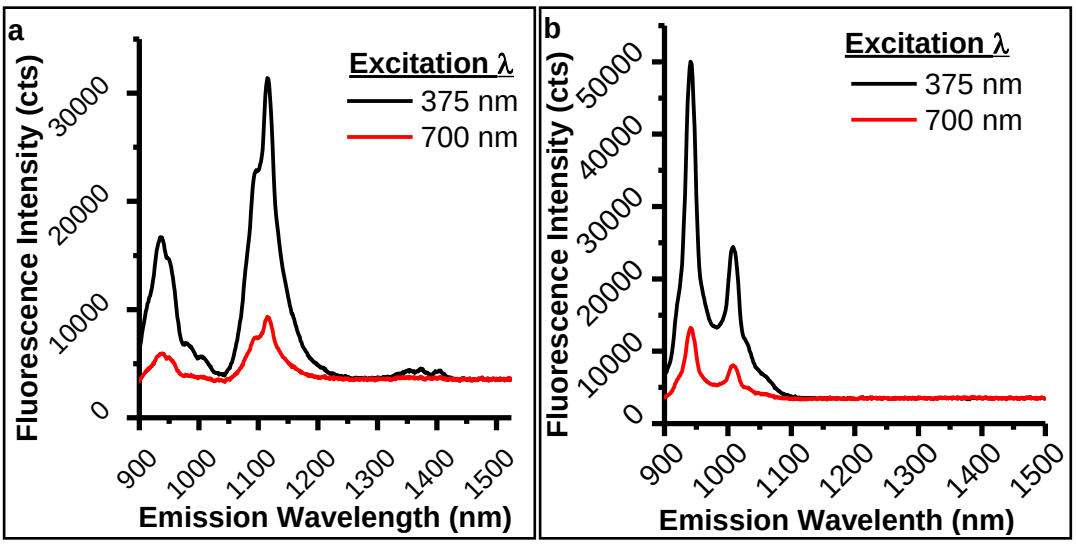

Figure 6.21 *NIR fluorescence of (a) 5% Nd-CeO_2 and (b) 5% Yb-CeO_2 nanocubes with excitation at 375 nm and 700 nm.*

The emission spectra of Nd-CeO_2 and Yb-CeO_2 nanocubes with 700 nm excitation mirrors the spectra using 375 nm excitation (

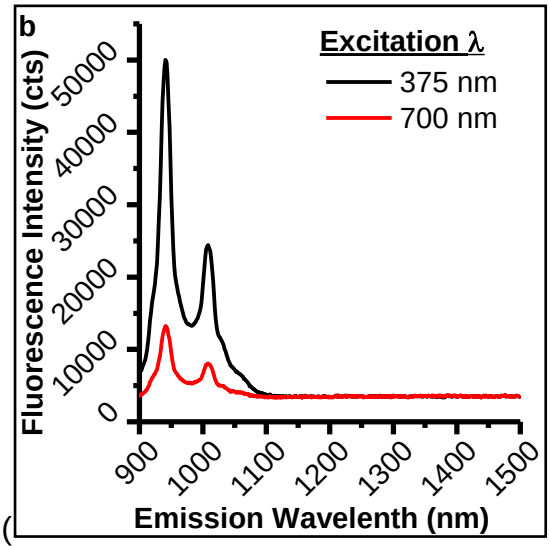

Figure 6.21). Both samples emit at similar wavelength, indicating similar transitions of the Ln^{3+} dopants. However, as observed in the emission-excitation mapping in Figure 6.19, the emission intensity is ~80% weaker with 700 nm excitation.

Finally, the Er-CeO_2 nanocubes fluoresce with 340 nm excitation. Two peaks at 956 nm and 1000 nm are assignable to Er^{3+} $^4I_{11/2} \rightarrow {}^4I_{15/2}$ transition.[228] A third, less intense

emission is also detectable near 1520 nm, attributed to the Er^{3+} $^4I_{13/2} \rightarrow {}^4I_{15/2}$ transition.[228] However, all three of the emissions observed in the Er-CeO_2 cubes have extremely low intensities relative to the emission observed from the Yb- and Nd-CeO_2 cubes (Figure 6.22).

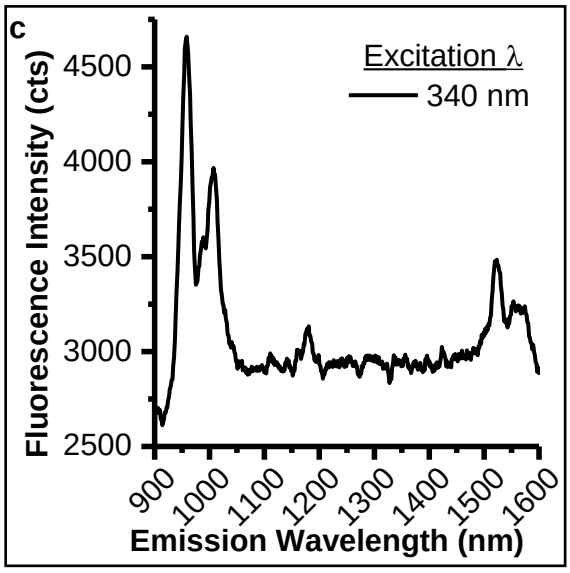

Figure 6.22 *Emission of 10% Er-CeO_2 nanocubes with excitation at 340 nm.*

6.5.4. Potential Fluorescence Mechanisms

The fluorescence of the Nd-, Yb-, and Er-CeO_2 cubes in the NIR following excitation at 340 nm is consistent with the fluorescence seen in the Eu-CeO_2 and Sm-CeO_2 nanocubes and likely proceeds through a similar mechanism. The CeO_2 host is excited through the O_{2p}-Ce_{4f} charge transfer band, centered near 340 nm. Energy is released through non-radiative relaxation within the CeO_2 host, with the remainder transferring to the Ln^{3+} dopant, as illustrated in Figure 6.14 and repeated in Figure 6.23. The excited Ln^{3+} ion then relaxes back to the ground state, releasing a photon in the process.

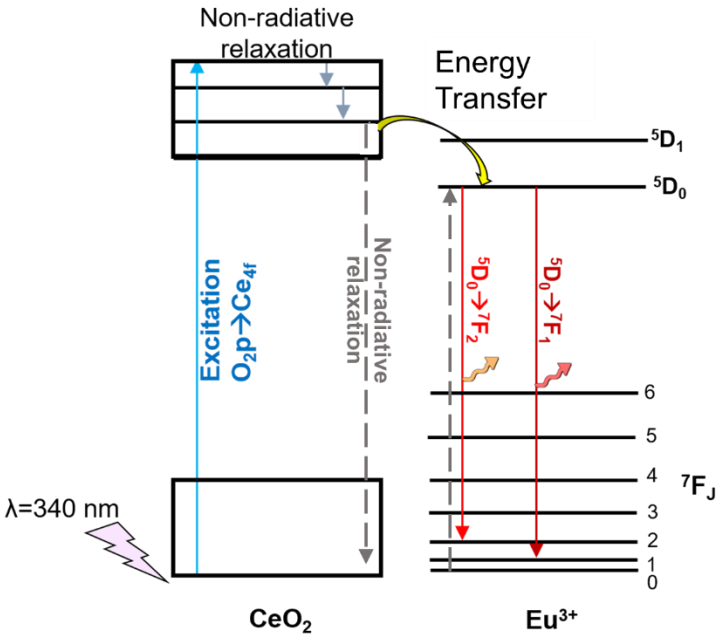

Figure 6.23 *Proposed mechanism of Ln^{3+} fluorescence under 340 nm excitation, using Eu^{3+} as an example dopant.*

The mechanism of fluorescence with excitation in the visible range is still undetermined. Yb^{3+} is not known to absorb in the visible region as its single transition, $^2F_{5/2} \rightarrow {}^2F_{7/2,}$ is centered near 980 nm.[80] The energy diagram of Nd^{3+} supports more transitions than Yb^{3+}, but these transitions are also centered in the near-IR range.[80] Additionally, the excitation range (~500 nm to ~700 nm) as well as peak excitation wavelength (640 nm) are similar for both the Yb-CeO_2 and Nd-CeO_2 nanocubes. If the nanocube fluorescence initiated with direct excitation of the Ln^{3+} dopant, the excitation wavelength would vary significantly between Yb^{3+} and Nd^{3+} doped cubes. The similarity in excitation wavelength, combined with the lack of Ln^{3+} transitions with suitable energy, suggests that the fluorescence at 640 nm does not progress through direct excitation of the Ln^{3+} dopants.

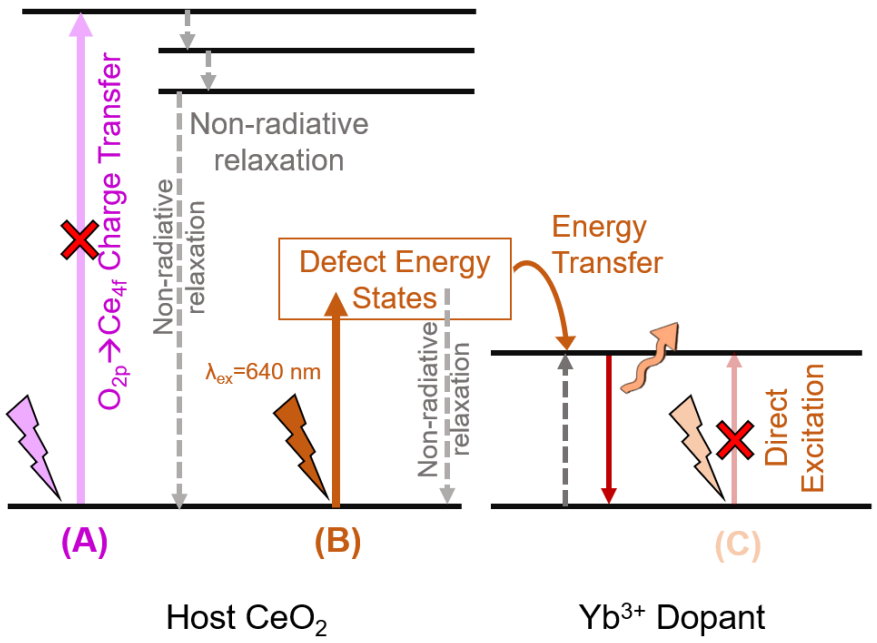

Figure 6.24 *Diagram of excitation mechanisms using Yb^{3+} as an example dopant. Grey dashed lines represent non-radiative transitions. Illustrated transitions include (A) O_{2p}→Ce_{4f} charge transfer, (B) excitation in defect trap sites, and (C) direct excitation of the Yb^{3+} ion.*

The alternative to direct excitation of the rare earth dopant is excitation of the host CeO_2, followed by energy transfer as discussed in the Eu-CeO_2 samples. The most commonly reported CeO_2-host excitation is the O_{2p}-Ce_{4f} charge transfer, but this transition has already been assigned to the 340 nm excitation. Another host-excitation mechanism proceeds through oxygen vacancies or Ce^{3+} defects within the CeO_2 crystal structure, capable of inserting energy traps into the CeO_2 band gap.[229] The CeO_2 host material may absorb energy into these traps, followed by energy transfer from the traps to the Ln^{3+} (Figure 6.24). The energy of this transition within a specific material is sensitive to several factors, including the density and distribution of the defects within the CeO_2 lattice, and the source of the defect. However, most literature reports excite these defects using wavelengths below 500 nm.[33,230]

While select possible mechanisms for visible range excitation of Ln-CeO_2 cubes has been proposed here, determination of the exact mechanism of Ln^{3+} excitation is beyond on the scope of this work and warrants further investigation.

6.6. Conclusions

This chapter presents the analysis of fluorescence provided by Ln^{3+} ions incorporated within various CeO_2 nanostructures. Significant research has investigated the optical properties of Ln-CeO_2 films and particles due to CeO_2's strong UV absorbance and ability to sensitize the fluorescence of selected rare earth ion dopants. Relatively little research into other morphologies is available.

This chapter first analyzes the differences in the Eu^{3+} fluorescence between the 8 at% Eu-CeO_2 nanorods, nanowires, nanocubes, and annealed nanorods. The Eu^{3+} fluorescence was then measured individually within the nanowire, nanorod, and nanocube systems. Finally, the nanocube morphology was used as a host for a large selection of other Ln^{3+} dopants, and any resulting fluorescence was analyzed.

The Eu-CeO_2 nanowires and nanocubes intrinsically fluoresce, while the nanorods require annealing to activate the Eu^{3+} fluorescence. The asymmetry ratio of the Eu^{3+} fluorescence was lowest for the nanocubes, indicating higher symmetry around the Eu^{3+} sites in the nanocubes relative to the nanowire and annealed nanorod morphologies. This may be attributed to the larger crystal domain size of the nanocubes, or residual defects not removed by annealing the nanorods or nanowires.

Annealing the nanorods gradually increased their Eu^{3+} fluorescence intensity, while also decreasing the asymmetry ratio. The intensification of Eu^{3+} fluorescence is due to

removal of crystal defects and surface and bulk hydroxyls which can quench the emission. The removal of the defects and oxidation of Ce^{3+} to Ce^{4+} also lowers the asymmetry around Eu^{3+}, reducing the asymmetry ratio.

Increasing the %Eu concentration in the nanowires corresponds to an increase in asymmetry ratio, matching literature precedence.[203] While the asymmetry ratio also increased with %Eu in the nanocubes, the Eu^{3+} fluorescence was very strong even at 1%Eu concentrations, with no loss in fluorescence intensity upon increasing from 1 %Eu to 8 %Eu. This strong fluorescence in the nanocubes across a wide range of dopant concentration makes the nanocubes promising candidates for doping with other fluorescent ions.

Therefore, the nanocubes were tested with a series of fluorescent Ln^{3+} dopants, with Sm^{3+} and Eu^{3+} fluorescing in the visible range, and Er^{3+}, Nd^{3+}, and Yb^{3+} fluorescing in the NIR. The Er-CeO_2, Sm-CeO_2, and Eu-CeO_2 all fluoresce upon excitation in the UV, likely due to charge transfer within the CeO_2 and subsequent energy transfer to the Ln^{3+}. In addition to the UV excitation, the Yb-CeO_2 and Nd-CeO_2 nanocubes also emit with upon excitation near 640 nm by an undetermined mechanism most likely involving the CeO_2 host.

The optical properties of the Ln^{3+} doped CeO_2 nanocube morphology are mostly unexplored, with only Sm- and Eu-CeO_2 cubes synthesized and only Sm-CeO_2 nanocube fluorescence reported.[225] The NIR fluorescence observed in the Nd- and Yb-CeO_2 nanocubes has potential application in bioimaging, particularly with excitation at 700 nm. Further work is necessary to further clarify the excitation mechanism and strengthen the NIR fluorescence intensity of the doped nanocubes.

Chapter 7: Eumelanin Fluorescence Suppression by Eu-CeO_2 Nanomaterials

7.1. Overview

Following the synthesis of europium doped cerium oxide (Eu-CeO_2) nanorods, annealed nanorods, nanocubes, and nanowires described in Chapters 2-4, Chapter 6 covered an analysis of the Eu^{3+} fluorescence of these materials. Significant differences in the fluorescence were noted between these morphologies, with fluorescence quenching driven primarily by hydroxyl groups and crystalline defects in a given nanostructure. Chapter 7 compares the surface chemistry of the four morphologies, probed by their impact on the auto-oxidation of L-3,4-dihydroxyphenylalanine (L-Dopa) and eventual synthesis of eumelanin. The interaction of the Eu-CeO_2 materials with L-Dopa during the synthesis of eumelanin is measured through uv-vis absorbance and fluorescence spectroscopies, as well as visual changes in a given Eu-CeO_2 nanomaterial.

L-Dopa is a naturally occurring catecholamine amino acid, frequently used in treatment of Parkinson's disease, as it can cross the blood brain barrier and undergo decarboxylation to dopamine.[231] Other research has highlighted L-Dopa's contribution to mussel adhesive proteins, attributed to cross-linking of oxidized L-Dopa derivatives and its binding to organic and inorganic surfaces.[232] L-Dopa is also a common precursor in the synthesis of eumelanin, one of several complex pigments found in the skin, hair, and brain.[233]

Recent research by Andreescu *et al.* has explored the interaction of CeO_2 nanoparticles with catecholamines, particularly dopamine.[100,234-236] The CeO_2 nanoparticles oxidize the catechol functional group to a quinone, followed by adsorption

of the quinone to the surface of the CeO_2. This binding has been utilized to develop electrochemical sensors for dopamine and several of its derivatives.[234]

However, while the Andreescu group has done extensive work establishing the CeO_2-dopamine chemistry, most of the work has focused on very small (<20 nm) undoped CeO_2 nanoparticles (NPs), with some studies including Sm^{3+}- or Eu^{3+}- doped CeO_2 NPs.[235,237] Furthermore, these studies have been performed at or below physiological pH, at which dopamine is unable to auto-oxidize and polymerize into polydopamine, a eumelanin mimic. Finally, there has been very limited research into the influence of different CeO_2 morphologies. One article, comparing CeO_2 nanorods and nanoparticles coated with polyacrylic acid, found that the nanorods had the stronger electrochemical activity with a derivative of dopamine, but no explanation was provided.[238]

Upon exposure to L-Dopa, CeO_2 nanomaterials have a distinctive color change associated with oxidation and adsorption of L-Dopa. Adding CeO_2 to solutions of L-Dopa during auto-oxidation also influences the intensity of UV-Vis absorbance and visible fluorescence peaks associated with the synthesis of eumelanin. The CeO_2 color and L-Dopa solution spectral changes make this system appealing as a probe of Eu-CeO_2 chemistry.

L-Dopa, melanin, and CeO_2 are all biologically relevant, with several similar applications (anti-oxidant/radical scavenging,[84,117,239] neurological disorder treatment,[240,241] etc.) Therefore, it is of fundamental interest to understand the influence of the Eu-CeO_2 morphology on its interaction with the eumelanin species.

This chapter first describes the progression of the fluorescence and absorbance spectra of L-Dopa solutions during its auto-oxidation into eumelanin. The influence of Eu-

CeO_2 nanorods, nanowires, annealed nanorods, and nanocubes on this process was then measured by tracking changes in L-Dopa fluorescence and absorbance in reactions where Eu-CeO_2 is present.

The nature of the interaction between Eu-CeO_2 and L-Dopa varies as a function of morphology. A possible explanation explaining the different reactivities is proposed, based on differences in several physical properties between the morphologies.

7.2. Introduction

7.2.1. Melanin

The term melanin describes a group of pigments, all based on oligomers of tyrosine derivatives.[242] Several types of melanin occur naturally within the human body, including eumelanin, pheomelanin, and neuromelanin. [233,243] Eumelanin, derived from L-Dopa, is a brown-black pigment located primarily in the skin. Pheomelanin incorporates cysteine groups and is the red pigment found in lips and hair. Finally, neuromelanin, a black pigment found in the brain, likely uses both L-dopa or dopamine, as well as the cysteine-derivative.

Neuromelanin concentrations are frequently elevated in patients with neurological diseases such as Alzheimer's and Parkinson's and may serve a neuroprotective role due to its radical scavenging activity and ability to bind transition metal ions such as copper, iron, and manganese.[244] Conversely, oxygen radicals are a byproduct of neuromelanin synthesis and may contribute to oxidative stress in the brain. Neuromelanin may also leech out captured toxins over time, particularly with the progression of neuron death.[241]

Neuromelanin is only found in very low concentrations within the brain, and between 5 and 30 human brains are required to isolate 1 mg of neuromelanin, depending on the part of brain harvested.[245] Due to the potential neurological importance of neuromelanin, eumelanin has been used as a model in analyzing the synthesis and chemical reactivity of neuromelanin.

Eumelanin is naturally produced when cells called melanocytes are stimulated with UV light. [246,247] Eumelanin serves as a photoprotective agent against UV radiation damage due to its strong absorbance in the UV region and radical scavenging activity.[247]

7.2.2. General Structure of Eumelanin

Eumelanin is primarily composed of two L-Dopa derivatives, 5,6-dihydroxyindole (DHI) and 5,6-dihydroxyindole carboxylic acid (DHICA), which are drawn in Figure 7.1. These monomers, along with several related quinones, and other intermediates are typically linked by the formation of carbon-carbon bonds at the 2, 3, 4, and 7 positions.[248] The specific concentrations of DHI, DHICA and other monomers are dependent upon the reaction protocol. DHI is the dominant species present in lab-synthesized pigments, as naturally occurring enzymes such as tyrosinase-related protein 2 (tyrp2), also known as dopachrome tautomerase, are required for production of DHICA.[117,242,249]

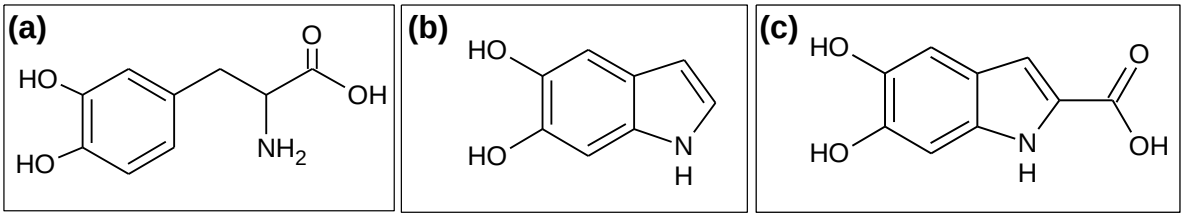

Figure 7.1 *Chemical structures of (a) L-Dopa, (b) DHI, and (c) DHICA.*

Originally, eumelanin was believed to be an extended sheet of the polymerized monomers. In the early 2000s, quantum chemical calculations and scanning tunneling electron microscopy proposed a secondary structure of stacked oligomers.[250] These oligomers can contain up to eight monomers but are typically limited to four or five. The oligomers link together three-dimensionally through π conjugation and hydrogen-bonding interactions.[251,252] As a result, the eumelanin aggregates over time, typically forming rod-like particles,[251] spherical particles,[253] or fibrils,[254] based on the eumelanin composition and work up.

7.2.3. Synthesis of Eumelanin

Naturally occurring eumelanin is synthesized by derivatization and polymerization of tyrosine, as controlled by a series of enzymes.[249] Isolation of biologically synthesized eumelanin is difficult, as surrounding tissues, proteins, and lipid layers require harsh conditions for extraction that may damage the structure of the complex. Fortunately, eumelanin may also be synthesized in the laboratory using simpler and less expensive protocols. Laboratory synthesis of eumelanin typically starts with tyrosine or L-Dopa, although DHI, DHICA, and dopamine have also been used to give melanin-like materials.[249,255,256] The starting monomers can be oxidized by several methods, including auto-oxidation in basic solution, enzymatic use of tyrosinase, or oxidizing agents such as $KMnO_4$ and H_2O_2.[246,249,257]

Figure 7.2 illustrates the typical synthetic pathway regarding the transformation of L-Dopa into the various monomers which combine into eumelanin. The catechol group is oxidized first to a semiquinone radical, then to the more stable quinone, dopaquinone.[249,256,258] Dopaquinone undergoes intramolecular molecular cyclization to

leucodopachrome, during which the oxygens are reduced from ketones to hydroxides and the benzene ring aromaticity is regained.[259] Oxidation of leucodopachrome's catechol oxygens then produces dopachrome.

Dopachrome can then either tautomerize to form DHICA or undergo decarboxylation to yield DHI.[260] These species, along with dopachrome, dopaquinone, and other intermediates are the monomers that combine to produce eumelanin.

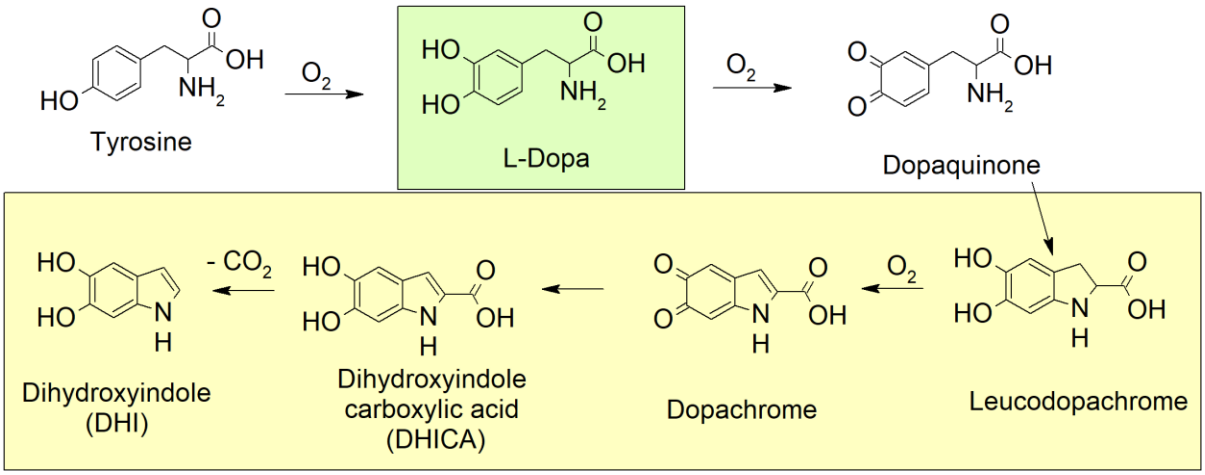

Figure 7.2 *Simplified reaction scheme for the progression from tyrosine to eumelanin. The starting monomer, L-Dopa is highlighted in green, while the primary monomers in eumelanin are highlighted in yellow. Adapted from Ref [249].*

7.2.4. Characterization of Melanin-Related Systems

Eumelanin has several properties that complicate the detailed analysis of its reaction products, intermediates, or final chemical structure. Due to π-stacking and subsequent aggregation of the oligomer sheets, eumelanin is highly insoluble in almost all solvents. However, eumelanin is partially soluble in aqueous solutions above pH 10. The increase in solubility may be attributed to disruption of the π-stacking, as well as increases in polarity to deprotonation of the hydroxyl groups.[257] The synthesis of melanin in DMSO or the use of solvent exchange can improve its solubility in other solvents.[257,261]

Solution-based NMR analysis on eumelanin is extremely rare due to the low solubility of the pigment and the complex signal of several monomers linked through varying sites.[262] Aside from the layering of oligomeric sheets, eumelanin has no crystal-like repetition, so crystallographic analysis yields very limited structural insight.[233,263]

The current model of eumelanin's structure relies on the combination of insights from several analytical techniques. UV-Vis and fluorescence spectroscopy of dilute solutions is typically used to track eumelanin's synthesis due to its strong UV-VIS absorbance and weak visible fluorescence.[264,265] Liquid chromatography, gas chromatography, and mass spectroscopy have been used to elucidate the monomeric linking and composition within eumelanin.[257,266] Microscopy such as TEM, SEM, and AFM have been used to examine the nature of eumelanin's 3D growth and aggregation.[267,268] Computational modelling has compared various geometrical, structural, and redox states of the oligomers for accuracy in predicting physical properties as observed in synthetic and naturally occurring eumelanin.[269,270]

The poor quantum yield of eumelanin fluorescence has been attributed to the intense absorbance of eumelanin across a range of energies, which prevents efficient transmission of excitation and emission light through the solution.[271] Due to the heterogeneous nature of the pigment, eumelanin has a complex fluorescence, with emission wavelength dependent on the excitation wavelength.[271-273] This chapter features fluorescence using excitation at 375 nm with emission at 470 nm based on precedence by Birch *et al.*[254]

Eumelanin has intense UV absorbance, with no defined maximum peak wavelength, but rather a gradually decreasing absorbance intensity as the wavelength increases.[264]

Traditionally, this strong but featureless absorbance has been explained by a chemical disorder model, where absorbances of the numerous species comprising eumelanin superimpose to yield the eumelanin absorbance spectrum.[264,270] Recently, computation studies have suggested that an additional contribution arises from geometric order within the aggregates. Interactions of oligomers through π-stacking enhances the delocalization of excitons, broadening the absorbance peaks of the individual species.[269,270,274]

Some of the monomers have distinct absorbances that can be analyzed to track the progression from L-Dopa to eumelanin. L-Dopa is typically assigned an absorbance at 280 nm,[256] while dopachrome is reported to absorb near 450-500 nm.[254,275] A series of indole derivatives, including DHI and DHICA monomers and dimers, all absorb between 290 nm and 360 nm.[276]

During the synthesis of eumelanin, several of the DHI and DHICA monomers and dimers are likely present together in the reaction solutions. This broadens the absorbance signal between 280 nm and 400 nm and prevents assignment of specific species. Therefore, any absorbance in this range will be given a general *DHI species* assignment.

7.2.5. Metal-Eumelanin Chemistry

Melanin pigments are well known as metal ion chelators, highlighted by neuromelanin which may bind metal ions, with a possible dual protective and toxic role in Parkinson's and Alzheimer's diseases.[277,278] Most metals bind to eumelanin through the catechol oxygens, although some ions such as Fe^{3+} also bind to the amine, and Zn^{2+} prefers the carboxylic acid.[244,279] Particularly relevant to CeO_2 is the bidentate binding to a metal ion

through the oxygens, with evidence that the catechol is actually partially oxidized to the seminquinone species, or fully to the quinone, by the metal ions.[280]

In addition to binding to the individual monomers, metal ions can influence the monomeric composition of the eumelanin aggregates.[281] For example, copper can accelerate the onset of eumelanin production, and may increase the ratio of DHICA to DHI within the synthesized pigment, while suppressing the eumelanin's fluorescence.[281] As the DHICA:DHI ratio controls the eumelanin properties such as solubility and antioxidant activity, knowledge of metal ion's influence over the monomer ratio is essential for application of the synthesized pigment.

L-Dopa, dopamine, and other derivatives are known to bind to numerous metal and metal oxide surfaces, including TiO_2 and MnO_2, typically through the catechol groups as seen with metal ions.[232,282] Binding often proceeds through an electron transfer from the catechol to the metal oxide, reducing the metal ion and oxidizing the catechol to the semiquinone, or eventually to the quinone.[283,284] Eumelanin's UV-Vis absorbance, dual radical production and scavenging ability, binding capabilities, and semi-conductivity[117,285] give these metal oxide-melanin composites promise in several applications, including photovoltaics and biomaterials[286-288]

7.2.6. CeO_2 - Catechol Chemistry

Cerium oxide has demonstrated similar activity with L-dopa and dopamine as other metal ions and metal oxides, as reported by Andreescu *et al.* among others.[235,236,289] The semiquinone or quinone acts as a bidentate ligand, binding to the surface of the CeO_2, with CeO_2 turning dark brown or black instead of white or yellow due to the establishment of a charge transfer species (Figure 7.3).[235] The catechol group is essential, as absence

of either hydroxyl group prevents activity with CeO_2, as seen with phenylalanine and seratonin.[236]

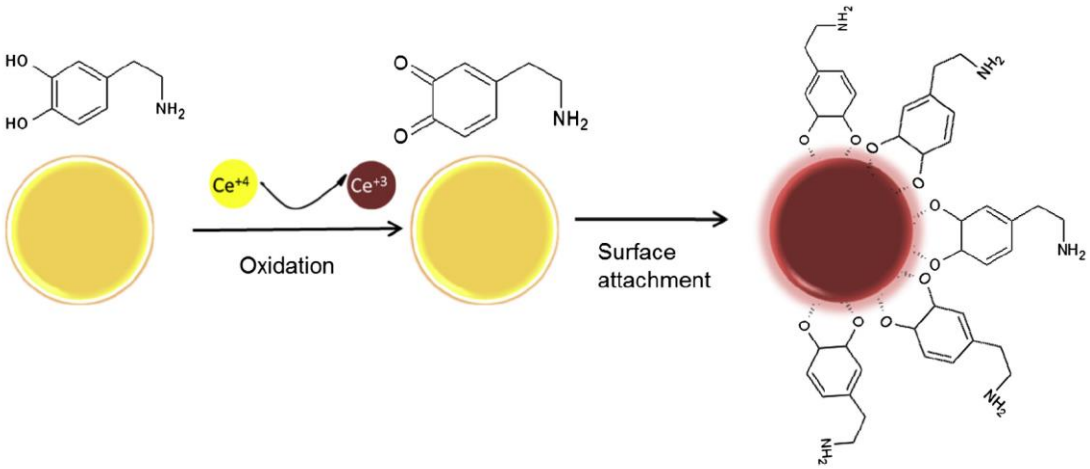

Figure 7.3 *Diagram of dopamine interaction with CeO_2 nanoparticle, indicating oxidation of the catechol by CeO_2 followed by adsorption to the CeO_2 through the quinone group.*[235]

In solutions with pH > 10, electrostatic attractions between surface cerium ions and the deprotonated catechol groups are also possible. If this attraction is purely electrostatic with no transfer of electrons from the catechol to CeO_2, the color change observed by Andreescu would not be present. Alternatively, adsorption of dark eumelanin pigments produced later in the auto-oxidation of L-Dopa may explain the nanomaterial's color change, although this is inconsistent with the rapid color change of CeO_2.

There is a possibility that CeO_2 may mimic the enzyme, dopachrome tautomerase (DCT), which suppresses the decarboxylation of dopachrome to DHI, increasing the DHICA:DHI monomer ratio in melanin.[290] DHICA-rich melanins often have a reduced UV-VIS absorbance overall compared to DHI-melanin,[291] except for a peak near 320 nm. The fluorescence at 470 nm has been attributed to DHICA monomers within eumelanin.[254,271]

This particular mechanism is typically quantified by monomer ratios as determined by GC-MS or HPLC analysis, which is beyond the scope of this work, but the possibility of DCT-like activity by Eu-CeO_2 must still be considered.

7.3. Methods and Materials

7.3.1. Chemicals

All purchased chemicals were of analytical grade used as received with no further purification. L-dihydroxyphenylalanine (L-Dopa) was purchased from Acros Organics, and ammonium hydroxide was purchased from Pharmco-Aaper. CeO_2 nanoparticles (<20 nm diameter), and fumed silica (200-300 nm diameter aggregates) were purchased from Sigma Aldrich.

7.3.2. Synthesis of Eumelanin

Eumelanin was synthesized through the autoxidation of L-Dopa in basic conditions as adjusted from Birch *et al*.[254] All reaction solutions and dilutions were prepared using DI H_2O adjusted to pH 10 using NH_4OH, unless otherwise noted. A 2 mM stock solution of L-Dopa was prepared by dissolving L-Dopa in pH 10 H_2O, and stirring for a minimum of 15 minutes or until the L-Dopa finished dissolving. The reaction solution was prepared by transferring a portion (typically 1 mL to 10 mL) of stock solution to a glass vial and diluting the solution to 1 mM L-Dopa using an equal portion of pH 10 H_2O. The vial was capped, wrapped in aluminum foil, and placed in a shaking incubator. The reaction solution was then incubated at 37 °C in the dark with shaking for up to 48 hours, with solution removed at regular intervals for analysis. This procedure for melanin synthesis is referred to as the *control procedure*.

Eu-CeO_2/L-Dopa samples were prepared by modification of the *control procedure.* The chosen Eu-CeO_2 morphology (nanorods, nanocubes, annealed nanorods, or nanowires) was dispersed in pH 10 H_2O to make samples with concentrations of 0.25 mg Eu-CeO_2 nanomaterial per mL H_2O. These stock solutions (Eu-CeO_2 stock) were sonicated for 5 minutes using a horn sonicator to break apart aggregates. The L-Dopa stock solution was diluted with the Eu-CeO_2 stock instead of pH 10 H_2O. The reaction solution therefore had 1 mM L-Dopa and 0.2 g/mL Eu-CeO_2 nanomaterials.

7.3.3. Spectroscopic Measurements

Fluorescence and UV-Vis absorbance spectra were collected at 15 minutes, 1 hr, 3 hr, 5 hr, 10 hr, 24 hr, and 48 hr. 200 µL of the reaction solution was removed and centrifuged at 7000 rpm for 5 minutes. The supernatant was removed and centrifuged a second time to ensure complete removal of any Eu-CeO_2 sample, if applicable. 100 µL of this supernatant was diluted using 2 mL DI H_2O. This final solution represents a theoretical 50 µM L-Dopa concentration and is used for the UV-VIS and fluorescence measurements.

UV-Vis spectra were collected on an Agilent Technologies Cary 60 UV-Vis spectrometer scanning from 200 nm to 800 nm using a 1 cm path length. Steady-state fluorescence spectra were collected on a Shimadzu RF-5301PC Spectrofluorometer with slit widths of 10 mm, using a 1 cm x 1 cm quartz cuvette. Emission was measured between 400 nm and 600 nm following excitation at 375 nm.

7.4. Results: Spectroscopic Features of Eumelanin Synthesis

7.4.1. Baseline Melanin Synthesis (37 °C, pH 10)

Upon dissolving L-Dopa in pH 10 H_2O, the solution rapidly turned a light yellow, deepening over time to orange then brown, then darkening so the solution appeared black unless diluted, at which point it was a tan color. These color changes overall match the literature progression from L-Dopa to synthetic melanin, except for the absence of the red-color attributed to dopachrome.[254]

Exciting the L-Dopa solution at 375 nm initially produces fluorescence with maximum intensity at 520 nm, and within hours this emission maxima shifts to ~470 nm (Figure 7.4a). The red-shift has been attributed to the consumption of intermediate species such as dopachrome.[254] As seen in Section 7.5.2, the peak shift from 520 nm to 470 nm is observed in all samples on similar time scales following excitation at 375 nm. Once the shift to 470 nm is completed, the emission continues to increase in intensity at this wavelength for the remainder of the experiment.

When measuring UV-Vis absorbance, only the L-Dopa absorbance at 280 nm is observed at the 15-minute time point. This sample also has a strong background absorbance, most likely from scattering of undissolved L-Dopa. Dopachrome evolves within the first hour, identified by the broad peak at 475 nm.[292] At the 5 hour time point, the dopachrome peak is minimized due to the production of eumelanin and is fully obscured by 24 hours.

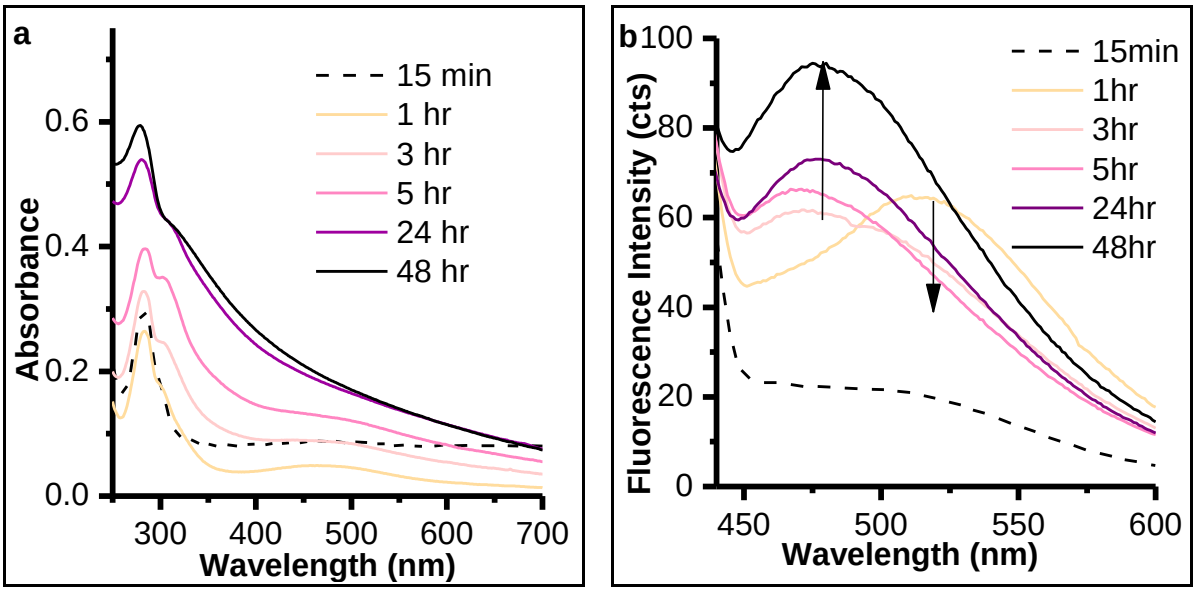

Figure 7.4. *L-Dopa (a) UV-Vis absorbance spectra, and (b) fluorescence spectra over time with excitation at 375 nm, with L-Dopa solutions at 37 °C and pH 10.*

The broad and monotonically decreasing absorbance of eumelanin dominates the solution's absorption spectrum after 24 hours. The increase in absorbance by eumelanin in the UV region cannot be decoupled from the L-Dopa and DHI species absorbance, preventing quantifiable comparisons of concentrations over time. However, the presence of a peak at 280 nm after 48 hours indicates unreacted L-Dopa in solution, with the shoulder near 320 nm presumably due to DHI species.[251]

7.4.2. Effect of temperature and pH

The effects of temperature and reaction pH were optimized before using the eumelanin synthetic system as a probe of the relative chemical reactivities of the Eu-CeO_2 nanomaterials. Slow or inefficient conversion of L-Dopa to eumelanin introduces error due to a high signal to noise ratio, as dilute concentrations of eumelanin have extremely weak fluorescence. Furthermore, slow melanin synthesis is time inefficient.

Conversely, a fast reaction can convert all L-Dopa to melanin before the L-Dopa has an opportunity to react with the Eu-CeO_2 nanomaterials.

Birch *et al.* reported auto-oxidation of L-Dopa in both basic and neutral solutions, with melanin synthesized at both room temperature and at 37 °C. Increasing the reaction temperature and pH increased the rate of eumelanin production. In addition, the 520 nm→470 nm peak shift was not observed at pH 7.[254]

To confirm these results, melanin was synthesized from L-Dopa solutions using either DI H_2O or pH 10 H_2O, with the reactions run at either room temperature or at 37°C. Figure 7.5 shows the fluorescence of the four L-Dopa solutions after 24 hours. While the reactions in DI H_2O do exhibit some fluorescence assignable to melanin, the intensity was very weak and barely stronger than the baseline. Increasing the pH to 10 drastically increases the fluorescence intensity. The L-Dopa amine, carboxylic acid and one catechol oxygen are all deprotonated,[293] facilitating its oxidation to dopaquinone and starting the cascade through the various monomers composing melanin.

Increasing the reaction temperature to 37 °C very slightly increased the melanin fluorescence intensity compared to reactions at room temperature, independent of solution pH. Due to the extremely weak fluorescence of samples using DI H_2O, reactions incorporating Eu-CeO_2 materials were run using pH 10 H_2O.

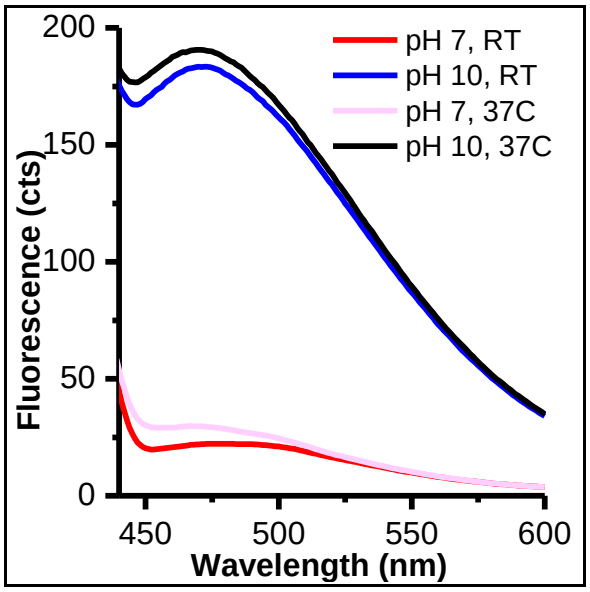

Figure 7.5 *48-hour fluorescence spectra of L-Dopa solutions with different solution pH and reaction temperatures.*

7.5. Results: Influence of Eu-CeO_2 Nanomaterials on Eumelanin Synthesis

7.5.1. Eu-CeO_2 Nanomaterials

Eumelanin was synthesized from L-Dopa in the presence of Eu-CeO_2 nanowires, nanorods, annealed nanorods, and nanocubes discussed in Chapters 2-4. The interaction of L-Dopa with the Eu-CeO_2 materials was evaluated three ways: changes in Eu-CeO_2 color, changes in fluorescence intensity of the L-Dopa solution, and changes in UV-VIS absorbance of the L-Dopa solution. Representative TEM images of the various Eu-CeO_2 morphologies utilized in these experiments are provided in Figure 7.6.

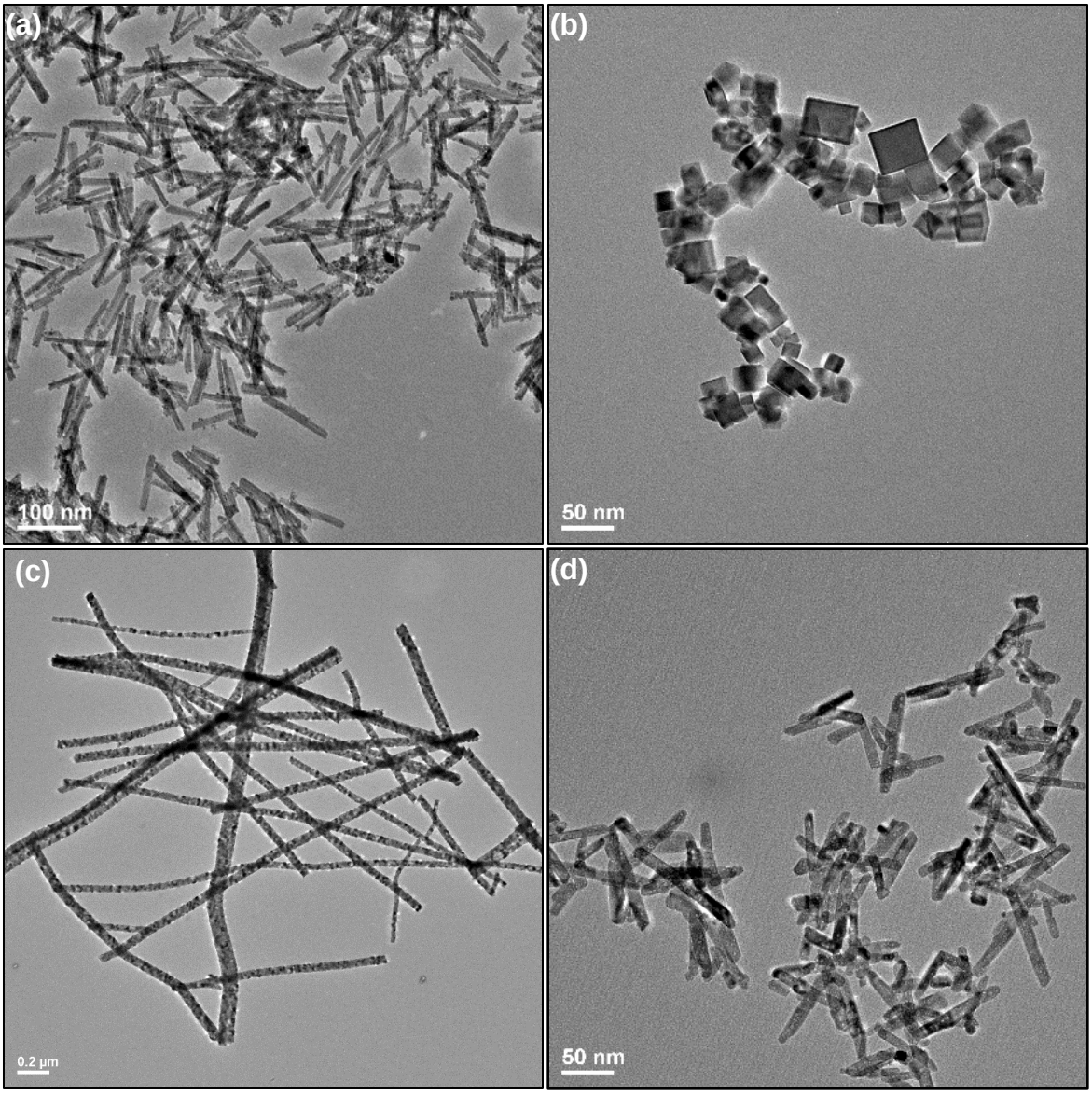

Figure 7.6 *Representative TEM images of Eu-CeO_2 (a) nanorods, (b) nanocubes, (c) nanowires, and (d) annealed nanorods.*

7.5.2. Color Changes

Photographs of Eu-CeO_2 suspensions were acquired prior and shortly after addition of L-Dopa (Figure 7.7). The concentrations, as detailed in Section 7.3.2, are too dilute for useful imaging, so the suspensions in Figure 7.7 are more concentrated with ~1-2 mg Eu-CeO_2/mL and ~5 mM L-Dopa concentrations. These solutions are only used here to

represent the visual color changes consistent with those seen under with more dilute concentrations. All quantifiable optical analysis (fluorescence, UV-Vis) is discussed later using the concentrations described in Sections 7.3.2 and 7.3.3.

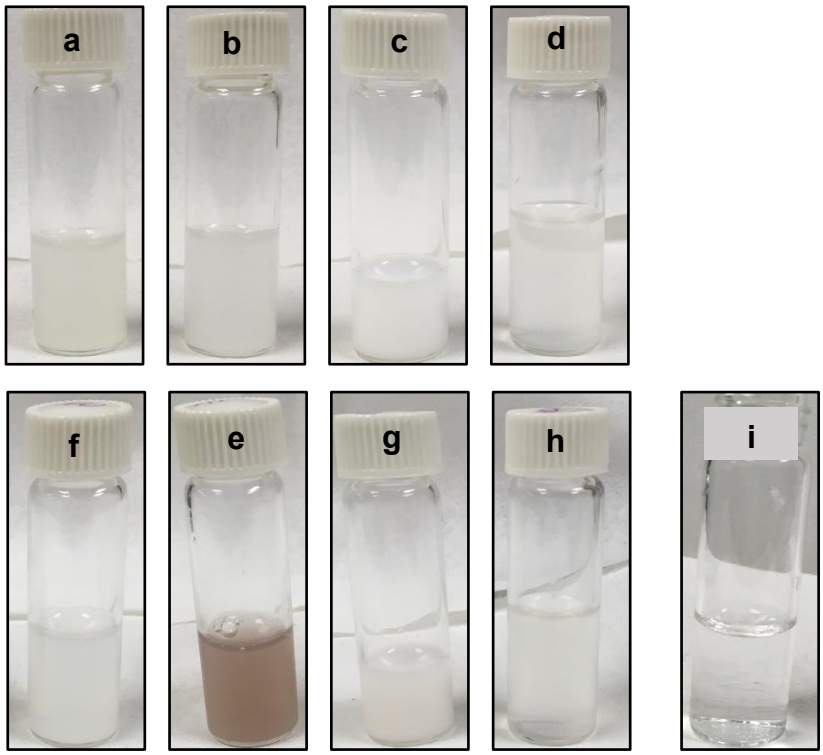

Figure 7.7 *Photographs of suspensions of Eu-CeO_2 nanomaterial before and shortly after addition of L-Dopa. Top Row: Eu-CeO_2 (a) nanowires, (b) nanorods, (c) nanocubes, and (d) annealed nanorods prior to addition of L-Dopa. Bottom Row: Eu-CeO_2 (f) nanowires, (e) nanorods, (g) nanocubes, (h) annealed nanorods, and (i) control samples 2 minutes after addition of L-Dopa.*

All Eu-CeO_2 suspensions are cloudy and slightly off-white, while the L-Dopa stock solution is colorless, with a trace orange color visible to the unaided eye but undetectable to the camera. Upon mixing, the annealed nanorod, nanowire, and nanocube suspensions show no difference in color. Only the nanorod sample turns dark pink within seconds, and dark brown within three minutes. After several hours, the other nanomaterial samples turn a similar dark brown along with the control sample. The dark

color of the nanorod suspension may be attributed to a color change in the nanorods, not observed in the other morphologies.

DI H_2O was also used to prepare the Eu-CeO_2 suspensions and L-Dopa solutions. By decreasing the pH from 10 to ~7, the L-Dopa catechol and amine groups are no longer protonated, significantly slowing the auto-oxidation of L-Dopa to melanin. After 48 hours, all samples, including the nanorods, progress to dopachrome, indicated by a yellow supernatant. Most Eu-CeO_2 nanomaterials remain white, with only the nanorods turning black. This matches the rapid color change of the rods at pH 10, suggesting that the unique chemical activity of the nanorods is active with the early monomers.

7.5.3. Fluorescence Suppression

The fluorescence of L-Dopa solutions was measured to quantify any differences in the synthesis of eumelanin. These samples were prepared and analyzed as described in Section 7.3, with Eu-CeO_2 removed through centrifugation. Unless otherwise indicated, Eu-CeO_2 *samples* or *solutions* refer to supernatants of the L-Dopa/nanomaterial samples after centrifugation and dilution which should, at most, contain only traces of the nanomaterials.

All four of the Eu-CeO_2 stock solutions were mixed with an aliquot of the same L-Dopa solution within 1 minute of each other. A control sample with no Eu-CeO_2 material was also prepared at the same time using the same L-Dopa stock, and is referred to as the *control sample*. Divergence of the Eu-CeO_2 samples from the control can be attributed to chemical reactivity of the Eu-CeO_2.

The addition of Eu-CeO_2 nanowires or annealed nanorods has a minimal influence over the synthesis of melanin, as determined by fluorescence at 470 nm (Figure 7.8b,d). In general, this emission steadily increases in both samples over the 48 hours, except for unexpectedly intense emission from the nanowire sample at 5 hours. Except for the nanowire 5-hour measurement, this matches the evolution of fluorescence observed in the control sample (Figure 7.4a).

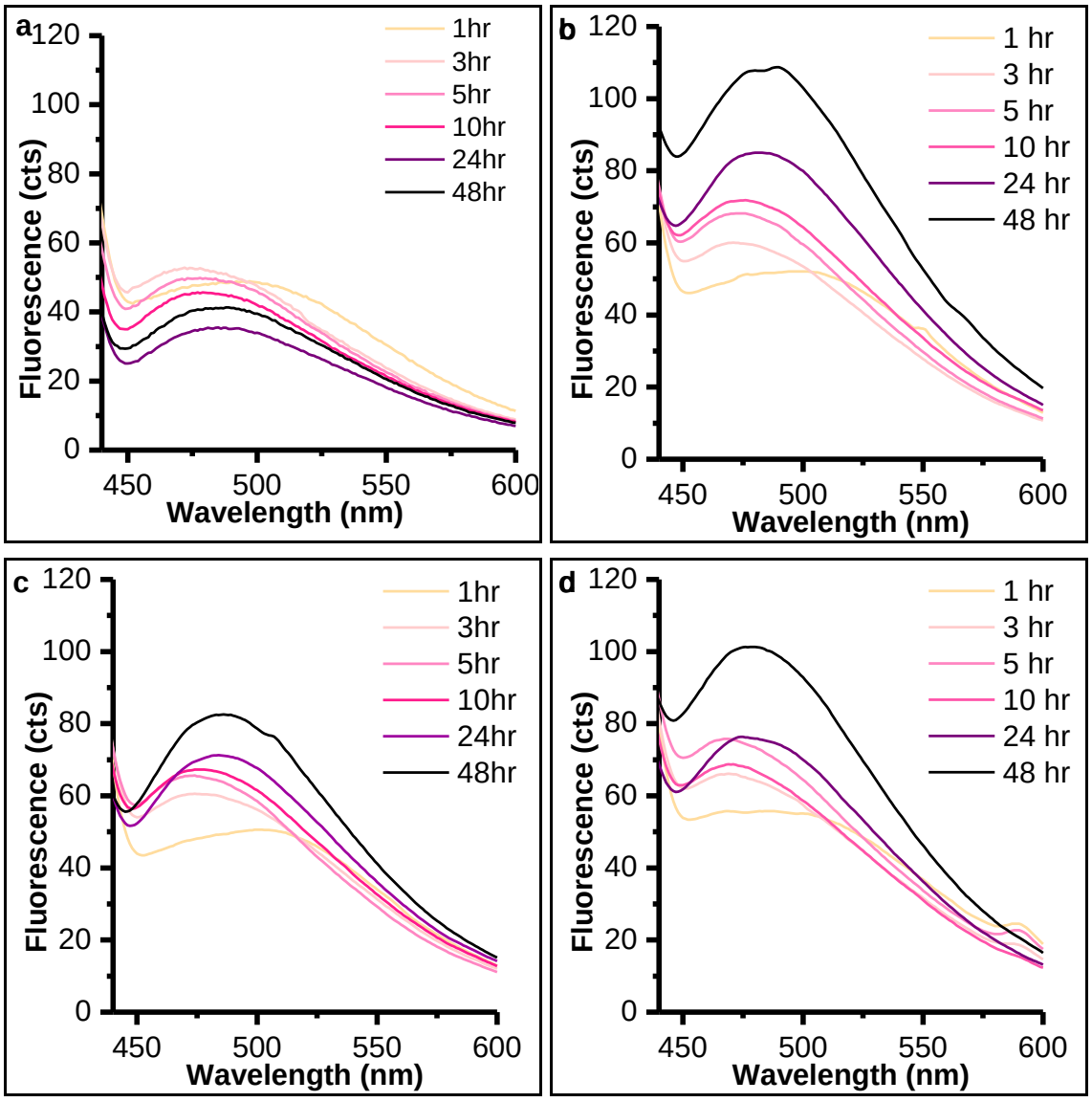

Figure 7.8 *Fluorescence spectra following excitation at 375 nm for (a) nanorods (b) annealled nanorods, (c) nanocubes, and (d) nanowires. The minor fluorescence near 590 nm observed in (d) is attributed to trace Eu^{3+} in unremoved nanowires.*

In contrast to wires and annealed rods, the unannealed morphologies (nanorods and nanocubes) both significantly suppress the melanin-associated fluorescence compared to the control sample (Figure 7.8a,b, Figure 7.4a). The nanorods are particularly active in fluorescence suppression, with only a slight increase in emission at 470 nm for the first 3 hours (Figure 7.8c). For the remainder of the first 24 hours, the emission at 470 nm steadily decreases before intensifying over the last 24 hours.

7.5.4. Normalized Fluorescence Suppression

The 15-minute control sample is assumed to represent all L-Dopa solutions in the instant prior to addition of Eu-CeO_2. At each time point, the raw fluorescence intensity at 470 nm of each sample is normalized to the control's raw intensity at 15 minutes. This normalization is calculated as $I_t/I_{Control(15min),}$ where I_t is the raw intensity of a specific sample at time t, and $I_{control(15min)}$ is the raw intensity of the control at 15 minutes.

The normalization allows easier comparison of samples over time, as well as to each other. A normalized intensity of 4.0 indicates a sample's fluorescence has increased 4-fold relative to the control at 15 minutes. The change in fluorescence over a time period for a specific sample is described as a percent change relative to the first intensity. If the intensity increases from 4.0 to 5.0 at the next time point, this is a 25% increase in the fluorescence intensity, while a decrease in normalized intensity from 4.0 to 3.5 would be a 12.5% decrease in intensity.

The progression of melanin-associated fluorescence can be separated into three stages: a rapid intensification in the first hour, slower intensification between 1 and 5 hours, then finally plateauing from 10 to 48 hours (Figure 7.9).

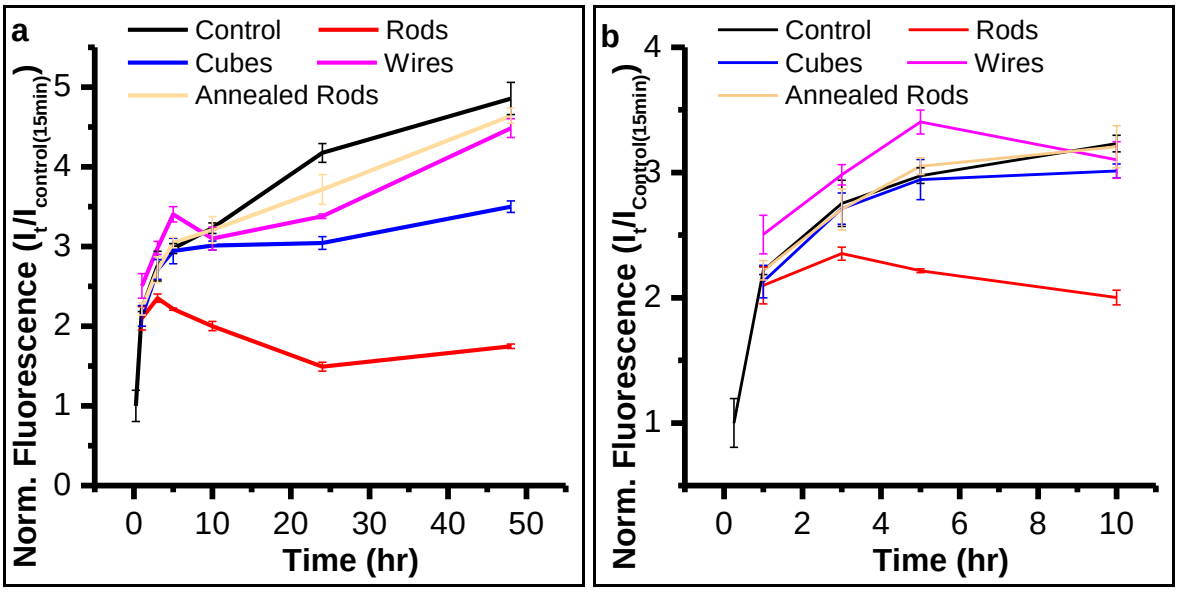

Figure 7.9 *Plots of normalized fluorescence intensities of the samples (a) for the full 48 hours and (b) over the first 10 hours.*

The increase in fluorescence during the first stage (15 minutes to one hour) is likely due to both the oxidation of L-Dopa to the various monomers and the establishment of the initial dimeric and some higher order oligomers. After 1 hour, the normalized intensities indicate a 2-fold increase in fluorescence intensity for all samples relative to the control at 15 minutes, except the nanowire sample which intensifies 2.5 fold.

The second stage of the fluorescence evolution lasts from 1 hour to 5 hours, as remaining L-Dopa continues to oxidize into its various derivatives. The 4- or 5-member oligomeric structures are also established in this time and begin stacking through π-interactions and hydrogen bonding.[265] The production of oligomers increases the fluorescence intensity, although the rate of fluorescence intensification slows over time as most monomers are incorporated into the oligomers, and the main chemical activity shifts to aggregation. The emission peak shifts from 520 nm to 470 nm, attributed to the progression from early intermediates to the final DHI/DHICA monomers.[254]

The control, nanocube, and annealed nanorod samples all show an increase in normalized intensity from about 2.1 at 1 hour to about 3.0 after 5 hours, representing an increase of about 40% during this time. During this time range, the nanorod sample's normalized fluorescence increases from 2.1 to 2.2, representing a meager 5% increase in eumelanin fluorescence.

The nanowire sample also appears to be an outlier in this time range, emitting significantly stronger than the other samples with a normalized intensity of 2.5 at 1 hour and 3.4 at 5 hours, an increase of about 35%. This stronger emission may be due to trace nanowires remaining in solution through the first five hours, artificially elevating the emission intensity. Eu^{3+} fluorescence at 590 nm was detected in these samples but was absent in samples starting at 10 hours (Figure 7.8d). The nanowire emission increases at a similar rate as the control sample throughout the 48-hour experiment, except for the decrease in the nanowire intensity between 5 and 10 hours. The similar intensification rates suggest that the rate of conversion of L-Dopa is comparable in both solutions.

The final stage, from 10 hours to 48 hours, is characterized by the slow but steady increase in fluorescence intensity by most samples (Figure 7.9b). While some monomers are still oligomerizing, the primary activity during this phase is geometric arrangement of the sheets. The normalized fluorescence of the control increases from 3.2 at 10 hours to 4.8 at 48 hours, equal to a 50% increase. The nanowires and annealed nanorods have very similar intensities to the control, increasing from about 3.2 to 4.5 during the same range, which is about a 45% increase.

The nanocube sample shows some suppression of the eumelanin fluorescence starting at 10 hours, increasing from 3.0 at 10 hours to 3.5 after 48 hours, which is a 16%

increase. The nanorod sample is still the most active of the four morphologies, decreasing 10% from 2.0 to 1.8 over the same time range.

The extent of fluorescence suppression by a sample is calculated by comparing its fluorescence intensity to the intensity of the control at a given time point, as defined in Equation 7.1 and detailed in Table 7.1. $I_{Control(t)}$ is the normalized intensity of the control at a given time *t* and $I_{Sample(t)}$ is the normalized intensity of a sample at time *t.*

$$\%Suppression = \frac{I_{Control(t)} - I_{Sample(t)}}{I_{Control(t)}} \quad \text{(Eqn 7.1)}$$

Table 7.1 *Summary of normalized fluorescence intensities and % suppression for samples after 48 hours.*

Sample	**Norm. Fluor, 48 hr**	**% Suppression**
Control	4.9 (± 0.2)	0%
Nanowires	4.5 (± 0.1)	8.9%
Annealed Nanorods	4.6 (± 0.1)	6.5%
Nanocubes	3.5 (± 0.1)	28.6%
Nanorods	1.75 (± 0.03)	64.2%

The calculated % suppression at 48 hours further highlights the differences between samples, with the nanorods suppressing almost 65% of the melanin fluorescence observed in control, while the annealed materials suppress the eumelanin fluorescence by less than 10%.

7.5.5. UV-Vis Absorbance

UV-Vis absorbance spectroscopy was used in conjunction with the fluorescence to track production and consumption of the monomers.

After 1 hour, all samples have similar spectral features, with dopachrome and L-Dopa peaks at 475 nm and 280 nm respectively, and the DHI species shoulder at 320 nm

(Figure 7.10a, c). Eumelanin-associated absorbance is very weak at 1 hour, with a significant valley present near 375 nm in all samples.

Two offsets in sample absorbance separate the five samples into three groups: the control, the nanowires, and the other three Eu-CeO_2 materials. These offsets are likely caused by scattering by melanin aggregates and/or trace Eu-CeO_2 nanomaterials within the solution, as indicated by the absorbance at 700 nm. The non-zero absorbance at 700 nm in the control sample can only originate from eumelanin. The increased absorbance by the Eu-CeO_2 samples suggests both eumelanin and Eu-CeO_2 scattering. The scattering is most significant in the nanowire sample, which is consistent with the Eu^{3+} fluorescence.

Two differences suggest chemical reactivity by the Eu-CeO_2 materials. First, the control and nanorod samples have near-identical absorbance values at 280 nm. As the nanorod sample has Eu-CeO_2 scattering, the absorbance by L-Dopa is lower in the nanorod sample than the control. The L-Dopa concentration may be lower in the nanorod sample, due to either oxidation of L-Dopa or adsorption of the monomer to the nanorods.

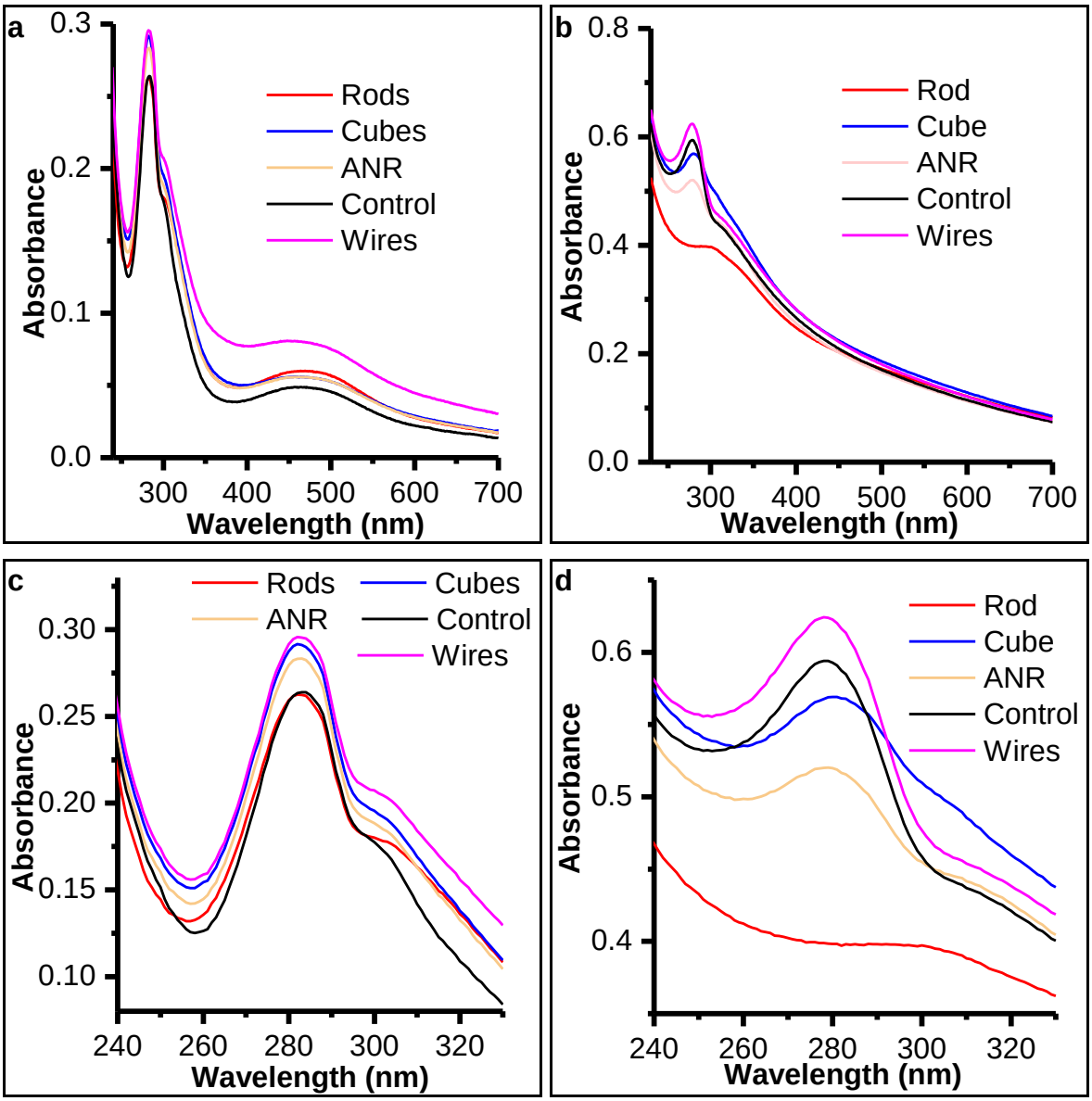

Figure 7.10 *UV-Vis absorbance of reaction solutions after removing Eu-CeO_2 materials at time (a,c) 1 hour and (b,d) 48 hours.*

Also, despite near identical absorbance intensities at 280 nm, the DHI species shoulder is weaker and less defined in the control sample compared the nanorod sample. This indicates the nanorods may accelerate production of DHI species. The other Eu-CeO_2 samples appear to also have more defined shoulders, but these samples have more intense L-Dopa peaks which prevents direct comparison.

After 48 hours (Figure 7.10b, d), all samples absorb similarly from 450 nm to 700 nm, with only the eumelanin-like signal observed. The absorbance of all samples at 700 nm is likely not from Eu-CeO_2 scattering, but rather the tail of eumelanin absorbance or eumelanin scattering. The dopachrome signal is undetectable in all samples, either obscured by eumelanin or consumed by the production of eumelanin.

The primary differences in absorbance at 48 hours are in the UV region, due to differences in L-Dopa or DHI species concentrations of the samples. The absorbance values in the control and nanowire samples are visually similar, both featuring strong L-Dopa peaks with slight shoulders due to DHI species. The nanocube and annealed nanorods also exhibit a L-Dopa peak, but with a more dominant DHI species shoulder as compared to the control and nanowire samples. Finally, the nanorod sample has significantly reduced absorbance through the region, with strongly suppressed L-Dopa leading to a plateau instead of a peak and shoulder.

Table 7.2 lists the absorbances and standard deviations for each sample at 280 nm and 320 nm after 48 hours, enabling comparisons of the L-Dopa and DHI species concentrations, respectively. The standard deviations minimize most differences between samples, except in the nanorod and annealed nanorod samples. For the nanocube sample, the ratio of the L-Dopa and DHI species absorbance values after 48 hours is consistent between trials, with the standard deviation at 280 nm and 315 nm due to differences in the baseline absorbance. Therefore, the strong DHI shoulder relative to the L-Dopa peak may still be significant.

Table 7.2 *Absorbance values of melanin solutions after 48 hours, measured at 280 nm and 320 nm, and calculated ratio of 315 nm: 280 nm absorbance.*

Sample	**Abs at 280 nm**	**Abs at 315 nm**	**$Abs_{315\ nm}$: $Abs_{280\ nm}$**
Control	0.59 (± 0.01)	0.43 (± 0.01)	0.73
Nanowires	0.62 (± 0.05)	0.44 (± 0.04)	0.71
Annealed Nanorods	0.52 (± 0.01)	0.43 (± 0.01)	0.82
Nanocubes	0.57 (± 0.04)	0.47 (± 0.03)	0.82
Nanorods	0.39 (± 0.01)	0.38 (± 0.01)	0.97

The ratio of the DHI species absorbance to L-Dopa absorbance increases in the order of control ≈ nanowires < nanocubes ≈ annealed nanorods < nanorods. Except for the nanocubes, this trend is consistent with the fluorescence suppression discussed in Section 7.5.3. The nanorods again appear to interact with L-Dopa through a different mechanism than the other samples, with significant reduction in eumelanin fluorescence, as well as in L-Dopa and DHI species absorbances.

7.5.6. SiO_2 and CeO_2 Nanoparticles

Fumed silica (SiO_2) and commercially produced CeO_2 nanoparticles (CeO_2 NPs) were compared with Eu-CeO_2 nanorods to test the L-Dopa adsorption to surfaces other than Eu-CeO_2. The SiO_2 had a 200-300 nm reported diameter, but upon sonication in H_2O, a heavily aggregated network of small particles was observed, with particle diameters of 15 (± 4) nm (Figure 7.11a). CeO_2 NPs were a mixture of very large and very small cubes, prisms, and spherical particles, with an average diameter of 13 (± 10) nm (Figure 7.11b). Reaction samples with SiO_2 and CeO_2 NPs were assembled described in Section 7.3.2, by preparation followed by mixing of nanomaterial and L-Dopa stock solutions. The final concentration of the fumed silica and CeO_2 NPs are increased to 1 mg/mL, compared to the Eu-CeO_2 nanorod concentration of 0.2 mg/mL, to enhance any effect of the SiO_2 or CeO_2 NPs on the auto-oxidation of L-Dopa.

The fluorescence of the control, SiO_2, CeO_2 and Eu-CeO_2 samples are shown in Figure 7.12, normalized to the control sample's fluorescence at 15 minutes. The fumed silica has no influence on the production of eumelanin, with a comparable normalized intensity relative to the control. The CeO_2 nanoparticles do suppress the eumelanin fluorescence, although not as effectively as the Eu-CeO_2 nanorod sample. The nanoparticle suspension is five times more concentrated than the nanorod suspension, so the nanoparticle's activity is further reduced compared to the nanorod activity.

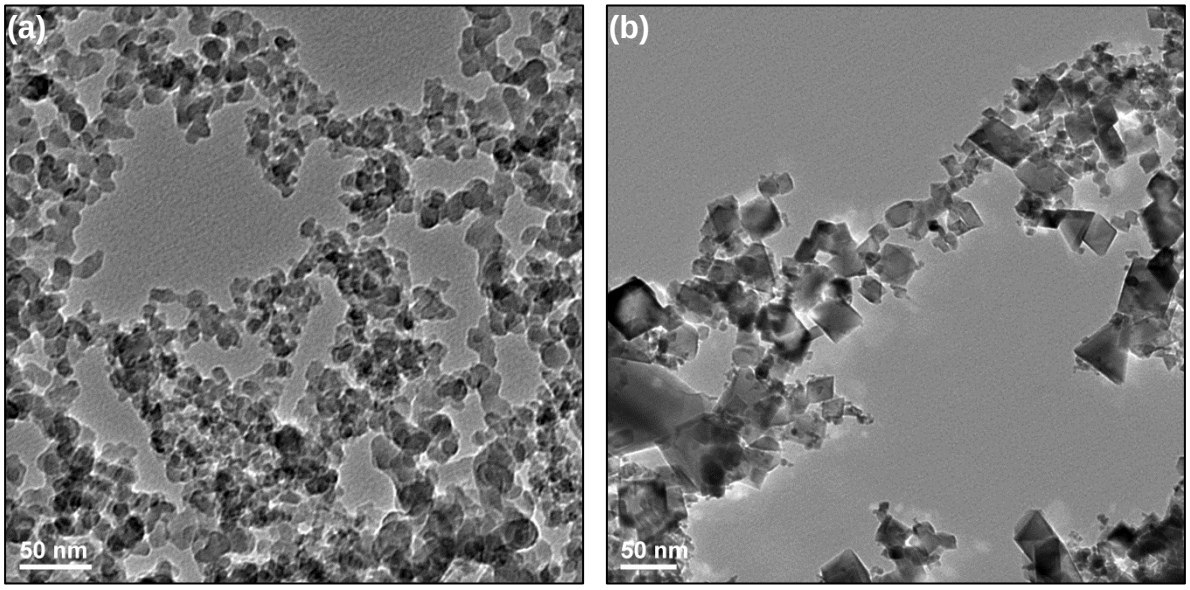

Figure 7.11 *Representative TEM images of (a) fumed silica (SiO_2), and (b) CeO_2 nanoparticles.*

These results indicate the fluorescence suppression is not caused by simple adsorption of monomers to any surface, but rather that the CeO_2 host structure is chemically active with L-Dopa and its derivatives. The reduced activity of the nanoparticles, relative to the nanorods, confirms the enhanced activity of the nanorods relative to other CeO_2 morphologies.

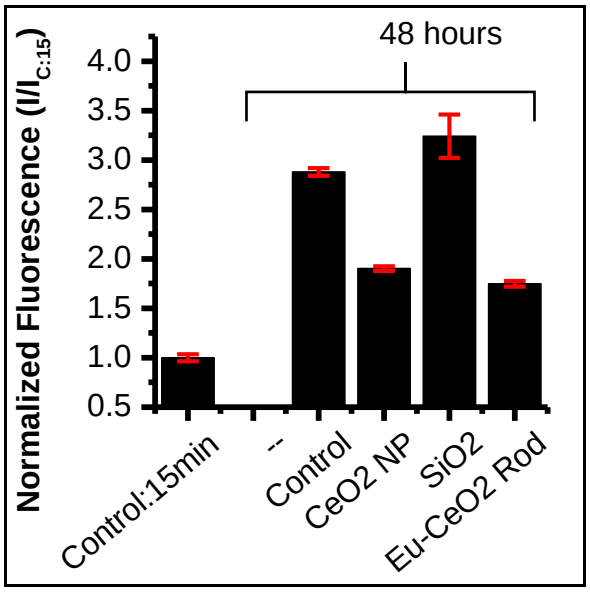

Figure 7.12 *Plot of fluorescence intensities of the control SiO_2, CeO_2 NP, and Eu-CeO_2 nanorod samples after reacting for 48 hours. Intensities are normalized to the control fluorescence at 15 minutes.*

7.6. Results: Influence of Eu^{3+} and Nanorod Concentration

7.6.1. Eu^{3+} Concentration

If the enhanced activity of the nanorods is supported by the oxidation state, increasing the Ce^{3+} concentration should have a significant influence. To probe this, the concentration of Eu^{3+} within the Eu-CeO_2 nanorod was varied from 0% to 18% by adjusting the concentration of $EuCl_3$ during synthesis (Chapter 2). As more Eu^{3+} is incorporated into the CeO_2 lattice, the concentrations of O^{2-} vacancies and Ce^{3+} defects increase due to charge balance.[25]

Samples were analyzed using 1 mg/mL Eu-CeO_2 nanorods and 1 mM L-Dopa. Adjusting the Eu^{3+} doping concentration does not significantly influence the nanomaterial size, so differences in light scattering should ideally be negligible between samples. As

a result, all spectra were collected as described in Section 7.3.3, but with no removal of nanorods by centrifugation.

As seen in Figure 7.13, all three nanorod samples exhibit significant suppression of the eumelanin fluorescence, compared to the control. The eumelanin fluorescence was identical for all three of these samples, so Eu^{3+} does not contribute to any eumelanin fluorescence suppression by Eu-CeO_2 nanorods within the range tested. Since adding Eu^{3+} should increase Ce^{3+} concentrations, this consistency suggests the enhanced activity of the nanorods relative to other morphologies is not driven by differences in oxidation states at these concentrations.

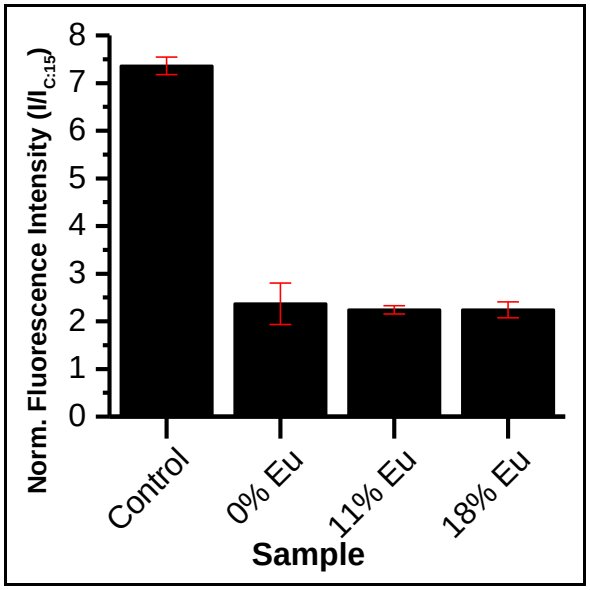

Figure 7.13 *Plot of fluorescence intensity (λ_{ex}=375 nm, λ_{em}=470 nm) after 48 hours of reaction time of Eu-CeO_2 nanorods with 0 at%, 11 at%, and 18 at% Eu. Fluorescence intensities are normalized to the control at 15 minutes.*

7.6.2. Eu-CeO_2 Nanorod Concentration

The Eu-CeO_2 nanorod concentration was varied to detect any influence of the nanorod concentration on the eumelanin fluorescence suppression. Increasing the nanorod

concentration increases the total nanorod surface area available to interact with the L-Dopa and its derivatives. If the nanorod's interaction is surface-area dependent, reducing the nanorod concentration should increase eumelanin fluorescence.

The Eu-CeO_2 2 mg/mL nanorod stock solution was diluted to concentrations between 1 mg/mL and 0.02 mg/mL. These stock solutions were then mixed with the L-Dopa stock solution as described in Section 7.3.2 to give final nanorod concentrations ranging from 0.5 mg/mL to 0.01 mg/mL. The eumelanin concentration after 48 hours was analyzed by fluorescence as described in Section 7.3.3.

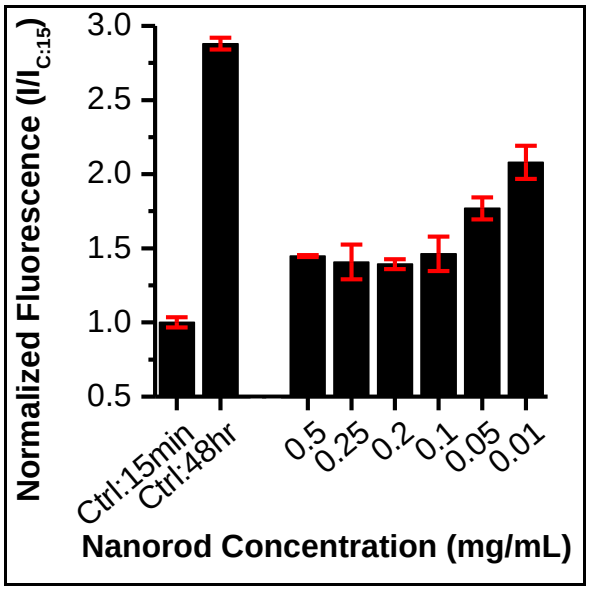

Figure 7.14 *Normalized eumelanin fluorescence intensities (λ_{ex}=375 nm, λ_{em}=470 nm) of samples with varying Eu-CeO_2 nanorod concentrations after 48 hours of reaction time.*

As seen in Figure 7.14, even 0.01 mg/mL concentrations of nanorods are still active against eumelanin, reducing the fluorescence intensity by about a third compared to the control sample after 48 hours. As the nanorod concentration is increased from 0.01 mg/mL to 0.1 mg/mL, suppression of eumelanin fluorescence also increases. However, nanorod concentrations above 0.1 mg/mL have no further impact on the eumelanin

fluorescence, which has slightly less than doubled relative to the control at 15 minutes. Therefore, above 0.1 mg/mL concentration, the nanorod concentration is in excess with regard to fluorescence quenching ability.

7.7. Discussion: Possible Mechanisms

The results of Sections 7.4, 7.5, and 7.6 repeatedly demonstrate a rapid and strong interference of Eu-CeO_2 nanorods on the synthesis of eumelanin as judged by color changes, fluorescence suppression, and changes in UV-Vis absorbance spectra. Other Eu-CeO_2 materials, such as the nanocubes and annealed nanorods also demonstrate similar, but significantly weaker activity. The nanowires overall appear inert to L-Dopa and its derivatives.

To determine the source of these different chemical reactivities, the mechanism of interactions between Eu-CeO_2 nanomaterials and the L-Dopa system must be determined. The most likely mechanism of interaction, as discussed in Section 7.2.6, is the accepted oxidation of the catechol and adsorption of the quinone. However, simple electrostatic adsorption of L-Dopa to CeO_2 or dopachrome tautomerase-like catalyzation of dopachrome to DHICA instead of DHI are also possible. The various strengths and weaknesses of these mechanisms will be discussed below.

Subsequently, the difference in physical properties of the Eu-CeO_2 nanomaterials will be highlighted with respect to potential influence on the L-Dopa system through the various mechanisms.

7.7.1. Possible L-Dopa/Eu-CeO_2 Interaction Mechanisms

Dopachrome tautomerase (DCT) mimetic activity. The least likely mechanism is controlled conversion of dopachrome to DHICA or DHI, facilitated by the Eu-CeO_2. This mechanism is primarily supported by overall reduced UV absorbance in the nanorod sample, with a defined peak near 300 nm. However, dopachrome is not present in significant amounts when the stock solutions are mixed, as determined by the absorbance of the control (Figure 7.4b) and cannot be cause the color change of the nanorods. No experiments performed thus far have indicated DCT-like activity by CeO_2, so while not impossible, it is unlikely that significant differences in chemical activity of the Eu-CeO_2 is driven by DCT-like chemistry.

Electrostatic Adsorption. The electrostatic adsorption of L-Dopa monomers or eumelanin aggregates to the surface of Eu-CeO_2 is mostly supported by the fluorescence suppression (due to removal and likely inactivation of the monomers) as well as the suppressed L-Dopa absorbance in the UV-absorbance spectra. The adsorption of eumelanin is supported by the very dark brown-black color of the nanomaterials after several days. However, the slow production of eumelanin is not consistent with the instantaneous color change. Electrostatic attraction of L-Dopa or similar monomers would not explain the nanorod color change attributed to a charge transfer, which requires partial oxidation of the L-Dopa.

Oxidation and Adsorption of L-Dopa. The most likely reaction between Eu-CeO_2 and L-Dopa is the accepted mechanism with oxidation of the catechol group, followed by adsorption to the Eu-CeO_2 surface. This mechanism is associated with a rapid color change in CeO_2 from off-white to dark brown, as observed in the nanorod sample. The

adsorption of the monomers would explain the suppression of eumelanin fluorescence. However, the high Ce^{3+} concentration in the nanorods should reduce its activity compared to the other samples, inverse to the observed effect. Additionally, doping with Eu^{3+} should increase the Ce^{3+} concentration, also reducing the oxidative power of the material. Instead, there is no impact on the eumelanin fluorescence.

7.7.2. Influence of Eu-CeO_2 Morphology

The different chemical abilities of the Eu-CeO_2 nanomaterials in terms of influencing the synthesis of eumelanin must be explained by differences in the material's physical properties. The most likely candidates include surface area, crystalline domain size, oxidation state, and surface functionalization.

Table 7.3 summarizes the main physical and elemental characteristics of the various Eu-CeO_2 morphologies, including physical dimensions, doping concentrations, colors, crystalline domain sizes, and the calculated surface area (S.A.) to volume ratio. This ratio uses the average dimensions of each material, assuming the nanocubes are ideal cubes, and the nanorods, nanowires, and annealed nanorods are ideal cylinders. Assuming the total mass of Eu-CeO_2 is consistent between reactions, morphologies with higher ratios will have more exposed surface area to react with melanin species.

An example of the calculations for the cylindrical materials is provided in Equations 7.2 – 7.4 using nanorods with a length (*h*) of 70 nm and diameter of 10 nm, or radius (*r*) of 5 nm. Equations 7.5 – 7.7 show the calculations for the nanocubes, with edge lengths (*a*) of 24 nm.

. *Cylindrical Materials (Rods, Wires):*

$$S.A. = 2\pi r^2 + 2\pi rh = 2\pi(5\ nm)^2 + 2\pi(5\ nm)(70\ nm) = 2356\ nm^2 \quad \text{(Eqn 7.2)}$$

$$Volume = \pi r^2 h = \pi(5\ nm)^2(70\ nm) = 5497\ nm^3 \quad \text{(Eqn 7.3)}$$

$$S.A./Volume = 2356\ nm^2/5497\ nm^3 = 0.43\ nm^{-1} \quad \text{(Eqn 7.4)}$$

Nanocubes:

$$S.A. = 6a^2 = 6(24\ nm)^2 = 3456\ nm^2 \quad \text{(Eqn 7.5)}$$

$$Volume = a^3 = (24\ nm)^3 = 13,824\ nm^3 \quad \text{(Eqn 7.6)}$$

$$S.A./Volume = 3456\ nm^2/13{,}824\ nm^3 = 0.25\ nm^{-1} \quad \text{(Eqn 7.7)}$$

Table 7.3 Summary of TEM-determined nanomaterial dimensions, EDX-determined at% Eu, XRD-determined crystalline domain size, and calculated surface area for the Eu-CeO_2 materials discussed in Section 7.5.

Sample	Dimensions (nm)	% at Eu	Domain Size (nm)	Color	Surface Area:Volume Ratio (nm^{-1})
Nanowires	Length: 1046 (± 1089) Width: 99 (±17)	8.5 ± 0.5	17.1	White	0.04
Annealed Nanorods	Length: 50 (± 22) Width: 10 (± 2)	8.2 ± 0.4	15.6	White	0.44
Nanocubes	Edge Length: 24 (±15)	8.0± 1.7	22.5	White/ Grey-Pink	0.25
Nanorods	Length: 70 (± 20) Width: 10 (± 3)	8.2 ± 0.4	6.05	Pale Yellow	0.43

Table 7.4 summarizes the fluorescence, absorbance, and observed color changes from Section 7.5.

Table 7.4 *Summary of fluorescence suppression and absorbance by Eu-CeO_2, and color changes of the Eu-CeO_2 material.*

Sample	Fluorescence Suppression (48hr)	Absorbance (48hr)	Eu-CeO_2 Color Change
Control	0%	L-Dopa peak, small DHI species shoulder	-----
Nanowires	8.9%	Identical to control	None
Annealed Nanorods	6.5%	Suppressed L-Dopa	Brown after hours
Nanocubes	28.6%	Elevated DHI relative to L-Dopa	Brown after hours
Nanorods	64.2%	Strongly suppressed L-Dopa and DHI	Immediately

Surface Area. The simplest explanation for the differences in chemical reactivity is the range of surface areas of the four morphologies, with high surface areas enhancing the effect of all three mechanisms. The four nanomaterials have calculated surface areas increasing from nanowires > nanocubes > nanorods > annealed nanorods (Table 7.4). Except for the annealed nanorods, this matches the trend of fluorescence suppression. Increasing total exposed surface area of the nanorods also increases the eumelanin fluorescence suppression, as seen in Section 7.6.2, below 0.2 mg/mL nanorods.

However, differences in surface area cannot explain the lack of color change of the nanowires from white to black upon exposure to L-Dopa solution, as seen in the other materials. Furthermore, the annealed nanorods have a comparable surface area to the unannealed rods, with significant differences in chemical activity.

Ce^{3+}/Ce^{4+} Ratio. The accepted mechanism of CeO_2 oxidation of the catechol group requires reduction of Ce^{4+} ions followed by adsorption of the oxidized quinone.[235] Due to this reaction's dependence on Ce^{4+}, samples with high Ce^{3+} should exhibit less activity.

The influence of Ce^{3+} concentration is first analyzed by comparing the activity of Ce^{3+}-rich morphologies with Ce^{3+}-poor morphologies. Nanocubes and nanorods were designated Ce^{3+}-rich due to their yellow/off-white color, while the white nanowires and annealed nanorods were Ce^{3+}-poor. These assignments match literature precedence in the undoped CeO_2 counterparts.[50,120,147,294] However, the Ce^{3+}-rich morphologies suppressed the eumelanin fluorescence more than the Ce^{4+}-richer materials.

In addition, increasing the Eu^{3+} concentration should increase the Ce^{3+}/Ce^{4+} ratio within a given morphology, in turn affecting the activity of that sample. However, no difference in reactivity is seen across the entire range of Eu^{3+} concentrations tested in the nanorod samples.

Since Ce^{3+}/Ce^{4+} ratio has no influence on the reactivity of the nanomaterials, another physical property must be responsible for the activity of the nanorods. The Ce^{4+}-rich morphologies may be redox active with L-Dopa but unable to adsorb the monomers, and Ce^{3+}-rich morphologies still have high concentrations of Ce^{4+} capable of oxidizing the L-Dopa.

Exposed Planes/Surface Termination. L-Dopa and its derivatives are known chelators, donating electrons from catechol, carboxylic acid, or ketone oxygens to metal ions. Therefore, the presence exposed cerium sites, as determined by the Eu-CeO_2 surface chemistry, could be vital for adsorption of the monomers. In addition, surface hydroxyls

may undergo hydrogen bonding to the catechol hydroxyls aiding adsorption of the monomers to Eu-CeO_2.

Prior to annealing, CeO_2 nanomaterials typically have a coating of various functional groups, established through molecular or dissociative adsorption of H_2O and CO_2, or remaining from the synthetic process.[295-298] During annealing, the majority of these groups are converted to oxygen to yield CeO_2 with oxygen termination. In basic aqueous solutions (pH >8), the surface oxygens of CeO_2 are converted to hydroxides.[295] This applies to all four morphologies, but samples with higher ratios of surface O:Ce will have high densities of surface hydroxyls. While the hydroxyls can help stabilize adsorption via hydrogen bonding, they can also compete with the monomers for access to the cerium sites, preventing the monomer's oxidation and the establishment of the charge transfer to CeO_2.

The (111) plane is typically O-terminated,[20] the (220) is stoichiometrically Ce- and O-terminated,[21] and (200) is O-terminated but with half of the oxygen removed.[21] Exposed (220) and (200) are associated with enhanced catalytic activity, with energy of CeO_2 planes increases as 111 < 220 < 200.[12]

The unannealed nanorods expose predominantly (111) and (200) planes, while the cubes expose (220) and (200). In contrast, the annealed nanowires and annealed nanorods both exhibit lattice fringes associated with exposed (111) planes. Since the nanocubes and nanorods have exposed planes with Ce-termination, they may have more sites available for interactions with L-Dopa.

Crystalline Defects/Oxygen Defects. Crystal defects are often sites of enhanced chemical activity for a given nanomaterial, due to lattice strain from Ce^{3+} and other contaminants, or under-coordination of cerium ions due to oxygen vacancies.

Small crystalline domains increase the number of defects within a given crystal structure, possibly increasing the chemical reactivity of the material. As listed in Table 7.4, the Eu-CeO_2 morphologies range in crystalline domain size in the order of nanorods < annealed nanorods~nanowires < nanocubes. Except for the nanocubes, this order is consistent with the extent of eumelanin fluorescence and UV range absorbance suppression by the materials.

More relevant than the crystalline domain size may be the concentration of oxygen vacancies on the surface of the crystal lattice. These vacancies are balanced by Ce^{3+} defects typically located not as *nearest* neighbors, but rather *next-nearest* neighboring ions (Figure 7.15) according to some reports.[299] The oxygen vacancies therefore expose Ce^{4+} ions, which are exposed for adsorption through oxygen in L-Dopa and its materials. Materials with more surface oxygen vacancies may have significantly higher binding activity during the synthesis of eumelanin,

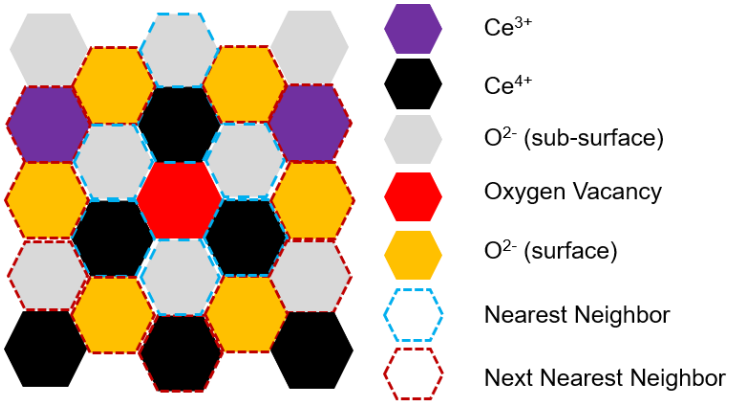

Figure 7.15 *Diagram showing oxygen vacancy on surface of CeO_2 (111) plane. Nearest neighboring and next nearest neighboring atoms are outlined in blue and red respectively. Adapted from Reference [299].*

Annealing oxidizes Ce^{3+} to Ce^{4+} and removes oxygen vacancies from the CeO_2 lattice. The nanorods and nanocubes likely have oxygen vacancies dispersed within the lattice, with even more vacancies at the surface near the edges of crystalline domains. Due to their smaller crystalline domains, the nanorods likely have more vacancies than the nanorods. The order of oxygen vacancies likely increases from annealed nanorods ≈ nanowires < nanocubes < nanorods, matching both the spectroscopic trends and the color changes of the different morphologies with L-Dopa.

Overall Mechanism

As described by Andreescu *et al.,* Ce^{4+} ions likely oxidize L-Dopa to the semiquinone or dopachrome, reducing the Ce^{4+} to Ce^{3+}, establishing a charge transfer between the monomer and CeO_2, and binding the oxidized monomer to the Eu-CeO_2 surface.[235]

The unannealed nanorods had the highest reactivity, due to their small crystalline domain, high Ce^{3+} defect and oxygen vacancy concentrations, high surface area, and higher energy (200) planes of the nanorods which facilitate binding and oxidation of L-Dopa to exposed Ce^{4+} ions. In contrast, the annealed nanomaterials have limited chemical reactivity, due to their large crystalline domains, few exposed Ce^{4+} ions, and low energy crystal planes. The nanocubes fall in the middle of the two groups, with activity supported by moderate Ce^{3+} and oxygen vacancy concentrations, as well as the highest surface area and highest energy exposed planes of the four morphologies. However, the larger crystalline domains and fewer Ce^{3+} defects reduce the nanocube activity relative to the nanorods.

7.8. Conclusions

The focus of this chapter explored the differences in Eu-CeO_2 morphologies, using the synthesis of eumelanin as a probe. First, the baseline reaction conditions of the synthesis of eumelanin from L-Dopa were established, monitored by fluorescence and UV-Vis absorbance intensities. Eu-CeO_2 nanorods, nanocubes, nanowires, and annealed nanorods were then mixed with L-Dopa very early in the reaction. Any influence of the Eu-CeO_2 materials was determined by differences in the absorbance and fluorescence of supernatant solutions, as well as color changes of the nanomaterials themselves. The highly active nanorods, as indicated by of suppression of eumelanin fluorescence, changes in the UV-Vis spectra, and a color change to black, were selected for further analysis.

Tracking the fluorescence with varying nanorod concentrations implicated the importance of the surface area for optimal activity, although above 0.2 mg/mL no further fluorescence suppression was observed with 1 mM L-Dopa solutions. Comparing the Eu-CeO_2 nanorods to CeO_2 nanoparticles and fumed silica also confirms the selectivity of this chemical activity to CeO_2, as the SiO_2 was inactive. Furthermore, the nanoparticles had significantly reduced chemical activity relative to the nanorods.

It was determined that several physical properties worked in conjunction to enhance the chemical activity of Eu-CeO_2 nanorods relative to the other morphologies. In particular, their increased oxygen vacancy concentration facilitated binding of L-Dopa. The increased surface area and crystalline defects of the nanorods relative to the other morphologies further support the chemical activity of the nanorods.

The most accepted mechanism of CeO_2:L-Dopa chemistry appears to explain most of the results, which in this work were limited to steady state absorbance and fluorescence measurements. However, other mechanisms, such as dopachrome tautomerase-like activity, interruption of oligomerization or oligomer stacking have been briefly mentioned in literature for other metal ions.[281,300,301] Therefore, further research determining the monomer ratios, oligomer size, and fluorescence lifetime measurements could better clarify the effect of Eu-CeO_2 on the properties of synthesized eumelanin.

The range of interactions between L-Dopa and the various Eu-CeO_2 morphologies also invites further research in controlling and applying this chemical reactivity. As CeO_2 can bind L-Dopa, dopamine and other molecules with biological implications, the presence of the metal oxide may prevent proper biological functioning or medical treatments.[302] However, if the CeO_2 surface chemistry can be adjusted to neutralize the material's binding capability, this risk may be significantly reduced. This may be essential, particularly for the proposed neurological applications of CeO_2

Research by Andreescu on the functionalization of CeO_2 by eumelanin-family derivatives has also demonstrated some changes in the chemistry of the CeO_2 particles, such as radical scavenging activity and oxidizing capability.[236] This research was limited to commercially available CeO_2 nanoparticles, so it would be interesting to also compare other morphologies to give a range of monomer adsorption. Eumelanin and CeO_2 may have several areas of synergetic chemistry, such as radical scavenging and electron conductivity.

Further research into properties of functionalized CeO_2 or Eu-CeO_2 systems would likely find photocatalytic, bioprotective, or photovoltaic applications of these materials.

Furthermore, the intrinsic complexities of both melanin and CeO_2 materials makes the composite an incredibly manipulatable platform that has only modestly been investigated.

Chapter 8: Concluding Remarks

8.1. Results

This work has demonstrated the successful synthesis of a variety of Eu-CeO_2 nanomaterials. Eu-CeO_2 nanorods and nanocubes were synthesized by hydrothermal reactions, and likely grew starting with precipitation of $Ce(OH)_3$ nuclei. The nanocubes were oxidized *in situ* and grew as CeO_2 through Oriented Attachment. The nanorods grow as $Ce(OH)_3$ through Ostwald Ripening, and were rapidly oxidized during washing and drying to yield Eu-CeO_2 nanorods. Eu-CeO_2 nanowires were synthesized by an electrospinning and annealing protocol.

The yellow nanorods were initially polycrystalline with high Ce^{3+} concentrations and surface hydroxyls but were converted to white monocrystalline nanorods with low Ce^{3+} concentrations and no surface hydroxyls by annealing. The individual small nanocubes are monocrystalline but tend to fuse at a common crystallographic plane to establish large crystalline domains. The nanocubes likely have a Ce^{3+} concentration between the nanorod and annealed nanorods, due to their off-white color. The white nanowires are Ce^{3+} poor and are overall polycrystalline but comprised of fused monocrystalline particles.

Each Eu-CeO_2 morphology provided a unique combination of physical properties like surface area, oxidation, crystallinity, and surface termination relative to the others. For example, the small, Ce^{3+}-rich, hydroxyl and water coated nanorods, contrast with the bulky, Ce^{3+}-poor, annealed nanowires.

Eu-CeO_2 nanorods had the weakest Eu^{3+} fluorescence and highest asymmetry ratio of the four morphologies due to increased oxygen vacancy and crystalline defect

concentrations, and the presence of surface hydroxyls. Annealing the nanorods removes these defects, reducing the asymmetry ratio, and eliminating sources of Eu^{3+} fluorescence quenching. The nanowires had a similar ratio, while large crystalline domains gave the cubes the highest symmetry of all materials.

The nanocubes were also doped with other lanthanide ions with known fluorescent transitions. Upon excitation of the $O_{2p} \rightarrow Ce_{4f}$ charge transfer transition near 375 nm, Sm-, Yb-, and Nd-CeO_2 nanocubes had intense emission in the visible or NIR region, and Er-CeO_2 nanocubes had weak NIR fluorescence. The Yb- and Nd-CeO_2 nanocubes also emitted upon excitation near 640 nm, but the exact transition of this excitation is still undetermined.

The four morphologies were evaluated for any influence on the synthesis of eumelanin from L-Dopa, as determined by the fluorescence and UV-Vis absorbance of the reaction solution, as well as color changes of the Eu-CeO_2 nanomaterials. The nanomaterials oxidized L-Dopa and removed the quinone and its derivatives from solution, preventing the production of eumelanin. The nanorods were most active, followed by the nanocubes, annealed nanorods, and finally the relatively inert nanowires. The elevated activity by nanorods is possibly due to the more numerous oxygen vacancies, exposed cerium sites, smaller crystalline domains, and higher surface area of the nanorods.

Finally, Eu-CeO_2 nanotubes were synthesized by layered deposition of Ce^{3+}/Eu^{3+} with OH^- to form a Eu-$Ce(OH)_3$ shell on sacrificial ZnO nanowires. Oxidizing the shell followed by acid etching of the ZnO core produced highly porous and polycrystalline nanotubes with wall thicknesses below 20 nm. The length and inner diameter of the nanotubes were controlled by the ZnO template.

8.2. Future Work

The strong binding of L-Dopa to the Eu-CeO_2 nanorods, and nanocubes to a lesser extent, presents an opportunity for further research. Eumelanin and CeO_2 may have synergetic properties, such as enhanced UV-Vis absorbance and anti-oxidant activity. In addition, the L-Dopa:CeO_2 interaction has not been tested for reversibility, which could have applications in drug delivery of L-Dopa.

The synthesis of Eu-CeO_2 nanotubes by an electrospinning-based deposition technique, while promising, has only been briefly investigated thus far. Following optimization of the synthetic route, the nanotubes have potential as drug delivery vectors.

The fluorescence of the Eu-CeO_2 nanomaterials synthesized in this work, particularly the nanocubes, coupled with their presumed antioxidant activity potential in biological applications, including bioimaging. Promising work is currently underway focusing on near infrared imaging following cellular uptake of the Yb-CeO_2 and Nd-CeO_2 cubes.

REFERENCES

1. *The rare-earth elements—Vital to modern technologies and lifestyles: U.S. Geological Survey Fact Sheet 2014–3078;* Interior, U. D. o. t., 2014.
2. H. Bill Wells, W.; L. Wells, V.: The Lanthanides, Rare Earth Elements. In *Patty's Toxicology*; Bingham, E., Cohrssen, B., Eds.; John Wiley & Sons: N.J., 2001.
3. Shannon, R. D.; Prewitt, C. T. *Acta Crystallogr. Sect. B: Struct. Sci.* **1969**, *25*, 925-946.
4. Lang, P. F.; Smith, B. C. *J. Chem. Educ.* **2010**, *87*, 875-881.
5. Zhang, D.; Du, X.; Shi, L.; Gao, R. *Dalton Trans* **2012**, *41*, 14455-14475.
6. Skorodumova, N. V.; Simak, S. I.; Lundqvist, B. I.; Abrikosov, I. A.; Johansson, B. *Phys. Rev. Lett.* **2002**, *89*, 166601.
7. Putnam, R. L.; Navrotsky, A.; Cordfunke, E. H. P.; Huntelaar, M. E. *J. Chem. Thermodyn* **2000**, *32*, 911-921.
8. Montini, T.; Melchionna, M.; Monai, M.; Fornasiero, P. *Chem. Rev.* **2016**, *116*, 5987-6041.
9. Huntelaar, M. E.; Booij, A. S.; Cordfunke, E. H. P.; van der Laan, R. R.; van Genderen, A. C. G.; van Miltenburg, J. C. *J. Chem. Thermodyn* **2000**, *32*, 465-482.
10. "Standard Thermodynamic Properties of Chemical Substances". In *CRC Handbook of Chemistry and Physics*; Lide, D. R., Ed.; CRC Press: Boca Raton, FL, 2005.
11. Han, W.-Q.; Wu, L.; Zhu, Y. *J. Am. Chem. Soc.* **2005**, *127*, 12814-12815.
12. Mullins, D. R. *Surf. Sci. Rep.* **2015**, *70*, 42-85.
13. Sun, C.; Li, H.; Chen, L. *Energy Environ. Sci.* **2012**, *5*, 8475.
14. Deshpande, S.; Patil, S.; Kuchibhatla, S. V. N. T.; Seal, S. *Appl. Phys. Lett.* **2005**, *87*, 133113.
15. Stetsovych, V. Experimental control of Ce3+ concentration in ceria based model catalysts. Doctoral Thesis, Charles University, 2015.
16. Weck, P. F.; Kim, E. *PCCP* **2016**, *18*, 26816-26826.
17. Chueh, W. C.; Haile, S. M. *Philos. Trans. Royal Soc. A* **2010**, *368*, 3269-3294.
18. Xue, Y.; Luan, Q.; Yang, D.; Yao, X.; Zhou, K. *J. Phys. Chem. C* **2011**, *115*, 4433-4438.
19. Korsvik, C.; Patil, S.; Seal, S.; Self, W. *Chem. Commun.* **2007**, *10*, 1056-1058.
20. Sayle, T. X. T.; Parker, S. C.; Catlow, C. R. A. *Surf. Sci.* **1994**, *316*, 329-336.
21. Lin, Y.; Wu, Z.; Wen, J.; Poeppelmeier, K. R.; Marks, L. D. *Nano Lett.* **2014**, *14*, 191-196.
22. Chen, L.; Fleming, P.; Morris, V.; Holmes, J. D.; Morris, M. A. *J. Phys. Chem. C* **2010**, *114*, 12909-12919.
23. Tsunekawa, S.; Ishikawa, K.; Li, Z. Q.; Kawazoe, Y.; Kasuya, A. *Phys. Rev. Lett.* **2000**, *85*, 3440-3443.
24. Yao, H. C.; Yao, Y. F. Y. *J. Catal.* **1984**, *86*, 254-265.
25. Suresh, B.; Ranjith, T.; Talgat, I.; Richard, D.; Artëm, E. M.; Alfons, S.; Sudipta, S. *Nanotechnology* **2009**, *20*, 085713.
26. Ansari, S. A.; Khan, M. M.; Ansari, M. O.; Kalathil, S.; Lee, J.; Cho, M. H. *RSC Adv.* **2014**, *4*, 16782-16791.
27. Zhang, Y.-W.; Si, R.; Liao, C.-S.; Yan, C.-H.; Xiao, C.-X.; Kou, Y. *J. Phys. Chem. B* **2003**, *107*, 10159-10167.

28. Liyanage, A. D.; Perera, S. D.; Tan, K.; Chabal, Y.; Balkus, K. J. *ACS Catal.* **2014**, *4*, 577-584.
29. Tsunekawa, S.; Fukuda, T.; Kasuya, A. *J. Appl. Phys.* **2000**, *87*, 1318-1321.
30. Patsalas, P.; Logothetidis, S.; Sygellou, L.; Kennou, S. *Phys Rev B* **2003**, *68*, 035104.
31. Khan, M. M.; Ansari, S. A.; Pradhan, D.; Han, D. H.; Lee, J.; Cho, M. H. *Ind. Eng. Chem. Res.* **2014**, *53*, 9754-9763.
32. Krishnan, A.; Sreeremya, T. S.; Murray, E.; Ghosh, S. *J. Colloid Interface Sci.* **2013**, *389*, 16-22.
33. Mochizuki, S.; Fujishiro, F. *Phys. Status Solidi B* **2009**, *246*, 2320-2328.
34. Tamizhdurai, P.; Sakthinathan, S.; Chen, S.-M.; Shanthi, K.; Sivasanker, S.; Sangeetha, P. *Sci. Rep.* **2017**, *7*, 46372.
35. Dahle, J. T.; Arai, Y. *Int. J. Environ. Res. Public Health* **2015**, *12*, 1253-1278.
36. Zhou, K.; Wang, X.; Sun, X.; Peng, Q.; Li, Y. *J. Catal.* **2005**, *229*, 206-212.
37. Chen, P.-L.; Chen, I.-W. *J. Am. Ceram. Soc.* **1993**, *76*, 1577-1583.
38. Zhou, X.-D.; Huebner, W.; Anderson, H. U. *Appl. Phys. Lett.* **2002**, *80*, 3814-3816.
39. Si, R.; Zhang, Y.-W.; You, L.-P.; Yan, C.-H. *J. Phys. Chem. B* **2006**, *110*, 5994-6000.
40. Pan, C.; Zhang, D.; Shi, L. *J. Solid State Chem.* **2008**, *181*, 1298-1306.
41. Ji, Z.; Wang, X.; Zhang, H.; Lin, S.; Meng, H.; Sun, B.; George, S.; Xia, T.; Nel, A. E.; Zink, J. I. *ACS Nano* **2012**, *6*, 5366-5380.
42. Mai, H.-X.; Sun, L.-D.; Zhang, Y.-W.; Si, R.; Feng, W.; Zhang, H.-P.; Liu, H.-C.; Yan, C.-H. *J. Phys. Chem. B* **2005**, *109*, 24380-24385.
43. Yang, S.; Gao, L. *J. Am. Chem. Soc.* **2006**, *128*, 9330-9331.
44. Fu, X. Q.; Wang, C.; Yu, H. C.; Wang, Y. G.; Wang, T. H. *Nanotechnology* **2007**, *18*, 145503.
45. Zhou, K.; Yang, Z.; Yang, S. *Chem. Mater.* **2007**, *19*, 1215-1217.
46. Huang, W.; Shuk, P.; Greenblatt, M. *Chem. Mater.* **1997**, *9*, 2240-2245.
47. Voorhees, P. W. *J. Stat. Phys.* **1985**, *38*, 231-252.
48. Zhang, J.; Huang, F.; Lin, Z. *Nanoscale* **2010**, *2*, 18-34.
49. Taniguchi, T.; Katsumata, K.-i.; Omata, S.; Okada, K.; Matsushita, N. *Cryst. Growth Des.* **2011**, *11*, 3754-3760.
50. Sakthivel, T.; Das, S.; Kumar, A.; Reid, D. L.; Gupta, A.; Sayle, D. C.; Seal, S. *ChemPlusChem* **2013**, *78*, 1446-1455.
51. Wu, Q.; Zhang, F.; Xiao, P.; Tao, H.; Wang, X.; Hu, Z.; Lü, Y. *J. Phys. Chem. C* **2008**, *112*, 17076-17080.
52. Lin, M.; Fu, Z. Y.; Tan, H. R.; Tan, J. P. Y.; Ng, S. C.; Teo, E. *Cryst. Growth Des.* **2012**, *12*, 3296-3303.
53. Hua, G.; Zhang, L.; Fei, G.; Fang, M. *J. Mater. Chem.* **2012**, *22*, 6851-6855.
54. Zhang, D.; Fu, H.; Shi, L.; Fang, J.; Li, Q. *J. Solid State Chem.* **2007**, *180*, 654-660.
55. Strandwitz, N. C.; Stucky, G. D. *Chem. Mater.* **2009**, *21*, 4577-4582.
56. Ji, P.; Zhang, J.; Chen, F.; Anpo, M. *J. Phys. Chem. C* **2008**, *112*, 17809-17813.
57. Melchionna, M.; Marchesan, S.; Prato, M.; Fornasiero, P. *Catal. Sci. Technol.* **2015**, *5*, 3859-3875.
58. Titirici, M.-M.; Antonietti, M.; Thomas, A. *Chem. Mater.* **2006**, *18*, 3808-3812.

59. Yu, K.-L.; Ruan, G.-L.; Ben, Y.-H.; Zou, J.-J. *Mater. Sci. Eng., B* **2007**, *139*, 197-200.
60. Chen, G.; Xu, C.; Song, X.; Zhao, W.; Ding, Y.; Sun, S. *Inorg. Chem.* **2008**, *47*, 723-728.
61. Pan, C.; Zhang, D.; Shi, L.; Fang, J. *Eur. J. Inorg. Chem.* **2008**, *2008*, 2429-2436.
62. Masui, T.; Fujiwara, K.; Machida, K.-i.; Adachi, G.-y.; Sakata, T.; Mori, H. *Chem. Mater.* **1997**, *9*, 2197-2204.
63. Kuiry, S. C.; Patil, S. D.; Deshpande, S.; Seal, S. *J. Phys. Chem. B* **2005**, *109*, 6936-6939.
64. Cargnello, M.; Doan-Nguyen, V. V. T.; Gordon, T. R.; Diaz, R. E.; Stach, E. A.; Gorte, R. J.; Fornasiero, P.; Murray, C. B. *Science* **2013**, *341*, 771.
65. Cargnello, M.; Wieder, N. L.; Montini, T.; Gorte, R. J.; Fornasiero, P. *J. Am. Chem. Soc.* **2010**, *132*, 1402-1409.
66. Li, Y.; Fu, Q.; Flytzani-Stephanopoulos, M. *Appl. Catal., B* **2000**, *27*, 179-191.
67. Xu, L.; Wang, J. *Environ. Sci. Technol* **2012**, *46*, 10145-10153.
68. Xiao, X.; Sheng, Z.; Yang, L.; Dong, F. *Catal. Sci. Technol.* **2016**, *6*, 1507-1514.
69. Liu, B.; Wang, Q.; Yu, S.; Zhao, T.; Han, J.; Jing, P.; Hu, W.; Liu, L.; Zhang, J.; Sun, L.-D.; Yan, C.-H. *Nanoscale* **2013**, *5*, 9747-9757.
70. Dong, H.; Du, S.-R.; Zheng, X.-Y.; Lyu, G.-M.; Sun, L.-D.; Li, L.-D.; Zhang, P.-Z.; Zhang, C.; Yan, C.-H. *Chem. Rev.* **2015**, *115*, 10725-10815.
71. Elias, J. S.; Risch, M.; Giordano, L.; Mansour, A. N.; Shao-Horn, Y. *J. Am. Chem. Soc.* **2014**, *136*, 17193-17200.
72. Pandiyan, A.; Meena, M.; Krishna Moorthy, S. B. *Nanomaterials and Energy* **2012**, *1*, 288-305.
73. Mahato, N.; Gupta, A.; Balani, K. *Nanomaterials and Energy* **2011**, *1*, 27–45.
74. Xiong, Y.; Yamaji, K.; Horita, T.; Sakai, N.; Yokokawa, H. *J. Electrochem. Soc.* **2004**, *151*, A407-A412.
75. Kharton, V. V.; Figueiredo, F. M.; Navarro, L.; Naumovich, E. N.; Kovalevsky, A. V.; Yaremchenko, A. A.; Viskup, A. P.; Carneiro, A.; Marques, F. M. B.; Frade, J. R. *J. Mater. Sci.* **2001**, *36*, 1105-1117.
76. Mantlikova, A.; Bittova, B.; Burianova, S.; Vejpravova, J.; Niznansky, D.; Holec, P. *WDS'12 Proceedings of Contributed Papers* **2012**, *3*, 12-17.
77. Li, G.-R.; Qu, D.-L.; Arurault, L.; Tong, Y.-X. *J. Phys. Chem. C* **2009**, *113*, 1235-1241.
78. Ranjith, K. S.; Saravanan, P.; Chen, S.-H.; Dong, C.-L.; Chen, C. L.; Chen, S.-Y.; Asokan, K.; Rajendra Kumar, R. T. *J. Phys. Chem. C* **2014**, *118*, 27039-27047.
79. Eriksson, P.; Tal, A. A.; Skallberg, A.; Brommesson, C.; Hu, Z.; Boyd, R. D.; Olovsson, W.; Fairley, N.; Abrikosov, I. A.; Zhang, X.; Uvdal, K. *Sci. Rep.* **2018**, *8*, 6999.
80. Bünzli, J.-C. G.; Eliseeva, S. V.: Basics of Lanthanide Photophysics. In *Lanthanide Luminescence: Photophysical, Analytical and Biological Aspects*; Hañninen, P., Härmä, H., Eds.; Springer-Verlag: Berlin, 2010; Vol. 7; pp 1-45.
81. Channei, D.; Inceesungvorn, B.; Wetchakun, N.; Ukritnukun, S.; Nattestad, A.; Chen, J.; Phanichphant, S. *Sci. Rep.* **2014**, *4*, 5757.
82. Jayapalan, S.; Ranjith, K. S.; Padmanapan, S.; Mangalaraj, D.; Rt, R. *Mater. Sci. Semicond. Process.* **2014**, *26*, 218–224.
83. Prahdan, G. K.; Parida, K. M. *Int. J. Eng. Sci. Technol.* **2010**, *2*, 53-65.

84. Celardo, I.; Pedersen, J. Z.; Traversa, E.; Ghibelli, L. *Nanoscale* **2011**, *3*, 1411-1420.
85. Xu, C.; Qu, X. *NPG Asia Mater.* **2014**, *6*, e90.
86. Pirmohamed, T.; Dowding, J. M.; Singh, S.; Wasserman, B.; Heckert, E.; Karakoti, A. S.; King, J. E.; Seal, S.; Self, W. T. *Chem Commun (Camb)* **2010**, *46*, 2736-2738.
87. Das, M.; Patil, S.; Bhargava, N.; Kang, J. F.; Riedel, L. M.; Seal, S.; Hickman, J. J. *Biomaterials* **2007**, *28*, 1918-1925.
88. Tarnuzzer, R. W.; Colon, J.; Patil, S.; Seal, S. *Nano Lett.* **2005**, *5*, 2573-2577.
89. Schieber, M.; Chandel, N. S. *Curr. Biol.* **2014**, *24*, R453-R462.
90. Poljsak, B.; Suput, D.; Milisav, I. *Oxid. Med. Cell. Longev.* **2013**, *2013*, 11.
91. Gubernatorova Ekaterina, O.; Liu, X.; Othman, A.; Muraoka Wayne, T.; Koroleva Ekaterina, P.; Andreescu, S.; Tumanov Alexei, V. *Adv. Healthc. Mater.* **2017**, *6*, 1700176.
92. Das, J.; Choi, Y.-J.; Han, J. W.; Reza, A. M. M. T.; Kim, J.-H. *Sci. Rep.* **2017**, *7*, 9513.
93. Dowding, J. M.; Das, S.; Kumar, A.; Dosani, T.; McCormack, R.; Gupta, A.; Sayle, T. X. T.; Sayle, D. C.; von Kalm, L.; Seal, S.; Self, W. T. *ACS Nano* **2013**, *7*, 4855-4868.
94. Perez, J. M.; Asati, A.; Nath, S.; Kaittanis, C. *Small* **2008**, *4*, 552-556.
95. Xu, C.; Lin, Y.; Wang, J.; Wu, L.; Wei, W.; Ren, J.; Qu, X. *Adv. Healthc. Mater.* **2013**, *2*, 1591-1599.
96. Krishnamoorthy, K.; Veerapandian, M.; Zhang, L.-H.; Yun, K.; Kim, S. J. *J. Ind. Eng. Chem.* **2014**, *20*, 3513-3517.
97. Shah, V.; Shah, S.; Shah, H.; Rispoli, F. J.; McDonnell, K. T.; Workeneh, S.; Karakoti, A.; Kumar, A.; Seal, S. *PLoS One* **2012**, *7*, e47827.
98. Farias, I. A. P.; Santos, C. C. L. d.; Sampaio, F. C. *BioMed Res. Int.* **2018**, *2018*, 14.
99. Singh, S.; Dosani, T.; Karakoti, A. S.; Kumar, A.; Seal, S.; Self, W. T. *Biomaterials* **2011**, *32*, 6745-6753.
100. Ornatska, M.; Sharpe, E.; Andreescu, D.; Andreescu, S. *Anal. Chem.* **2011**, *83*, 4273-4280.
101. Izu, N.; Shin, W.; Murayama, N.; Kanzaki, S. *Sens. Actuators, B* **2002**, *87*, 95-98.
102. Yang, Z.-M.; Huang, G.-F.; Huang, W.-Q.; Wei, J.-M.; Yan, X.-G.; Liu, Y.-Y.; Jiao, C.; Wan, Z.; Pan, A. *J. Mater. Chem. A* **2014**, *2*, 1750-1756.
103. Channei, D.; Inceesungvorn, B.; Wetchakun, N.; Phanichphant, S.; Nakaruk, A.; Koshy, P.; Sorrell, C. *Ceram. Int.* **2013**, *39*, 3129-3134.
104. Choudhury, B.; Chetri, P.; Choudhury, A. *RSC Adv.* **2014**, *4*, 4663-4671.
105. Yang, K.; Li, D.-F.; Huang, W.-Q.; Xu, L.; Huang, G.-F.; Wen, S. *Appl. Phys. A* **2016**, *123*, 96.
106. Tang, Z.-R.; Zhang, Y.; Xu, Y.-J. *RSC Adv.* **2011**, *1*, 1772-1777.
107. Stambouli, A. B.; Traversa, E. *Renew. Sust. Energy Rev.* **2002**, *6*, 433-455.
108. Wachsman, E. D.; Lee, K. T. *Science* **2011**, *334*, 935.
109. Aneggi, E.; Wiater, D.; de Leitenburg, C.; Llorca, J.; Trovarelli, A. *ACS Catal.* **2014**, *4*, 172-181.
110. Laosiripojana, N.; Assabumrungrat, S. *Appl. Catal., B* **2005**, *60*, 107-116.

111. Gawande, M. B.; Bonifácio, V. D. B.; Varma, R. S.; Nogueira, I. D.; Bundaleski, N.; Ghumman, C. A. A.; Teodoro, O. M. N. D.; Branco, P. S. *Green Chem* **2013**, *15*, 1226.
112. Kašpar, J.; Fornasiero, P.; Graziani, M. *Catal. Today* **1999**, *50*, 285-298.
113. Furler, P.; Scheffe, J.; Gorbar, M.; Moes, L.; Vogt, U.; Steinfeld, A. *Energy Fuels* **2012**, *26*, 7051-7059.
114. Monte, R. D.; Kašpar, J. *Top. Catal.* **2004**, *28*, 47-57.
115. Tanaka, A.; Hashimoto, K.; Kominami, H. *J. Am. Chem. Soc.* **2012**, *134*, 14526-14533.
116. Tamura, M.; Tomishige, K. *Angew. Chem. Int. Ed.* **2015**, *54*, 864-867.
117. Meredith, P.; Sarna, T. *Pigment Cell Res* **2006**, *19*, 572-594.
118. Hernández-Castillo, Y.; García-Hernández, M.; López-Marure, A.; Luna-Domínguez, J. H.; López-Camacho, P. Y.; Morales-Ramírez, Á. d. J. *Ceram. Int.* **2019**, *45*, 2303-2308.
119. Primus, P.-A.; Ritschel, T.; Sigüenza, P. Y.; Cauqui, M. A.; Hernández-Garrido, J. C.; Kumke, M. U. *J. Phys. Chem. C* **2014**, *118*, 23349-23360.
120. Babu, S.; Schulte, A.; Seal, S. *Appl. Phys. Lett.* **2008**, *92*, 123112.
121. Tiseanu, C.; Parvulescu, V. I.; Boutonnet, M.; Cojocaru, B.; Primus, P. A.; Teodorescu, C. M.; Solans, C.; Dominguez, M. S. *PCCP* **2011**, *13*, 17135-17145.
122. Gao, W.; Li, J.; Zhou, X.; Zhang, Z.; Ma, Y.; Qu, Y. *J. Mater. Chem. C* **2014**, *2*, 8729-8735.
123. Hayes, S. A.; Yu, P.; O'Keefe, T. J.; O'Keefe, M. J.; Stoffer , J. O. *J. Electrochem. Soc.* **2002**, *149*, C623-C630.
124. Zou, H.; Lin, Y. S.; Rane, N.; He, T. *Ind. Eng. Chem. Res.* **2004**, *43*, 3019-3025.
125. Morris, V.; Fleming, P. G.; Holmes, J. D.; Morris, M. A. *Chem. Eng. Sci.* **2013**, *91*, 102-110.
126. Du, N.; Zhang, H.; Chen, B.; Ma, X.; Yang, D. *J. Phys. Chem. C* **2007**, *111*, 12677-12680.
127. Hu, Z.; Oskam, G.; Penn, R. L.; Pesika, N.; Searson, P. C. *J. Phys. Chem. B* **2003**, *107*, 3124-3130.
128. National Institute of Standards and Technology, U. S. D. o. C.: SRM 674; CeO_2. In *Gaithersburg, MD*, 29 September 2007.
129. Wang, W.; Howe, J. Y.; Li, Y.; Qiu, X.; Joy, D. C.; Paranthaman, M. P.; Doktycz, M. J.; Gu, B. *J. Mater. Chem.* **2010**, *20*, 7776.
130. Sultana, S.; Mansingh, S.; Parida, K. M. *J. Mater. Chem. A* **2018**.
131. Bezkrovnyi, O.; Małecka, M. A.; Lisiecki, R.; Ostroushko, V.; Thomas, A. G.; Gorantla, S.; Kepinski, L. *CrystEngComm* **2018**, *20*, 1698-1704.
132. Sun, C.; Li, H.; Zhang, H.; Wang, Z.; Chen, L. *Nanotechnology* **2005**, *16*, 1454-1463.
133. Heiba, Z. K.; Akin, Y.; Sigmund, W.; Hascicek, Y. S. *J. Appl. Crystallogr.* **2003**, *36*, 1411-1416.
134. Zhou, X. D.; Huebner, W. *Appl. Phys. Lett.* **2001**, *79*, 3512-3514.
135. Monshi, A.; Foroughi, M. R.; Monshi, M. R. *World J. Nanosci. Eng.* **2012**, *2*, 7.
136. Zhu, Y.-J.; Chen, F. *Chem. Rev.* **2014**, *114*, 6462-6555.
137. Ansari, A. A.; Kaushik, A. *J Semicond* **2010**, *31*, 033001.
138. Wu, N. C.; Shi, E. W.; Zheng, Y. Q.; Li, W. J. *J. Am. Ceram. Soc.* **2002**, *85*, 2462-2468.

139. Deori, K.; Gupta, D.; Saha, B.; Deka, S. *ACS Catal.* **2014**, *4*, 3169-3179.
140. Lin, K. S.; Chowdhury, S. *Int J Mol Sci* **2010**, *11*, 3226-3251.
141. Zhang, D.; Fu, H.; Shi, L.; Pan, C.; Li, Q.; Chu, Y.; Yu, W. *Inorg. Chem.* **2007**, *46*, 2446-2451.
142. Klara, C.; Ales, M.; Eva, B.; Jaroslav, C.; Petr, V.; Jaroslav, C. *J. Am. Ceram. Soc.* **2016**, *99*, 1155-1163.
143. Pautrot-d'Alençon, L.; Barboux, P.; Boilot, J.-P. *J. Sol-Gel Sci. Technol.* **2006**, *39*, 261-267.
144. Pal, P.; Pahari, S. K.; Sinhamahapatra, A.; Jayachandran, M.; Kiruthika, G. V. M.; Bajaj, H. C.; Panda, A. B. *RSC Adv.* **2013**, *3*, 10837-10847.
145. Trovarelli, A. *Catalysis Reviews* **1996**, *38*, 439-520.
146. Li, M.-M.; Long, Y.-Z.; Yin, H.-X.; Zhang, Z.-M. *Chinese Physics B* **2011**, *20*, 048101.
147. Hwang, A.-R.; Park, J.; Kang, Y.-C. *Bull. Korean Chem. Soc.* **2011**, *32*, 3338-3342.
148. Berutti, F. A.; Alves, A. K.; Bergmann, C. P.; Clemens, F. J.; Graule, T. *Particul. Sci. Technol.* **2009**, *27*, 203-209.
149. Yang, Z.-M.; Hou, S.-C.; Huang, G.; Duan, H.-G.; Huang, W.-Q. *Mater. Lett.* **2014**, *133*, 109–112.
150. Azad, A.-M.; Matthews, T.; Swary, J. *Mater. Sci. Eng., B* **2005**, *123*, 252-258.
151. Shi, X.; Zhou, W.; Ma, D.; Ma, Q.; Bridges, D.; Ma, Y.; Hu, A. *J Nanomater* **2015**, *2015*, 20.
152. Li, D.; Xia, Y. *Nano Lett.* **2004**, *4*, 933-938.
153. Liu, Y. C.; Zhang, N.; Jiao, L. F.; Chen, J. *Adv. Mater.* **2015**, *27*, 6702-+.
154. Zhang, C.-L.; Yu, S.-H. *Chem. Soc. Rev.* **2014**, *43*, 4423-4448.
155. Pillay, V.; Dott, C.; Choonara, Y. E.; Tyagi, C.; Tomar, L.; Kumar, P.; du Toit, L. C.; Ndesendo, V. M. K. *J Nanomater* **2013**, *2013*, 22.
156. Agarwal, S.; Wendorff, J. H.; Greiner, A. *Polymer* **2008**, *49*, 5603-5621.
157. Sridhar, R.; Lakshminarayanan, R.; Madhaiyan, K.; Amutha Barathi, V.; Lim, K. H. C.; Ramakrishna, S. *Chem. Soc. Rev.* **2015**, *44*, 790-814.
158. Zhang, P.; Zhao, X.; Ji, Y.; Ouyang, Z.; Wen, X.; Li, J.; Su, Z.; Wei, G. *J. Mater. Chem. B* **2015**, *3*, 2487-2496.
159. Hwang, T. H.; Lee, Y. M.; Kong, B. S.; Seo, J. S.; Choi, J. W. *Nano Lett.* **2012**, *12*, 802-807.
160. Huang, Z.-M.; Zhang, Y. Z.; Kotaki, M.; Ramakrishna, S. *Compos. Sci. Technol.* **2003**, *63*, 2223-2253.
161. Formo, E.; Lee, E.; Campbell, D.; Xia, Y. N. *Nano Lett.* **2008**, *8*, 668-672.
162. Adomavičiūtė, E.; Milašius, R.: The influence of applied voltage on poly(vinyl alcohol) (PVA) nanofibre diameter. In *5th Central European Conference on Fibre-Grade Polymers*, 2007; Vol. 15; pp 69-72.
163. Bhardwaj, N.; Kundu, S. *Biotechnol. Adv.* **2010**, *28*, 325-347.
164. Taylor Geoffrey, I. *Proc. R. Soc. Lond. A Math. Phys. Sci.* **1964**, *280*, 383-397.
165. Deitzel, J.; D. Kleinmeyer, J.; Harris, D. E. A.; Beck Tan, N. C. *Polymer* **2001**, *42*, 261-272.
166. Fong, H.; Chun, I.; Reneker, D. H. *Polymer* **1999**, *40*, 4585-4592.
167. Reneker, D. H.; Chun, I. *Nanotechnology* **1996**, *7*, 216-223.
168. Li, D.; Xia, Y. N. *Adv. Mater.* **2004**, *16*, 1151-1170.

169. Yang, Q.; Li, Z.; Hong, Y.; Zhao, Y.; Qiu, S.; Wang, C.; Wei, Y. *J. Polym. Sci., Part B: Polym. Phys.* **2004**, *42*, 3721-3726.
170. Matthews, J. A.; Wnek, G. E.; Simpson, D. G.; Bowlin, G. L. *Biomacromolecules* **2002**, *3*, 232-238.
171. Son, W. K.; Youk, J. H.; Lee, T. S.; Park, W. H. *Polymer* **2004**, *45*, 2959-2966.
172. Sill, T. J.; von Recum, H. A. *Biomaterials* **2008**, *29*, 1989-2006.
173. Ramakrishna, S.; Fujihara, K.; Teo, W.-E.; Yong, T.; Ma, Z.; Ramaseshan, R. *Mater. Today* **2006**, *9*, 40-50.
174. Wu, H.; Pan, W.; Lin, D.; Li, H. *Journal of Advanced Ceramics* **2012**, *1*, 2-23.
175. Li, D.; Xia, Y. *Nano Lett.* **2003**, *3*, 555-560.
176. Allen, P. G.; Bucher, J. J.; Shuh, D. K.; Edelstein, N. M.; Craig, I. *Inorg. Chem.* **2000**, *39*, 595-601.
177. Teksöz, S.; Acar, Ç.; Ünak, P. *J. Chem. Eng. Data* **2009**, *54*, 1183-1188.
178. Danks, A. E.; Hall, S. R.; Schnepp, Z. *Materials Horizons* **2016**, *3*, 91-112.
179. Baqer, A. A.; Matori, K. A.; Al-Hada, N. M.; Shaari, A. H.; Saion, E.; Chyi, J. L. Y. *Results in Physics* **2017**, *7*, 611-619.
180. Wang, Z.; Wang, Q.; Liao, Y.-C.; Shen, G.-L.; Liu, H.-D.; Chen, Y.-F. *J. Nanopart. Res.* **2011**, *13*, 4969.
181. Lee, D.; Kim, B. Y.; Lee, S. J.; Lee, M. H.; Song, Y. S.; Lee, J. Y. *J. Korean Phys. Soc* **2006**, *48*, 1686-1690.
182. Taylor Geoffrey, I.; Van Dyke, M. D. *Proc. R. Soc. Lond. A Math. Phys. Sci.* **1969**, *313*, 453-475.
183. Megelski, S.; Stephens, J. S.; Chase, D. B.; Rabolt, J. F. *Macromolecules* **2002**, *35*, 8456-8466.
184. Sener, A. G.; Altay, A. S.; Lokumcu Altay, F. In *Tilte*2011.
185. Luo, C. J.; Stride, E.; Edirisinghe, M. *Macromolecules* **2012**, *45*, 4669-4680.
186. Haider, A.; Haider, S.; Kang, I.-K. *Arab. J. Chem.* **2015**.
187. Macak, J. M.; Tsuchiya, H.; Ghicov, A.; Yasuda, K.; Hahn, R.; Bauer, S.; Schmuki, P. *Curr. Opin. Solid State Mater. Sci.* **2007**, *11*, 3-18.
188. Choi, J. H.; Nguyen, F. T.; Barone, P. W.; Heller, D. A.; Moll, A. E.; Patel, D.; Boppart, S. A.; Strano, M. S. *Nano Lett.* **2007**, *7*, 861-867.
189. Correa-Duarte, M. A.; Grzelczak, M.; Salgueiriño-Maceira, V.; Giersig, M.; Liz-Marzán, L. M.; Farle, M.; Sierazdki, K.; Diaz, R. *The Journal of Physical Chemistry B* **2005**, *109*, 19060-19063.
190. Bianco, A.; Kostarelos, K.; Partidos, C. D.; Prato, M. *Chem. Commun.* **2005**, 571-577.
191. Bae, C.; Yoo, H.; Kim, S.; Lee, K.; Kim, J.; Sung, M. M.; Shin, H. *Chem. Mater.* **2008**, *20*, 756-767.
192. Huang, X.; Gonzalez-Rodriguez, R.; Rich, R.; Gryczynski, Z.; Coffer, J. L. *Chem. Commun.* **2013**, *49*, 5760-5762.
193. González-Rovira, L.; Sánchez-Amaya, J. M.; López-Haro, M.; del Rio, E.; Hungría, A. B.; Midgley, P.; Calvino, J. J.; Bernal, S.; Botana, F. J. *Nano Lett.* **2009**, *9*, 1395-1400.
194. Tang, C. C.; Bando, Y.; Liu, B. D.; Golberg, D. *Adv. Mater.* **2005**, *17*, 3005-3009.
195. Wu, X.; Kawi, S. *Cryst. Growth Des.* **2010**, *10*, 1833-1841.
196. Wang, T.; Zhang, L.; Zhang, J.; Hua, G. *Microporous Mesoporous Mater.* **2013**, *171*, 196-200.

197. Feng, Y.-j.; Liu, L.-l.; Wang, X.-d. *J. Mater. Chem.* **2011**, *21*, 15442-15448.
198. Binnemans, K. *Coord. Chem. Rev.* **2015**, *295*, 1-45.
199. Kumar, A.; Babu, S.; Karakoti, A. S.; Schulte, A.; Seal, S. *Langmuir* **2009**, *25*, 10998-11007.
200. Li, L.; Yang, H. K.; Moon, B. K.; Fu, Z.; Guo, C.; Jeong, J. H.; Yi, S. S.; Jang, K.; Lee, H. S. *J. Phys. Chem. C* **2009**, *113*, 610-617.
201. Vimal, G.; Mani, K. P.; Biju, P. R.; Joseph, C.; Unnikrishnan, N. V.; Ittyachen, M. A. *Appl Nanosci* **2015**, *5*, 837-846.
202. Liu, X.; Chen, S.; Wang, X. *J. Lumin.* **2007**, *127*, 650-654.
203. Fang, D.; Zhang, M.; Luo, Z.; Cao, T.; Wang, Q.; Zhou, Z.; Jiang, M.; Xiong, C. *Opt. Mater.* **2014**, *38*, 1-5.
204. Harris, D. C.: *Quantitative Chemical Analysis*; 1st ed.; W.H. Freeman and Co.: U.S.A., 2007.
205. Corma, A.; Atienzar, P.; García, H.; Chane-Ching, J.-Y. *Nat Mater* **2004**, *3*, 394.
206. Wang, Z.; Quan, Z.; Lin, J. *Inorg. Chem.* **2007**, *46*, 5237-5242.
207. Choudhury, B.; Dey, M.; Choudhury, A. *Appl Nanosci* **2014**, *4*, 499-506.
208. Housecroft, C. E.; Sharpe, A. G.: *Inorganic Chemistry*; Pearson Education Limited: England, 2001.
209. Bünzli, J.-C. G.; Piguet, C. *Chem. Soc. Rev.* **2005**, *34*, 1048-1077.
210. Qin, X.; Liu, X.; Huang, W.; Bettinelli, M.; Liu, X. *Chem. Rev.* **2017**, *117*, 4488-4527.
211. Dodson, C. M.; Zia, R. *Phys Rev B* **2012**, *86*, 125102.
212. Walsh, B.: Judd-Ofelt theory: Principles and practices. In *Advances in Spectroscopy for Lasers and Sensing*, 2005; pp 403-433.
213. Stouwdam, J. W.; Raudsepp, M.; van Veggel, F. C. J. M. *Langmuir* **2005**, *21*, 7003-7008.
214. Luo, W.; Li, R.; Chen, X. *J. Phys. Chem. C* **2009**, *113*, 8772-8777.
215. Babu, S.; Cho, J. H.; Dowding, J. M.; Heckert, E.; Komanski, C.; Das, S.; Colon, J.; Baker, C. H.; Bass, M.; Self, W. T.; Seal, S. *Chem Commun* **2010**, *46*, 6915-6917.
216. D., C.; J., K.; V., D.; S., S. N.; Y., P. *Luminescence* **2015**, *30*, 1201-1206.
217. Shehata, N. Design of optical characteristics of ceria nanoparticles for applications including gas sensing and up-conversion. Doctoral Thesis, Virginia Polytechnic Institute and State University, 2012.
218. Cho, J.-H.; Bass, M.; Babu, S.; Dowding, J. M.; Self, W. T.; Seal, S. *J. Lumin.* **2012**, *132*, 743-749.
219. Fujihara, S.; Oikawa, M. *J. Appl. Phys.* **2004**, *95*, 8002-8006.
220. Judd, B. R. *J Chem Phys* **1966**, *44*, 839-840.
221. Sharma, A.; Varshney, M.; Park, J.; Ha, T. K.; Chae, K. H.; Shin, H. J. *PCCP* **2015**, *17*, 30065-30075.
222. Kolesnikov, I. E.; Povolotskiy, A. V.; Mamonova, D. V.; Kolesnikov, E. Y.; Kurochkin, A. V.; Lähderanta, E.; Mikhailov, M. D. *J. Rare Earth* **2018**, *36*, 474-481.
223. Moon, T.; Hwang, S.-T.; Jung, D.-R.; Son, D.; Kim, C.; Kim, J.; Kang, M.; Park, B. *J. Phys. Chem. C* **2007**, *111*, 4164-4167.
224. Li, Y.; Wang, J.; Zhou, W.; Zhang, G.; Chen, Y.; Su, Q. *Appl Phys Express* **2013**, *6*, 082301.
225. Yoshida, Y.; Fujihara, S. *Eur. J. Inorg. Chem.* **2011**, *2011*, 1577-1583.

226. Florea, M.; Avram, D.; Cojocaru, B.; Tiseanu, I.; Parvulescu, V.; Tiseanu, C. *PCCP* **2016**, *18*, 18268-18277.
227. Tamrakar, R. K.; Tiwari, N.; Dubey, V.; Upadhyay, K. *J Radiat Res Appl Sci* **2015**, *8*, 399-403.
228. Rakhmatullin, R. M.; Kurkin, I. N.; Pavlov, V. V.; Semashko, V. V. *Phys. Status Solidi B* **2014**, *251*, 1545-1551.
229. Chen, M. Y.; Zu, X. T.; Xiang, X.; Zhang, H. L. *Phys Status Solidi B* **2007**, *389*, 263-268.
230. Choudhury, B.; Choudhury, A. *Mater. Chem. Phys.* **2012**, *131*, 666-671.
231. Pardridge, W. M. *Drug Discovery Today* **2007**, *12*, 54-61.
232. Lee, H.; Scherer, N. F.; Messersmith, P. B. *PNAS* **2006**, *103*, 12999-13003.
233. Solano, F. *New. J. Sci.* **2014**, *2014*, 28.
234. Njagi, J.; Chernov, M. M.; Leiter, J. C.; Andreescu, S. *Anal. Chem.* **2010**, *82*, 989-996.
235. Hayat, A.; Andreescu, D.; Bulbul, G.; Andreescu, S. *J. Colloid Interface Sci.* **2014**, *418*, 240-245.
236. Bülbül, G.; Hayat, A.; Liu, X.; Andreescu, S. *RSC Adv.* **2016**, *6*, 60007-60014.
237. Othman, A.; Hayat, A.; Andreescu, S. *ACS Appl. Nano Mater.* **2018**, *1*, 5722-5735.
238. Weiqin, S.; Liang, Z.; Yan, L.; Xueqin, Z.; Jian, W.; Yang, Z. *Nanotechnology* **2017**, *28*, 365504.
239. Ju, K.-Y.; Lee, Y.; Lee, S.; Park, S. B.; Lee, J.-K. *Biomacromolecules* **2011**, *12*, 625-632.
240. Walkey, C.; Das, S.; Seal, S.; Erlichman, J.; Heckman, K.; Ghibelli, L.; Traversa, E.; McGinnis, J. F.; Self, W. T. *Environmental Science: Nano* **2015**, *2*, 33-53.
241. Zucca, F. A.; Segura-Aguilar, J.; Ferrari, E.; Muñoz, P.; Paris, I.; Sulzer, D.; Sarna, T.; Casella, L.; Zecca, L. *Prog. Neurobiol.* **2017**, *155*, 96-119.
242. d'Ischia, M.; Napolitano, A.; Ball, V.; Chen, C.-T.; Buehler, M. J. *Acc. Chem. Res.* **2014**, *47*, 3541-3550.
243. Fedorow, H.; Tribl, F.; Halliday, G.; Gerlach, M.; Riederer, P.; Double, K. L. *Prog. Neurobiol.* **2005**, *75*, 109-124.
244. Hong, L.; Liu, Y.; Simon, J. D. *Photochem. Photobiol.* **2004**, *80*, 477-481.
245. Engelen, M.; Vanna, R.; Bellei, C.; Zucca, F. A.; Wakamatsu, K.; Monzani, E.; Ito, S.; Casella, L.; Zecca, L. *PloS one* **2012**, *7*, e48490-e48490.
246. Ito, S.; Wakamatsu, K. *Pigment Cell Research* **2003**, *16*, 523-531.
247. Brenner, M.; Hearing, V. J. *Photochem. Photobiol.* **2008**, *84*, 539-549.
248. d'Ischia, M.; Napolitano, A.; Pezzella, A.; J. Land, E.; A. Ramsden, C.; Riley, P.: *5,6-Dihydroxyindoles and Indole5,6-diones*, 2005; Vol. 89.
249. Ito, S. *Biochim. Biophys. Acta Gen. Subj.* **1986**, *883*, 155-161.
250. Zajac, G. W.; Gallas, J. M.; Cheng, J.; Eisner, M.; Moss, S. C.; Alvarado-Swaisgood, A. E. *Biochim. Biophys. Acta Gen. Subj.* **1994**, *1199*, 271-278.
251. Panzella, L.; Gentile, G.; D'Errico, G.; Della Vecchia, N. F.; Errico, M. E.; Napolitano, A.; Carfagna, C.; d'Ischia, M. *Angew. Chem. Int. Ed. Engl.* **2013**, *52*, 12684-12687.
252. Alfieri, M. L.; Micillo, R.; Panzella, L.; Crescenzi, O.; Oscurato, S. L.; Maddalena, P.; Napolitano, A.; Ball, V.; d'Ischia, M. *ACS Appl Mater Interfaces* **2018**, *10*, 7670-7680.

253. Büngeler, A.; Hämisch, B.; Huber, K.; Bremser, W.; Strube, O. I. *Langmuir* **2017**, *33*, 6895-6901.
254. McQueenie, R.; Sutter, J.; Karolin, J.; Birch, D. J. S.; . *J. Biomed. Opt.* **2012**, *17*, 7.
255. Orlow, S. J.; Osber, M. P.; Pawelek, J. M. *Pigment Cell Research* **1992**, *5*, 113-121.
256. Mason, H. S. *J. Biol. Chem.* **1948**, *172*, 83-99.
257. Riesz, J. The Spectroscopic Properties of Melanin. Doctoral Thesis University of Queensland, 2007.
258. Raper, H. S. *Physiological Reviews* **1928**, *8*, 245-282.
259. Sugumaran, M. *Int. J. Mol. Sci.* **2016**, *17*, 1576.
260. Kishida, R.; Saputro, A. G.; Kasai, H. *Biochim. Biophys. Acta Gen. Subj.* **2015**, *1850*, 281-286.
261. da Silva, M. I. N.; Dezidério, S. N.; Gonzalez, J. C.; Graeff, C. F. O.; Cotta, M. A. *J. Appl. Phys.* **2004**, *96*, 5803-5807.
262. Katritzky, A. R.; Akhmedov, N. G.; Denisenko, S. N.; Denisko, O. V. *Pigment Cell Research* **2002**, *15*, 93-97.
263. Watt, A. A. R.; Bothma, J. P.; Meredith, P. *Soft Matter* **2009**, *5*, 3754-3760.
264. Tran, M. L.; Powell, B. J.; Meredith, P. *Biophys. J.* **2006**, *90*, 743-752.
265. Sutter, J. U.; Bidláková, T.; Karolin, J.; Birch, D. J. S. *Appl. Phys. Lett.* **2012**, *100*, 113701.
266. Napolitano, A.; Pezzella, A.; Prota, G.; Seraglia, R.; Traldi, P. *Rapid Commun. Mass Spectrom.* **1996**, *10*, 468-472.
267. Clancy, C. M. R.; Nofsinger, J. B.; Hanks, R. K.; Simon, J. D. *J. Phys. Chem. B* **2000**, *104*, 7871-7873.
268. Liu, Y.; Simon, J. D. *Pigment Cell Research* **2003**, *16*, 606-618.
269. Chen, C.-T.; Chuang, C.; Cao, J.; Ball, V.; Ruch, D.; Buehler, M. J. *Nat. Commun.* **2014**, *5*, 3859.
270. Meng, S.; Kaxiras, E. *Biophys. J.* **2008**, *94*, 2095-2105.
271. Nighswander-Rempel, S. P.; Riesz, J.; Gilmore, J.; Meredith, P. *J Chem Phys* **2005**, *123*, 194901.
272. Nighswander-Rempel, S. P.; Mahadevan, I. B.; Rubinsztein-Dunlop, H.; Meredith, P. *Photochem. Photobiol.* **2007**, *83*, 1449-1454.
273. Nighswander-Rempel, S. P.; Riesz, J.; Gilmore, J.; Bothma, J. P.; Meredith, P. *J. Phys. Chem. B* **2005**, *109*, 20629-20635.
274. Micillo, R.; Panzella, L.; Iacomino, M.; Prampolini, G.; Cacelli, I.; Ferretti, A.; Crescenzi, O.; Koike, K.; Napolitano, A.; d'Ischia, M. *Sci. Rep.* **2017**, *7*, 41532.
275. Winder, A. J.; Harris, H. *Eur. J. Biochem.* **1991**, *198*, 317-326.
276. Corani, A.; Huijser, A.; Iadonisi, A.; Pezzella, A.; Sundström, V.; d'Ischia, M. *The Journal of Physical Chemistry B* **2012**, *116*, 13151-13158.
277. Sulzer, D. *Trends Neurosci.* **2007**, *30*, 244-250.
278. Zecca, L.; Zucca, F. A.; Wilms, H.; Sulzer, D. *Trends Neurosci.* **2003**, *26*, 578-580.
279. Stainsack, J.; Mangrich, A. S.; Maia, C. M. B. F.; Machado, V. G.; dos Santos, J. C. P.; Nakagaki, S. *Inorg. Chim. Acta* **2003**, *356*, 243-248.
280. Felix, C. C.; Hyde, J. S.; Sarna, T.; Sealy, R. C. *J. Am. Chem. Soc.* **1978**, *100*, 3922-3926.

281. Sutter, J. U.; Birch, D. J. S. *Methods Appl Fluoresc* **2014**, *2*, 024005.
282. Xu, C.; Xu, K.; Gu, H.; Zheng, R.; Liu, H.; Zhang, X.; Guo, Z.; Xu, B. *J. Am. Chem. Soc.* **2004**, *126*, 9938-9939.
283. Bahri, S.; Jonsson, C. M.; Jonsson, C. L.; Azzolini, D.; Sverjensky, D. A.; Hazen, R. M. *Environ. Sci. Technol* **2011**, *45*, 3959-3966.
284. Salomaki, M.; Tupala, M.; Parviainen, T.; Leiro, J.; Karonen, M.; Lukkari, J. *Langmuir* **2016**, *32*, 4103-4112.
285. Mostert, A. B.; Powell, B. J.; Pratt, F. L.; Hanson, G. R.; Sarna, T.; Gentle, I. R.; Meredith, P. *PNAS* **2012**, *109*, 8943.
286. Lai, M.; Cai, K.; Zhao, L.; Chen, X.; Hou, Y.; Yang, Z. *Biomacromolecules* **2011**, *12*, 1097-1105.
287. Nam, H. J.; Kim, B.; Ko, M. J.; Jin, M.; Kim, J. M.; Jung, D.-Y. *Chem. Eur. J.* **2012**, *18*, 14000-14007.
288. Ye, Q.; Zhou, F.; Liu, W. *Chem. Soc. Rev.* **2011**, *40*, 4244-4258.
289. Hegazy, M. A. E.; Maklad, H. M.; Abd Elmonsif, D. A.; Elnozhy, F. Y.; Alqubiea, M. A.; Alenezi, F. A.; Al abbas, O. M.; Al abbas, M. M. *Alexandria Med. J.* **2017**, *53*, 351-360.
290. Tsukamoto, K.; Jackson, I. J.; Urabe, K.; Montague, P. M.; Hearing, V. J. *The EMBO Journal* **1992**, *11*, 519-526.
291. Micillo, R.; Panzella, L.; Koike, K.; Monfrecola, G.; Napolitano, A.; d'Ischia, M. *Int. J. Mol. Sci.* **2016**, *17*, 746.
292. Solano-Muñoz, F.; Peñafiel, R.; Galindo, J. D. *Biochem. J.* **1985**, *229*, 573-578.
293. Hamada, Y.; Rogers, C. *J. Coord. Chem.* **2007**, *60*, 2149-2163.
294. Sonsupap, S.; Kidkhunthod, P.; Chanlek, N.; Pinitsoontorn, S.; Maensiri, S. *Appl. Surf. Sci.* **2016**, *380*, 16-22.
295. Huang, X.; Wang, B.; Grulke, E. A.; Beck, M. J. *J Chem Phys* **2014**, *140*, 074703.
296. Wu, Z.; Mann, A. K. P.; Li, M.; Overbury, S. H. *J. Phys. Chem. C* **2015**, *119*, 7340-7350.
297. Molinari, M.; Parker, S. C.; Sayle, D. C.; Islam, M. S. *J. Phys. Chem. C* **2012**, *116*, 7073-7082.
298. Li, C.; Sakata, Y.; Arai, T.; Domen, K.; Maruya, K.-i.; Onishi, T. *J. Chem. Soc., Faraday Trans. 1* **1989**, *85*, 929-943.
299. Su, Y.-Q.; Filot, I.; Jin-Xun, L.; Tranca, I.; J. M. Hensen, E. *Chem. Mater.* **2016**, *28*, 5652-5658.
300. Leonard, L. J.; Townsend, D.; King, R. A. *Biochemistry* **1988**, *27*, 6156-6159.
301. Gallas, J. M.; Littrell, K. C.; Seifert, S.; Zajac, G. W.; Thiyagarajan, P. *Biophys. J.* **1999**, *77*, 1135-1142.
302. Andreescu, D.; Bulbul, G.; Özel, R. E.; Hayat, A.; Sardesai, N.; Andreescu, S. *Environ. Sci.: Nano* **2014**, *1*, 445-458.

VITA

Anne D'Achille was born in Rogers, Arkansas on September 21, 1980. She is the child of Patricia and Paul Moffitt. She graduated in 2012 from Grove City College, Grove City, Pennsylvania. She got a Bachelor in of Science with a major in Chemistry. Anne enrolled at Texas Christian University in Summer 2012 under the direction of Dr. Jeffery L Coffer to do research on cerium oxide nanomaterials.

She is married to Adam D'Achille of Beaver Falls, Pennsylvania. They have one child.

ABSTRACT

SYNTHESIS AND REACTIVITY OF FLUORESCENT RARE-EARTH DOPED CERIUM OXIDE NANOMATERIALS

by

Anne D'Achille

Department of Chemistry & Biochemistry

Advisor: Dr. Jeffery L. Coffer, Professor of Chemistry

Nanomaterials based on cerium (IV) oxide, or CeO_2, have been investigated due to interesting chemistry from the readily accessible Ce^{3+}/Ce^{4+} transition. This transition is accompanied by a gain or loss in CeO_2 oxygen and/or electrons. As a result, CeO_2 has demonstrated reversible antioxidant activity and enzyme mimetic activity, and has also been used in oxygen transport, photocatalysis, and small molecule oxidation applications. Doping CeO_2 with lower valent ions creates oxygen vacancies and increases the Ce^{3+}/Ce^{4+} ratio within the lattice. The dopant may also contribute properties such as fluorescence or magnetism to compliment the CeO_2 chemistry.

This work presents the synthesis of several europium doped-CeO_2 (Eu-CeO_2) morphologies, the investigation into parameters controlling their size, morphology, and elemental composition. Select applications highlighting differences in the materials synthesized were also investigated.

Eu-CeO_2 nanorods and nanocubes were synthesized using a hydrothermal procedure. The nanorods were also annealed to enhance their Eu^{3+} fluorescence. An electrospinning and annealing procedure was used to synthesize nanowires. The Eu:Ce

ratio for all the rods, cubes, and wires were controlled by changing the Eu^{3+} precursor concentration. Manipulation of the precursor concentrations provided minor dimension control of the rods, while changing of Ce^{3+} precursor and hydrothermal reaction time influenced the nanocube morphology.

Finally, Eu-CeO_2 nanotubes have been synthesized by layered deposition of $Ce(OH)_3$ on a sacrificial ZnO nanowire array. The hydroxide was oxidized to Eu-CeO_2 and the ZnO core etched to produce the nanotube morphology. The nanotube dimensions were controlled by the ZnO core, but low yield demands further optimization prior to use in the intended drug delivery applications.

One synthesized, the rods, cubes, and wires were analyzed for Eu^{3+}-contributed fluorescence. While the cubes and wires fluoresced as synthesized, the nanorods required annealing above 500 °C to fluoresce. Nanocubes were also synthesized with neodymium and ytterbium instead of europium. These cubes fluoresce at 800-1000nm, which is useful in bioimaging applications.

The four materials (rods, annealed rods, cubes, and wires) were also compared for their effect on the transformation of di-hydroxyphenylalanine (L-Dopa) to eumelanin. Previous CeO_2 nanoparticles have captured catechol-containing molecules by oxidation and conjugation with the -OH groups. Our Eu-CeO_2 materials suppressed eumelanin-associated fluorescence by up to 60% when added to L-Dopa early in it's transformation to eumelanin. The four morphologies exhibited very different activities, with higher Ce^{3+} concentrations and smaller crystalline domains associated with enhanced suppression of eumelanin synthesis.